Scanning Tunneling Studies on Patterned Noble Metal (111) Substrates

Dissertation
zur Erlangung des Doktorgrades
der Mathematisch-Naturwissenschaftlichen Fakultät
der Christian-Albrechts-Universität zu Kiel

vorgelegt von
Henning Jensen
Kiel, 2017

Erster Gutachter: Prof. Dr. Richard Berndt
Zweiter Gutachter: Prof. Dr. Kai Roßnagel
Tag der mündlichen Prüfung: 9. März 2018

Kurzdarstellung

Diese Arbeit beinhaltet eine Reihe von Experimenten zur Rastertunnelmikroskopie (STM) und -spektroskopie (STS). Diese wurden bei Tieftemperatur im Ultrahochvakuum an einem in der Arbeitsgruppe Prof. Berndt an der CAU Kiel entworfenen Instrument durchgeführt. Die Arbeit umfasst zwei Hauptthemenbereiche.

Den ersten Teil bildet eine Untersuchung der elektronischen Struktur der dekorierten Silber-(111)-Oberfläche. Im Brennpunkt steht hierbei die Energieabhängigkeit der Lebensdauer von Quasielektronen in Shockley-Oberflächenzuständen. Um diese experimentell zugänglich zu machen, werden durch Beschuss der Oberfläche mit Argonionen und kontrollierten Spitze–Probe-Kontakt einatomar tiefe, einige nm durchmessende, sechseckige und dreieckige Fehlstellenresonatoren erzeugt. Tunnelspektroskopie innerhalb der Resonatoren ergibt eine Reihe von energetisch verbreiterten, gebundenen Zuständen der Oberflächenelektronen. Diese lassen sich gut mit einem zweidimensionalen Potentialtopfmodell wiedergeben.

Die extrahierten Linienbreiten zeigen eine näherungsweise lineare Abhängigkeit von der Bindungsenergie. Die zwei Hauptbeiträge sind die intrinsische Breite, die aus Elektron–Elektron- und Elektron–Phonon-Übergängen erwächst, und verlustbehaftete Streuung an den Rändern der Resonatoren. Eine Abschätzung der relativen Stärken dieser Beiträge ergibt, dass für die Resonatoren der letztere den begrenzenden Faktor für die Lebensdauer darstellt. Erst unter dieser Berücksichtigung ergibt der Vergleich von verschiedenen experimentellen und errechneten Lebensdauerdaten aus der Literatur ein konsistentes Bild.

Ergänzende Experimente auf derselben Oberfläche befassen sich mit künstlichen eindimensionalen atomaren Ketten und Fehlstellenreihen. Aus den umgebenden Friedeloszillationen lässt sich die Dispersionsrelation $k(E)$ der Oberflächenelektronen ermitteln. Spektroskopie auf einatomaren Ketten weist eine Transmissionsresonanz bei 1.7 V auf. Der Vergleich mit Oligomeren Ag_n, $n \leq 3$ ergibt eine sinkende Resonanzenergie bei steigender Clustergröße. Die Fowler-Nordheim-Spektroskopie bei noch höheren Energien gibt Aufschluss über den Verlauf der Tunnelbarriere. Insbesondere lässt sich relativ zur unbedeckten Oberfläche eine Senkung der Austrittsarbeit auf atomaren Ketten beobachten.

Der zweite Teil behandelt die Adsorptionseigenschaften des Moleküls Perylen-3,4,9,10-tetracarboxyl-dianhydrid (PTCDA) auf den (111)-vizinalen Goldoberflächen Au(788), Au(433) und Au(877), bei Bedeckungen unterhalb einer Monolage. Die Substrate zeichnen sich durch eine Vielfalt an Oberflächenstrukturen in der Größenskala des Moleküls aus. Substratbereiche mit einer hohen Stufendichte begünstigen die Adsorption in Form von Molekülketten entlang der Stufen, vornehmlich solcher des {111}-Stufentyps. Andere Substrate zeigen ungestörtes zweidimensionales Inselwachstum, in den von der Au(111)-Grundoberfläche bekannten quadratischen und Fischgräten-Gitterphasen. Bei ansteigender Probenspannung findet bei den Molekülen ein Kontrastübergang statt, wobei die Übergangsenergie abhängig von der Phase um 0.35 V verschoben ist. Eine DFT-Modellrechnung identifiziert den Übergang mit dem niedrigsten unbesetzten Molekülorbital (LUMO) und erklärt die Verschiebung mit der unterschiedlichen Bindungsstärke der Wasserstoffbrücken zwischen den Molekülen.

Abstract

This thesis comprises a series of scanning tunneling microscopy (STM) and scanning tunneling spectroscopy (STS) experiments. These were performed at low temperatures, in ultra-high vacuum, on an instrument designed and built within the working group of Prof. Berndt, at CAU Kiel. The thesis covers two main topics.

Firstly, the electronic structure of the decorated (111) face of silver is explored, with a special focus on the energy dependence of quasielectron lifetimes in Shockley surface states. These are made experimentally accessible by constructing resonators in the shape of monatomically deep hexagonal and triangular surface vacancies. A few nm across, these are created by argon ion bombardment and controlled tip–substrate impacts. Within the resonators, STS shows the surface electrons confined to a series of broadened standing wave states. These are found to be described well by a particle-in-a-box model.

The linewidths show an approximately linear increase with binding energy. The two main contributions identified are the intrinsic linewidth, due to electron–electron and electron–phonon interaction, and lossy scattering at the resonator boundary. An estimate of the relative strength shows that for the resonators, the latter is the limiting factor for lifetime. With this result, comparison of various previously published experimental and calculated lifetime data yields a consistent picture.

Supplementary experiments on the same surface concern artificial one-dimensional atomic chains and vacancy rows. Study of the surrounding Friedel oscillations yields access to the surface state dispersion $k(E)$. Spectroscopy reveals a transmission resonance peak at 1.7 V on the monatomic chain. Comparison to adsorbed oligomers Ag_n, $n \leq 3$ shows a decrease in energy with increasing cluster size. At even higher energies, Fowler-Nordheim spectroscopy allows access to the shape of the tunneling barrier. Specifically, the sample work function is found to be reduced on the nanostructures, relative to clean Ag(111).

The second part explores the adsorption characteristics of submonolayers of the perylene-3,4,9,10-tetracarboxylic-dianhydride (PTCDA) molecule on the vicinal gold (111) surfaces Au(788), Au(433), and Au(877), known for several structural features at the molecular scale. Substrate areas with a high step density are found to prefer formation of molecular chains along the steps, with a strong preference of {111} type steps. Otherwise undisturbed island formation in the herringbone and square phases known from Au(111) is seen, with a substrate-influenced lattice orientation. With increasing sample bias, the molecules were found to undergo a contrast transition in STM, at an energy that is shifted by 0.35 V between the two phases. A DFT model calculation suggests that the transition energy correlates to the LUMO, and the shift is due to a variation in intermolecular hydrogen bond strength.

Preface

My STM and STS efforts encompass multiple broad topics, all of which have come to fruition in the form of articles, or parts thereof, in peer-reviewed journals. These results, and some additional unpublished ones, are compiled here. Additionally, I have included a detailed description of the instrumental setup and operating techniques, with a special emphasis on the properties of the lock-in amplifier, an invaluable tool in STS.

The first part deals with the confinement of Shockley surface states [210] on a Ag(111) surface within closed resonators on the nanometer scale, constructed out of monatomic surface steps. The main focus lies on modeling the resulting bound states of the quasielectrons and gaining access to their mean lifetimes.

Related experiments have previously been done by Li *et al.* [142], for upward steps (island resonators). It is known that ion bombardment of the same surface allows to easily create hexagonal vacancy resonators (downward steps) [163, 197], and these complementary structures are excellent candidates for continuing this line of inquiry, examining the influence the step type has on the confinement. This also provides continuation of my diploma research [108], that aimed to reproduce the results of Li *et al.* on the newly home-built instrument, in order to test its function and capabilities.

A variety of vacancy resonators are characterized by STM and point spectroscopy, and the linewidths and lifetimes of the bound states are extracted, both by a individual peak-fitting approach and from a more general particle-in-a-box model. These lifetimes are compared with previous data, from hexagonal islands [142], quantum corrals [29, 122], single and double steps [31, 32], and theoretical results [58, 231]. The apparent initial disagreement between these sources is addressed by ascertaining the relative contributions of the individual possible decay paths, in order to provide a more unified picture.

Another experiment dealt with the deposition of small clusters Ag_n, $n \leq 3$ from the substrate-covered tip, by controlled contacts [145]. The electronic structure of the deposited oligomers is compared to previous results on other materials [64, 133, 173], where a downward shift of a transmission resonance peak with cluster size is seen. As an offshoot, the substrate damage incurred by stronger tip indentations may give rise to artificial surface structures such as perfectly triangular vacancy islands, and atomic chains and trenches. The former are used to complement the lifetime studies above, while the latter are examined for transmission resonance, surface state dispersion, and tunneling barrier measurements.

The second part of my work focused on the self-assembly of molecular monolayers. In a time where organic semiconductors are rapidly making the transition from laboratory specimens to the consumer goods industry, insights on the arrangement and properties of molecular films, as they are grown in a top-down fashion, promise broad technical relevance.

As organic semiconductors go, the robust planar molecule PTCDA is a preferred model system, into which much research interest has previously been focused. Here, the idea is to influence its adsorption behavior by choosing vicinal Au(111) substrates [12], which can be considered variants of the base surface (whose PTCDA adsorption behavior has previously been well characterized [39, 205]), introducing an additional one- or two-dimensional periodicity at the size scale of the molecules [201]. This allows to ascertain which geometries of step arrays, refaceting, and reconstruction modify the make-up of a PTCDA film.

An available transition metal dichalcogenide (TMDC) crystal, 2H–$NbSe_2$, provides a radically different substrate with another type of surface periodicity beyond the atomic lattice scale, in the form of a charge-density wave (CDW) instability [169], the influence of which on a nascent PTCDA film can be assessed.

Table of contents

List of figures and tables

Chapter 1

Introduction

As the name implies, the scanning tunneling microscope (STM) combines two experimental procedures to provide a device capable of imaging at small scales: real-space two-dimensional scanning and measurement of a current due to quantum mechanical tunneling of electrons.

Preceding quantum theory, the tunnel effect was experimentally observed in field emission and radioactivity experiments. First formulations of the discovery of the effect were presented by Hund in 1927 [102], in the context of molecular isomerism, and Gamov in 1928 [73], as a mathematical explanation for alpha decay. Experimental results of tunneling across solid body interfaces were presented in the 1960s by Giaever and others in the context of metal–insulator–metal sandwich structures [76]. These catalyzed the development of a body of theoretical models and methods that would, twenty years later, serve as the foundation of STM theory.

Experimental progress toward STM has been accomplished at NIST, in the 1970s: Imagery by means of scanning a probe across a sample region was previously obtained by the STM's direct developmental precursor, the Topografiner [241] presented by Young, Ward and Scire in 1972. In this device, probe–sample interaction was mediated by field emission rather than by the quantum mechanical tunnel effect. Tunneling across a controllable vacuum gap was realized by Teague in 1978 [223]. In 1981, Binnig, Rohrer, Gerber, and Weibel merged the concepts of vacuum tunneling with an adjustable gap [20] and a scanning probe, to present the Scanning Tunneling Microscope [19]. The scanning tunneling microscope, for the first time, allowed a nanoscopic glimpse into the world of solid body surfaces, realizing a long-held desire to directly visualize discrete structures on an atomic scale. The potential of the device was demonstrated early on, when it resolved the long-standing structural mystery of the Si(111)–7×7 reconstruction [21, 53]. The invention earned Gerd Binnig and Heinrich Rohrer the 1986 Nobel Prize in Physics. The palpable real-space nanoscopic imagery of STM provided a stark contrast – and a welcome complement – to the plethora of modern approaches to measure atomic structure indirectly, such as electron diffraction and grazing incidence X-ray scattering.

Since then, the realm of scanning probe methods has been constantly expanding in both breadth and depth, ranging from custom-built laboratory setups to standard instruments available from a multitude of commercial vendors, supplying thousands of installations in the fields of physics, chemistry, microbiology, and others.

Many variant techniques based on STM have been developed. Exploring the point spectroscopy capabilities of the STM afforded a uniquely localized method for probing the electronic structure of conducting surfaces [208], supplementing spectroscopy techniques averaging over extended surface regions, such as photoelectron spectroscopy. Video-STM employs ultra-fast scanners designed to visualize the temporal progress of, *e.g.*, diffusion processes, at frame rates of multiple images per second. Light emitted from the tunneling junction allows to locally study electronic relaxation processes [45, 113]. Spin polarized STM uses probes coated with a magnetic material and allows spin-sensitive imaging of magnetic surface phenomena, such as the exact geometry of domain wall boundaries, and switching of magnetic particles [24, 237].

In the related technique of atomic force microscopy (AFM), presented in 1986 by Binnig, Quate, and Gerber [18], the interaction between sample and probe is mediated by the forces present between them, instead of a tunneling current, thereby extending scanning probe methods to non-conducting surfaces.

1.1 The one-dimensional rectangular barrier

The interaction of a free electron with a rectangular potential barrier is a classical textbook topic [214] that can serve as a simple model for the treatment of a tunneling problem. The potential is parametrized by its width z_0 and barrier height U_0,

$$U(z) := \begin{cases} 0 & \text{for } z < 0 \\ U_0 & \text{for } 0 < z < z_0 \\ 0 & \text{for } z > z_0. \end{cases} \tag{1.1}$$

The wavefunction of an electron within this potential is calculated using the one-dimensional time-independent Schrödinger equation,

$$-\frac{\hbar^2}{2m_\mathrm{e}}\psi''(z) = [E - U(z)]\psi(z), \tag{1.2}$$

and the solution depends on the relation between barrier height and particle energy E. In the case $E < U_0$, the barrier is classically impenetrable. The solutions to (1.2) are free electron waves outside of the barrier, with a wavenumber $k := \sqrt{2m_\mathrm{e}E}\big/\hbar$, and behave exponentially within, with a decay constant $\varkappa := \sqrt{2m_\mathrm{e}(U_0 - E)}\big/\hbar$. The local solutions left, inside, and right of the barrier, respectively, are

$$\psi(z) = \begin{cases} \psi_1(z) := a\exp(\mathrm{i}kz) + r\exp(-\mathrm{i}kz) & \text{for } z < 0 \\ \psi_2(z) := c\exp(-\varkappa z) + d\exp(\varkappa z) & \text{for } 0 \le z \le z_0 \\ \psi_3(z) := t\exp(\mathrm{i}kz) + b\exp(-\mathrm{i}kz) & \text{for } z > z_0. \end{cases} \tag{1.3}$$

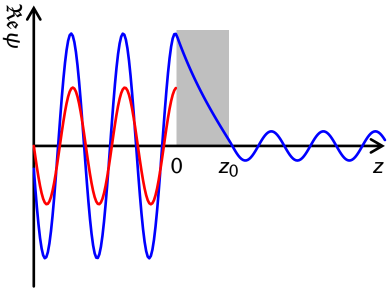

Figure 1.1 – Tunneling through a rectangular barrier (gray) whose height exceeds the electron energy. The solution is calculated for $k = 2\pi/z_0$, $T = 1/16$, for an outbound wave on the right hand side (see text). The wavefunction (blue) is oscillatory in the allowed regions outside the barrier and decays exponentially inside. Most of the incident part of the wavefunction (red) is reflected at the barrier.

Joining them in a way that both the global solution and its derivative are continuous, then eliminating the coefficients inside the barrier, c and d, yields expressions for t and r, as functions of a and b:

$$t = \frac{2\exp(-\mathrm{i}kz_0)a - \mathrm{i}\left(\frac{\varkappa}{k} + \frac{k}{\varkappa}\right)\exp(-2\mathrm{i}kz_0)\sinh(\varkappa z_0)b}{2\cosh(\varkappa z_0) + \mathrm{i}\left(\frac{\varkappa}{k} - \frac{k}{\varkappa}\right)\sinh(\varkappa z_0)} \tag{1.4}$$

and

$$r = \frac{2\exp(-\mathrm{i}kz_0)b - \mathrm{i}\left(\frac{\varkappa}{k} + \frac{k}{\varkappa}\right)\sinh(\varkappa z_0)a}{2\cosh(\varkappa z_0) + \mathrm{i}\left(\frac{\varkappa}{k} - \frac{k}{\varkappa}\right)\sinh(\varkappa z_0)}. \tag{1.5}$$

For the tunneling problem, it is assumed that the wave is incident from the left only, hence $a \neq 0$, $b := 0$. Transmission and reflection probabilities can be obtained from the coefficients for the transmitted (outbound right) and reflected (outbound left) wave, t and r, via

$$T = \left.\frac{|t|^2}{|a|^2}\right|_{b=0} = \frac{4}{4 + \left(\frac{\varkappa}{k} + \frac{k}{\varkappa}\right)^2 \sinh^2(\varkappa z_0)} = \frac{4}{4 + \frac{U_0^2}{E(U_0 - E)}\sinh^2(\varkappa z_0)} \tag{1.6}$$

and

$$R = \left.\frac{|r|^2}{|a|^2}\right|_{b=0} = \frac{\left(\frac{\varkappa}{k} + \frac{k}{\varkappa}\right)^2 \sinh^2(\varkappa z_0)}{4 + \left(\frac{\varkappa}{k} + \frac{k}{\varkappa}\right)^2 \sinh^2(\varkappa z_0)} = 1 - T. \tag{1.7}$$

For suitably high and wide barriers, $\varkappa z_0 \gg 1$, (1.6) can be approximated, and the transmissivity decays exponentially with the barrier width:

$$T(z_0) \propto \exp(-2\varkappa z_0) = \exp\left(-\frac{\sqrt{8m_\mathrm{e}(U_0 - E)}}{\hbar} z_0\right). \tag{1.8}$$

For shallow barriers, where $U_o < E$, the solutions remain oscillatory inside the barrier, with a wavenumber $\gamma := \sqrt{2m_\mathrm{e}(E - U_0)}\big/\hbar$. The calculation of T and R proceeds analogously, and the solutions above can be reused with $\varkappa := -\mathrm{i}\gamma$. In contrast to the classical case, where $T \equiv 1$, the transmissivity is slightly oscillatory in character.

1.2 The tunneling current

An analytical solution of the tunneling problem is only viable for very simple potentials. Tunneling through an arbitrarily shaped potential barrier $U(z)$ can be treated using the semiclassical WKB method. This technique [105] was introduced by Wentzel, Kramers, and Brillouin [30, 125, 236] to obtain approximate solutions for the Schrödinger equation. These solutions are characterized by constant amplitude and varying phase in the classically allowed regions, and constant phase and varying amplitude within the classically forbidden regions. The WKB method gives a value of

$$T_U(z_0,E) \approx \exp\left[-\frac{\sqrt{8m_\mathrm{e}}}{\hbar}\int\limits_0^{z_0}\sqrt{U(z)-E}\,\mathrm{d}z\right] \tag{1.9}$$

for the tunneling probability of an electron of energy E through a potential barrier $U(z) > E$, $0 \le z \le z_0$. The actual shape of the potential barrier depends on the work functions Φ_T, Φ_S for the two electrodes, and an externally applied voltage V between them. Neglecting the influence of the image potential (see section 4.3), the barrier takes on a trapezoidal shape [211]. The energy levels involved in this calculation are illustrated in fig. 1.2. The potential is given by

$$U(z) = E_\mathrm{FS} + \left(\Phi_T + q_\mathrm{e}V\right) + \left(\Phi_S - \Phi_T - q_\mathrm{e}V\right)\frac{z}{z_0}. \tag{1.10}$$

The integral in (1.9) is approximated by a rectangular barrier with an apparent height [135], by evaluating the integrand at a representative position [123]. At $\frac{z_0}{2}$, this gives

$$\int\limits_0^{z_0}\sqrt{U(z)-E}\,\mathrm{d}z \approx \sqrt{\frac{\Phi_T+\Phi_S+q_\mathrm{e}V}{2}-(E-E_\mathrm{FS})}\,z_0. \tag{1.11}$$

With this and (1.9), a tunneling probability of

$$T(z_0,V,E) \approx \exp(-2\kappa z_0) \quad \text{with} \quad \kappa(V,E) = \sqrt{\frac{2m_\mathrm{e}}{\hbar^2}\left[\frac{\Phi_T+\Phi_S+q_\mathrm{e}V}{2}-(E-E_\mathrm{FS})\right]} \tag{1.12}$$

is obtained[1].

Densities of states. Additionally, realistic calculations of the tunneling junction need to take into account the electronic structure of the electrodes. In the context of metal–insulator–metal junctions, a many-body approach was proposed by Bardeen in 1961 [9], that is also applicable to elastic vacuum tunneling. The occupation of electronic states in

---

[1] For a typical metal–vacuum–metal tunneling setup, realistic values of $q_\mathrm{e}V \ll \Phi_T \approx \Phi_S \approx 4.5$ eV yield a κ^{-1} around 0.09 nm. Under such conditions, the tunneling current changes by almost an order of magnitude when varying the tip z position by just a tenth of a nanometer.

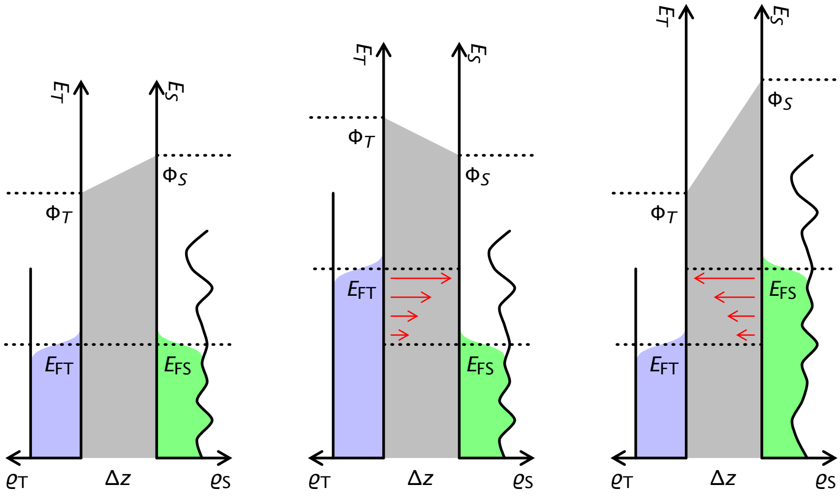

Figure 1.2 – Schematic energy diagram of the tunneling junction, after Simmons [211]. **(a)** The graphs represent densities of states of tip (ϱ_{T}, left) and sample (ϱ_{S}, right), filled up with electrons up to their respective Fermi energies E_{FT}, E_{FS} (colored regions). The distances between Fermi and vacuum levels are given by the work functions, Φ_T and Φ_S. The spatial shape of the tunnel barrier (in trapezoidal approximation) is shown in the center of the image (gray region). At zero bias voltage, tip and sample Fermi energies are identical. **(b)** A positive sample bias V results in a relative shift of Fermi levels, giving $E_{\mathrm{FT}} = E_{\mathrm{FS}} + q_{\mathrm{e}} V$. Elastic tunneling is possible in the energy range between the two Fermi levels, where occupied tip states and unoccupied sample states are matched up across the junction. Higher energies contribute more strongly to the total tunneling current (arrows). They have a higher transition probability, as they face a lower apparent height of the tunneling barrier. **(c)** Likewise, a negative sample bias results in a relative shift in the opposite direction, allowing a corresponding electron flow from occupied sample states to vacant tip states.

both tip and sample, as a function of electron energy E, is governed by the Fermi-Dirac distribution F, which is given by

$$F(E) = \frac{1}{1 + \exp((E - E_{\mathrm{F}})/k_{\mathrm{B}} T)}. \tag{1.13}$$

Thus, given a density of tip states ϱ_{T}, the density of occupied tip states ϱ_{To} at a given energy E_T (and that of occupied sample states at E_S accordingly) can be calculated by

$$\begin{aligned} \varrho_{\mathrm{To}}(E_T) &= \varrho_{\mathrm{T}}(E_T) F(E_T - E_{\mathrm{FT}}) \\ \varrho_{\mathrm{So}}(E_S) &= \varrho_{\mathrm{S}}(E_S) F(E_S - E_{\mathrm{FS}}). \end{aligned} \tag{1.14}$$

Likewise, the densities of unoccupied tip and sample states at the same energies are given by

$$\begin{aligned} \varrho_{\mathrm{Tu}}(E_T) &= \varrho_{\mathrm{T}}(E_T) \bar{F}(E_T - E_{\mathrm{FT}}) \\ \varrho_{\mathrm{Su}}(E_S) &= \varrho_{\mathrm{S}}(E_S) \bar{F}(E_S - E_{\mathrm{FS}}), \end{aligned} \tag{1.15}$$

with the inverse Fermi-Dirac function,

$$\bar{F}(E) := 1 - F(E) = F(-E). \tag{1.16}$$

For elastic tunneling processes, E_S and E_T must be equal. Additionally, when an external sample bias voltage is applied, the energy levels shift as in fig. 1.2b,c, giving

$$E_S - E_{\mathrm{FS}} = E_T - E_{\mathrm{FT}} + q_{\mathrm{e}}V =: \epsilon. \tag{1.17}$$

The current contributed by electrons tunneling elastically from tip to sample can be calculated by energetically juxtaposing occupied tip states and vacant sample states:

$$\begin{aligned} I_{\mathrm{T}\to\mathrm{S}} &= \int_{-\infty}^{\infty} \varrho_{\mathrm{To}}(E_{\mathrm{FT}} - q_{\mathrm{e}}V + \epsilon)\varrho_{\mathrm{Su}}(E_{\mathrm{FS}} + \epsilon)T(z_0, V, E_{\mathrm{FS}} + \epsilon)\mathrm{d}\epsilon \\ &= \int_{-\infty}^{\infty} \varrho_{\mathrm{T}}(E_{\mathrm{FT}} - q_{\mathrm{e}}V + \epsilon)F(\epsilon - q_{\mathrm{e}}V)\varrho_{\mathrm{S}}(E_{\mathrm{FS}} + \epsilon)\bar{F}(\epsilon)T(z_0, V, E_{\mathrm{FS}} + \epsilon)\mathrm{d}\epsilon. \end{aligned} \tag{1.18}$$

Similarly, the current from sample to tip can be obtained by

$$I_{\mathrm{S}\to\mathrm{T}} = \int_{-\infty}^{\infty} \varrho_{\mathrm{T}}(E_{\mathrm{FT}} - q_{\mathrm{e}}V + \epsilon)\bar{F}(\epsilon - q_{\mathrm{e}}V)\varrho_{\mathrm{S}}(E_{\mathrm{FS}} + \epsilon)F(\epsilon)T(z_0, V, E_{\mathrm{FS}} + \epsilon)\mathrm{d}\epsilon. \tag{1.19}$$

In the limit of low temperatures, the Fermi-Dirac distribution approximates a step function, sharply cutting off the occupation of states above the Fermi level,

$$\lim_{T\to 0} F(E - E_{\mathrm{F}}) = \Theta(E_{\mathrm{F}} - E) := \begin{cases} 1 \text{ for } E < E_{\mathrm{F}} \\ \frac{1}{2} \text{ for } E = E_{\mathrm{F}} \\ 0 \text{ for } E > E_{\mathrm{F}} \end{cases} \tag{1.20}$$

and

$$\lim_{T\to 0} \int_{-\infty}^{\infty} g(\epsilon)\bar{F}(\epsilon - E_0)F(\epsilon - E_1)\mathrm{d}\epsilon = \begin{cases} \int_{E_0}^{E_1} g(\epsilon)\mathrm{d}\epsilon & \text{for } E_0 < E_1 \\ 0 & \text{for } E_0 \geq E_1. \end{cases} \tag{1.21}$$

Hence, in the low temperature limit, the currents are given by

$$I_{\mathrm{T}\to\mathrm{S}} = \begin{cases} 0 & \text{for } V \leq 0 \\ \int_0^{q_{\mathrm{e}}V} \varrho_{\mathrm{T}}(E_{\mathrm{FT}} - q_{\mathrm{e}}V + \epsilon)\varrho_{\mathrm{S}}(E_{\mathrm{FS}} + \epsilon)T(z_0, V, E_{\mathrm{FS}} + \epsilon)\mathrm{d}\epsilon & \text{for } V > 0 \end{cases} \tag{1.22}$$

and

$$I_{\mathrm{S}\to\mathrm{T}} = \begin{cases} \int_{q_{\mathrm{e}}V}^0 \varrho_{\mathrm{T}}(E_{\mathrm{FT}} - q_{\mathrm{e}}V + \epsilon)\varrho_{\mathrm{S}}(E_{\mathrm{FS}} + \epsilon)T(z_0, V, E_{\mathrm{FS}} + \epsilon)\mathrm{d}\epsilon & \text{for } V < 0 \\ 0 & \text{for } V \geq 0. \end{cases} \tag{1.23}$$

It follows that regardless of the polarity of V, the expression for the net tunneling current is

$$I(V) = I_{\mathrm{T}\to\mathrm{S}} - I_{\mathrm{S}\to\mathrm{T}} = \int_0^{q_{\mathrm{e}}V} \varrho_{\mathrm{T}}(E_{\mathrm{FT}} - q_{\mathrm{e}}V + \epsilon)\varrho_{\mathrm{S}}(E_{\mathrm{FS}} + \epsilon)T(z_0, V, E_{\mathrm{FS}} + \epsilon)\mathrm{d}\epsilon. \tag{1.24}$$

Lateral resolution. In the preceding sections, the developed theory has been strictly one-dimensional. Hence, it makes no statements regarding the relationship between the tunneling current and the lateral geometry of the tip–sample junction. A seminal treatment of this problem was presented by Tersoff and Hamann in 1983 [224], and is briefly outlined below.

The current between tip and sample is calculated according to Bardeen's tunnel matrix element formalism [9]. In this, the electronic structures of isolated tip and sample are considered. The interaction is calculated from the overlap of the undisturbed wavefunctions. This involves integrating the current operator across a surface within the gap separating tip and sample. The exact topography of this boundary surface is not relevant, as long as it lies well within the evanescent regions of both tip and sample wavefunctions.

The surface electronic structure is expanded in terms of Bloch functions. The tip model is restricted to a locally spherical apex. As the tip states are generally not known, its electronic structure is modeled using radially symmetric wavefunctions. The tunneling current is then roughly proportional to the electron density of the noninteracting sample at the center of the tip curvature.

The lateral resolution obtainable in practice, however, is significantly finer than the tip apex. A method of considering further tip states within the same framework is given by Chen's derivative rule [37].

1.3 The differential tunneling conductance

The differential conductance is defined as the derivative of the net tunneling current (1.24), with regard to the applied sample bias. Calculating this quantity gives

$$\begin{aligned}\frac{\mathrm{d}I}{\mathrm{d}V}(V) = & -q_\mathrm{e}\int_0^{q_\mathrm{e}V}\frac{\mathrm{d}\varrho_\mathrm{T}}{\mathrm{d}E}(E_\mathrm{FT}-q_\mathrm{e}V+\epsilon)\varrho_\mathrm{S}(E_\mathrm{FS}+\epsilon)T(z_0,V,E_\mathrm{FS}+\epsilon)\mathrm{d}\epsilon \\ & +\int_0^{q_\mathrm{e}V}\varrho_\mathrm{T}(E_\mathrm{FT}-q_\mathrm{e}V+\epsilon)\varrho_\mathrm{S}(E_\mathrm{FS}+\epsilon)\frac{\partial T}{\partial V}(z_0,V,E_\mathrm{FS}+\epsilon)\mathrm{d}\epsilon \\ & +q_\mathrm{e}\varrho_\mathrm{T}(E_\mathrm{FT})\varrho_\mathrm{S}(E_\mathrm{FS}+q_\mathrm{e}V)T(z_0,V,E_\mathrm{FS}+q_\mathrm{e}V).\end{aligned} \tag{1.25}$$

The main objective of STS is the recovery of the sample LDOS from this expression. Various methods have been devised to this end [123, 219, 227, 243]. The three terms making up (1.25) can be considered individually. The third term in (1.25) contains ϱ_S at the energy $q_\mathrm{e}V$, multiplied by the constant $\varrho_\mathrm{T}(E_\mathrm{FT})$. This means that when the other two terms can be eliminated, the density of sample states remains, although weighted with the exponentially (and thus, monotonously) increasing transmission probability. The first term in (1.25) varies when different tip and sample states are matched up energetically, while they undergo a relative energy shift due to the sample bias (see fig. 1.2). It contains the energy derivative of the density of tip states. Therefore, it vanishes when ϱ_T is constant. This can be worked toward by the choice of suitable tip material preparation techniques.

The second term reflects how a change in the bias voltage affects the transmission probability via the effective height of the tunneling barrier. A detailed discussion of this term, and a method to correct for it, were given by Koslowski *et al.* [123]. For bias voltages well below the effective barrier height, $|2q_\mathrm{e}V| \ll \Phi_T + \Phi_S$, the decay length from (1.12) can be expanded, giving

$$\kappa(V,E) \approx \sqrt{\kappa_0^2 + \frac{2m_\mathrm{e}q_\mathrm{e}V}{\hbar^2}} \approx \kappa_0 + \frac{m_\mathrm{e}q_\mathrm{e}V}{\hbar^2\kappa_0} + \mathcal{O}\left(V^2\right), \tag{1.26}$$

resulting in

$$\frac{\partial T}{\partial V}(z_0,V,E) = -2z_0\exp(-2\kappa z_0)\frac{\partial}{\partial V}\kappa(V,E) \approx -\frac{2m_\mathrm{e}q_\mathrm{e}z_0}{\hbar^2\kappa_0}T(z_0,V,E). \tag{1.27}$$

Hence, the second term in (1.25) is roughly proportional to the tunneling current (1.24) itself. In principle, since the tunneling current can be acquired simultaneously, this term can be compensated for. There is, however, a dependence on the potential barrier shape, the work functions Φ_T, Φ_S, and the effective tunneling gap, z_0.

Without such a correction, this term still conveys a monotonous background which is smooth and structureless in voltage ranges where there are no abrupt variations in density of sample states. Its presence does not preclude a qualitative interpretation of spectral features, although such a background may energetically shift certain features [123, 134, 243].

1.4 STM operating modes

Even a basic STM is a versatile instrument that can be operated in a variety of lateral scanning and point spectroscopy modes, exploring the tunneling gap properties in $I(V)$, $I(z)$, $z(V)$, and their derivatives. The following common modes of operation were used in this work.

Topography. In principle, the geometric structure of the sample can be assessed by scanning the tip across the surface, and monitoring the tunneling current. As shown in (1.12), the current has an exponential relation to the gap separation, hence a high current corresponds to elevated surface areas, and a low current to depressions.

In practice, the range of permissible surface elevations is severely restricted. At too large gap separations, the exponentially decreasing current falls below the detection limit. If the elevation of a surface feature exceeds the initial gap size, an uncontrolled and potentially destructive tip–sample contact will result. Additional disturbances may result from nonlinearities in the piezo response, and mismatch between sample and scan planes.

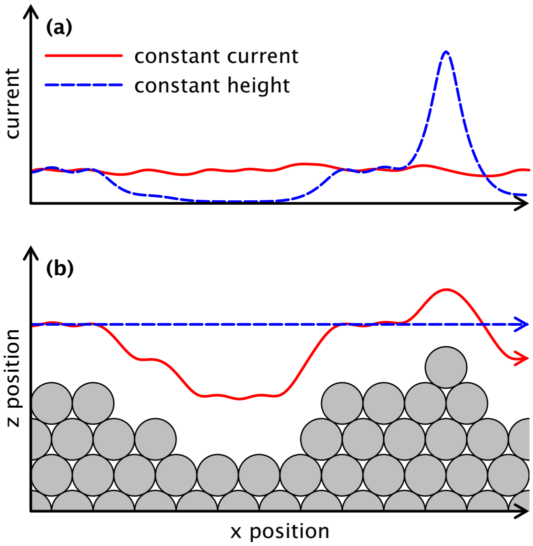

Figure 1.3 – Scanning in topography mode. As the tip is moved laterally across the surface at a constant z position, the tunneling current varies exponentially with the local gap separation (blue curve). The sample corrugation is reflected in the current signal, albeit at low z range and linearity. If a feedback loop adjusts the tip z position, maintaining a constant current, the z control signal follows a trajectory of constant integral LDOS (red curve, see text). This allows to map the surface topography of highly corrugated samples.

Due to this, measurements of the sample topography are customarily done with an activated $z(I)$ feedback loop that adjusts the tip z position in order to keep the tunneling current constant. If this is done, the corrugation of the sample can be recovered from the z control signal. At predetermined points during the scan (typically forming an equidistant grid), the tip z position (or the feedback loop output) is sampled. A two-dimensional contour image is then constructed from the sampled data points.

Strictly speaking, the notion of an exact topographic boundary of a surface is invalid in quantum mechanics. This operating mode generates a map of z positions where the tunneling current is equal to a specific setpoint value. As shown in (1.24), assuming a suitable tip, this corresponds to a contour where the integral (from the Fermi level up to the selected sample bias voltage) over the density of states (weighted by the tunneling probability) is constant.

Constant height spectroscopy. Another frequently performed task is the acquisition of a constant height $\mathrm{d}I/\mathrm{d}V$ spectrum, in order to probe the local density of states of the sample. This can be done in a standalone fashion or as a part of an ongoing lateral scan, in which the tip movement is paused and acquisition is triggered at specified points.

To acquire a constant height spectrum, the feedback loop is suspended, and both the lateral position of the tip and the tip-sample distance are held fixed. The sample bias is then ramped across the desired voltage range. During the ramp, a series of values for the tunneling current can be sampled. As demonstrated in (1.25), the derivative of the $I(V)$ curve corresponds to the local density of states. However, a numerical derivative of a current curve tends to over-emphasize high frequency noise present in the spectrum.

To overcome this, the derivative of the tunneling current, $\mathrm{d}I/\mathrm{d}V$, is measured using a lock-in amplifier. A small sinusoidal modulation is added to the bias voltage, and the spectral component of the tunneling current at the modulation frequency is detected, while performing the ramp. Details for this technique are given in appendix A. Before a set of measurements, the lock-in phase is adjusted with the tip retracted, to eliminate the capacitive response.

At each data point, the voltage is maintained for a specific dwell time, in order for the lock-in amplifier output to settle. After this, the lock-in output is recorded, along with bias voltage and tunneling current values. For further processing, rescaling to physical quantities and normalization may have to be performed, described below. To improve signal quality, oversampling may be employed at each data point. Additionally, several spectra are typically acquired sequentially at the same lateral position, to be averaged later. The feedback loop can then be engaged briefly between spectra, to reposition the tip and account for thermal drift and piezo creep effects[2].

Constant current spectroscopy. If the z feedback loop is kept active during spectroscopy, the resulting spectra are called constant current spectra. The tip–sample distance is varied at each data point, usually increasing monotonously with the absolute value of the sample bias.

Due to the variable gap during the spectrum, the obtained spectra are more difficult to interpret in physical terms. However, constant current spectroscopy can be advantageous when measuring across large voltage ranges. Since the $I(V)$ curve often has an exponential behavior, constant height spectroscopy may exhaust the input ranges of transimpedance and lock-in amplifiers. As a drawback of the constant current method, if the voltage range crosses or approaches zero, the feedback loop, while trying to maintain the target current, may drive the tip into uncontrolled physical contact with the sample. Hence, constant current spectroscopy is usually restricted to one side of the voltage axis, probing either occupied or vacant states during a single run.

Differential conductance mapping. The lateral scanning from the topography mode can be combined with the detection of the local density of states. Scanning on a fixed plane is problematic for most surfaces, due to the risk of tip–sample contacts, and the small z range in which the signal is detectable. This means that differential conductance maps are usually taken with activated feedback loop, in constant current mode.

Typically, several maps are acquired in sequence, with one setting for the sample bias per image, or occasionally, a single image with one voltage per scanline. The maps show the spatial distribution of the local density of states or, more exactly, the relative contribution of sample states at the bias energy to the total tunneling current.

Offset correction. The signal path may induce both current and voltage offsets. These may be catastrophic if undetected, as a voltage offset results in an unwarranted artificial energy shift of spectral features. Furthermore, once a measurement is finished, the

---

[2] The magnitude of these effects can be ascertained, *e.g.*, by reversing the ramp direction and comparing the resulting spectra.

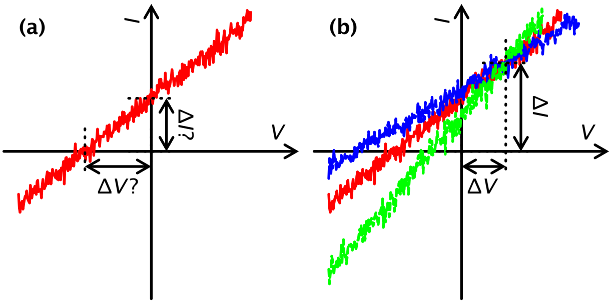

Figure 1.4 – Offset correction example for constant height current spectra (simulated data). **(a)** If an $I(V)$ curve misses the zero point, this cannot be unambiguously identified as a bias or current offset. **(b)** The tunneling gap is manually varied during a series of spectra. The real zero point is located where the line bundle intersects.

datasets cannot be unambiguously corrected for these offsets. Hence, care must be taken to detect and eliminate such offsets during the measurement.

If a constant height $I(V)$ curve shows a nonzero current at zero bias, this indicates a problem, but gives no indication if this is due to an offset in bias, current, or the interplay of both (see fig. 1.4a). Even if the intercept current is zero, a coincidental canceling of bias and current offset effects cannot be ruled out.

To independently determine bias and current offsets, the width of the tunneling gap is manually varied while acquiring a series of spectra. This produces a bundle of differently sloped curves that should, disregarding noise, meet in a single point (see fig. 1.4b). Offset correction may then be applied to move this point to zero bias, zero current. After that, measurements can commence for as long as these offsets are stable for, *e.g.*, thermal drift, while regularly rechecking.

Rescaling to physical quantities. The output signal of a standalone lock-in amplifier is given in volts, relative to full scale, and depends on the specific amplifier model, range and sensitivity settings. While this may be sufficient for a qualitative overview of spectral features, the recorded output needs to be normalized in order to recover a meaningful physical quantity.

In the case of constant height spectroscopy, normalization can be performed when tunneling current and $\mathrm{d}I/\mathrm{d}V$ signals are acquired simultaneously, as is usually the case. The tunneling current itself is acquired in absolute physical units, and while the $\mathrm{d}I/\mathrm{d}V$ may in principle be obtained by numerical differentiation, noise typically precludes a accurate normalization on this basis. However, the inverse approach can be used. Assuming the lock-in output is given by a scaled multiple m of the real $\mathrm{d}I/\mathrm{d}V$ signal, plus a constant offset from, *e.g.*, imperfect phase setting,

$$D_{\mathrm{meas.}} = mD_{\mathrm{phys.}} + D_0, \tag{1.28}$$

this can be numerically integrated, giving a synthetic current signal

$$I_{\text{synth.}} = mI_{\text{phys.}} + D_0V + I_0 \approx mI_{\text{meas.}} + D_0V + \tilde{I}_0. \tag{1.29}$$

By fitting this re-synthesized current to the measured signal, the coefficients m and D_0 are obtained, and by inserting those into (1.28), the $\mathrm{d}I/\mathrm{d}V$ signal in absolute physical units (*e.g.*, in Ω^{-1}). In constant current measurements, this technique is unavailable.

Normalization. As stated above, the density of sample states ϱ_S in (1.25) (first term) is weighted by the transmission probability, which is dependent on both the sample bias and the effective gap width. This distorts the relative amplitudes of spectral features, obstructing the comparison of spectra taken with different gap geometries. To correct for this effect, several different approaches have been developed. Feenstra *et al.* have suggested to obtain ϱ_S from the logarithmic derivative

$$\varrho_\mathrm{S}(E_\mathrm{FS} + q_\mathrm{e}V) \propto \frac{\mathrm{d}\ln I(V)}{\mathrm{d}\ln V} = \frac{\mathrm{d}I(V)/\mathrm{d}V}{I(V)/V} \tag{1.30}$$

instead [62]. Starting from the expressions for current and differential conductivity, (1.24) and (1.25), for a constant density of tip states, $\varrho_\mathrm{T}(E_T) = \bar{\varrho}_\mathrm{T}$,

$$\frac{\mathrm{d}I}{\mathrm{d}V}(V) = q_\mathrm{e}\bar{\varrho}_\mathrm{T}\varrho_\mathrm{S}(E_\mathrm{FS} + q_\mathrm{e}V)T(z_0, V, E_\mathrm{FS} + q_\mathrm{e}V) - \frac{2m_\mathrm{e}q_\mathrm{e}z_0}{\hbar^2\kappa_0}I(V) \tag{1.31}$$

the logarithmic derivative is given by

$$\begin{aligned}\frac{\mathrm{d}I(V)/\mathrm{d}V}{I(V)/V} &\propto \frac{q_\mathrm{e}V\varrho_\mathrm{S}(E_\mathrm{FS} + q_\mathrm{e}V)T(z_0, V, E_\mathrm{FS} + q_\mathrm{e}V)}{\int_0^{q_\mathrm{e}V}\varrho_\mathrm{S}(E_\mathrm{FS} + \epsilon)T(z_0, V, E_\mathrm{FS} + \epsilon)\mathrm{d}\epsilon} - \frac{2m_\mathrm{e}q_\mathrm{e}z_0}{\hbar^2\kappa_0}V \\ &= \frac{\varrho_\mathrm{S}(E_\mathrm{FS} + q_\mathrm{e}V)}{\frac{1}{q_\mathrm{e}V}\int_0^{q_\mathrm{e}V}\varrho_\mathrm{S}(E_\mathrm{FS} + \epsilon)\frac{T(z_0, V, E_\mathrm{FS} + \epsilon)}{T(z_0, V, E_\mathrm{FS} + q_\mathrm{e}V)}\mathrm{d}\epsilon} - \frac{2m_\mathrm{e}q_\mathrm{e}z_0}{\hbar^2\kappa_0}V\end{aligned} \tag{1.32}$$

Of these two terms, the second one is a background term, which is roughly linear in V. For the first term, it is argued that the transmission coefficients in the integral cancel since, at sufficiently small sample bias, they grow similarly with both z_0 and V. As their ratio approaches 1, the denominator approximates the average sample LDOS within the voltage range.

Hence, disregarding the background term, this procedure normalizes the spectra relative to integral LDOS, giving a dimensionless quantity. Note that, by definition, the obtained curves have a value of 1 at the Fermi level. The technique is only an approximation and fails to improve accuracy of results in certain circumstances [97]. Furthermore, in practice, given any level of input noise or offset, these errors are greatly amplified near the Fermi level, where the denominator in (1.30) is close to zero. Note that this problem disappears if instead of the measured current, the re-synthesized current (1.29) obtained from numerical integration of the properly scaled $\mathrm{d}I/\mathrm{d}V$ signal is used.

1.5 Description of the instrument

The instrument used in the measurements presented in this work is a custom-built low-temperature ultra high vacuum scanning tunneling microscope, described in detail in ref. [95]. The instrument consists of two main vacuum vessels, designated preparation chamber and analysis chamber. To transfer parts into and out of the evacuated system, a smaller load lock chamber is connected to the preparation chamber. The chambers are separated by manually actuated vacuum gate valves and connected by manually operated linear magnetic motion drives.

To decouple the system from mechanical vibrations, it is mounted on profiled struts resting on a set of four air-damping springs[3]. These, in turn, are placed in a basement room, on a section of floor excised from the building's foundation.

Bulk evacuation is provided by a set of three turbomolecular pumps[4]. Their pre-vacuum outlet is connected via corrugated hose to a buffer vessel in an adjacent room, that is evacuated by several rotating vane vacuum pumps[5]. Analysis and preparation chambers are each fitted with a titanium sublimation pump[6] and an ion getter pump[7], separable from their respective chambers by valves. The pressures are monitored by cold cathode gauges[8] inside the three chambers, and Pirani gauges[9] on the pre-vacuum side.

The preparation chamber is equipped with the following facilities:

- A linear magnetic motion drive dedicated to sample movement within the chamber during preparation.
- A wobble-stick manipulator[10].
- A 'carousel' with 16 receivers for storage of temporarily unused components.
- A sputtering ion source[11].
- A leak valve[12] for the sputtering gas supply.
- A heating station with a fixed filament and electrical connectors.
- A top-mounted receiver for an evaporator.

---

[3] Stabilizer I-2000, Newport Corp., Irvine, CA, USA

[4] TMU261 and TMU071P, Pfeiffer Vacuum GmbH, Asslar, Germany

[5] DUO 10 and DUO 5, Pfeiffer Vacuum GmbH, Asslar, Germany

[6] VACOM, Jena, Germany

[7] Meca 2000, Vernouillet, France

[8] IKR270, Pfeiffer Vacuum GmbH, Asslar, Germany

[9] TPR265, Pfeiffer Vacuum GmbH, Asslar, Germany

[10] WM40-150, SemiSupply AG, Walchwil, Switzerland

[11] ISE 5, Omicron Vakuumphysik GmbH, Taunusstein, Germany

[12] ZLVM940R, Thermo Electron Corp., Hastings, UK

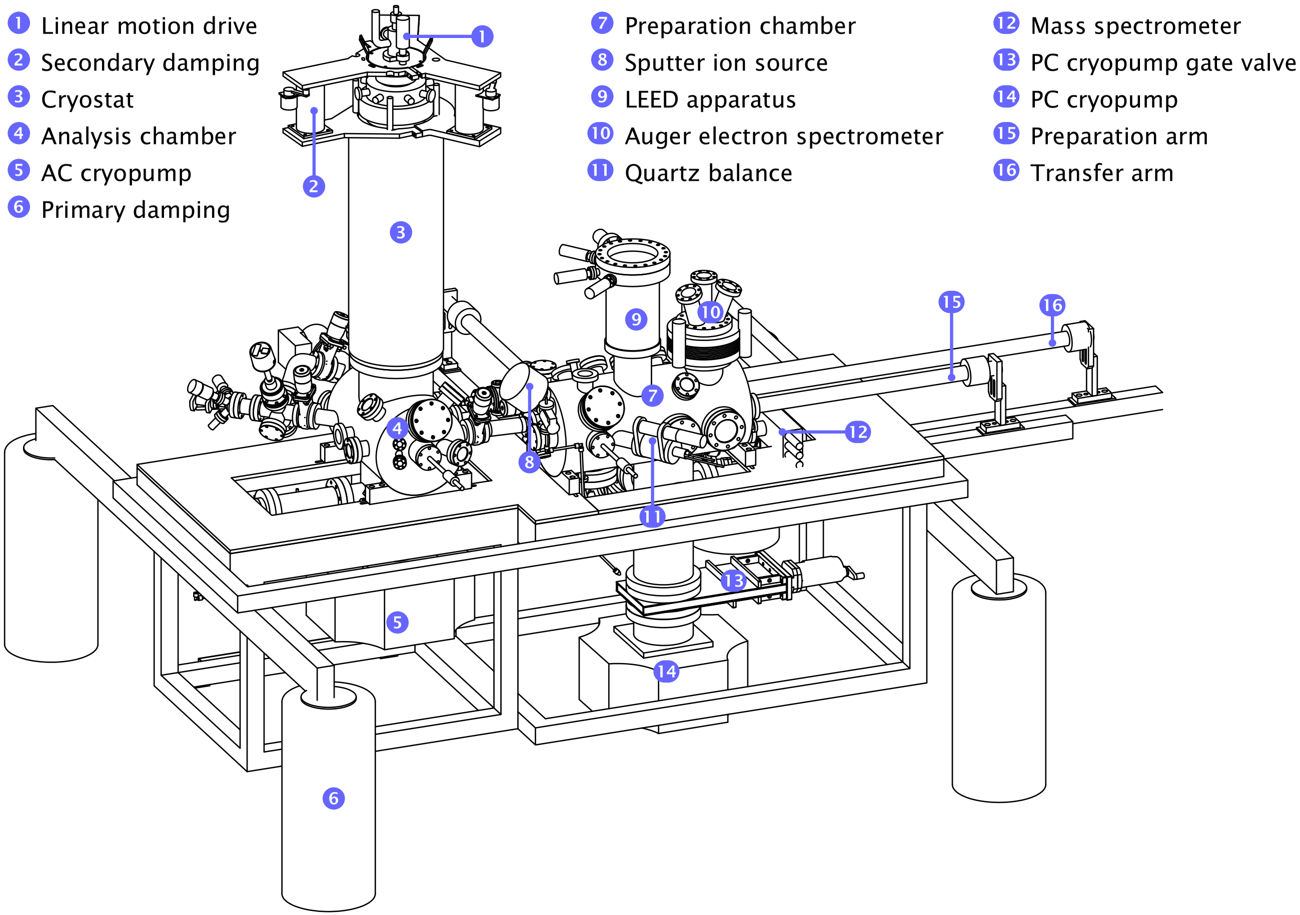

Figure 1.5 – **Overview of the apparatus (front view).**

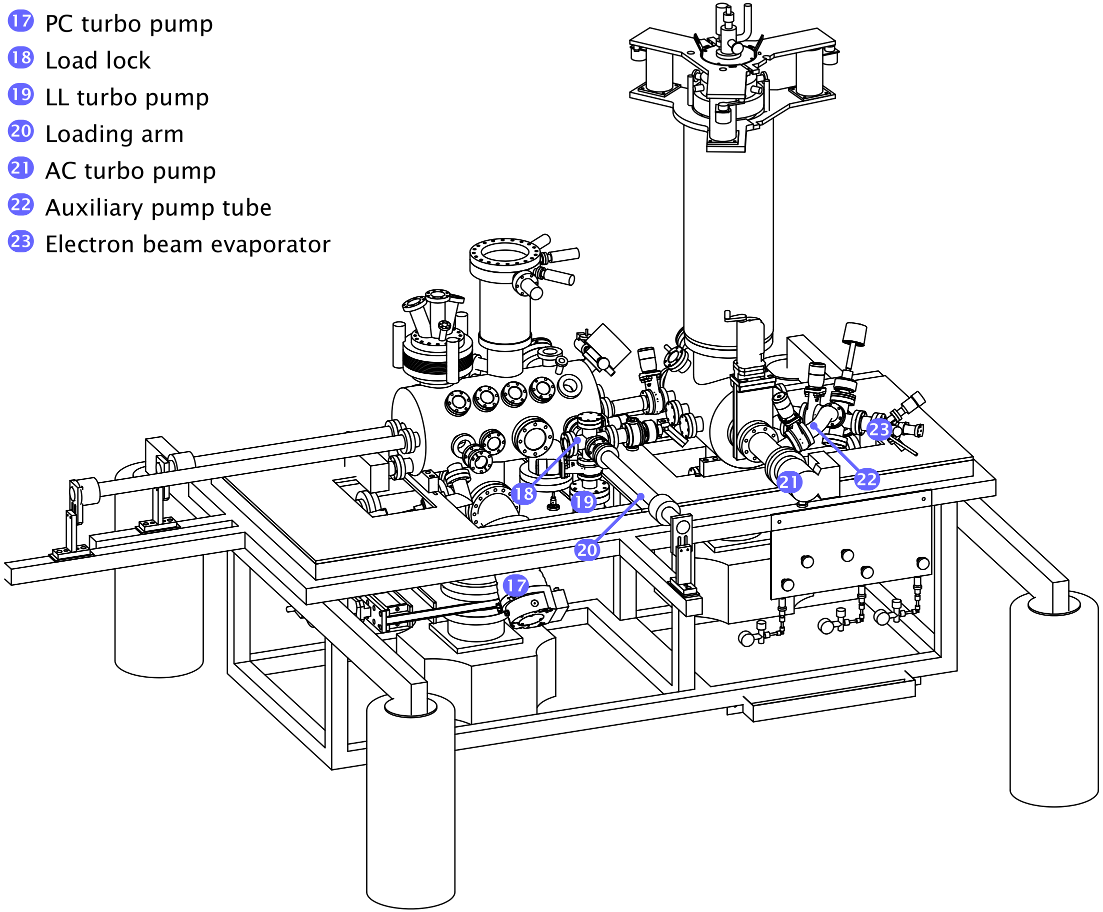

Figure 1.6 – Overview of the apparatus (back view).

- A quartz balance[13] mounted on a linear feedthrough, that can be moved into the evaporator's field of vision.
- A Low Energy Electron Diffraction (LEED) apparatus[14], with top-mounted electron source and screen.
- An Auger electron spectrometer[15].
- A quadrupole mass spectrometer[16], for leak detection and residual gas analysis.

Tip holders, samples, filaments and miscellaneous components to be transferred around the experiment are mounted or plugged on standardized stainless steel carriers. These exist in bulk metal and insulated two-terminal varieties and contain pairs of holes of standard caliber [80]. All manipulators, preparation and analysis stations and the STM proper provide prongs, with pairs of pins fitting these holes.

Cooling in the analysis chamber is provided by a custom-designed cryostat[17]. It consists of an outer vessel with a capacity of 15 l, and an inner vessel with a capacity of 4 l. They are separated by a shield that is cooled by the evaporated coolant from the inner vessel. For low-temperature operation, the outer vessel is filled with liquid nitrogen, and the inner vessel can be filled with liquid helium or liquid nitrogen, depending on experimental requirements. The inner vessel is furthermore isolated from external vibration as it is top-mounted on a supporting plate, which is positioned on three vibration isolation mounts[18], and otherwise connected to the instrument by a flexible metal bellows.

Below the cryostat, the shielding containment for the STM proper is situated, consisting of two fixed shields, and two that can be rotated in tandem, using the wobble-stick. Each of the shields contains a rectangular opening, making the STM accessible to the wobble-stick, when the shields are suitably turned. Another set of openings allows exposure of the sample to an electron beam evaporator[19], for low-temperature preparation.

The STM body consists of a circular base plate, with three vertical struts that support a top railing, and contain eyes for mounting of metal springs. During operation, the STM body is suspended on these springs to further decouple it from vibration. Otherwise it is depressed into cooling contact, *i.e.*, into a solid copper receptacle on the bottom of the containment, by screwing a triad of top-mounted rods onto the top railing.

The STM itself is of the slider type, and is an adaptation of a previous design described in ref. [72]. The coarse approach is done by a slip–stick system, shown in fig. 1.7, consisting of three hollow tube piezos ⓑ, which are glued horizontally into brackets on the base plate. They are contacted by an inner electrode, and an outer

---

[13] IL150, Intellemetrics Ltd., Glasgow, UK

[14] ErLeed, SPECS GmbH, Berlin, Germany

[15] ESA 100, Staib Instrumente GmbH, Langenbach, Germany

[16] VacScan 100D, Spectra SensorTech Ltd., Crewe, UK

[17] Cryovac GmbH & Co. KG, Troisdorf, Germany

[18] VIBRAPLANE Model 1206, Kinetic Systems, Inc., Boston, MA, USA

[19] EFM 3, FOCUS GmbH, Hünstetten, Germany

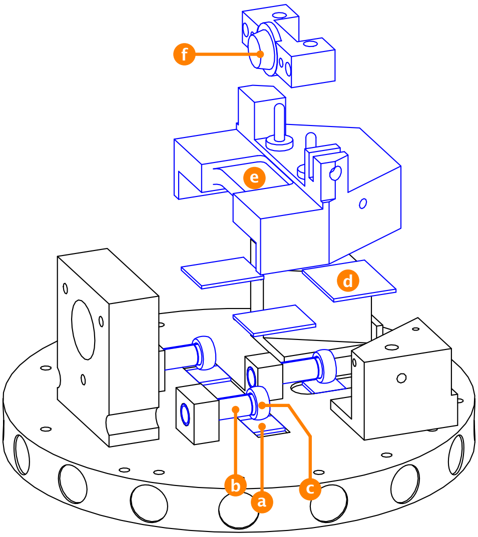

ⓐ Base sapphire plate
ⓑ Coarse approach piezo
ⓒ Titanium ring
ⓓ Slider sapphire plate
ⓔ Slider
ⓕ Sample on sample holder

Figure 1.7 – Slip-stick coarse approach system. Movement of the slider is done with three segmented tubular piezos. Sapphire plates are mounted on the contact areas, providing heat transport, electric insulation, and low friction.

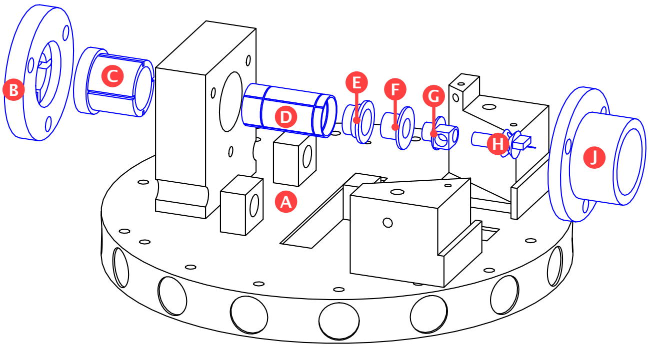

Ⓐ STM base body
Ⓑ Back plate
Ⓒ Macor® pod
Ⓓ Scan piezo
Ⓔ Screening ring
Ⓕ Isolation ring
Ⓖ Tip receiver
Ⓗ Tip holder with tip
Ⓙ Screening shroud

Figure 1.8 – The scan head assembly. The scan head components are glued together and clamped to the base body.

electrode segmented into parts, left and right. Wires are attached to these electrodes with conductive epoxy resin. Titanium rings ⓒ are glued to the front ends of the piezos. The slider ⓔ has sapphire plates mounted on the bottom ⓓ, with which it rests on the rings. Below the rings, on the base plate, an additional set of sapphire plates ⓐ is situated, to support the loaded piezos and to improve heat transport from the slider.

The slider can be arrested in a fully retracted position by a screw, for a sample change or initial cooldown, or rest freely on the coarse approach piezos during the experiment. By applying a suitable voltage waveform to the individual electrodes, the slider can then be moved longitudinally and laterally, or rotated [108].

The scan head assembly is shown in fig. 1.8. The scan head Ⓓ is a tubular piezo with an inner and an outer electrode, the latter being segmented into four quadrants. Alignment, active length, and material of coarse and scan piezos are designed to match, minimizing the effects of linear thermal expansion. For a discussion of the quantitative deflection and the nonlinearity of the scan head, see ref. [108].

The back part of the piezo is glued to a pod Ⓒ clamped to the base plate. Onto the front part, in sequence, a titanium shielding ring Ⓔ, an insulation ring Ⓕ and the tip receiver Ⓖ are glued. The latter contains a threaded hole for a locking screw, and a frontal hole for the tip holder. The tip holder Ⓗ consists of a rotational assembly suitable for insertion and transport via a clamp, and a base. To join a tip to its holder, the tip is placed onto the base, and arrested there by spot-welding a piece of tantalum foil across.

1.6 Electronics

To convert the tunneling current into a voltage suitable for acquisition, a transimpedance amplifier[20] is connected to the current output. To minimize noise pickup, the amplifier is directly connected to the vacuum feedthrough on top of the cryostat assembly. It provides selectable amplifications of $10^3 \ldots 10^9$ VA^{-1} in low-noise mode, and up to 10^{11} VA^{-1} in high-sensitivity mode. They can be remotely selected from the operator's room, using a custom-built interface.

The STM is connected to a commercial controller setup[21], consisting of a monolithic, rack-mounted unit, a breakout box providing additional analog BNC connectors, a data acquisition card[22] for the PCI bus of a connected PC, and a software package. The system is of a hybrid analog–digital design, governing generation of X, Y, Z positional, bias voltage, and spectroscopy ramp signals, digital acquisition of tunneling current, Z position and auxiliary signals (such as lock-in amplifier output), and mixing in of externally supplied voltage and Z position modulations.

The feedback loop can operate in linear and logarithmic modes, selectable by front panel switch. Current setpoint and gain can be set via front panel potentiometers. The feedback generator output can further be reset to zero (via front panel switch), held or set to a specific value (in software).

For the generation of X and Y piezo signals, base offsets can be set via front panel potentiometers. Onto this, the output from the internal DSP scan generator is added. Also, a hardware slope compensation system is provided, allowing to add scaled copies of the X and Y outputs onto the Z signal, to minimize load on the feedback loop and to make best use of feedback ADC headroom.

---

[20] DLPCA-200, FEMTO Messtechnik GmbH, Berlin, Germany

[21] SPM 1000, RHK Technology, Inc., Troy, MI, USA

[22] DT3016, Data Translation, Inc., Marlboro, MA, USA

To generate the Z scan signal, the unit provides fine (×1) and coarse (≈ ×9) Z offset potentiometers to select a signal floor. The Z output is then the sum of these values, the output of the slope compensation circuit, and the output of the feedback generator.

A lock-in amplifier[23] is used to acquire the differential conductance signal. This is a DSP-based digital device that contains a signal generator to provide sinusoidal modulation signals, with amplitude and frequency freely selectable. This signal, an externally provided one, or higher harmonics thereof can be used as a reference for demodulation. On the input side, the device can simultaneously process in-phase and quadrature signals. The demodulation filter has a selectable roll-off of 6...24 dB/oct., and an adjustable time constant above 5 ms. The latter is implemented as a cascade of first-order exponentially-weighted moving average filters, and the selected time constant corresponds to a single 6 dB stage (see appendix A).

Depending on the type of spectroscopy required—$I(z)$, $I(V)$, or $z(V)$—the signal input is taken from the the transimpedance amplifier output or the z positional feedback monitor signal, while the modulation output is connected to the z position modulation input or the bias modulation amplifier. The latter is a home-built external amplifier that sums the auxiliary output used for the voltage ramp (×1) and the lock-in modulation signal (×0.01). This sum is connected to the V modulation input. For the slip–stick coarse approach, a home-built controller unit is used, which synthesizes suitable high voltage waveforms for the coarse approach piezos, to move and rotate the slider in the x–z plane. A detailed description of this unit, which can be triggered by remote control and by the main electronics unit, is given in ref. [108].

1.7 Operating procedures

Tip preparation. The ideal SPM probe has a low aspect ratio, inhibiting low-frequency mechanical vibrations, and a single protruding cusp that is both monatomically sharp and has a smooth and featureless density of states. In practice, these requirements somewhat run counter to each other. Also, the extent to which a given tip satisfies each of them is not readily apparent, unless each tip is individually characterized by field ion microscopy (FIM) and testing on known surfaces. As this is typically seen as prohibitive, most STM experiments rely on a suitably weighted combination of luck and reproducibility of the chosen method.

A wide corpus of preparation recipes has evolved. Depending on the tip metal used, the source wire is initially subjected to macroscopic techniques such as cutting, grinding, tearing, fracturing, or electrochemical etching. This precursor tip may then be further refined by, *e.g.*, sputtering, field emission, or controlled tip–surface contacts.

In the experiments presented in this work, tungsten tips are used throughout. These tips are prepared by an electrochemical etching technique [103], which is known to yield usable tip precursors in a fairly reproducible manner. A segment of 0.1 mm diameter tungsten wire is fixed to the base of a stainless steel tip holder, by spot-welding a small

---

[23] SR830, Stanford Research Systems, Inc., Sunnyvale, CA, USA

sheet of tantalum foil across. It is then partially lowered into a small vessel of 1-molar sodium hydroxide solution. A control unit supplies a voltage between the wire and a submerged ring-shaped steel cathode, monitoring the current. The wire is predominantly etched radially near the surface, up to a point where the lower portion tears off. This leads to a sudden drop in current, which is detected and triggers the voltage supply to shut off[24].

Before the first use and after every contact to ambient air, the tip needs to be deoxidized. For this, it is heated shortly within the preparation chamber, and sputtered once with Ar^+ ions (see below) for 30 minutes (750 eV, 3 µA). Further tip preparation may be done *in situ*, depending on what the sample allows. The tip may be restructured with bias voltage pulses. For noble metal samples, the tip may also brought in physical contact to the surface, in order to pick up or drop off material, restructuring the tip apex.

Sample preparation. Details on how the individual samples are prepared are given in the relevant sections. Unless specifically mentioned, surfaces are generally prepared by cycles of alternating sputtering and annealing, with customary parameters given below.

Sputtering describes surface bombardment with energetic ions. This produces collision cascades and, depending on the materials involved, leads to an embedding of the ions into the surface or the ejection of surface material. Using Ar^+ inert gas ions, this is used to remove the topmost surface layers, including adsorbed impurities. The sputtering ion source is supplied with a suitable high voltage (1.2 kV). The sample is placed on the preparation arm, in the ion source focus position. Ar gas is fed into the preparation chamber through a leak valve, until an ion current is detected. This happens as the total detected pressure reaches $\approx 3 \times 10^{-4}$ Pa. The gas purity is regularly checked with the mass spectrometer. The ion current is monitored, and the Ar influx is adjusted to maintain the target current of ≈ 10 µA, for 10...20 minutes.

After sputtering, the surface is expected to be roughened [116]. To obtain a crystallographically smooth surface layer, the surface is then annealed. This accelerates surface diffusion and ripening processes. Annealing is done by radiative heating of the sample from below. The sample is placed on the heating station and put to a potential of 650 V, and the filament is heated with a current of ≈ 3.7 A. This leads to an emission current of about 8 mA. The surface temperature is monitored with a pyrometer through the top viewport, to not exceed 450°C. A heating cycle takes 10 minutes, counted from when the temperature first reaches 400°C. As due to bulk diffusion, bulk contaminants may reach the surface during annealing, this sequence of sputtering and annealing is repeated several times. After the final heating cycle, the filament current is reduced slowly, to ensure a gradual sample cooldown.

---

[24] Both the switching speed of the circuit and the weight of the submerged length of wire remain as free parameters in this setup, influencing the final geometry of the tip [103].

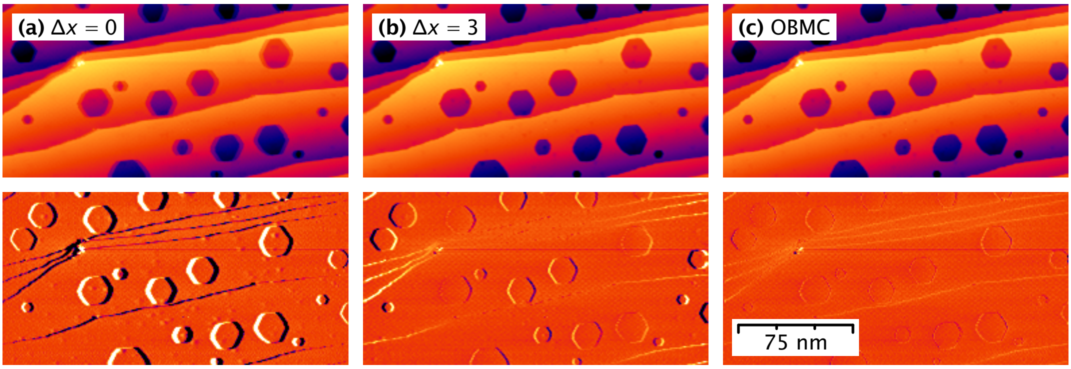

Figure 1.9 – Merging fore- and backscan via a motion compensation scheme, demonstrated on a 128×256 pixel example dataset. Top row shows the combined z maps, bottom row shows residue Δz between fore- and backscan, with persistent color scale within each row. **(a)** The unshifted source data yield a poor match, with double features and lack of sharpness in the merged z maps. **(b)** A global relative shift of 3 pixels leads to acceptable image quality. However, the displacement is overestimated at the sides, and underestimated in the center of the image, seen as a contrast inversion of the hexagonal features in the Δz image. **(c)** The OBMC scheme (15 macroblocks, 0.1 pixel resolution) provides a nearly featureless Δz.

Sample transfer and cooldown. If the sample has just been freshly annealed, it is left to cool for about 30 minutes, until it reaches ambient temperature. After that, the following steps are performed in order, while monitoring the slider temperature and pausing suitably to see it stabilize.

The STM base body is pressed into cooling contact, with the slider fixed in the retracted home position. Then the sample is transferred into the analysis chamber, placed onto the designated position on the slider, and affixed with a screw. After initial cooldown, the slider is loosened and coarsely approached to the the tip manually and by the approach system. The two-layered radiative shielding is closed, and the pusher rods are retracted to suspend the STM. After the slider temperature has stabilized, a bias voltage is applied, and the approach routine is enabled to establish tunneling contact.

Creep and drift correction. When acquiring an STM image, the tip is typically moved across the image width and back once per scanline, before advancing along the slow scan direction. Hence, two submaps, forescan and backscan, can be acquired in tandem. To reduce noise and asymmetry due to the scan direction, the submaps can be merged. Simply averaging the submaps falls short in the presence of feedback loop lag, pipeline delays, thermal drift, and piezo creep. The former two can be partially remedied by globally shifting the submaps relative to each other.

In this work, a more complex custom scheme is used throughout. Using parlance from the field of compressed video encoding, the submaps are merged by an overlapped block motion compensation (OBMC) technique [174, 234], permitting fractional motion vectors. The $X \times Y$ pixel submaps are each sliced into N identically sized stripes, along the slow scan direction. $N-1$ overlapping macroblocks of $(2X/N) \times Y$ pixels are formed from two adjacent stripes. For a set of candidate motion vectors, the absolute differences between the shifted submaps in each macroblock are calculated. The best match vectors are recorded as a function of macroblock barycenter, giving a displacement curve with $N-1$ points, which is extrapolated to X points. The joined map is assembled from fore- and backscans, using cubic interpolation, with the displacement function split symmetrically among the submaps[25].

The efficiency of the merging schemes can be ascertained by visualizing the difference between the shifted fore- and backscans before joining. Fig. 1.9 demonstrates the OBMC scheme on an example dataset. The extent to which outlines of topographic features are visible in the Δz images indicate the mismatch between fore- and backscan.

The method fails if there is too little topographic structure in a macroblock to reliably obtain an optimum motion vector. A value of $X/N = 64$ was found to be a good default for most cases. If the displacement function looks suspect for a given image, the number of macroblocks needs to be reduced accordingly. Note that, if both z and $\mathrm{d}I/\mathrm{d}V$ maps are acquired during a single run, the latter yields a different displacement function, which is typically larger due to filter and pipeline delays.

Slope correction. Depending on the exact orientation of the slider to the tip, and the nonlinearities of the scanner, raw topographs typically contain an unwanted additive background. To remove this, a suitable synthesized floor is subtracted from the images. One common method, best used on flat substrates, is the use of a global planar or parabolic background, with best fit parameters taken from an NLS optimization. The locations of known surface structures are excluded from the fit region of interest.

If the focus lies on the intralayer corrugation in a stepped region, visual contrast can be enhanced by aligning the terraces with the image plane[26]. In a properly aligned topograph, the z values are strongly quantized, and should appear as a series of equidistant peaks in a z histogram. To align, the topograph is first dithered with $\pm\frac{1}{2}$ LSB of uniformly distributed noise to eliminate z ADC quantization effects. Then, a synthetic (planar or parabolic) floor is generated, whose starting parameters are picked by hand, and further optimized, *e.g.*, by the Nelder-Mead simplex technique [170, 171]. For each evaluation, the candidate floor is subtracted from the map, and a z histogram of the residual map with globally fixed bins is generated. If the outermost bins are non-empty, the attempt is rejected outright. Otherwise the fitness function is generated from the standard deviation of the histogram frequencies. A high value indicates a rough histogram, and thus a strong quantization of z values.

---

[25] As a cheap way to reduce computational complexity, the displacement Δx can also be split near-symmetrically such that the fractional part is restricted to one submap only. Shifting fore- and backscan by $\Delta x_F := \left\lfloor \frac{\Delta x}{2} \right\rceil$ and $\Delta x_B := \Delta x_F - \Delta x$, respectively, allows to omit one interpolation in favor of a faster lookup.

[26] In such a case, the tip z position can be displayed modulo the step height, spreading the available z display range across each terrace and thereby enhancing visual contrast of intralayer features. Instances in this work where this has been done are marked with an asterisk in the topograph's z scale bar.

Part I

Surface states on nanostructured Ag(111)

Chapter 2

Introduction

In the history of scanning tunneling experiments, copper, silver, and gold, the nonradioactive members of the 11th group in the periodic table, also known as the coinage metals, have played a prominent role. In particular, their crystal faces with the {111} Miller index [166] remarkably feature experimentally accessible Shockley-type surface states. These have found widespread use within the scientific community as a model system approximating the behavior of a two-dimensional free electron gas.

A variety of experiments has been performed on this model system within the scope of this work, in order to explore the electronic characteristics of the interaction of the Ag(111) surface state with a selection of artificially created nanostructures. These experiments are reproduced in this chapter, which is structured as follows:

A general introduction to the Ag(111) surface and its electronic structure is given. The Shockley surface states, their lifetimes and decay channels are introduced. Several surface restructuring techniques, extending makeup and experimental accessibility of surface states, are discussed. The primary experiment of this chapter deals with the confinement of surface states within monatomically deep surface cavities. Both spatial and energetic structures of the resulting quantum resonance patterns are explored. The measured results are compared with theoretical models and other published data.

Supplementary experiments provide a further insight into the unoccupied states of the restructured Ag(111) surface. These include, in the order of increasing binding energy, studies of the surface state dispersion at linear scatterers, of transmission resonance effects in adsorbed oligomers and one-dimensional chains, and of resonant states within the vacuum gap, in the field emission regime.

Publications

Several of these topics have merited publication during the course of this work. A discussion on the suitability of resonator geometries for the study of lifetimes was published as

> S. Crampin, H. Jensen, J. Kröger, L. Limot, and R. Berndt, *Resonator design for use in scanning tunneling spectroscopy studies of surface electron lifetimes*, Phys. Rev. B **72** (3), 035443(6) (2005), DOI: `10.1103/PhysRevB.72.035443`.

The corresponding experimental study of monatomic vacancy resonators, a discussion of the obtained lifetimes, and comparisons with previously published results have been reproduced in

> H. Jensen, J. Kröger, R. Berndt, and S. Crampin, *Electron dynamics in vacancy islands: Scanning tunneling spectroscopy on Ag(111)*, Phys. Rev. B **71** (15), 155417(5) (2005), DOI: `10.1103/PhysRevB.71.155417`.

In the course of the latter, a mathematical disagreement in published data was discovered, which has been commented on in

> S. Crampin, J. Kröger, H. Jensen, and R. Berndt, *Phase coherence length and quantum interference patterns at step edges*, Phys. Rev. Lett. **95** (2), 029701(1) (2005), DOI: `10.1103/PhysRevLett.95.029701`.

Furthermore, the resonator lifetime study has been published as part of two review articles on surface state electron dynamics,

> J. Kröger, L. Limot, H. Jensen, R. Berndt, S. Crampin, and E. Pehlke, *Surface state electron dynamics of clean and adsorbate-covered metal surfaces studied with the scanning tunnelling microscope*, Prog. Surf. Sci. **80** (1–2), 26–48 (2005), DOI: `10.1016/j.progsurf.2005.10.002`

and

> J. Kröger, M. Becker, H. Jensen, T. von Hofe, N. Néel, L. Limot, R. Berndt, S. Crampin, E. Pehlke, C. Corriol, V. M. Silkin, D. Sánchez-Portal, A. Arnau, E. V. Chulkov, and P. M. Echenique, *Dynamics of surface-localized electronic excitations studied with the scanning tunnelling microscope*, Prog. Surf. Sci. **82** (4–6), 293–312 (2007), DOI: `10.1016/j.progsurf.2007.03.003`.

The experiment regarding transmission resonances in adsorbed Ag oligomers and chains has been published as part of

> H. Jensen, J. Kröger, N. Néel, and R. Berndt, *Silver oligomer and single fullerene electronic properties revealed by a scanning tunnelling microscope*, Eur. Phys. J. D **45** (3), 465–469 (2007), DOI: `10.1140/epjd/e2007-00157-x`.

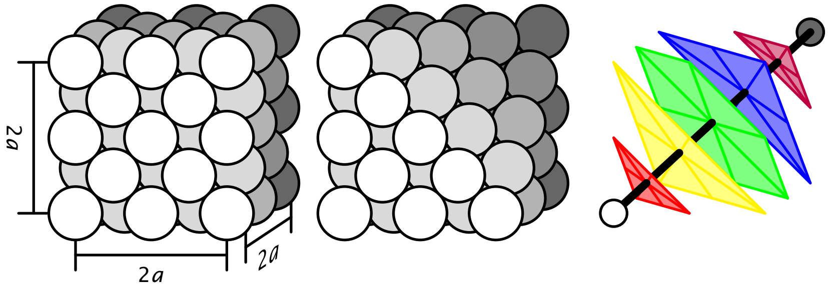

Figure 2.1 – Face-centered cubic structure of Ag(111). (a) $2 \times 2 \times 2$ unit cells of the Ag crystal are shown. **(b)** Cleaving the crystal along the (111) plane yields a hexagonal arrangement, with nearest neighbor distance of $d_\mathrm{N} = \sqrt{1/2}\, a \approx 0.2889$ nm. **(c)** The space diagonal of the shown arrangement has a length of $\sqrt{12}a$ and intersects 5 additional planes, giving an interlayer distance of $d_\mathrm{L} = \sqrt{1/3}\, a \approx 0.2359$ nm.

2.1 Surface states and the Ag(111) surface

Surface states are electronic states of bounded crystalline solids that are localized primarily at or near the surface. If an infinite crystal is assembled from individual atoms, their atomic orbitals overlap and form bulk states that are delocalized across the entire crystal. Their formerly discrete energy levels assemble into continuous energy bands. If the crystal symmetry is broken by a surface, additional electronic structures may arise. Such electronic states whose dispersion lies within the bulk band gap are unable to propagate into the bulk, and are called surface states. In contrast, states whose dispersion overlaps a bulk band, and thus are somewhat coupled to bulk states, are called surface resonances.

Surface states were first predicted by Igor Tamm in 1932 [222], within the tight-binding approach. Solutions for the bulk Schrödinger equation are formed from linear combinations of atomic wave functions. The coefficients in these linear combinations are obtained by considering nearest-neighbor interactions only. Hence, the local environment is the same for all atoms in the bulk, but differs for atoms at the boundary. If this perturbation is sufficient, surface-localized states appear as solutions.

In 1939, William Shockley found that surface states may arise even in a potential without local coordination effects [210], by considering the evolution of energy levels in a finite atomic chain with decreasing lattice constant. The initially identical energies for the separated atoms fan out to form energy bands that widen as the separation decreases, and eventually cross. Beyond the crossing points of the band boundaries, inverted band gaps reopen that contain pairs of surface-localized states.

An additional class of surface-localized states are image potential states, which are situated outside of the solid. The electric field of an electron in proximity to a conducting surface leads to a modification of the charge distribution within the surface.

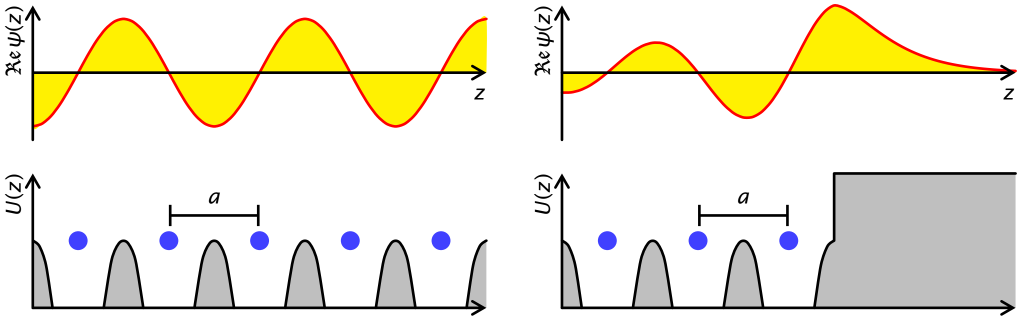

Figure 2.2 – Potential model for the Shockley surface state at a metal–vacuum boundary (simplified). **(a)** Within the periodic ion core potential $U(z)$, the electron wavefunctions $\psi(z)$ are given by the product of a plane wave and a Bloch function. **(b)** A vacuum boundary disrupts the lattice periodicity, allowing surface-localized solutions that decay exponentially in both bulk and vacuum directions.

This induced image potential may give rise to a series of bound states for the electron.

The coinage metals (copper, silver and gold) have a face-centered cubic (fcc) crystal structure. Their $\{111\}$ lattice planes provide model systems for the Shockley surface state that are readily accessible by STM. The bulk electronic structure of the coinage metal crystals has an sp-inverted band gap (the $\mathrm{L}_2' \rightarrow \mathrm{L}_1$ gap) around the L point that straddles the Fermi level [40]. If the crystal is terminated along a $\{111\}$ plane, this leads to a projected band gap around the $\bar{\Gamma}$ point of the surface Brillouin zone, within which a Shockley surface state exists. First experimental observations of both occupied [74] and vacant [212] surface states on Cu(111) by ARPES and IPES, respectively, have found that the states can be characterized as a two-dimensional free-quasiparticle system. They have an isotropic, parabolic dispersion characterized by an onset energy of E_0 at the $\bar{\Gamma}$ point, and a positive effective mass m^*. The surface state of Ag(111) has been thoroughly characterized over the years, with both PES [91, 118, 179, 191] and STM methods [140]. These provide a value of $E_0 = (-67 \pm 2)$ meV for the onset energy, which was found to vary slightly with temperature, following a similar variation of the supporting bulk band gap [179]. The effective mass was found to be $m^* = (0.42 \pm 0.02)m_\mathrm{e}$.

The lattice constant of silver is about $a = 0.4086$ nm under ambient conditions [51, 146]. The $\{111\}$ lattice planes have a hexagonal structure, with a nearest-neighbor distance of $d_\mathrm{N} = \sqrt{1/2}\,a = 0.2889$ nm and an in-plane distance between adjacent atomic rows of $d_\mathrm{R} = \sqrt{3/8}\,a = 0.2498$ nm. Atomic layers are stacked in an ABCABC sequence, with a perpendicular interlayer distance of $d_\mathrm{L} = \sqrt{1/3}\,a = 0.2359$ nm.

2.2 Surface state lifetimes

A mobile charged particle, such as a surface state electron, against a homogeneous, polarizable charge background envelops itself with a screening cloud. The screened particle can be modeled by a free quasiparticle, whose effective interaction and mobility differ from the original particle. The energy involved in the formation of a quasiparticle, relative to the free particle, is called the quasiparticle self-energy Σ. A quasiparticle with a finite lifetime can be modeled by introducing a negative imaginary part to the self-energy, $\Im\mathfrak{m}\Sigma < 0$. This implies that the probability of the state decays exponentially with time,

$$|\psi(t)|^2 = |\psi(0)|^2 \exp\frac{2\Im\mathfrak{m}\Sigma t}{\hbar} =: |\psi(0)|^2 \exp -\frac{t}{\tau}. \tag{2.1}$$

The quantity $\tau := -\frac{\hbar}{2\Im\mathfrak{m}\Sigma}$ is called the lifetime of the quasiparticle. For a surface state electron, the principal decay paths, besides scattering at surface lattice defects [225], are inelastic electron–electron (e–e) [71, 121] and electron–phonon (e–φ) [57, 58] interactions.

The two main approaches to study surface state lifetimes with STM are the analysis of phase coherence lengths [29, 31] and spectroscopic lineshapes [141], respectively. The former exploits that surface structures such as adsorbed atoms [50] or surface steps [90] scatter the surface state, inducing variations in the density of surface states around them, the so-called Friedel oscillations [70]. The spatial decay of these quantum interference patterns [2] is quantified, and lifetime information is obtained from the decay length and the group velocity. The lineshape analysis involves differential conductance measurements at a fixed point, extracting the lifetime information from the shape and width of the detected spectral features. On an unstructured surface, the only such feature is the onset of the surface state. The lineshape of this onset, which approximates the arctan function, has previously been studied in detail [141], and a surface state lifetime of (67 ± 8) fs has been obtained.

To access additional energies, the surface needs to be structured in a way that additional spectral features arise. To this end, electron resonators can be constructed by, *e.g.*, lithography, single adatom manipulation [50], or self-assembly [7] techniques. These provide a spectral structure with a series of resonances, with quantized energy levels governed by the specific resonator geometry. Each of these levels allows access to the corresponding lifetime data, by analyzing the width of the resonant peak in STS.

The lifetime detected in this manner deviates from the intrinsic lifetime, however, as it includes limiting contributions by lossy scattering at the boundaries (where applicable), as well as thermal and instrumental broadening effects. To recover the intrinsic lifetime as a quantity independent from the specific measurement technique, these must be accounted for.

An estimate of the contribution due to the partial reflectivity of the resonator boundary, following the lines of ref. [47], is given below. The broadening induced by the experimental method of STS, using a lock-in amplifier and a finite bias modulation amplitude, is described in section A.3.

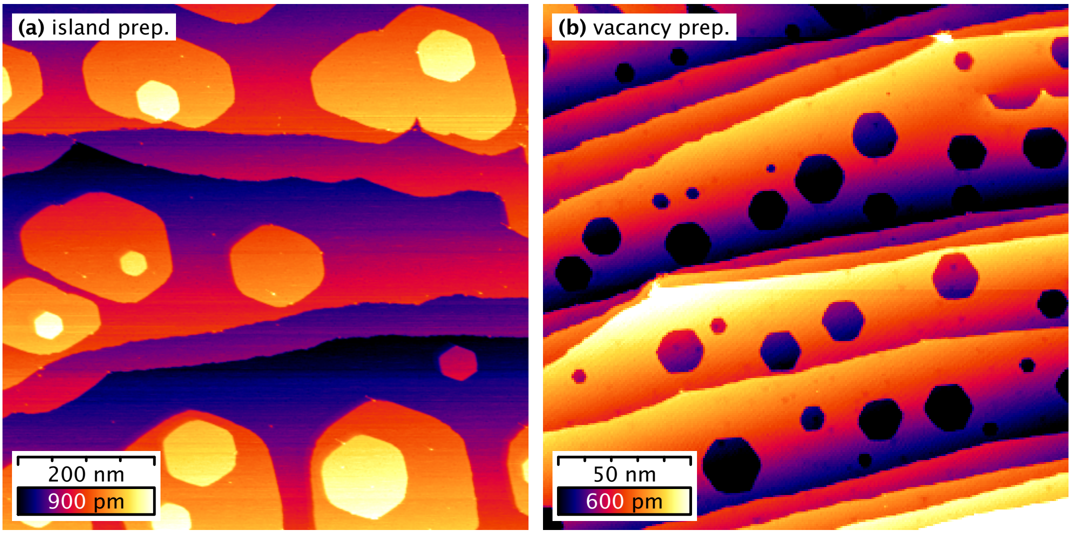

Figure 2.3 – Resonator preparation results on Ag(111). **(a)** Island resonators. (770 nm)^2 topograph, $V = +100$ mV, $I = 200$ pA, after 15 s of Ag evaporation, heating current 1.2 A. **(b)** Vacancy resonators. (200 nm)^2 topograph, $V = +200$ mV, $I = 200$ pA, after 5 s of Ar$^+$ ion bombardment, ion current 5 μA at 600 V.

2.3 Resonator preparation

During and after the preparation, the surface may undergo equilibrium processes that provide a further temporal evolution of the nanostructured surface. This is especially the case when preparation is performed at elevated surface temperatures, when the experiment is performed at temperatures far from absolute zero, or when a significant period of time elapses between preparation and complete sample cooldown.

In the instrument, most preparations are performed in the preparation chamber, which operates at ambient temperature. During preparation and sample transfer, the surface structure is subject to equilibrium processes including surface diffusion, desorption and Ostwald ripening. Consequently, only surface structures that are stable against these processes, or created by them, can be prepared this way. Otherwise, preparation has to be performed *in situ*, on the previously transferred sample at low temperature.

In the present work, the three preparation techniques used for creating the Ag(111) nanostructures are homoepitaxic growth, argon ion bombardment (at ambient temperature) and controlled tip indentations of various intensities (at cryogenic temperatures). In the following sections, these techniques will be briefly illustrated.

Homoepitaxic growth. This describes lattice locked adsorption of a species identical to the substrate. Depending on the preparation environment, the processes determining the final morphology of the treated surface are largely identical to those governing the equilibrium structure of the surface. In other words, homoepitaxy can be regarded as the continuation of the crystal growth process itself, albeit possibly with a vastly different set of parameters. In consequence, the established models for crystal growth, as well as a plethora of prior experimental results, can be employed to discuss the morphology of homoepitaxically grown nanostructures.

In this discussion, the understanding of the underlying kinetic growth modes is of great importance. Atoms arriving from the vapor phase may diffuse across the surface individually, until two of these interact and form a dimer, which is generally less mobile and serves as a nucleus. Additional atoms may aggregate at these nuclei, resulting in emergence and growth of a new monatomic island. Diffusing atoms may also be trapped at and incorporated into surface steps, cross them, or desorb from the surface again. The ratio of occurrence of these processes determines the temporal evolution of the surface structure, and is governed by tunable parameters, mainly temperature and adsorbate flux.

Activation barriers in diffusion differ between intra-terrace locomotion and descent across a step edge [55]. The excess energy of the latter can be thought of as a reflective barrier for the diffusing atom, located at the step edge [206], the *Ehrlich–Schwoebel (ES) barrier*. At high temperatures and low adsorbate flux, where this step edge barrier is easily overcome, and formation of nucleation centers is rare, high-symmetry oriented surfaces grow in a strictly layer-by-layer fashion. In this growth mode, the surface structure oscillates between a maximum roughness and a smooth, completed layer. Observable physical properties of the surface may also demonstrate oscillations, their period correlating with the layer deposition time [27].

At moderate temperatures, where the ES barrier is energetically relevant, impinging particles tend to demonstrate *diffusion bias* [230], a preference for incorporation into the ascending step. The rationale for this is that to be incorporated into the descending step, the diffusing atom needs to cross the step edge to descend to the lower terrace, overcoming the step edge barrier, and afterwards adds to the terrace from the lower-hand side.

For stepped surfaces, such as vicinal surfaces (see section 7.1), the preference for adsorption on the ascending step encourages a *step flow* growth mode, where incorporation occurs primarily at ascending steps, resulting in a continuous net movement of the steps into the descending direction. This typically results in uniformization of the terrace size distribution, as large terraces will provide bigger adsorption targets, leading to their preferred overgrowth by the upper-hand adjacent terrace [82].

For high-symmetry surfaces, adsorption at moderate temperatures results in a growth that is not strictly layer-by-layer, with several incomplete monolayers on the surface, typically forming a hill-and-valley morphology whose details depend on the material's base crystal structure. Generally, prolonged exposure yields an equilibrium roughness value depending on temperature and adsorbate flux.

In the particular case of Ag(111) homoepitaxic growth, previous experiments have shown that at room temperature, the ES barrier is not typically overcome by migrating atoms [94], resulting in a gradual surface roughening and the formation of a characteristic topography featuring rather uniformly tapered hillocks of stacked islands, prominently retaining the hexagonal symmetry of the base structure, and locally uniform step distance [160]. This process has been found to persist for prolonged evaporation, up to island thicknesses of 25 nm. For higher coverages, where the substrate is no longer smooth at the scale of the hillock base dimensions, the surface structure is found to become ‘cloudy’ and irregular, and individual atomic layers can no longer be readily resolved in STM [94].

Ion bombardment. While leaving the chemical composition of the surface largely unchanged, sputtering with argon ions induces changes in the surface morphology and related properties. While these changes could be quantified macroscopically, only the advent of SPM techniques allowed for a detailed insight into the material transfer during sputtering [163], and following that, the use of sputtering as a method of roughening and structuring of substrate surfaces [61].

For example, in Pt(111), it was found that sputtering primarily creates monovacancies, *i.e.*, isolated sites of single missing atoms [187]. The resulting surface morphology is determined by their mobility. Its temperature dependence was previously studied in detail [165]. Primarily, the creation of monatomically deep vacancy islands was observed, whose geometry was found to be elongated, branched and irregular at temperatures below 500 K, while increasingly preferring a distorted hexagonal shape at higher temperatures.

The mechanism for formation of these vacancies was reported to be coalescence of mobile monovacancies (single missing atoms), created by the sputtering process. Furthermore, it was found that above 700 K, second-layer monovacancies were increasingly filled in by atoms mobilized from ascending step edges, discouraging the formation of second-layer vacancy islands. Beyond 900 K, this effect results in a strict layer-by-layer surface erosion [164].

Beyond this erosion, the formation of adatom islands on top of the original surface layer was also observed as a result of sputtering, at temperatures below 550 K, indicating the production of adatoms by the process [165]. At higher temperatures, formation of adatom islands is inhibited. For adatoms with high mobility and a kinetic energy is sufficient to overcome the ES barrier, the adatoms will preferably bind to a step edge encompassing a nearby vacancy island. Also, the decomposition of already formed adatom islands by overgrowing a nearby vacancy island is observed [198]. This slower process bears similarity to Ostwald ripening and takes place even at lower temperatures.

These properties of the sputtering process can be employed to engineer resonator geometries on the Ag(111) surface. It has been established that roughening of a surface prior to a period of homoepitaxic growth can provide additional nucleation centers, increasing the yield of island resonators similarly to the use of surfactants [199].

In the present work, however, the near-hexagonal vacancy islands created by sputtering and subsequent surface relaxation are directly used as resonators. These vacancy

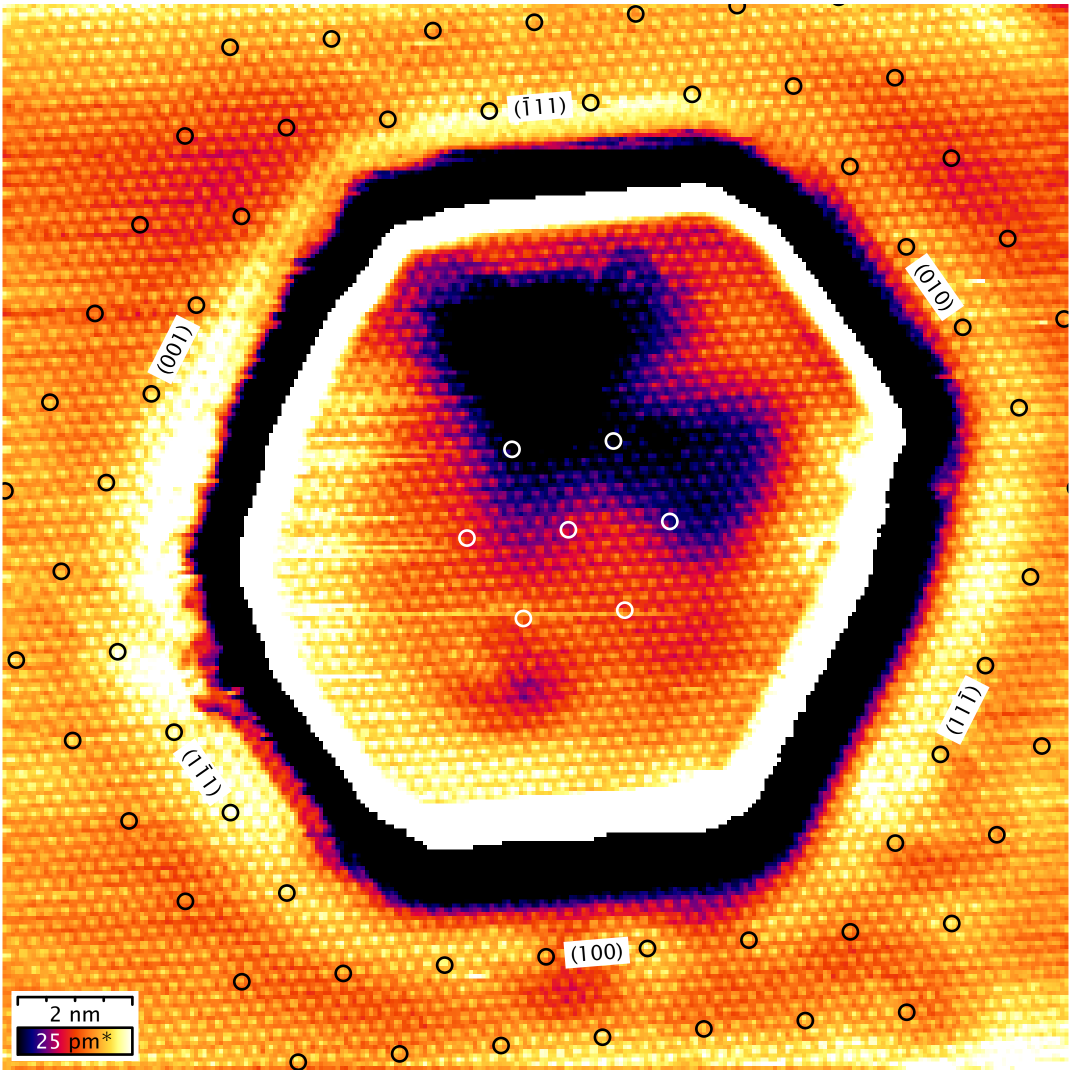

Figure 2.4 – Ag(111) vacancy island with atomic resolution, (18.6 nm)^2 topograph, $V = +200$ mV, $I = 90$ pA (z contrast enhanced). Owing to an serendipitously laterally sensitive tip state, the hexagonal lattice of Ag(111) is visible both within and outside of the structure. This allows an accurate lateral recalibration of the scan piezo, as well as insight into the step edge orientation and microfacet types. The outer lattice (black circles: every sixth atom) is extrapolated into the vacancy center (white circles). The relative displacement between inner actual and extrapolated lattices suggests the annotated microfacet types, with the $\{100\}$ type at the top left, top right, and bottom boundaries.

resonators can be thought of as the complementary structures to the island resonators, with a similar geometry, yet their confinement established by upward steps instead of downward ones.

Controlled tip indentation. The aforementioned techniques involve a preparation on a macroscopic level, creating a large manifold of potential structures. The unique advantage of STM is the ability to directly operate in real space, allowing to visualize individual structures and select the most suitable ones for experimentation. Furthermore, structures may even be manipulated, modified and possibly created by controlled tip–sample interaction. A wide selection of surface manipulation experiments demonstrates this capability. It can be used to complement top-down techniques, as has been done to further arrange previously adsorbed objects [56], engineering nanostructures of the desired geometry [50].

Direct tip–sample contact is usually undesired in STM, except in specialized applications such as the controlled drop-off of small amount of tip material, or jump-to-contact measurements emulating break junction experiments [79]. These techniques require careful control of tunneling parameters and tip position. The surface can be decorated with a controllable amount of tip material, or other material the tip has previously been coated with [145]. The progress of this deposition is typically accompanied by transients in the resistance of the tunneling junction, as the contact geometry is established.

More intensive tip indentations can cause uncontrolled material transfer between tip and sample and heavy damage to the affected sample region, rendering it unsuitable for further experimentation. Depending on contact intensity, damage can radiate further outward, and can manifest in a plethora of dislocation geometries. The most frequent of these are straight surface steps along the principal crystallographic axes. Occasionally, other structures such as narrow lines or trenches, or more complex geometries can form. In contrast to the other aforementioned preparation techniques, which can only be done at ambient temperature, tip indentations are done with the STM proper, at operating temperatures, where most diffusion processes are frozen out.

Chapter 3

Surface state electron confinement in monatomic resonators

In the following section, a series of experiments are presented concerning the confinement of surface state electrons within small regularly shaped Ag(111) surface areas, fully enclosed by monatomic steps. Specifically, the shapes involved are triangles and relaxed hexagons (with rounded corners), in both island (bounded by descending steps) and vacancy (ascending steps) configurations.

As the primary objective of these experiments, the apparent lifetimes of confined electrons are studied, by means of lineshape analysis of differential conductance spectra. The results are compared with a selection of previous lifetime-related experiments.

3.1 Experiment

For sample preparation, the Ag(111) crystal was cleaned by alternating cycles of Ar^+ ion sputtering and annealing, according to the procedure described in detail in section 1.7. Depending on the desired geometry of the resonators, a further preparation step was employed:

Hexagonal island resonator preparation. To create the hexagonal island resonators, the sample, initially at ambient temperature of $T \approx 300$ K within the preparation chamber, was exposed to the beam of a self-built silver evaporator. This evaporator is constructed by lodging a length of silver wire into a helical tungsten filament, mounted on a two-segment insulated stainless steel filament holder. Evaporation is performed in the preparation chamber by connecting the evaporator to a DC source and gradually increasing the current while monitoring the rate detected by the quartz microbalance. When a stable particle flux is attained (1.5 pm/s detected at 1.2 A, 2.0 V), the sample is exposed to the evaporator for a predetermined number of seconds, and subsequently

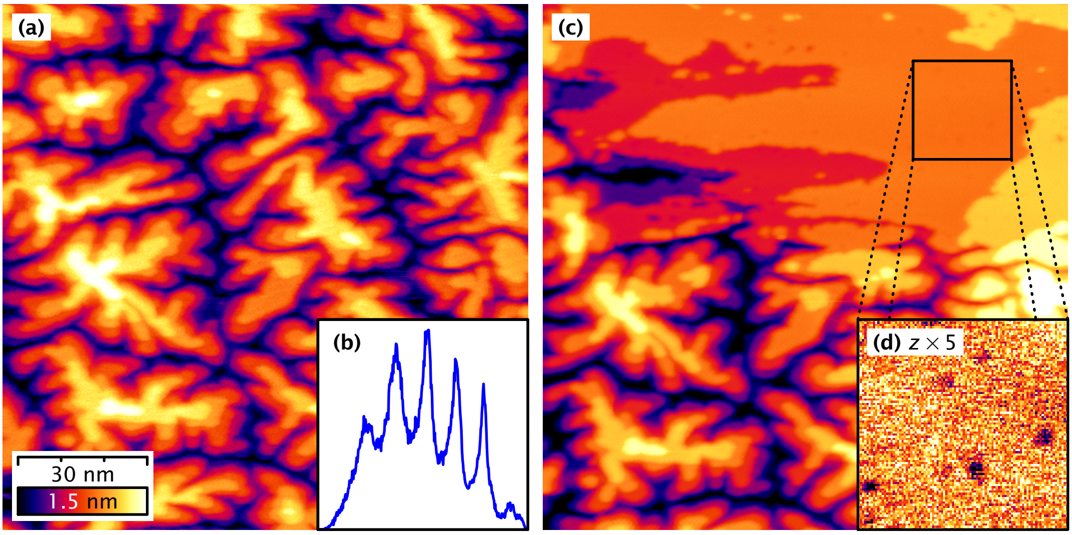

Figure 3.1 – Surface topography after multilayer Ag deposition. (250 nm)^2 topograph, $V = +200$ mV, $I = 190$ pA. **(a)** Excessive Ag evaporation leads to a dendritic surface structure. **(b)** The presence of a terrace structure can be verified by calculating a z histogram. **(c)** The same area, having been partially planished by scanning with the tip in contact. **(d)** Visual enhancement of z contrast shows impurities in the evaporant.

transferred into the pre-cooled analysis chamber within a time of 15 minutes, where it is allowed to cool down to the experimental temperature of $T = 7$ K.

The ideal exposure time is a function of the particle flux, the evaporation geometry and the specific adsorption probability. As the latter is not known *a priori*, the desired coverage had to be experimentally approximated. An initial exposure to 1.5 pm/s for 60 s yielded a multilayer silver coverage, with an irregular dendritic hill-and-valley structure, reproduced in fig. 3.1a, similar to the one described in ref. [94]. As a side note, it emerged that this structure could be locally planished with the tip, resulting in the topography of fig. 3.1c. The picture inlay shows a high-contrast close-up of a leveled region, showing impurities in the evaporated material.

An exposure to 1 pm/s for 15 s resulted in the desired level of coverage. The exact amount of adsorbed material, as well as the initial shape and size distribution of the adsorbed particles are not known. After evaporation, the sample is promptly transferred into the analysis chamber and cooled down.

At ambient temperature, the Ag/Ag(111) system undergoes an Ostwald ripening process where diffusion and nucleation of adsorbed material across the surface takes place. These processes freeze out at temperatures below a threshold of 200…260 K [199]. In the present case, the adatom islands assume a compact shape during sample transfer and cooldown, forming structures with a rounded hexagonal equilibrium geometry. An example image of a prepared region with several islands is reproduced in fig. 2.3a.

Hexagonal vacancy resonator preparation. The complementary structures, hexagonal vacancy resonators, were produced by exposing the clean Ag(111) surface to the Ar^+ ion beam from the sputtering source at ambient temperature, for $t = 3$ s, with the sputter gun operating at 600 V, 5 µA. As in the case of islands, the immediate structure after preparation is not known, since the treated surface reconstructs during transfer. The resulting surface structure consists of compact vacancies [161] and may still contain adatom islands [198], depending on the haste with which the sample is cooled down. A typical surface area after preparation is shown in fig. 2.3b.

Surface restructuring by tip indentation. Controlled tip indentations are not expected to reproducibly yield a specific surface geometry. Nevertheless, a search around the perimeter of a tip impact point may reveal suitable structures for surface state related measurements. Here, over the course of several deliberate indentations, two triangular resonators of monatomic height difference were created.

Additionally, during the course of this experiment, monatomic chain and trench structures emerged. These were used for supplementary dispersion measurements similar to those from ref. [31], described in section 4.1.

Mapping the differential conductance. Constant current differential conductance maps of the resonators were acquired in a range of sample bias voltages, to visualize the spatial distribution of surface state LDOS as a function of electron energy.

While scanning across the resonators, a sinusoidal modulation voltage of 3 mV_{rms} at a frequency of 10 kHz is applied to the sample bias. The current response is measured with a lock-in amplifier using the standard technique described in section 1.4. Being a rather time-consuming process, this is performed for a representative selection of available resonator geometries. Several series of these images, and their corresponding acquisition parameters, are reproduced in figs. 3.2, 3.3, and 3.4, below. Inside the resonators, strongly voltage-dependent features can be seen in the $\mathrm{d}I/\mathrm{d}V$ maps. These are attributed to standing waves of surface state electrons, that are confined by scattering at the resonator boundaries.

The two different hexagonal structures type show similar structures, matching the previously published results on hexagonal islands [142, 143]. With increasing sample bias, a pattern with a growing number of concentric rings is seen, their intensity modulated in a roughly sixfold azimuthal symmetry. For voltages below the Ag(111) surface state band edge of -67 mV, the interior of the resonator is featureless. The triangular resonators similarly show an interference pattern with a threefold azimuthal symmetry whose number of antinodes increases with the sample bias.

As the geometry of the hexagonal resonators is imperfect, the symmetry of the interference pattern is likewise partially distorted. In addition, the influence of the occasional subsurface defect can be seen.

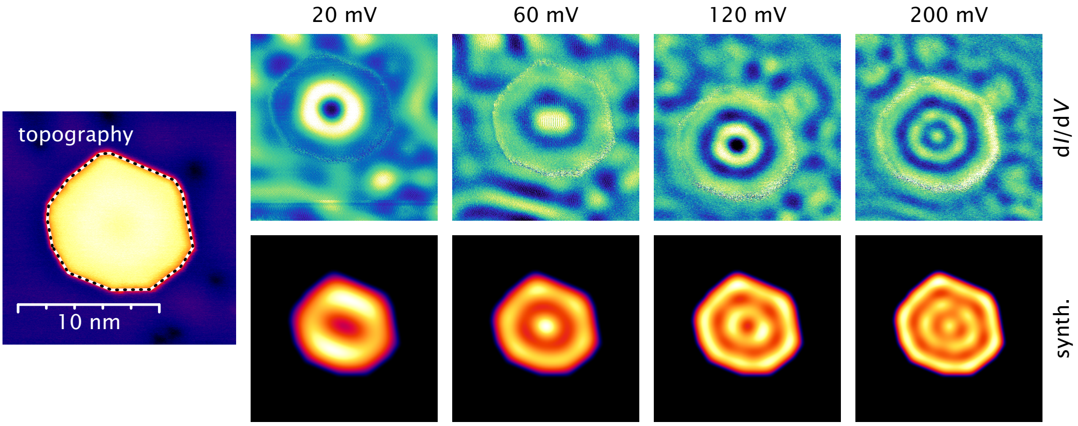

Figure 3.2 – Maps of a hexagonal island resonator. Topograph taken at $V = -40$ mV, $I = 20$ pA. Top row: dI/dV maps acquired at various voltages, corresponding to an increase in nodal rings. Bottom row: Simulated images for a polygonal waveguide whose boundary is given by the dashed line in the topograph.

Differential conductance spectroscopy. The main objective of the experimental part was the acquisition of energy-resolved LDOS information. For each resonator geometry, a set of constant height differential conductance spectra was acquired, with the tip situated on a representative location within the resonator. A two-step procedure was used:

Initially, an overview topograph of the resonator was acquired. From this scan, a suitable tip location for spectroscopy was chosen. Afterwards, a second scan was initiated, and as the preselected location was reached by the tip, the scan was interrupted by software, the z feedback loop was suspended, and a predetermined number of constant current spectra was acquired.

After completion of the spectra, the topography scan was resumed and archived together with the spectroscopy data. Thereby, the exact tip position during spectroscopy was recorded. Due to slight thermal drift and piezo creep, the interruption by the spectra causes a step-like jump in the topograph z data at the acquisition point. The amount of lateral drift can further be estimated by observing the slight displacement between parts of the image acquired before and after the spectroscopy.

The spectra comprise a series of peaks with Lorentzian shape, shown in fig. 3.5. The first peak is located just above the lower band edge of the Ag(111) Shockley surface state. As a general trend, the peak width increases with increasing energy.

3.2 Linewidths: the Lorentz model

The main features of the resonator spectra are a series of discrete peaks with a roughly Lorentzian lineshape, above the surface state onset. A first model assumes a one-to-one

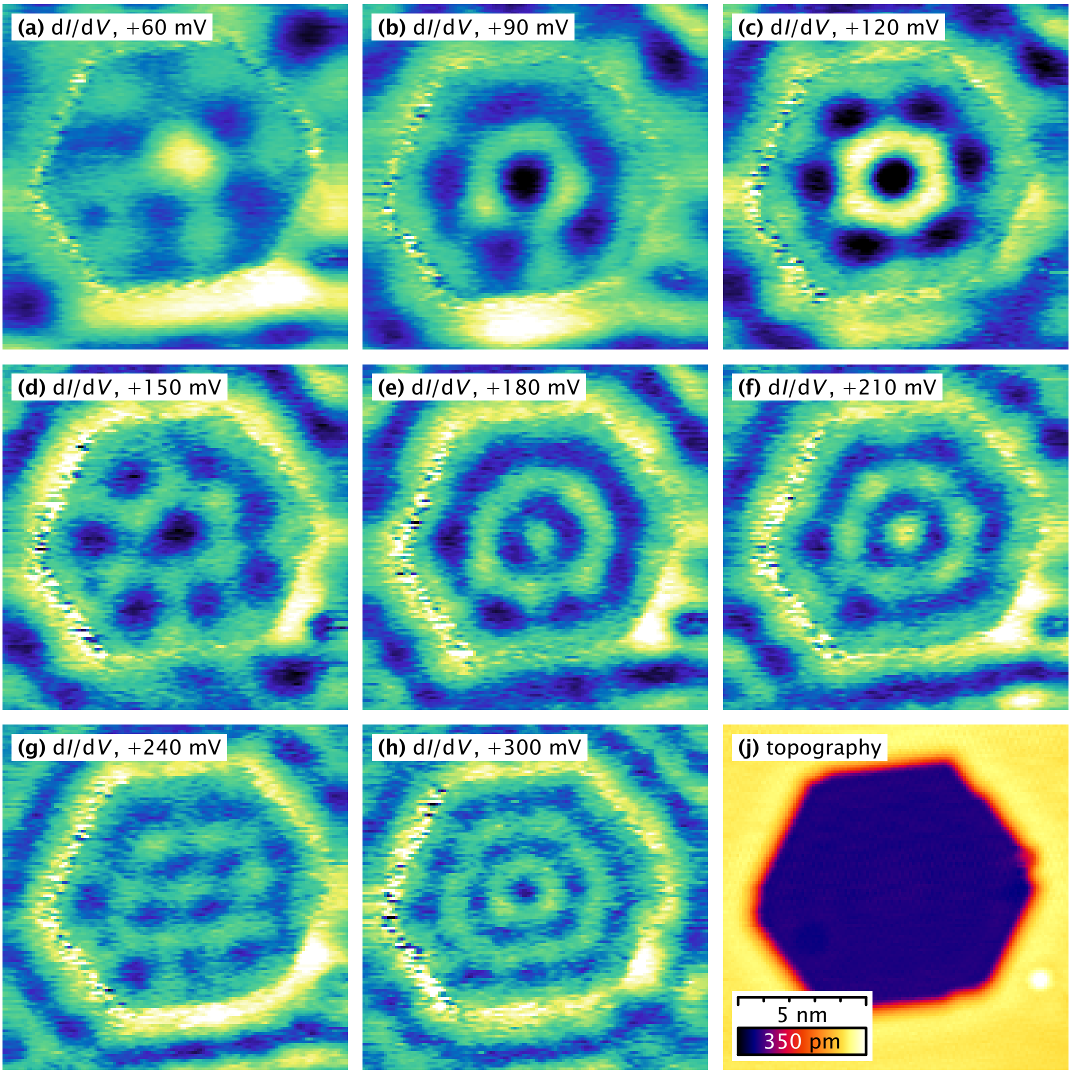

Figure 3.3 – Maps of a hexagonal vacancy resonator with an average edge length of ≈ 5.8 nm. The feedback loop was disengaged at a tunneling current of 0.5 nA. **(a–h)** Differential conductance maps are shown as a function of sample bias. Brighter regions correspond to a larger differential conductance. The interior of the resonator shows a standing wave pattern, with a number of nodes that increases with sample bias. **(j)** A topograph taken at $V = +300$ mV is included to show the resonator geometry.

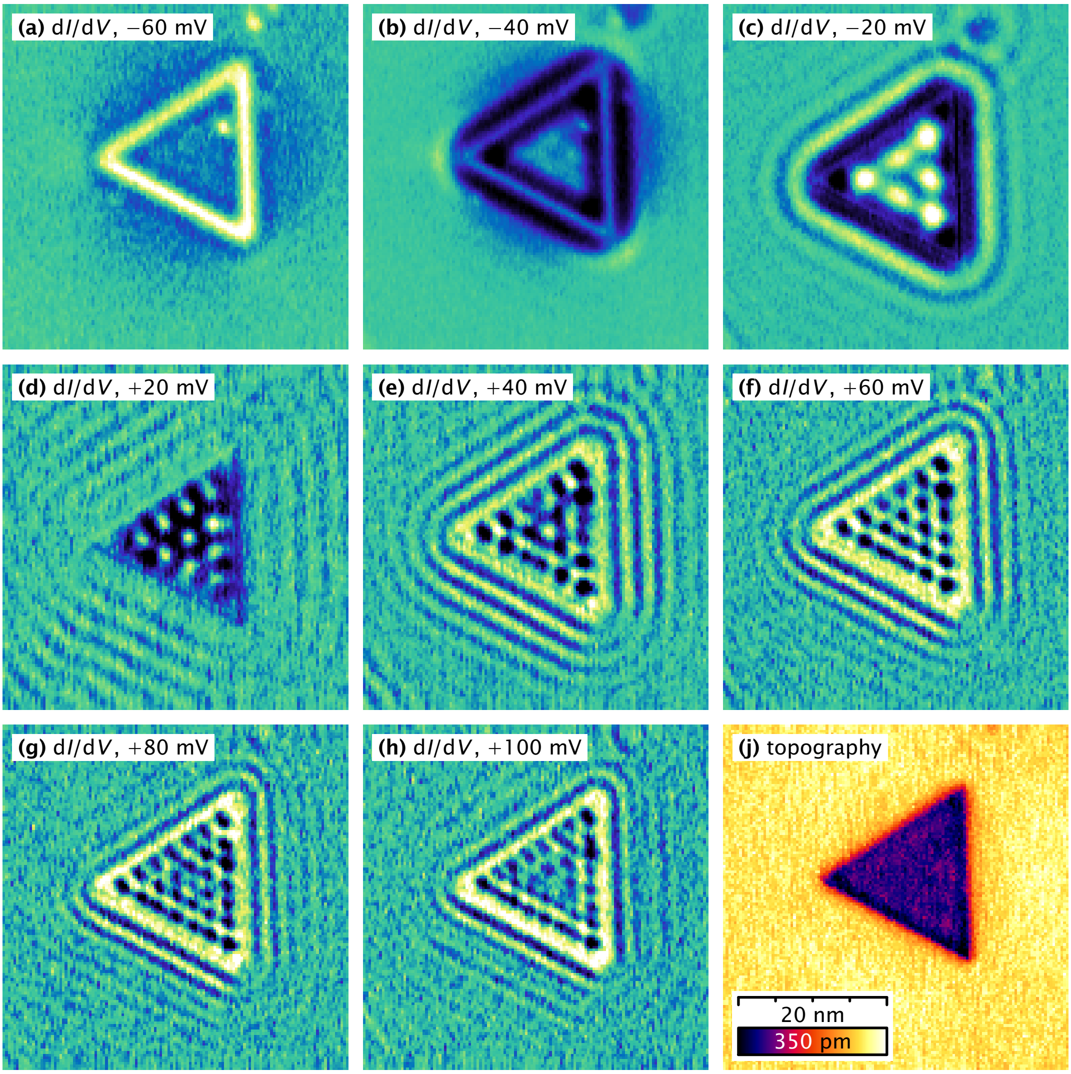

Figure 3.4 – Maps of a triangular vacancy resonator with an edge length of 22 nm. The feedback loop was disengaged at a tunneling current of 2 nA. **(a–h)** Differential conductance maps are shown as a function of sample bias. Brighter regions correspond to a larger differential conductance. The interior of the resonator shows a standing wave pattern, with a number of nodes that increases with sample bias. The single bright speck within the resonator, visible at low bias, is attributed to a subsurface defect. **(j)** Reference topograph taken at $V = -60$ mV.

correspondence between these peaks and the eigenstates of the mathematical waveguide problem [50]. This requires that the eigenenergies are energetically sufficiently apart for the peaks to be clearly discernible and not significantly overlap.

For symmetrical geometries, many of the eigenstates vanish at the origin[1]. These are expected to give a zero contribution when the spectra are nominally acquired in the center of the structure [139]. Irregularities in the resonator geometry, inaccuracies in tip positioning and the contributions due to a larger-than-punctiform tip may cause this approximation to fail.

Without specific knowledge of the eigenfunctions and their respective energies, the spectra can be analyzed in terms of Lorentzian functions. To this end, for each spectrum a candidate function

$$f(E) := f_0 + \sum_{i=1}^{n} L(a_i, \Gamma_i, E_i, E) \tag{3.1}$$

is introduced, consisting of a series of n Lorentz peaks

$$L(a_i, \Gamma_i, E_i, E) := \frac{2a_i}{\pi\Gamma_i}\left[1 + \frac{4(E - E_i)^2}{\Gamma_i^2}\right]^{-1}. \tag{3.2}$$

The parameters involved are the number of discernible peaks n, an additive spectral floor f_0, and for each peak, amplitude a_i, position E_i, and width (FWHM) Γ_i. The evanescent influence of peaks situated above the measured energy range is modeled by adding another fixed peak at 600 mV whose shoulder contributes to the spectral background.

The experimental spectra contain additional broadening sources, including a Gaussian broadening due to thermal noise and the effects of the lock-in technique (with a characteristic half-ellipse function depending on modulation amplitude, described in section A.3). Since numeric deconvolution of a noisy signal is usually not viable, the candidate functions are artificially broadened instead, by convolution with the aforementioned kernels. The parameters are initialized manually to a rough agreement with experimental data, then optimized with a NLS fit using the Levenberg-Marquardt method [138, 157]. For a selection of resonators, fig. 3.5 reproduces the experimental spectra and the best-fit candidate functions for a selection of resonators where the Lorentz fit was feasible. The (manually chosen) tip positions at which the spectra were acquired agree well with the barycenter of the enclosing polygon.

Fit results. The peak positions can be correlated to the expected eigenenergies for the respective regular resonators. This has previously been done for hexagonal adatom islands [139], where the energy levels were obtained with an embedding potential [104] to impose the zero amplitude boundary condition [49].

Fig. 3.6 shows the peak widths (FWHM) Γ_i as a function of peak position E_i, collected from all considered resonator geometries. Γ_i and the quasiparticle lifetime τ_i are related

---

[1] *E.g.*, for a circular resonator, this is the case for all solutions with nonzero angular momentum [50]. The remaining eigenstates form a sequence with uniformly increasing energetic separation.

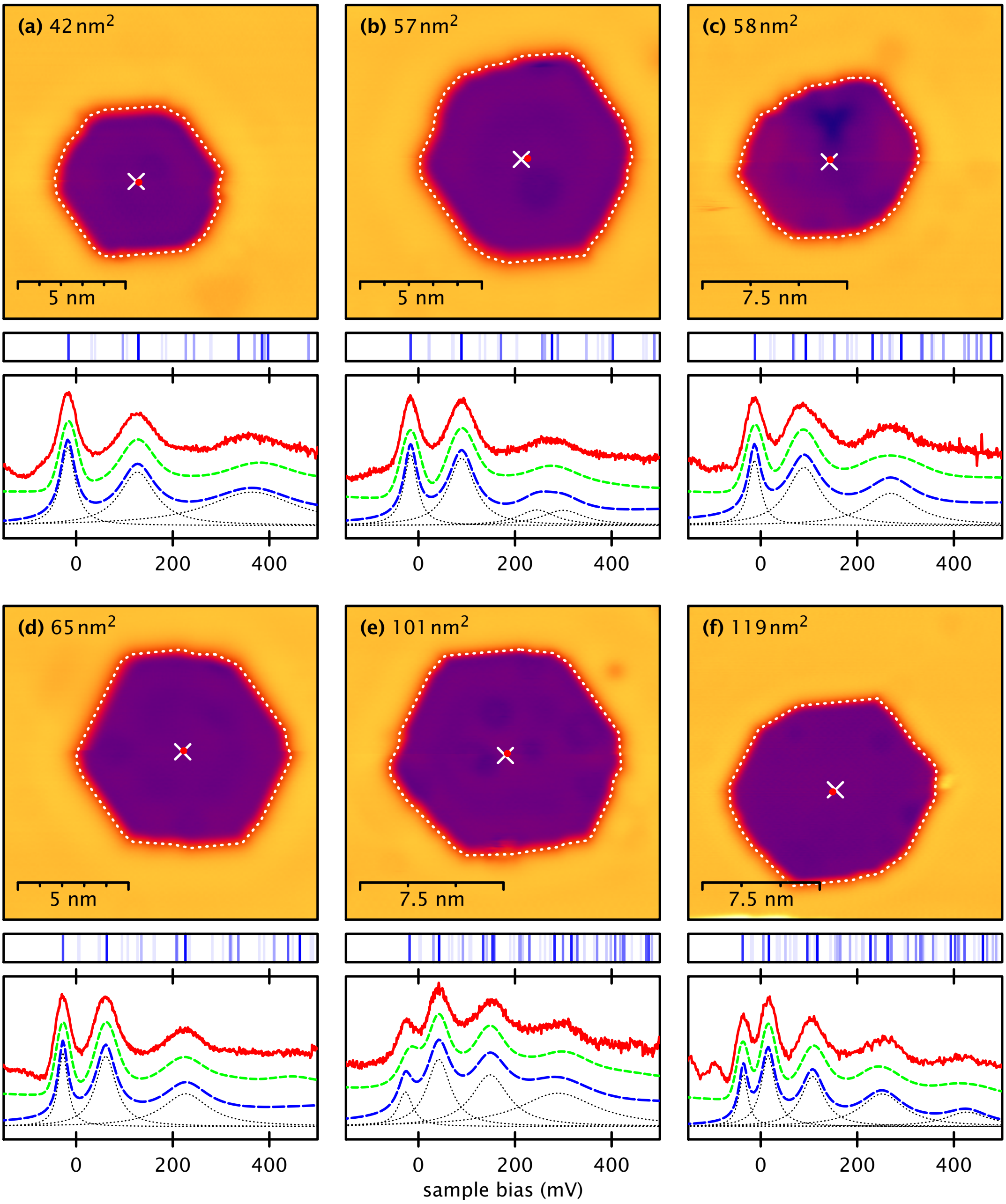

Figure 3.5 (continued on next page)

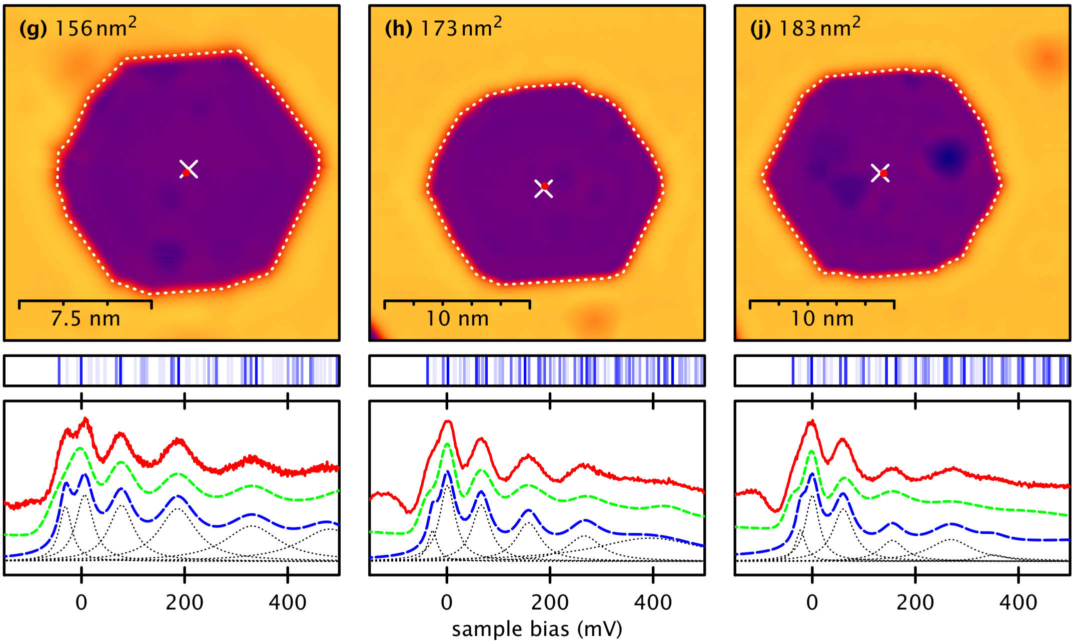

Figure 3.5 – Measured and calculated vacancy resonator spectra for a selection of resonators. Calculated curves are obtained from both Lorentz fit and a polygonal waveguide calculation using the ITP method. Top: resonator topography and approximated boundary polygon (dashed line, see text), polygon barycenter (red dot), and tip position for spectroscopy (white cross). Below: Series of lines denoting eigenenergies and relative weights of the calculated ITP eigenfunctions (darker hues corresponding to larger weights). The latter are obtained for a simulated spherical tip phantom positioned at the spectroscopy site (see text). Bottom (offset for legibility): Measured spectra (red line), synthetic spectrum from polygonal waveguide calculation (green line), Lorentz fit (blue line) and its constituent peaks (dashed lines).

by

$$\tau_i = \frac{\hbar}{\Gamma_i} \approx \frac{658.2\ \text{meV} \times \text{fs}}{\Gamma_i}. \tag{3.3}$$

As a general trend, Γ_i increases with energy. The presence of outliers may indicate cases where several energetically close, overlapping peaks have been misidentified as a single, wider peak. While the exact functional dependence is not evident from the graph, a linear approximation can be made, giving an empirical relation of

$$-\mathfrak{Im}\Sigma_i = \frac{\Gamma_i(E)}{2} \approx 17\ \text{meV} + 0.17(E_i - E_\text{F}). \tag{3.4}$$

A previous estimate of this effect has been given by Li *et al.* for hexagonal island resonators, where an expression of

$$-\mathfrak{Im}\Sigma_i \approx 0.2(E_i - E_\text{F}) \tag{3.5}$$

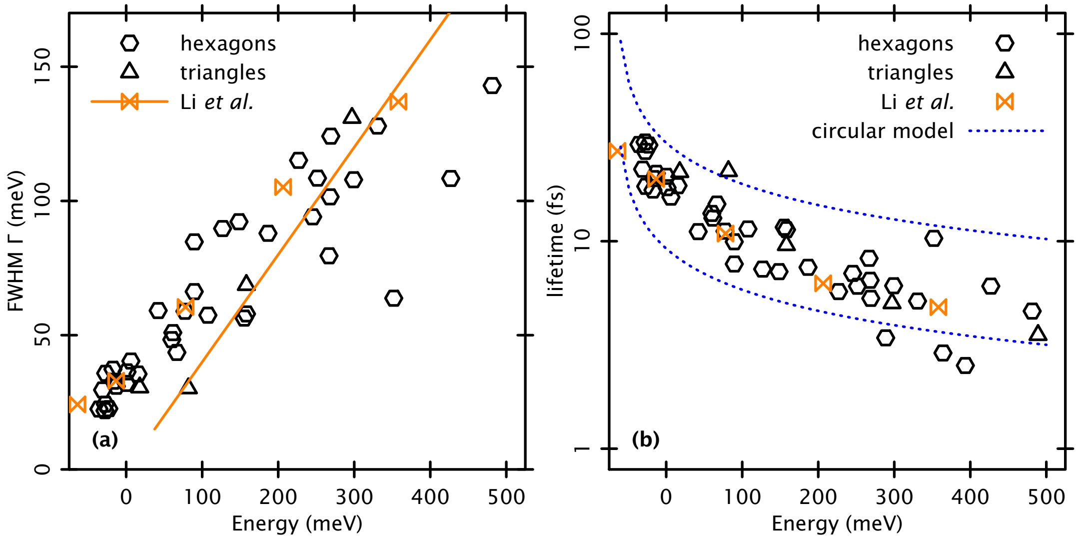

Figure 3.6 – Confinement parameters from Lorentz fit. **(a)** Widths (FWHM) Γ for vacancy hexagons and triangles are shown, as a function of binding energy. Raw widths for hexagonal adatom islands, and empirical relationship reported by Li *et al.* in ref. [142] added as reference. **(b)** Lifetimes τ, as a function of binding energy. The curves from the circular model, with resonator sizes of 4 and 8.5 nm, respectively (see text), provide lower and upper bounds for the experimental data.

was found [142].

3.3 Energy levels: the particle-in-a-box model

The electron confinement can be modeled by two-dimensional particle-in-a-box calculations. This assumes perfect confinement within the resonator. The Schrödinger equation

$$-\frac{\hbar^2}{2m^*}\Delta\psi = (U - E)\psi = 0, \tag{3.6}$$

or

$$\left[\Delta + {k_i}^2\right]\psi_i = 0 \quad \text{with} \quad {k_i}^2 := \frac{2m^* E_i}{\hbar^2}, \tag{3.7}$$

is solved to obtain the eigenfunctions ψ_i and eigenenergies E_i. The specific resonator geometry is introduced by imposing a Dirichlet boundary condition, *i.e.*, demanding $\psi_i = 0$ at the resonator borders. Initially, it is not clear where the boundaries have to be placed for any given geometry, relative to the topographic shape of the resonators. It has, however, previously established [142] that, in order to use such a potential to describe electron confinement in hexagonal islands, the half-height contour provides a sufficiently good match. Hence, a polygonal closed loop was matched to each of the measured topographs, adding vertices as needed to provide a subjectively fair approximation.

Circular resonator. For a circular resonator centered at the origin, the Schrödinger equation is written in polar coordinates,

$$\left[\frac{\partial^2}{\partial r^2}+\frac{1}{r}\frac{\partial}{\partial r}+\frac{1}{r^2}\frac{\partial^2}{\partial\varphi^2}\right]\psi+k^2\psi=0, \tag{3.8}$$

and, with the *ansatz*

$$\psi(r,\varphi)=:R(r)\Phi(\varphi) \tag{3.9}$$

this is separable into radial and azimuthal portions,

$$\frac{r^2R''+rR'+k^2R}{R}=-\frac{\Phi''}{\Phi}=:m^2. \tag{3.10}$$

The latter can be solved directly, giving

$$\Phi(\varphi)=\exp(\pm\mathrm{i}m\varphi)\quad\text{for integer } m, \tag{3.11}$$

and the former leads to

$$R''+\frac{1}{r}R'+\left(k^2-\frac{m^2}{r^2}\right)R=0, \tag{3.12}$$

which is Bessel's differential equation in the variable kr. Its solutions are of the general form

$$R(r)=a\mathrm{J}_{|m|}(kr)+b\mathrm{Y}_{|m|}(kr), \tag{3.13}$$

with $\mathrm{J}_\nu(x)$ and $\mathrm{Y}_\nu(x)$ denoting the Bessel functions of the first and second kinds, respectively, for the order ν. The latter have a singularity at $x=0$, and thus cannot appear in the solutions to the physical problem, leaving

$$\psi_{mn}(r,\varphi)=a\mathrm{J}_{|m|}(kr)\exp(\pm im\varphi). \tag{3.14}$$

To satisfy the boundary condition, the wavefunction must vanish at the encompassing circle, *i.e.*, $\mathrm{J}_{|m|}(kr_0)=0$, or $k=\frac{\zeta_{|m|,n}}{r_0}$, with $\zeta_{m,n}$ designating the $n+1$st positive root of J_m, resulting in n radial nodes and energy eigenvalues of

$$E_{mn}=\frac{\hbar^2}{2m^*r_0^2}\left(\zeta_{|m|,n}\right)^2. \tag{3.15}$$

Normalization requires that

$$a^{-2}=2\pi\int_0^{r_0}\mathrm{J}_{|m|}(kr)^2r\,\mathrm{d}r=\pi r_0^2\mathrm{J}_{|m|+1}(kr_0)^2. \tag{3.16}$$

The solutions in the form (3.14) are complex and twofold degenerate for $m\neq 0$. There are no degeneracies between states with differing m or n, according to Bourget's (since proven) hypothesis [235]. Pairs of real-valued solutions can be obtained, for $m>0$, by

$$\begin{aligned}\psi_{mn}^{+}&=\frac{1}{\sqrt{2}}(\psi_{mn}+\psi_{-mn})=\sqrt{2}a\mathrm{J}_m(kr)\cos(m\varphi)\\ \psi_{mn}^{-}&=\frac{1}{\sqrt{2}\mathrm{i}}(\psi_{mn}-\psi_{-mn})=\sqrt{2}a\mathrm{J}_m(kr)\sin(m\varphi).\end{aligned} \tag{3.17}$$

Some lowest-energy eigenmodes are represented graphically, in fig. 3.7, and by wavenumber, in fig. 3.8.

Triangular resonator. The eigenfunctions for a resonator in the shape of an equilateral triangle can also be expressed in closed form [144]. Given a triangle with the corner points $(0,0)$, $(\frac{1}{2}a, \frac{\sqrt{3}}{2}a)$, and $(a,0)$, and defining $r := -q - p$ and two helper functions,

$$\begin{aligned}\Phi_{p,q}(x,y) = {} & \cos\left[\frac{2\pi}{a}px\right]\sin\left[\frac{2\pi}{\sqrt{3}a}(q-r)y\right]\\ & +\cos\left[\frac{2\pi}{a}qx\right]\sin\left[\frac{2\pi}{\sqrt{3}a}(r-p)y\right]\\ & +\cos\left[\frac{2\pi}{a}rx\right]\sin\left[\frac{2\pi}{\sqrt{3}a}(p-q)y\right]\end{aligned} \tag{3.18}$$

and

$$\begin{aligned}\Xi_{p,q}(x,y) = {} & \sin\left[\frac{2\pi}{a}px\right]\sin\left[\frac{2\pi}{\sqrt{3}a}(q-r)y\right]\\ & +\sin\left[\frac{2\pi}{a}qx\right]\sin\left[\frac{2\pi}{\sqrt{3}a}(r-p)y\right]\\ & +\sin\left[\frac{2\pi}{a}rx\right]\sin\left[\frac{2\pi}{\sqrt{3}a}(p-q)y\right],\end{aligned} \tag{3.19}$$

the unnormalized eigenfunctions, depending on symmetry class [144], are given by

$$\begin{array}{rlr} \Phi_{p,q} & \text{with} & p = 0,1,2,\ldots \\ & \text{and} & q = p+1, p+2, p+3,\ldots \\ \Xi_{p,q} & \text{with} & p = 1,2,3,\ldots \\ & \text{and} & q = p+1, p+2, p+3,\ldots \\ \Phi_{p,q} + \mathrm{i}\Xi_{p,q} & \text{with} & p = \frac{1}{3}, \frac{2}{3}, \frac{4}{3}, \frac{5}{3}, \frac{7}{3}, \frac{8}{3}\ldots \\ & \text{and} & q = p+1, p+2, p+3,\ldots \end{array} \tag{3.20}$$

The corresponding eigenenergies are given by

$$E_{p,q} = \left(\frac{4\pi}{a}\right)^2 \left(p^2 + pq + q^2\right). \tag{3.21}$$

Hexagonal resonator. For the regular hexagon, only a portion of the eigenfunctions can be written in closed form, specifically those that have all three lines connecting opposite corners as nodal lines. These separate the hexagon into six equilateral triangles. The eigenfunctions can then be obtained by tiling the hexagon with the solutions for the triangle given above, with alternating sign in azimuthally adjacent sextants.

All other solutions, where the eigenfunction does not vanish on the sextant boundaries, can not be written in closed form. These eigenmodes and their corresponding

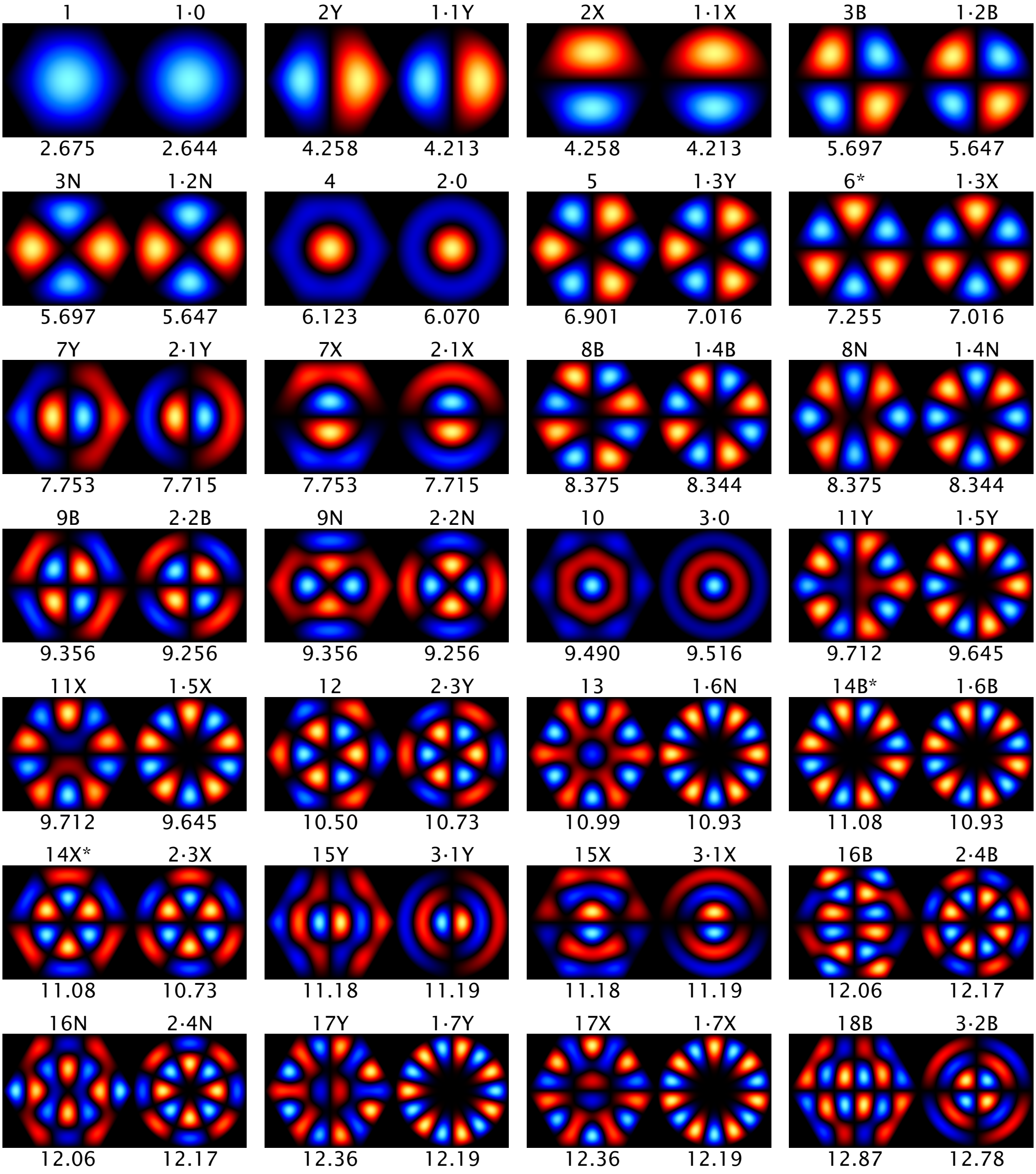

Figure 3.7 (continued on next page)

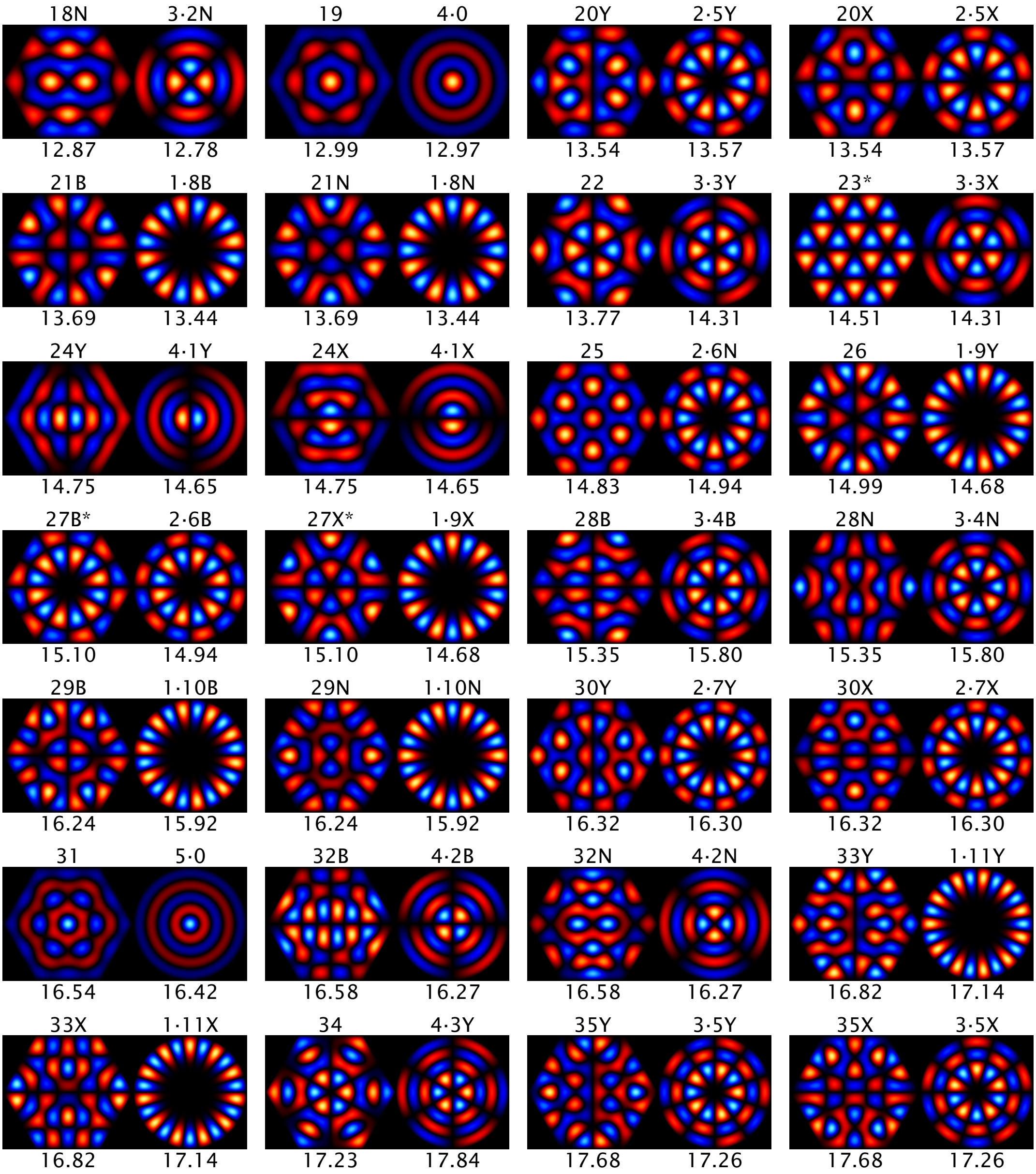

Figure 3.7 (concluded on next page)

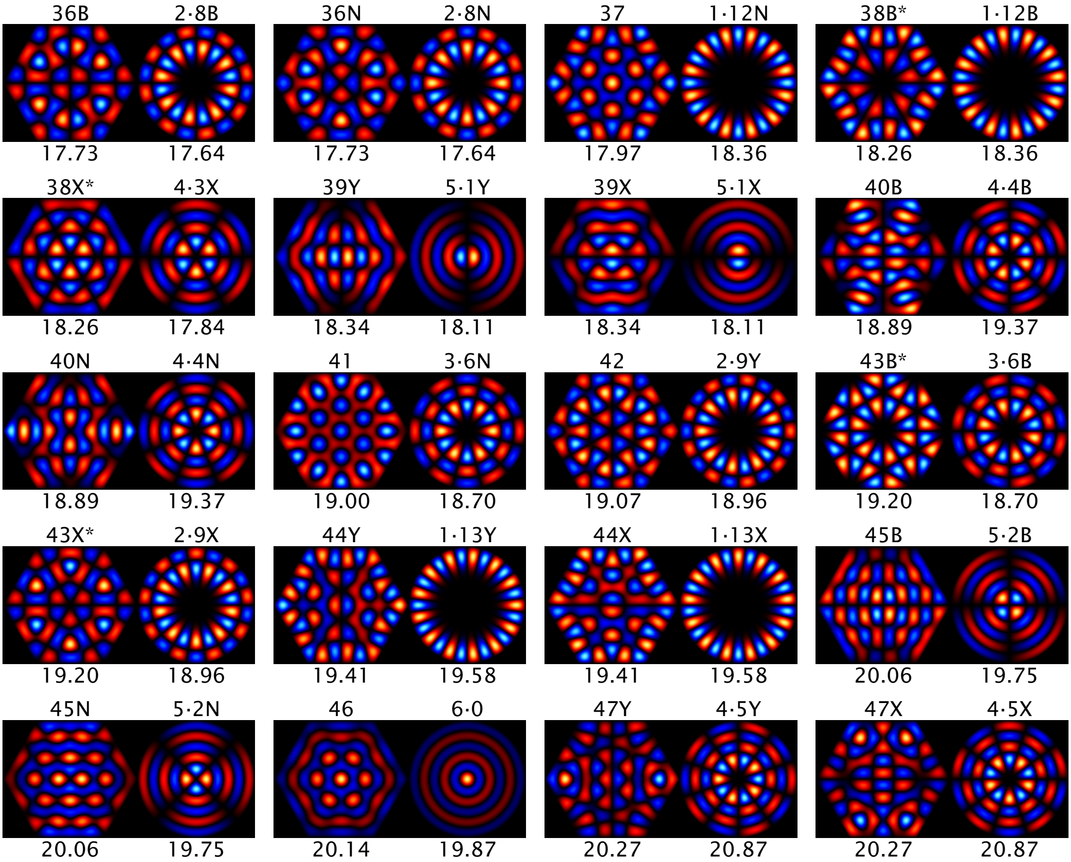

Figure 3.7 – Eigenmodes of hexagonal and circular waveguides of area $A = \pi$. Hexagon eigenmodes (sorted by eigenenergy) on the left, corresponding circular eigenmodes (see ref. [15]) on the right. The former are numbered by unique energy level, the latter by radial and azimuthal quantum number (as $n{\cdot}m$). Letters distinguish degenerate modes by their nodal lines. The triangle closed-form solutions are marked with asterisks. Wavenumbers k are given below.

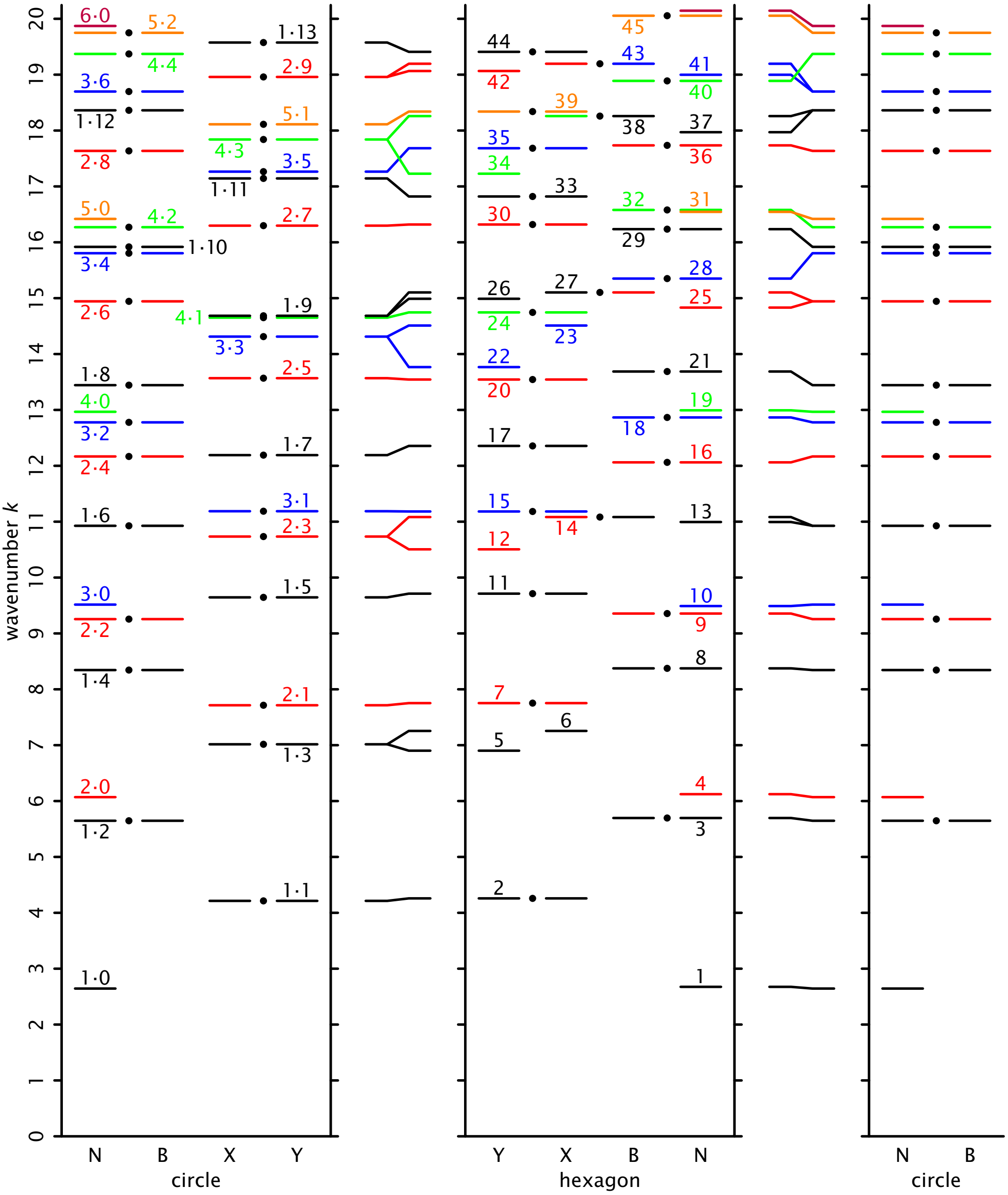

Figure 3.8 – Eigenstate wavenumbers of hexagonal and circular waveguides of area $A = \pi$. Lowest 74 eigenstates are shown, arranged by symmetry class (see text), with correspondences marked. For the circle, radial and azimuthal quantum numbers are given as $n{\cdot}m$. Hexagon eigenstates are numbered by unique energy levels. Eigenstates are colored by increasing n, and dots designate pairs of degenerate eigenmodes.

energy eigenvalues can be determined numerically [15]. For the calculation itself, the Imaginary Time Propagation method is used. The method, which has been independently implemented for this work, allows to obtain a sequence of eigenfunctions and their respective eigenenergies of a system, starting from the ground state. The functions are represented on a finite grid. More details on the method and its implementation are given in appendix B.

Defining the x axis as connecting two opposite corners, and the y axis connecting the midpoints of two opposing edges, the eigenfunctions can be classified, depending on whether one of the axes (X or Y), both (B) or none (N) of them form nodal lines. The wavefunctions can be tightly correlated to the eigenfunctions of the circular resonator, where classes B and N correspond to even m, and classes X and Y to odd m. It has been found that when the circle of equal area to the hexagon is used, the best match of eigenenergies is obtained, with typical deviations of a few percent [15].

Most hexagon states have the same degeneracies as the circular states (X with Y, and N with B where $m > 0$), with the notable exception of those states where m is a multiple of 3, where a different (X with B) degeneracy occurs. These are the triangle closed-form solutions.

Irregular polygonal resonator. The same procedure can be extended to resonators of arbitrary shape. This allows to more precisely model the near-hexagonal vacancies with rounded edges that were created by sputtering.

To this end, each vacancy is represented by a closed polygonal path along the perimeter. It has previously been reported that for adatom islands, the effective boundary lies close to the midpoint of the step edge as it appears in a topograph [142]. This observation is used here as a starting assumption for the vacancy resonator geometry. After applying slope and drift corrections, the apparent elevations of flat regions inside and outside the resonator, respectively, are averaged. The mean of these two values gives the threshold for a given pixel to be declared inside the resonator.

As a starting point, a closed polygonal path is manually drawn along the border of this inside region, adding vertices by eye as needed. The position of the individual vertices is then numerically optimized to best fit the inside region. This polygonal path forms the boundary for the region in which the calculation of eigenfunctions takes place.

Numerical method. The lateral resolution is obtained by placing a spherical tip model at the site of the experimental spectra, using the van der Waals radius of silver, 172 pm [26]. The weights a_i by which the individual eigenstates contribute to the spectrum are calculated from $|\psi|^2$ weighted by the tip model profile. To assemble a synthetic spectrum, a linear background and one Lorentzian per eigenstate, centered at the respective eigenenergy $E_0 + \alpha E_i$ are summed,

$$s(E) = s_0 + s_1 E + \sum_{i=1}^{n} \frac{2a_i}{\pi \Gamma_i} \left[1 + \frac{4(E - E_0 - \alpha E_i)}{\Gamma_i^2} \right]^{-1} \tag{3.22}$$

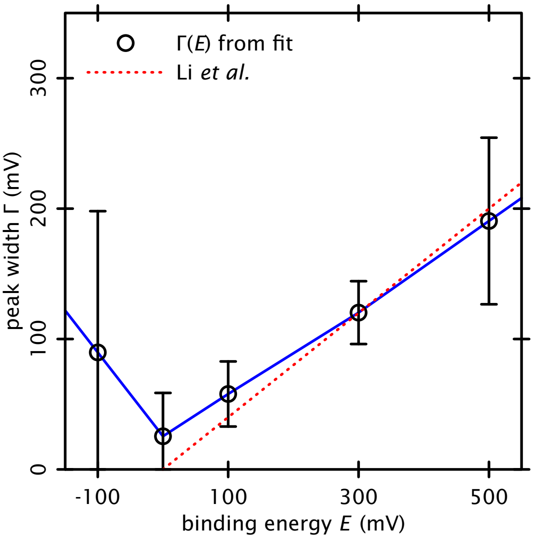

Figure 3.9 – Piecewise linear spectral width approximation. The candidate function Γ(*E*) (blue) is linearly interpolated from the shown five control points. At these, function values are obtained by fitting the resulting synthetic spectra to the experimental ones (see text). As a reference, the empirical relation (red) found by Li *et al.* [142] is included.

The scale factor $\alpha \approx 1$ is introduced to account for variations in the resonator size, which may be due to lateral piezo calibration uncertainties, and systematic errors in the determination of the boundaries (see below). The number n of eigenfunctions is chosen to generously exceed the experimental energy range (here, $q_e E_n > 800$ mV). The normalized amplitudes a_i are the weights calculated above, and the widths Γ_i are taken from a suitable candidate function $\Gamma(E)$, with $\Gamma_i = \Gamma(E_i)$.

As in the Lorentz model above, the synthetic spectra are artificially broadened to account for thermal effects and the lock-in technique. The resulting function is then optimized by an NLS fit, varying α, E_0, s_0, s_i and $\Gamma(E)$ until the overall spectra best match the experimental data. As a candidate for $\Gamma(E)$, a piecewise linear function is used. Control points are placed at fixed energies of $\{-100, 0, 100, 300, 500\}$ mV. The Γ values at these energies are varied independently by the fit, and values for other energies are obtained by linear interpolation. The fit results are given in fig. 3.9 for $\Gamma(E)$, and in fig. 3.5 for the resulting synthetic spectra. From the former, an agreement with the previously found empirical relation is readily seen. The data point at -100 mV shows a larger uncertainty, owing to a scarcity of experimental peaks well below the Fermi level. Otherwise, the choice of a linearly increasing $\Gamma(E)$ appears justified by the data.

Regarding the lineshapes themselves, it is evident from fig. 3.5 that the general shape of the experimental spectra is reproduced quite well, for different resonator geometries of varying area. The energy levels of the included eigenfunctions are shown as a series of lines (where the variations in color intensity signify the relative weights a_i). Within the energy range, there are many more eigenfunctions than is apparent from the three to six clear main spectral peaks. Depending on the resonator size, up to $n = 300$ eigenfunctions are used in the calculations. The spectral shape is reproduced with high accuracy, with relatively few fit variables, especially, without requiring individual peak positions, amplitudes, and widths as independent parameters.

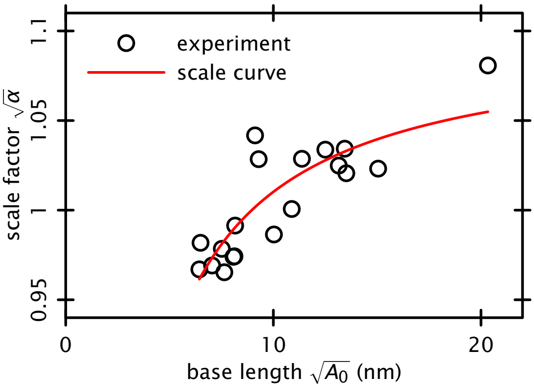

Figure 3.10 – Resonator apparent areas, with scale factors α obtained from the full eigenenergy fit. $\sqrt{\alpha}$ is shown as a function of base length (square root of resonator base area A_0). Line shows fit to the orthogonal edge displacement model (see text). For base geometries matching the real resonator shapes, a constant α is expected. A deviation toward lower values for small resonators indicates a systematic underestimation of resonator areas, due to tip size effects.

Geometry	m	k
Circle (radius a)	π	1
Hexagon (edge a)	$3\sqrt{3}/2$	$\sqrt{4/3}$
Square (edge a)	1	2
Equilateral triangle (edge a)	$\sqrt{3}/4$	$\sqrt{12}$

Table 3.11 – Geometry scale factors m and k, for orthogonal displacement of the resonator boundaries by d (positive outward). Areas are $A_0 = ma^2$ for the base geometry, $A_d = m(a + kd)^2$ for the resized geometry.

Geometry and scale effects. As stated above, for adatom islands, the halfway points of the apparent topographic rise provide a good model for the resonator boundary [142], from which the base area is obtained. This is not necessarily true for vacancy islands. Fig. 3.10 shows that the geometric scale factor as a function of resonator base area is not constant (modulo calibration noise), but has an obvious trend.

The density of eigenenergy levels scales linearly with resonator areas. Thus smaller values α correspond to denser than expected energy levels, and thus, to larger resonators. Specifically, for a base area A_0 and a rescaled area A_d,

$$\alpha = \alpha_0 \frac{A_0}{A_d}, \tag{3.23}$$

with a constant $\alpha_0 \approx 1$ describing the systematic calibration error. If the resonator geometries are approximated by one of the shapes in table 3.11, the areas can be calculated as a function of orthogonal edge displacement d, with $A_0 = ma^2$, $A_d = m(a + kd)^2$. With this, (3.23) leads to

$$\sqrt{\alpha} \approx \sqrt{\alpha_0}\left(1 - kd\sqrt{m}\Big/\sqrt{A_0}\right). \tag{3.24}$$

This expression can be fit to the data in fig. 3.10. Using the hexagon and circle parameter sets gives a mean value of $d \approx 0.65 \pm 0.02$ nm.

This positive value means that the real resonator boundaries are larger than the assumed base geometries. This is consistent with the expectation that a correct determination of surface features is, in principle, only possible with a punctiform tip. As the width of the tip apex increases, the apparent size of a vacancy resonator shrinks. More generally, any stepped features are smeared out toward the descending step direction.

Additionally, the model assumes a perfect confinement with total reflectivity at the boundaries. In reality, the surface state is only partially confined, with the tails of the wavefunctions leaking out of the boundaries, leading to a larger effective resonator size. In island resonators, these two effects compete and cancel out, as seen by Li *et al.*, while in vacancy resonators, they add up, leading to the reported geometric deviation.

3.4 Lifetime results and discussion

The three decay channels considered are electron–electron (e–e) scattering, electron–phonon (e–φ) scattering, and lossy scattering at the step edge. The former two processes are expected to vanish as the quasiparticle energy approaches the Fermi level, corroborating the observed increase in experimental lifetime. Discussing the relative magnitudes of the contributions, however, merits a more thorough analysis.

The experimental lifetimes given in fig. 3.6, especially the similarity of hexagon and triangle data, hint at a limited impact of the actual geometry on the measured lifetime. This advertises the use of a circular resonator of radius S as a modeling system, for which an analytic treatment can be made. Given a reflection coefficient R of the confining step, in order for a confined state with nonzero probability at the island center to occur, as shown in ref. [47], the quasiparticle energy must adhere to the condition

$$R \exp(2\mathrm{i}kS) \exp(-S/L_\Phi) \exp(-\mathrm{i}\pi/2) = 1, \tag{3.25}$$

where $k = \sqrt{2m^*(E - E_0)\hbar^{-2}}$ denotes the quasiparticle wavevector, and L_Φ is a phase relaxation length that contains e–e and e–φ effects. Eq. (3.25) can be understood by comparing with the phase accumulation model for quantum well states [180], which gives a similar phase condition for a surface state round trip. Writing R in terms of amplitude and phase,

$$R =: |R| \exp i\Phi_R = \exp[\mathrm{i}(\Phi_R - \mathrm{i}\ln|R|)], \tag{3.26}$$

eq. (3.25) is satisfied by the condition

$$\Phi_R - \mathrm{i}\ln|R| + 2kS + \mathrm{i}S/L_\Phi - \frac{\pi}{2} = 2\pi n \tag{3.27}$$

for any positive integer n. The solutions are the complex energies $E_n - \mathrm{i}\frac{\Gamma_n}{2}$ where the condition holds for a given n. Assuming $\Gamma_n \ll E_n - E_0$, the approximations for $y \ll x$,

$$\mathfrak{Re}\sqrt{x + \mathrm{i}y} \approx \sqrt{x} \quad \text{and} \quad \mathfrak{Im}\sqrt{x + \mathrm{i}y} \approx \frac{y}{2\sqrt{x}}, \tag{3.28}$$

can be employed, leading to

$$\mathfrak{Re}\, k_n \approx \frac{\sqrt{2m^*}}{\hbar}\sqrt{E_n - E_0} \tag{3.29}$$

and

$$\mathfrak{Im}\, k_n \approx \frac{\sqrt{2m^*}}{\hbar}\frac{\Gamma}{4\sqrt{E_n - E_0}}. \tag{3.30}$$

From the real part of (3.27), with (3.29),

$$\Phi_R + \frac{2}{\hbar}\sqrt{2m^*(E_n - E_0)}S = 2\pi\left(n + \frac{1}{4}\right), \tag{3.31}$$

the energy of the nth level is obtained,

$$E_n = E_0 + \frac{\hbar^2}{2m^* S^2}\left[\pi\left(n + \frac{1}{4}\right) + \frac{\Phi_R}{2}\right]^2. \tag{3.32}$$

The imaginary part of (3.27), with (3.30),

$$-\ln|R| + \frac{S}{L_\Phi} = 0, \tag{3.33}$$

when introducing the group velocity,

$$v_\mathrm{g} := \frac{\hbar k}{m^*}, \tag{3.34}$$

yields the width (FWHM) of the nth level,

$$\Gamma_n = \hbar v_\mathrm{g}\left[-\frac{\ln|R|}{S} + \frac{1}{L_\Phi}\right]. \tag{3.35}$$

This can be written in terms of lifetimes, becoming

$$\tau^{-1} = \tau_\mathrm{R}^{-1} + \tau_\mathrm{I}^{-1} \quad \text{with} \quad \tau := \frac{\hbar}{\Gamma_n}, \quad \tau_\mathrm{R} := -\frac{S}{v_\mathrm{g}\ln|R|}, \quad \tau_\mathrm{I} := \frac{L_\Phi}{v_\mathrm{g}}. \tag{3.36}$$

To compare this to the experimental lifetime results and to ascertain the relative strengths of the contributions, eq. (3.36) can be evaluated. This is done here for an example vacancy island whose area corresponds to an edge length of 7.5 nm, and an electron binding energy of 225 meV. Previous results for the inelastic contribution τ_I and the reflection coefficient R are available from literature:

τ_I has been calculated by Vitali *et al.* [231], using the GW approximation for e–e interactions and the full Eliashberg spectral function for e–φ interactions. At 225 meV, a value of $\tau_\mathrm{I} \approx 64$ fs was reported. Bürgi *et al.* [32] have presented measurements of the reflection coefficients R for surface state electron scattering at ascending and descending Ag(111) steps (reproduced in fig. 3.12b). At the Fermi level, R starts at a high value of about 0.5 (0.75) for ascending (descending) steps, respectively. It decreases with increasing energy to about 0.25 (0.45) at 75 meV, then remains constant for higher energies up to 200 meV. The reflection behavior was found to be identical between {111} and {100} type steps. Specifically, at 225 meV, they have found a value of $|R| \approx 0.23 \pm 0.07$.

The results are $\tau_\mathrm{R} \approx (9 \pm 2)$ fs, and $\tau \approx (7.9 \pm 1.5)$ fs. This is consistent with the lifetimes obtained in the experiment, as seen in fig. 3.6b. Evidently, at this energy, the surface state electrons are more likely to decay by lossy scattering at the boundary than by e–e and e–φ interactions, by about one order of magnitude.

This example calculation can be extended to varying energies and resonator sizes, to fully comprise the experimental gamut. The available resonator geometries are in the range of $S_\mathrm{min} = 4$ nm and $S_\mathrm{max} = 8.5$ nm. The lines in fig. 3.6b show the calculated lifetimes for resonators of S_min and S_max, respectively. Again, data for the inelastic contributions are taken from ref. [231]. Values of τ_R for the individual geometries are shown in fig. 3.12c, using an extrapolation of the reflectivity data from ref. [32].

For all vacancy geometries considered, lossy scattering at the boundary has been found to be the limiting factor to lifetime. This is also the dominant contribution when determining self energy as a function of binding energy,

$$-\mathfrak{Im}\Sigma = \frac{\Gamma}{2} \approx \frac{\hbar}{2\tau_\mathrm{R}} = -\frac{\hbar v_\mathrm{g} \ln|R|}{2S}. \tag{3.37}$$

The data from ref. [32] suggest that $-\ln|R|$ varies approximately as $(E - E_0)^{1/2}$. Hence, (3.37) together with $v_\mathrm{g} \propto (E - E_0)^{1/2}$ indicates that $-\mathfrak{Im}\Sigma$ increases roughly linearly with $E - E_0$. This matches the previous observation by Li *et al.*, who reported a self energy of $-\mathfrak{Im}\Sigma \approx 0.2(E - E_0)$, empirically derived by lineshape analysis of STS on adatom islands. As Bürgi *et al.* have found, while the overall reflectivity at a descending step is higher than at an ascending step, it varies in a similar fashion.

Various other published results for surface state electron lifetimes are included in fig. 3.12a. The phase coherence length can be obtained by examining the spatial decay of standing wave patterns at step edges. This was done by Bürgi *et al.* [31] and Vitali *et al.* [231] for surface state electrons, and by Wahl *et al.* [232] for image potential states. This technique allows direct access to a decay rate purely due to e–e and e–φ processes, thus the obtained lifetime corresponds to the τ_I lifetime.

In the experiment presented by Kliewer *et al.* [122], corrals of Mn atoms were lithographically constructed, and the linewidths of STS features acquired in the center of these corrals were studied. Following previous work by Heller *et al.* [93], the Mn atoms were modeled as perfectly absorbing, ‘black box’ s-wave scatterers, and the lifetime is obtained by varying the self energy $-\mathfrak{Im}\Sigma$ to match the experimentally obtained spectra.

A triangular corral of Ag adatoms on Ag(111) was constructed by Braun and Rieder [29], and the scattering properties of the adatoms were modeled, the model including an exponential spatial attenuation factor for the electron propagation, to obtain a best fit to the standing wave pattern inside the resonator. From this, the phase coherence length, and the total lifetime τ could be obtained. Also included are detailed spectroscopic data

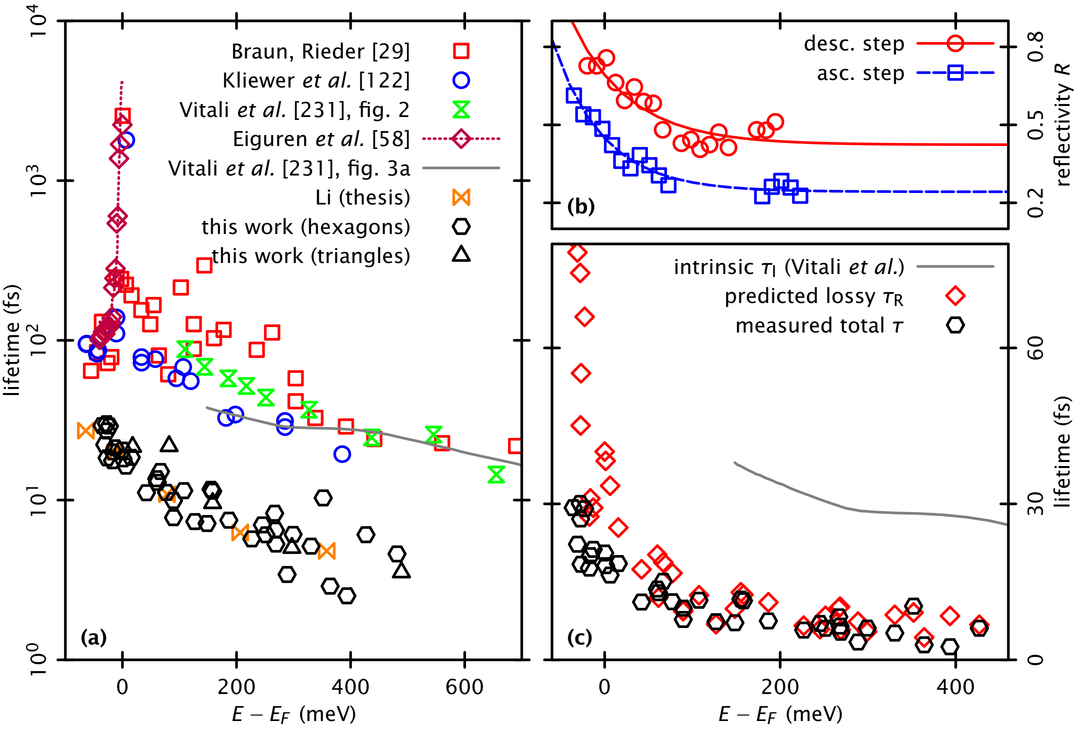

Figure 3.12 – Comparison of surface state lifetime results for the Ag(111) surface. **(a)** The following results are shown: Within adatom corrals, studies of phase relaxation length by Braun and Rieder [29], and point spectroscopy by Kliewer *et al.* [122]. At monatomic steps, phase relaxation length and corresponding theory by Vitali *et al.* [231]. Photoemission data and theoretical analysis by Eiguren *et al.* [58]. Point spectroscopy in hexagonal islands by Li [139], hexagonal and triangular vacancies (this work). Literature values corrected where necessary [48]. **(b)** Reflection coefficients for ascending and descending steps, used in the τ_R calculations below. Data interpolated from ref. [32]. **(c)** Measured lifetimes τ, compared with predicted values for intrinsic (τ_I, ref. [231]) and boundary (τ_R, eq. (3.37)) contributions. For all but the lowest binding energies, the latter is found to dominate, by at least half an order of magnitude.

from Jiutao Li's thesis [139], for a hexagonal island resonator of 9.8 nm inner diameter. During the course of this work it was found that, in some of the above publications, the coherence length had been misidentified by a factor of two. This has been commented on in

> S. Crampin, J. Kröger, H. Jensen, and R. Berndt, *Phase coherence length and quantum interference patterns at step edges*, Phys. Rev. Lett. **95** (2), 029701(1) (2005), DOI: `10.1103/PhysRevLett.95.029701`,

and the lifetimes in fig. 3.12 have been corrected from the original sources accordingly.

Chapter 4

Tunneling spectroscopy of clusters and linear nanostructures on Ag(111)

4.1 Surface state dispersion at linear nanostructures

In the preceding section, surface resonator geometries were constructed by controlled tip indentations into the cold Ag(111) surface. Another class of surface features that can occasionally arise are one-dimensional dislocations. These come in the forms of steps, chains and trenches. Notably, due to the preparation taking place at low temperature, diffusion processes are suppressed. Hence, *e.g.*, manufactured steps may be perfectly aligned with the bulk lattice on far larger scales, contrasting with the often imperfect equilibrium geometries of 'natural' step edges.

If such features are found after the preparation, they advertise themselves as prime candidates for measurements where geometric faultlessness is paramount. This experiment seizes the opportunity to use chain and trench geometries, that were obtained according to section 2.3, for spectroscopy and surface state dispersion measurements. For theoretical results for a similar setup on Cu(111), compare to ref. [98].

Line scatterer model. An impurity interacting with an otherwise free-electron system causes a local perturbation of the potential and induces modulations in the electron density, the so-called Friedel oscillations [70]. For a point scatterer, these take the form of alternating, concentric rings of increased and reduced electron density, readily seen with STM, that decay with distance in a manner characteristic to the system's dimensionality [2]. The phase shift of the scattered electrons is related to the charge of the impurity according to Friedel's sum rule.

A simple model for a line scatterer in a two-dimensional free-electron system can be given in terms of partial reflection of free electron waves (amplitude $a \equiv 1$) incident from $x > 0$ at a linear boundary along the y axis. This problem is trivially separable; The solutions for the wavefunction consist of the interference of incident and reflected waves, ψ_{x}, along the x direction, and a one-dimensional free electron wave ψ_{y} along the

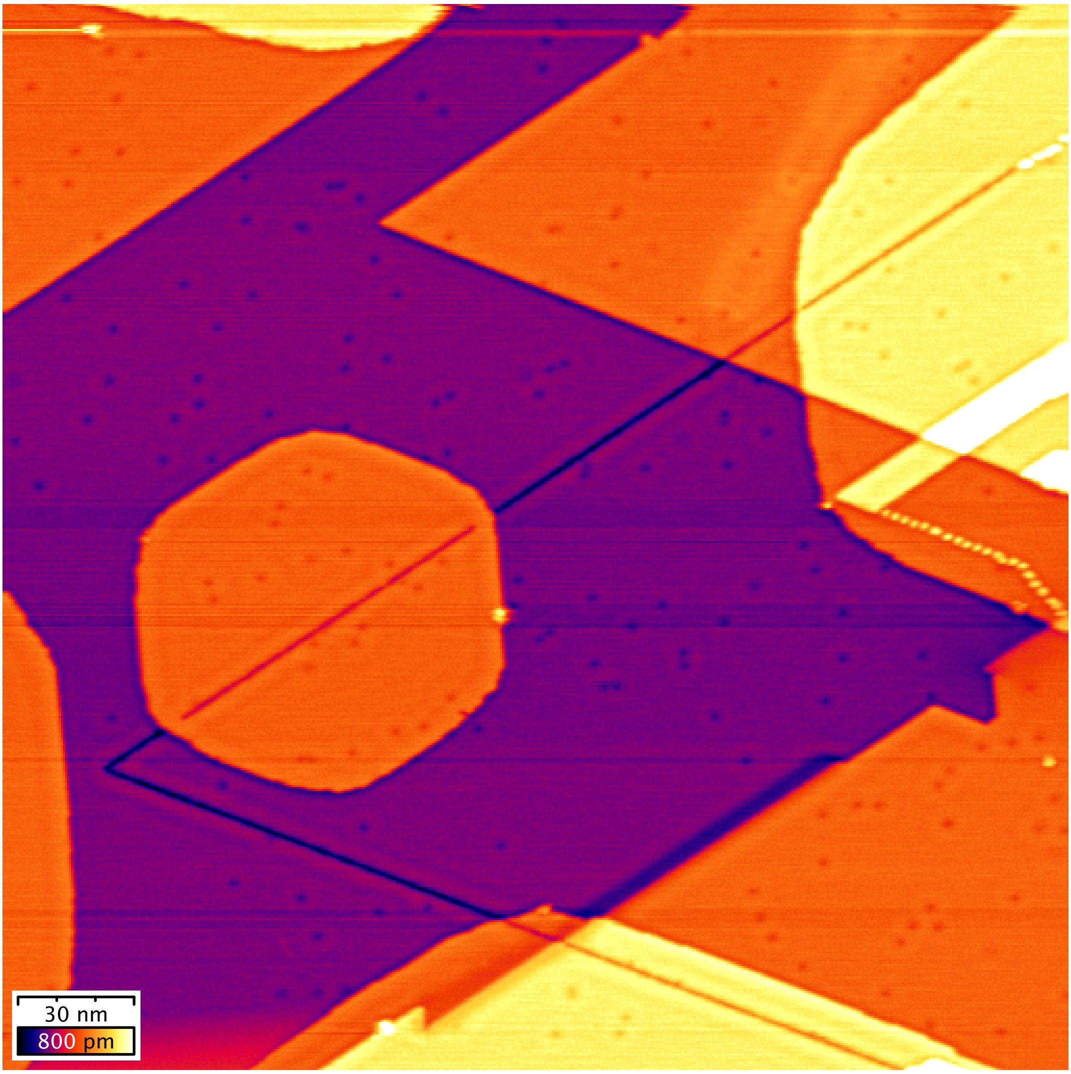

Figure 4.1 – Results of tip indentation on Ag(111). (275 nm)^2 topograph, $V = +100$ mV, $I = 200$ pA. The induced surface defects take the form of step edges and trenches. The sharp lines of the artificial structures prepared *in situ* contrast with the rounded edges of previously present surface features, which, like the hexagonal island pictured, have undergone diffusion and Ostwald ripening.

y direction,

$$\begin{aligned}\psi\left(k_\mathrm{x},k_\mathrm{y},x,y\right) &= \psi_\mathrm{x}(k_\mathrm{x},x)\psi_\mathrm{y}\left(k_\mathrm{y},y\right)\\ &= [\exp(-\mathrm{i}k_\mathrm{x}x) + r\exp(\mathrm{i}k_\mathrm{x}x)]\exp\left(\mathrm{i}k_\mathrm{y}y\right)\end{aligned} \tag{4.1}$$

using wavevectors $k_\mathrm{x} \geq 0$ and k_y, and an energy-dependent reflectivity coefficient r that characterizes the scatterer. The eigenenergies for these solutions are

$$E = E_\mathrm{x} + E_\mathrm{y} = \frac{\hbar^2}{2m^*}\left(k_\mathrm{x}^2 + k_\mathrm{y}^2\right) =: \frac{\hbar^2}{2m^*}k^2 \quad \Rightarrow \quad k_\mathrm{y}(k_\mathrm{x}) = \pm\sqrt{k^2 - k_\mathrm{x}^2}. \tag{4.2}$$

The probability density can then be calculated from (4.1),

$$\left|\psi\left(k_\mathrm{x},k_\mathrm{y},x,y\right)\right|^2 = |\psi_\mathrm{x}(k_\mathrm{x},x)|^2 = 1 + |r|^2 + 2\Re(r)\cos(2k_\mathrm{x}x) - 2\Im(r)\sin(2k_\mathrm{x}x). \tag{4.3}$$

The density of states ϱ at a given energy E can be obtained by integrating along the contour where k_x and k_y are such that (4.2) holds,

$$\begin{aligned}\varrho(E,x,y) &= 2\int_0^k |\psi_\mathrm{x}(k_\mathrm{x},x)|^2\sqrt{1 + k_\mathrm{y}{}'(k_\mathrm{x})^2}\,\mathrm{d}k_\mathrm{x}\\ &= 2k\int_0^k |\psi_\mathrm{x}(k_\mathrm{x},x)|^2\frac{1}{\sqrt{k^2 - k_\mathrm{x}^2}}\mathrm{d}k_\mathrm{x}.\end{aligned} \tag{4.4}$$

This integral can not generally be solved in closed form, unless r is energy-independent, in which case the solutions are given by

$$\frac{\varrho(E,x,y)}{\pi k} \approx 1 + |r|^2 + 2\Re(r)\mathrm{J}_0(2kx) - 2\Im(r)\mathrm{H}_0(2kx), \tag{4.5}$$

where $\mathrm{J}_0(x)$ and $\mathrm{H}_0(x)$ denote the Bessel and Struve functions of order 0, respectively [1]. For larger values of $|x|$, an approximation is given by

$$\begin{aligned}\frac{\varrho(E,x,y)}{\pi k} &\approx 1 + |r|^2 + \frac{2\Re(r)}{\sqrt{\pi kx}}\left[\cos\left(2kx - \frac{\pi}{4}\right)\right]\\ &\quad - \frac{2\Im(r)}{\sqrt{\pi kx}}\left[\sin\left(2kx - \frac{\pi}{4}\right) + \frac{1}{\sqrt{\pi kx}}\right] + \mathcal{O}\left(x^{-\frac{3}{2}}\right)\\ &= 1 + |r|^2 + \frac{2|r|}{\sqrt{\pi kx}}\cos\left(2kx - \frac{\pi}{4} + \eta\right) + \frac{2|r|\sin(\eta)}{\pi kx} + \mathcal{O}\left(x^{-\frac{3}{2}}\right),\end{aligned} \tag{4.6}$$

with $\eta := \arg(r)$. In the hard barrier limit, $r \approx -1$, and

$$\frac{\varrho(E,x,y)}{2\pi k} \approx 1 - \mathrm{J}_0(2kx) \approx 1 - \frac{1}{\sqrt{\pi kx}}\cos\left(2kx - \frac{\pi}{4}\right). \tag{4.7}$$

Experiment. The experiment comprises two types of linear structures. The first is a monatomic trench, *i.e.*, a single row of atoms missing from an otherwise undisturbed, flat Ag(111) surface region. The other, complementary structure is a monatomic chain, a single row of substrate atoms linearly arranged on the surface, in the proper lattice positions. Chains of this type have previously been constructed manually by manipulation of adsorbate atoms with the tip [173]. In this work, however, both types of structures have been obtained by controlled tip indentations.

On each of the examined structures, both topographs and constant current $\mathrm{d}I/\mathrm{d}V$ maps are acquired simultaneously, for a selection of positive sample bias $V < 500$ mV. Additionally, the trench measurements are supplemented by a set of constant height scans at low bias. The scan area is manually coarsely aligned to the feature, with the scan axes rotated away from the native axes of the scan piezo. For each given sample bias, the $\mathrm{d}I/\mathrm{d}V$ map is corrected for x–y slant, then averaged along the scatterer axis. The resulting average scanlines are plotted as a function of sample bias, given in figs. 4.4a and 4.5a, respectively, for chain and trench.

Direct fit of scanlines. If the thin elastic line scatterer model given above holds for the linear structures, the differential conductance linescans should appear like those in eq. (4.6). It has previously been shown that for dispersion measurements, more accurate results are expected when the normalization according to (1.30) is omitted [97]. A least squares fit of

$$d_k(x) = C_0 + \frac{C_1}{\sqrt{\pi k x}} \cos\left(2kx - \frac{\pi}{4} + \eta\right) \exp(-x/L_\Phi) \tag{4.8}$$

allows to obtain best-fit values for wavenumber k, scattering phase shift η, and coherence length L_Φ. The latter provides an exponential damping to account for the effects of a finite lifetime, according to

$$\tau = \frac{L_\Phi}{v_\mathrm{g}} = \frac{L_\Phi m^*}{\hbar k}. \tag{4.9}$$

In principle, this fit is expected to be inexact for constant current scanlines, where the z position follows the trajectory of the modulated topography [97]. The latter is a Friedel-like oscillation, with an energy-dependent weighting due to STM's transmission probability. Its spatial decay is of a higher order in $|x|$ than that of the $\mathrm{d}I/\mathrm{d}V$ oscillation. As seen in fig. 4.2, the topography is already approximately flat at $|x| > 5$ nm, where the decisive contribution to the fit parameters is obtained.

The constant height dataset has a non-uniform background due to piezo creep and thermal drift effects. Therefore, the fits are instead done with the numerical derivatives of linescans and candidates. This serves as a high-pass filter that largely eliminates the background. Fig. 4.3 reproduces the obtained phase shifts, which were found to be largely constant over the bias voltage range. A phase of $\eta_\mathrm{C} \approx -\pi$ indicates that the chain acts as a repulsive barrier with a near-total reflection coefficient of $r \approx -1$ [90]. At $\eta_\mathrm{T} \approx -\frac{3}{4}\pi$, the phase shift for the trench is slightly lower.

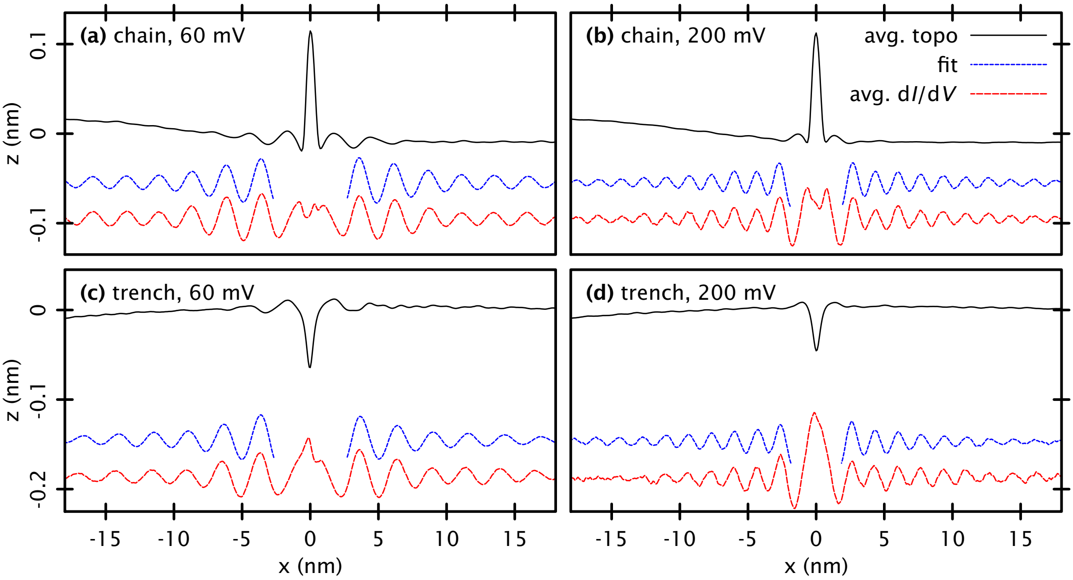

Figure 4.2 – Example constant current linescans for **(a,b)** chain and **(c,d)** trench structures. Graphs show averaged (see text) topography linescan (black line), dI/dV linescan (red line) and fit function (blue line). Both linescans show a symmetric oscillation around the scatterer whose wavevector increases with bias voltage, with a markedly shorter decay length in the topography.

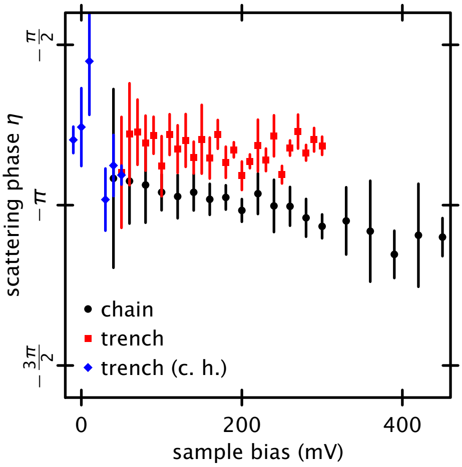

Figure 4.3 – Line scattering phase shift η, for chain (black) and trench (red: constant current, blue: constant height) structures. Data obtained from fit parameters (see text). A phase shift of $\eta = -\pi$ is seen in hard barriers.

The structures are intrinsically asymmetric along the scatterer axis (with the scatterer–substrate interface having different types of microfacets, {100} vs. {111}, on the two sides). Lacking atomic resolution, the faceting and alignment of the examined structures could not be determined; It is however known that both bulk-like and faulted stacking may exist in adsorbates [159]. The linescans were still examined for a possible influence of the microfacet type on the scattering process, by comparing one-sided fits. For both chain and trench, no evidence for systematic asymmetry was found in any of the fit parameters. This contrasts with the findings for single steps [90].

Momentum space analysis. The wavevectors k taken from the fit in the preceding section can be used to determine the surface state dispersion. Alternatively they can be obtained for a given set of linescans by Fourier transforming along x and determining the position of the respective peak in k-space. To obtain subpixel precision, a parabola is fit through the data points forming the peak apex.

The scanlines in real and Fourier space, and the extracted wavevectors are shown in figs. 4.4 for the chain and 4.5 for the trench. These show the free-electron-like dispersion that is expected for surface state electrons up to the bulk d band crossing. By fitting a parabolic dispersion curve, surface state onset energy and effective mass are obtained. The results are given in table 4.6.

Discussion. Regarding the effective mass, the results for the different systems are in very good mutual agreement. For comparison, previously observed values for m^*/m_e include 0.53 ± 0.01 [118] and 0.44 ± 0.04 [179]. Since the scans provide no direct indication of the absolute lateral dimensions of the surface (atomic resolution was not obtained), the lateral calibration of the scan head relies on predetermined data. The actual tip deflection is influenced by the tip length, operating temperature, and aging of the piezo polarization. Assuming an upper bound of 10% for the relative lateral calibration error leads to the error margins for the effective mass of the surface state electrons given in table 4.6. With these, the values are in agreement with the references given above.

The surface state onset energy E_0 does not depend on the aperture of the dispersion parabola. It is in this sense robust against lateral calibration errors. Literature values for the Ag(111) surface state onset, compiled in section 2.1, have been successfully refined over the years [91, 118, 140, 179, 191], to a reference value of $E_0 = (-67 \pm 2)$ meV. While there is a good match to the measurement on the chain, where $E_0 = (-63 \pm 3)$ meV was observed, the trench measurements show a marked deviation of the surface state energy toward a slightly higher value.

A fit with an onset value fixed at -67 meV gives a noticeably worse agreement to the data points. The reason for this observation, which is robust against variations in fit technique, could not be conclusively determined. The trench structure, being an actual defect in the topmost surface layer where the surface state resides in, may interact differently than the chain, an adsorbate on an undisturbed layer. Otherwise, the effect

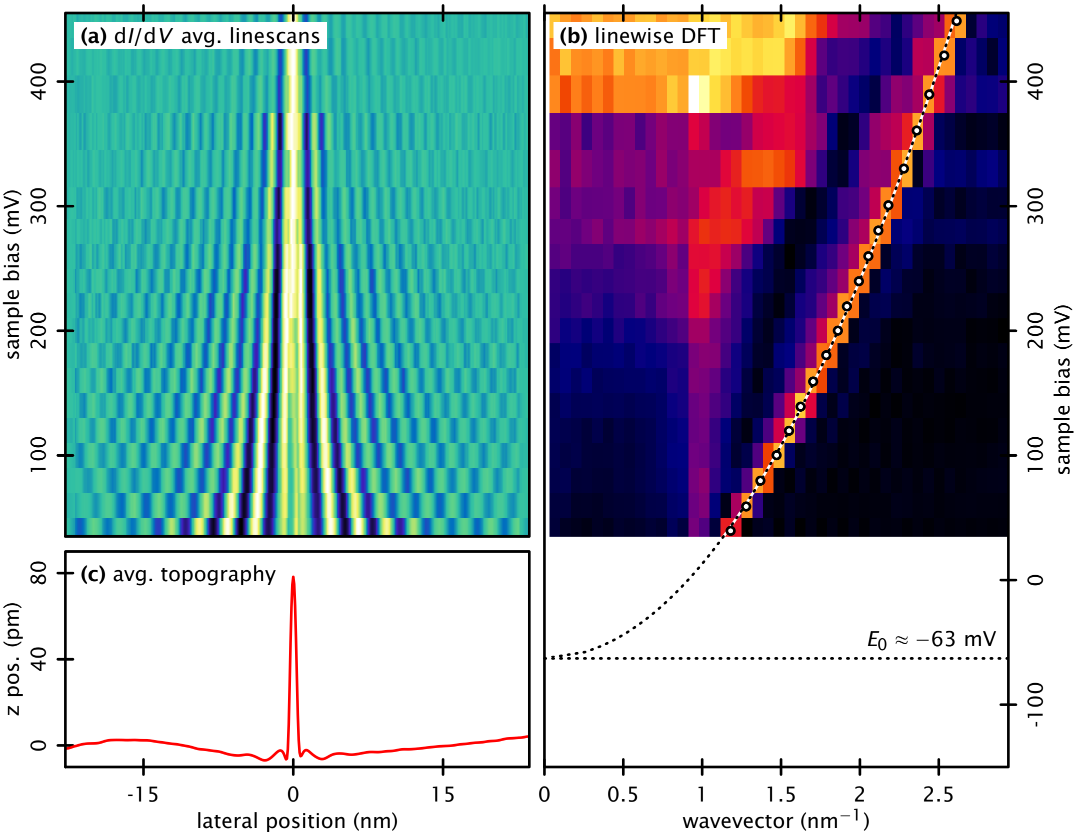

Figure 4.4 – Surface state dispersion across monatomic chain. **(a)** Collection of average d*I*/d*V* scanlines, plotted against sample bias, in real space. **(b)** Fourier transforms of d*I*/d*V* linescans. The detected wavevector is marked for each bias voltage, and a dispersion parabola fitted is fitted across the dataset. **(c)** Cross-sectional topography, averaged over all available linescans and bias voltages.

may be specific to the sample; The preparation may have induced subsurface defects, invisible in the topographs, influencing the surface state and effecting this shift.

4.2 Transmission resonances in adsorbed oligomers

The following experiment studies the spectral features of Ag_n oligomers on an Ag(111) surface. It was previously published as part of

> H. Jensen, J. Kröger, N. Néel, and R. Berndt, *Silver oligomer and single fullerene electronic properties revealed by a scanning tunnelling microscope*, Eur. Phys. J. D **45** (3), 465–469 (2007), DOI: `10.1140/epjd/e2007-00157-x`.

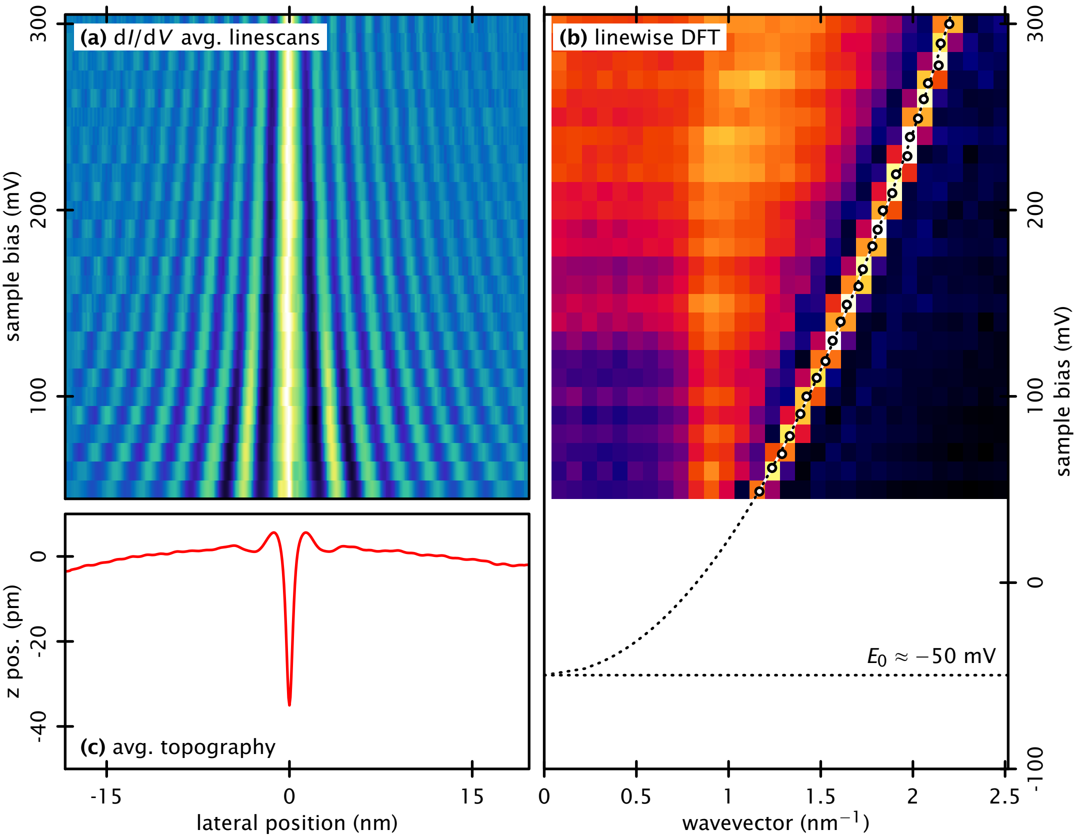

Figure 4.5 – Surface state dispersion across monatomic trench. **(a)** Collection of average dI/dV scanlines, plotted against sample bias, in real space. **(b)** Fourier transforms of dI/dV linescans. The detected wavevector is marked for each bias voltage, and a dispersion parabola is fitted across the dataset. **(c)** Cross-sectional topography, averaged over all available linescans and bias voltages.

System	Surface state onset	Effective mass
Trench	(-50 ± 2) meV	$(0.52 \pm 0.11)m_e$
Trench (constant height)	(-52 ± 2) meV	$(0.49 \pm 0.10)m_e$
Chain	(-63 ± 3) meV	$(0.50 \pm 0.11)m_e$

Table 4.6 – Ag(111) surface state dispersion parameters, averaged from fits of real-space scanlines and momentum space dispersion parabola.

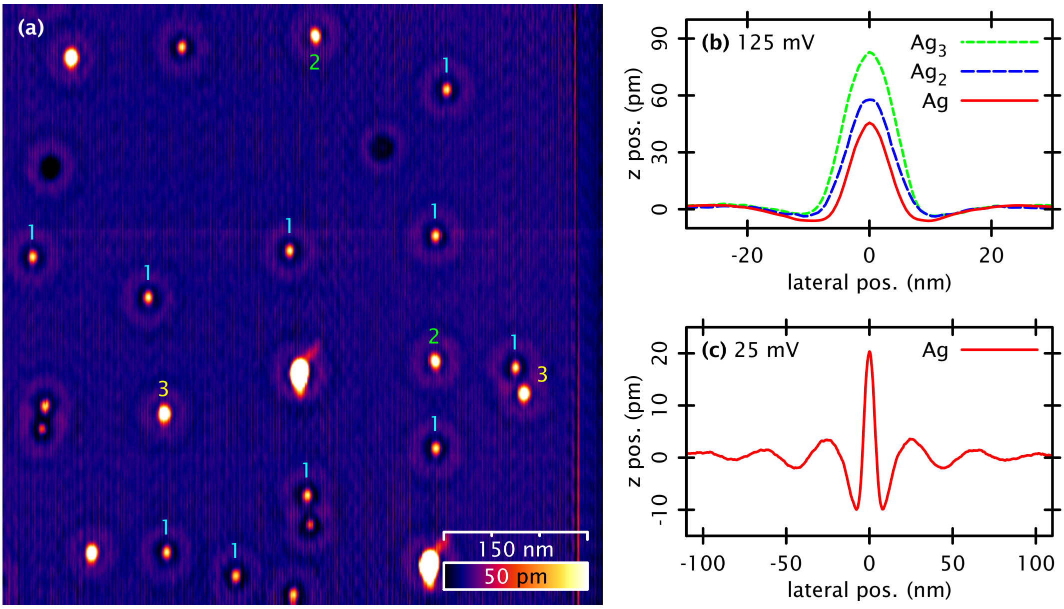

Figure 4.7 – Ag oligomers deposited by tip indentation on an Ag(111) substrate. **(a)** Representative (625 nm)^2 topograph, $V = +125$ mV, $I = 40$ nA. Different species appear as differently sized protrusions (see text). The marked adsorbates have been identified as single atoms, dimers and trimers, and dI/dV spectra have been subsequently taken on top. The dark spots are attributed to bulk impurities. **(b,c)** Topography cross-sections (radially averaged), demonstrating apparent height difference by cluster size, and surrounding Friedel oscillation.

Experiment. The oligomer preparation is rather straightforward, as surface material can be picked up by the tip in bulk, and then transferred back onto the surface by controlled contacts, in a procedure previously employed for Ag and Cu atoms [145]. At the outset, the pristine tungsten tip is dipped into the surface, remote from the region of interest, in order to cover it with Ag. Subsequently, the tip is positioned atop a clean, level region of the Ag(111) surface. At the desired location, the feedback loop is stabilized at a target current of 1 µA, at a sample bias of 100 mV. The loop is then suspended, and the tip z position is ramped toward the surface at a velocity of $\approx 300\ \mathrm{pm s^{-1}}$, while observing the $I(z)$ response. The latter shows a roughly exponential behavior, until, at a tip displacement between 100 and 200 pm, a discontinuity in the tunneling current is observed, indicating the formation of a tip-sample contact.

It has been previously shown that upon re-separation of such contact, there is a high probability of an adsorbed remnant on the surface, at the contact site. Given that both substrate and tip coating materials involved are identical, the adsorbate is assumed to be silver as well. The identity of the material has previously been verified by topographic and spectroscopic methods, as has the integrity of the underlying substrate lattice [145].

In the majority of cases, the dropped-off material comprises a single adatom, occasionally a dimer or trimer, and rarely a larger chunk of material. Fig. 4.7a shows a topograph of an indentation region. Radially averaged sections across the center of adsorbates at bias voltages of +30 and +125 mV are displayed in fig. 4.7b,c. In the former, the slow lateral decay of the surrounding Friedel oscillation is seen. The apparent height and width of the adsorbates is found to vary with tip state and sample bias. With the typical parameters from fig. 4.7a, single atoms are imaged as circular protrusions of 30 pm height, and a width (FWHM) of 0.75 nm.

The species next in size, with a height of 50 pm and a width (FWHM) of 1.0 nm, is identified as the Ag_2 dimer. Notably, its topographic appearance is also circular. A reason for this might be intracell diffusion at a timescale too fast to resolve by STM. It has previously been reported that the Cu_2 dimer on Cu(111) likewise appears as a circular object, at a temperature of 7 K, due to the motion of the two constituent atoms within a local hexagonal diffusion cell [195].

The trimer appears as a circular object of 60 pm height and a FWHM of 1.1 nm, suggesting a compact triangular structure. While rotational diffusion of the whole structure cannot be ruled out from the topographic data alone, simulations for Cu_3 on Cu(111) suggest a stable, stationary configuration at temperatures below 21 K [195]. From this, it may be inferred that the Ag_3 cluster is similarly immobile on Ag(111), at the temperature of 7 K at which the experiment is taking place.

To examine the electronic structure, tunneling spectroscopy on the various oligomers has been performed. At the outset, it was verified that spectra on clean substrate regions yield the expected shape of the Shockley surface state onset. Since the selected bias voltage range leads to a large variation in tunneling current, the constant current spectroscopy method was employed. The feedback loop is enabled during the scan, retracting the tip as the total current increases. This complicates a quantitative evaluation of the local density of states, however the general features of a spectrum, such as approximate peak position and width, are retained.

Results and discussion. The spectroscopic results are compiled in fig. 4.8, where averages of several spectra taken on top of the various adsorbates are shown. On the single Ag atoms, a single broad peak at an energy of about 2.95 eV above the Fermi level is observed. This marks an increase in conductance of the tunneling junction as the bias voltage increases beyond this energy, due to the additional possibility of tunneling through an unoccupied quasiatomic resonance. The spectral feature bears an approximately Gaussian shape. The peak width is measured by subtracting a linear spectral floor from the spectrum, within a region of interest bounded by the tails of the feature. By finding the voltages where the residual intersects an amplitude of half its peak value, a width (FWHM) of the feature of 0.65 eV can be obtained.

Spectra on the Ag_2 dimers show a broader peak whose parameters can be likewise determined, giving a position of 2.25 eV and an increased FWHM of 1.0 eV. The Ag_3

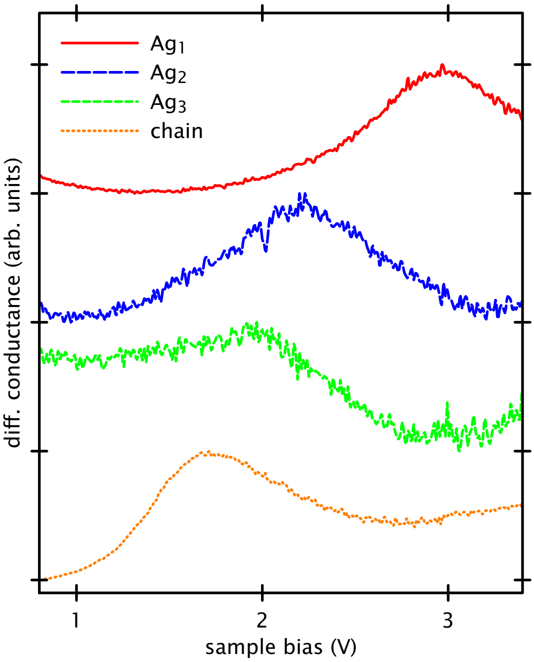

Figure 4.8 – Spectroscopy of Ag_n/Ag(111) oligomers and chain, each showing a single peak attributed to transmission resonance. The peak energy decreases with increasing cluster size, with 2.95 eV for the single atom, 2.25 eV for the dimer, 1.95 eV for the compact trimer, down to 1.7 eV for a monatomic chain.

trimers show a peak with a lower FWHM of 0.8 eV, and an energy position at 1.95 eV, even closer toward the Fermi level.

This apparent energy shift with increasing cluster size can be interpreted by a splitting of the observed monomer state, which in the dimer case is akin to the formation of bonding and anti-bonding 1*s* levels in the H_2 molecule. Of these, only the lower state is visible in the spectra, since the higher-energy state is expected to reside beyond 3.5 eV, outside of the measured voltage range. This type of splitting has previously been observed in several similar systems. One instance of this is a study of linear Cu_n oligomers on Cu(111) [64], where spectroscopy on the adsorbed monomer yields a peak at 3.3 eV, with a comparable FWHM of 0.6 eV. As the chain length increases, this evolves into a more complex set of resonances, with the lowest discernible peak shifting down to 2.6 eV for the dimer, with a broadened FWHM of 0.9 eV, to 2.0 eV for a linear trimer, and further down to 1.7 eV for a seven-atom chain. A multiple-scattering *ab initio* calculation for linear Cu_n chains on Cu(111) likewise shows a downshift of the lowest LDOS peak with increasing chain length [216].

Reference data for a compact Cu_3 cluster are taken from a study of compact triangular Cu clusters on Cu(111) [133]. The spectrum shows a single resonance at an energy of 2.1 eV. Au chains on NiAl(100) were found to be another similarly behaving system [173].

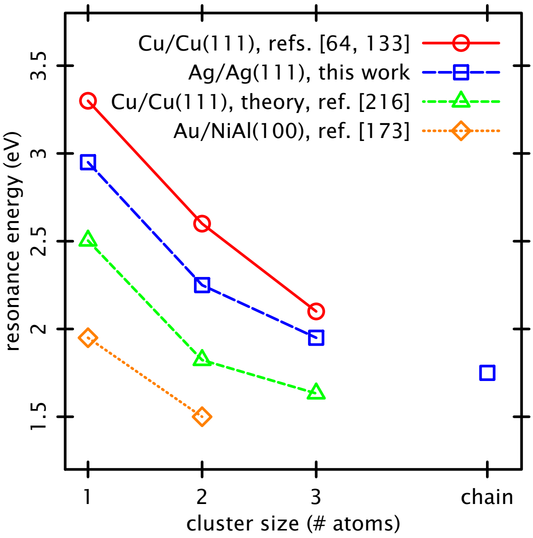

Figure 4.9 – Comparison of oligomer resonance data with previously published results. Experimental data for Cu and Cu_2 taken from ref. [64], compact Cu_3 cluster from ref. [133]. Cu_n linear chain *ab initio* calculation from ref. [216]. Data for Au_n on NiAl(100) reproduced from ref. [173]. In all cases, the resonance peak shifts toward lower binding energies as the cluster size increases.

4.3 Image and field states on linear chains

The preceding experiments have maintained bias voltages well below the vacuum level. In contrast, tunneling spectroscopy at energies near and beyond the substrate work function is also possible, and may provide valuable insights into the energy structure of the tunneling gap.

In the presence of a strong electric field, electrons from the tip can easily escape into the vacuum gap, overcoming the potential barrier, distorted by the field into a roughly trapezoidal shape, by means of Fowler–Nordheim tunneling [68]. This field electron emission process has been employed in various surface microscopy techniques, such as the field emission microscope, which yielded the first direct observation of the atomic structure of a sharp tip, and the Topografiner, the direct developmental precursor of the STM.

Differential conductance spectra acquired by STS within this Fowler–Nordheim region, with sample bias voltages in a range of 4 to 20 V, are characterized by a series of oscillations [16, 17]. These are attributed to the interference of standing wave states in the vacuum gap, partially confined between the trapezoidal barrier and the metal surface [86].

It follows from classical electrostatics that, when facing a conducting surface, a charged particle induces a local polarization on it, thereby experiencing an attractive force, the so-called image force. In the energy diagram of a tunneling junction, this effect causes a local drop in barrier potential near the electrodes. Within the confines of this image potential, a Rydberg-like series of bound electronic states may occur [54].

Access to these sample-bound image potential states by means of STS requires a significant positive sample bias. The voltage difference causes a local electric field within the tunneling gap, and thus, a field-induced potential gradient as seen in the energy

Figure 4.10 – Fowler-Nordheim spectra on Ag(111). (a) Constant current spectra on clean Ag(111) (red), monatomic (green) and diatomic (blue) chains. At energies near the work function, the spectra show a complex substructure depending on the sample geometry, likely due to overlap and interaction of Gundlach and transmission resonances. At higher energies, a clear oscillatory pattern emerges. The monatomic chain spectrum shows a single additional peak at 1.5 V. **(b)** Energy positions of the peaks from (a). The peak index axis is distorted for equidistant $\left(n-\frac{1}{4}\right)^{\frac{2}{3}}$, allowing a linear fit. Extrapolation of the fitted lines gives an estimate of the work function.

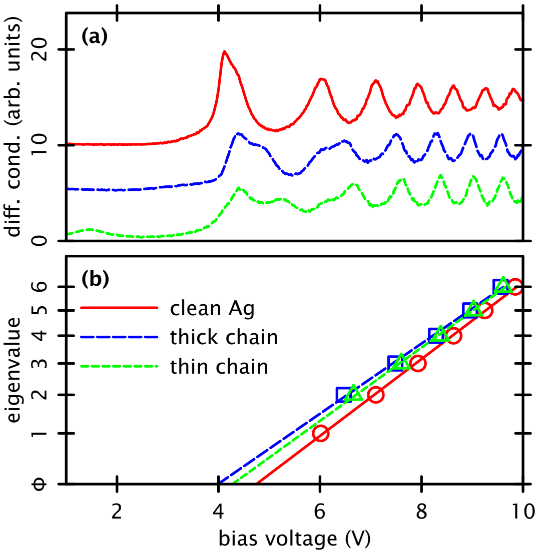

diagram. The combination of image and field potentials results in an enlarged potential well in the vacuum gap. This gives rise to a series of additional bound states associated with the triangular tail of the potential toward the vacuum level, as illustrated in fig. 4.11.

Deviations from the Gundlach oscillation pattern, observed in adsorbate-covered surface spectra [132], are attributed to transmission resonance effects. The reflectivity of both substrate-adsorbate and adsorbate-vacuum interfaces results in a series of electron energies for which the transmissivity of the adsorbate layer is maximized. Several of these energy levels may have energies coinciding with the Gundlach region.

Experiment. The experiment has been performed on the same sample used for the dispersion measurements in section 4.1. Starting from the clean sample, linear atomic chains have been prepared by the tip indentation method described previously. Fowler-Nordheim spectra have been acquired both on atomically flat, undisturbed surface regions and on top of atomic chains of various widths. Because of the large voltage range, corresponding to several orders of magnitude in current, the measurements were done in constant current mode. Due to the dependency of the energy levels on the electrostatic field in the gap (see below), which is determined by the shape of the tip apex, care has been taken to obtain a stable tip that remained unchanged during the experiment.

Also, measurements on deposited Ag adatoms were attempted, but it was found that the adatoms detectably jumped to adjacent lattice locations at bias voltages around 3 V. This could not be remedied by ordinary tip preparation, but is nevertheless probably due to the tip condition, as successful spectroscopy on a monomer up to 8 V with a different tip in the same instrument was reported elsewhere [215].

Fig. 4.10a shows the average of constant current $\mathrm{d}I/\mathrm{d}V$ spectra taken on 6 different clean sites of the Ag(111) surface. The highest-amplitude feature is located at an energy of ≈ 4.2 V above the Fermi level. The asymmetric shape suggests that the feature is the superposition of two adjacent peaks. One of these peaks may be due to the upper edge of the L band gap, for which published theory provides a value of $E \approx 3.9$ V [41].

The feature lies below the Ag(111) surface work function, which was reported at 4.46...4.8 V, depending on the density of bulk sulfur contaminants [36]. In this energy range, a standing wave state can exist in the potential well formed by the superposition of the trapezoidal electrostatic and image potentials. At higher energies, the spectrum shows a series of peaks with decaying amplitude. These are the Gundlach oscillations resulting from standing waves in the trapezoidal electrostatic potential well.

Regarding the decorated surface, fig. 4.10a includes averaged spectra acquired on 5 locations on single-row chains, and 8 on double-row chains, respectively. For the thin chain, the transmission resonance seen previously in section 4.2, at 1.5 V, falls into the energy range and is consequently visible as a small peak. At energies beyond 7 V, both types of chains show an unperturbed series of Gundlach resonances. At lower energies, however, the spectra appear markedly different from the clean surface, and each other. In the range of 4...7 V, several overlapping peaks of varying amplitude are visible, some of these possibly related to higher-order transmission resonances of the adsorbate. It has previously been observed in the Ag/Si(111)–7×7 system that the presence of such resonances can shift the energy levels of higher Gundlach peaks [220]. The specific identities of the peaks obtained in the range of 4...7 V, however, could not be conclusively determined.

Model and discussion. To determine the peak positions, a nonlinear least-squares fit of a superposition of Lorentzians to the experimental spectra was performed, using the Levenberg-Marquardt technique [138, 157]. The resulting fits are reproduced as lines in fig. 4.10b.

A simple model for the tunneling junction within the Fowler–Nordheim regime disregards image charge effects and models the potential within the gap as a triangular well. With the sample surface at $z = 0$, and the tunneling gap toward positive z, the model potential is given by

$$U(z) = \begin{cases} \Phi_S + q_\mathrm{e} F z & \text{for } z > 0 \\ +\infty & \text{for } z < 0, \end{cases} \tag{4.10}$$

where $F := (\Phi_T - \Phi_S - V)/(q_\mathrm{e}\Delta z)$ denotes the electrostatic field between tip and sample. The Schrödinger equation for an electron in this potential is

$$\psi''(z) = \frac{2m_\mathrm{e}}{\hbar^2}(\Phi_S + q_\mathrm{e} F z - E)\psi(z). \tag{4.11}$$

Substituting $\epsilon := \Phi_S - E + q_\mathrm{e} F z$ leads to Stokes' equation,

$$\psi''(\epsilon) = \frac{2m_\mathrm{e}\epsilon}{\hbar^2 q_\mathrm{e}^2 F^2}\psi(\epsilon), \tag{4.12}$$

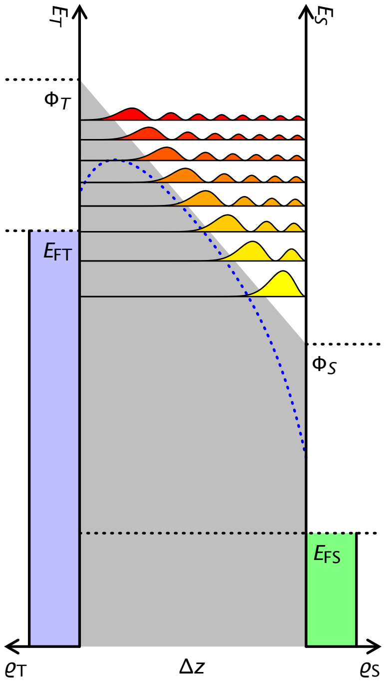

Figure 4.11 – Energy diagram for Fowler–Nordheim tunneling. With a large positive sample bias V, the potential within the gap assumes an approximately trapezoidal shape (gray area). At energies beyond the sample work function, a series of bound electronic states exists in front of the surface, within the vacuum gap. The actual shape of the potential is influenced by image charges and deviates from the trapezoid, especially near the electrodes (blue dotted line).

which has the general solution

$$\psi(\epsilon) = \alpha \mathrm{Ai}\left[\left(\frac{2m_{\mathrm{e}}}{\hbar^2 q_{\mathrm{e}}^2 F^2}\right)^{\frac{1}{3}} \epsilon\right] + \beta \mathrm{Bi}\left[\left(\frac{2m_{\mathrm{e}}}{\hbar^2 q_{\mathrm{e}}^2 F^2}\right)^{\frac{1}{3}} \epsilon\right], \tag{4.13}$$

where Ai and Bi denote the Airy functions of the first and second kinds, respectively. As the physical solutions must be square integrable, but $\mathrm{Bi}(z)$ diverges for $z \to +\infty$, it follows that $\beta = 0$. Since ψ has to vanish at the infinite potential wall at $z = 0$ (*i.e.*, at $\epsilon = \Phi_S - E$),

$$0 = \alpha \mathrm{Ai}\left[\left(\frac{2m_{\mathrm{e}}}{\hbar^2 q_{\mathrm{e}}^2 F^2}\right)^{\frac{1}{3}} [\Phi_S - E]\right]. \tag{4.14}$$

This allows to enumerate the solutions by index n, where ζ_n denotes the nth zero of $\mathrm{Ai}(z)$. An approximate formula for the ζ_n (maximum relative error $< 0.8\%$ at $n = 1$) is given by

$$(-\zeta_n) \approx \left[\frac{3\pi}{2}\left(n - \frac{1}{4}\right)\right]^{\frac{2}{3}}. \tag{4.15}$$

	Clean Ag(111)	Thin chain	Thick chain
Sample work function Φ_S	4.75 V	4.28 V	3.99 V
Electrostatic field F	0.78 V/nm	0.84 V/nm	0.89 V/nm

Table 4.12 – Tunnel gap parameters from Fowler–Nordheim spectra, obtained from fit coefficients.

The energy of solution n is then obtained by transforming (4.14), giving

$$\begin{aligned} E_n &= \Phi_S + (-\zeta_n)\left(\frac{\hbar^2 q_\mathrm{e}^2 F^2}{2m_\mathrm{e}}\right)^{\frac{1}{3}} \\ &\approx \Phi_S + \left(\frac{9\pi^2\hbar^2 q_\mathrm{e}^2 F^2}{8m_\mathrm{e}}\right)^{\frac{1}{3}}\left(n - \frac{1}{4}\right)^{\frac{2}{3}} \end{aligned} \tag{4.16}$$

for the approximate energy E_n of the nth Gundlach resonance within a triangular potential well, as a function of the sample work function Φ_S and the electrostatic field F in the tunneling gap [3]. The approximation is however limited in several ways:

- The approximation assumes that the electrostatic field is constant. However, a bias voltage ramp is applied in order to acquire the spectra. Also, since constant current mode is employed, the feedback loop varies the tip–sample distance throughout. In order for the approximation to hold, these two effects need to roughly cancel each other out.

- The considered potential (4.10) increases linearly to infinity in the tip direction. With a tunneling gap that is bounded on both sides, and a trapezoidal potential, the solutions have $\beta \neq 0$ in (4.13). A deviation from the $E_n(n)$ behavior is expected for high index resonances.

- The effect of the image potential, which causes a potential dropoff near the sample, is disregarded. This effect is expected to induce a downward energy shift of the bound states, especially for the lowest index resonances.

Fig. 4.10b shows a plot of the measured peak energies versus $\tilde{n} := \left(n - \frac{1}{4}\right)^{\frac{2}{3}}$, for the three sample geometries. The assignment of the index n to the individual peaks is unambiguous for the clean surface [220]. For the structured surfaces, where the lowest-order resonances are missing or perturbed, the peaks are indexed as shown in fig. 4.10. A linear function is fit through the pairs of $(E_n, \tilde{n})$, disregarding the data points for the lowest resonances, which are expected to be shifted downward by the image effect. From the slope and intercept, respectively, the experimental values for the electrostatic field F and the sample work function Φ_S are obtained.

On the clean surface, the work function of 4.75 V lies in the expected range [41, 77]. On the decorated surfaces, lower values of 4.28 V and 3.99 V, respectively, are recovered. The observation of a reduced work function in the vicinity of surface features is according to expectations. Similarly, a reduction near step edges on Au(111) has previously been reported [112].

Part II

PTCDA on vicinal Au(111) surfaces

Chapter 5

Introduction

The second part of this thesis concerns the adsorption geometry and electronic structure of a submonolayer film of the organic semiconductor molecule PTCDA on various substrates. The substrates employed are the Au(111) surface, several vicinals thereof, and the 2H–NbSe$_2$ layered crystal. Among these, surface reconstructions, regular and refaceted step arrays, and charge density waves provide a variety of one- and two-dimensional templates. The main objective of the experiments is to ascertain the extent to which these structures influence the adsorption geometry of the molecules.

Parts of the presented work have previously been published in peer-reviewed journals. The topographic observations and spectroscopic data for PTCDA on vicinal Au(111) surfaces have been presented as

> J. Kröger, N. Néel, H. Jensen, R. Berndt, R. Rurali, and N. Lorente, *Molecules on vicinal Au surfaces studied by scanning tunnelling microscopy*, J. Phys. Condens. Matter **18** (13), S51–S66 (2006), DOI: `10.1088/0953-8984/18/13/S04`.

A discussion of the observed molecular energy shift and the relevant theory have been given in

> J. Kröger, H. Jensen, R. Berndt, R. Rurali, and N. Lorente, *Molecular orbital shift of perylenetetracarboxylic-dianhydride on gold*, Chem. Phys. Lett. **438** (4–6), 249–253 (2007), DOI: `10.1016/j.cplett.2007.03.001`.

Finally, a supplementary study of PTCDA on 2H–NbSe$_2$, a transition metal dichalcogenide substrate, has been published in

> J. Kröger, H. Jensen, T. Jürgens, T. von Hofe, J. Kuntze, and R. Berndt, *Adsorption geometry of PTCDA on 2H–NbSe$_2$*, Appl. Phys. A **81** (6), 1285–1289 (2005), DOI: `10.1007/s00339-004-3039-6`.

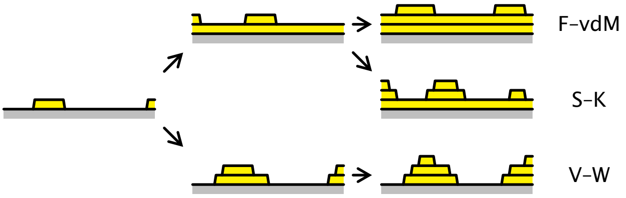

Figure 5.1 – Schematic representation of crystal growth modes for increasing monolayer coverage. Image shows, from top to bottom: **(a)** Frank–van-der-Merwe (layer) growth, **(b)** Stranski–Krastanov (layer-plus-island) growth, and **(c)** Volmer–Weber (island) growth.

5.1 Ultrathin molecular films

Historically, deposition of thin films has been done by submerging the substrate in a liquid medium. Specific types of organic molecules, when added to a liquid they are insoluble in, form ultrathin films on top of the liquid surface [186, 190]. Resulting thicknesses may be as low as a single monolayer, as seen in fatty acids on water [136]. From this, a deposition technique was developed where a submerged substrate slab gets lifted to the surface, displacing the liquid in the process, but retaining the thin molecular film on top [22, 23]. Films prepared in this fashion are known as Langmuir–Blodgett films.

Freely suspended films may be manufactured by drawing a spreader across a hole [240]. Once created, these films may then be subsequently transferred to a substrate surface [151]. More recently, a wet self-assembly technique for deposition of charged polymers was proposed [52], in which a charged substrate is alternatingly dipped in solutions of polycations and polyanions. In each cycle, a single organic layer is deposited [96].

All of the aforementioned methods are restricted to certain, narrow classes of molecules. In contrast, the organic molecular beam deposition (OMBD) technique permits working with a much wider range of adsorbate materials, and offers accurate control of film thickness within a fraction of a monolayer. Made possible by the availability of ultra-high vacuum systems, it has emerged as the method of choice for many applications.

Growth modes. The growth process of an ordered organic film on a substrate is described by both the sequence in which the layers are progressively built up, and the relationship between the forming adsorbate and substrate lattices. Regarding the former, typically three growth modes are distinguished [14, 229], as illustrated in fig. 5.1:

Volmer–Weber growth, or island growth, describes a process where, from its initial nucleation sites, the adsorbate grows in three-dimensional clusters on the substrate. The growth is characterized by the coexistence of clean substrate areas and islands of several molecular layers in height. It is typically found where the adsorbate molecules are bound more strongly to each other than to the substrate. In contrast, in *Frank–van-der-Merwe* *growth*, or layer growth, the adsorbate completes individual layers before forming a subsequent layer. A requirement for this growth mode is a monotonous behavior of the interlayer bond strength, starting from a relatively strong adsorbate–substrate bond.

A quite common intermediate case is given by *Stranski–Krastanov growth* [218], or layer-plus-island growth, which tends to complete the first molecular layer (or first few layers), but formation of additional monolayers beyond a certain thickness becomes successively unfavorable. This growth mode may occur when the interlayer binding energy exhibits any form of non-monotonous behavior. If, *e.g.*, a mismatch between substrate and bulk adsorbate lattice geometries is present, the first few monolayers may exhibit lattice distortions to comply with the substrate geometry, but these distortions are only maintained up to a certain film thickness, beyond which island growth is preferred. This is also called the Asaro–Tiller–Grinfel'd (ATG) instability [6, 84].

Another aspect of growth is the ordering of the nascent adsorbate layers with respect to the substrate lattice. The term *epitaxy* is used to describe a situation where there is a commensurate relationship between substrate and adsorbate lattices [8]. This means that there is a match between two low-integer linear combinations of base lattice vectors of substrate and adsorbate, respectively. In such cases, it is typically the adsorbate lattice that deviates from its bulk structure to match the undistorted substrate lattice. Depending on the bond type, classical epitaxy (chemisorption) and van der Waals epitaxy (physisorption) may be further distinguished. Since combinations of adsorbate and substrate with perfectly matching lattice geometries are rare, the film lattice is usually strained to some extent, leading to a prevalence of Stranski–Krastanov growth in epitaxic systems.

In contrast, the case where adsorbate and substrate lattices remain incommensurate is called *quasi-epitaxy* (QE). In some systems, however, the orientational relationship between film and substrate remains well defined. The lattice of quasi-epitaxically grown adsorbate films does not necessarily conform to the bulk equilibrium lattice, but may exhibit distortions. A variety of factors encourage the development of QE systems:

A necessary requirement is that translation of an adsorbed molecule across the surface is possible without a significant change in system energy. Specifically, the interlayer shear mobility needs to be far greater than the intralayer compressibility. This is generally not true for atomic films, but may be possible for molecular films, depending on the spatial extent and internal structure of the molecules [242]. Quasi-epitaxic growth is frequently encountered in systems grown outside of equilibrium conditions.

5.2 The PTCDA molecule

While the predominant interaction within a single organic molecule is the covalent bond, the interaction between individual molecules is typically conveyed by the London dispersion force. This weak attractive force occurs even in bonding partners without permanent multipole moments, by interaction of transient multipoles that appear due to the probabilistic charge distribution within a molecule [59]. The van der Waals (vdW)

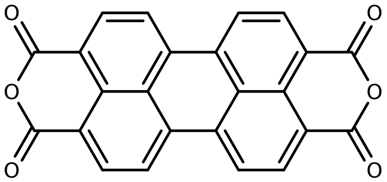

Figure 5.2 – Structural diagram of the PTCDA molecule.

force, *i.e.*, the combination of Pauli repulsion and attractive London force, is frequently described within the Lennard-Jones potential approximation [137, 233]. Additionally, a special form of dipole interaction is given by the hydrogen bond. It is an attractive interaction between a hydrogen atom bound to an electronegative atom, and another electronegative atom facing the former. This bond is generally not covalent in origin [75], but mainly due to electrostatic attraction.

To form a solid, a molecule aligns in a position where the total interaction potential between itself and the surrounding molecules finds a local minimum. Molecules whose interaction potential has a complex spatial distribution with many local minima (such as large, asymmetric protein molecules) will have many near-equivalent modes of alignment, allowing stable, unordered configurations. Thus, crystallization of these molecules is difficult. In contrast, alignment within a periodic lattice is facilitated if the potential, and the molecule itself, are geometrically simple and symmetric.

Perylene (*peri*-dinaphthylene) is a polycyclic aromatic hydrocarbon. Molecules whose core is an aromatic slab, such as derivatives of perylene, compose a model class of planar molecules. By attaching different functional groups to the core, the properties of the molecule can be varied, retaining the planar geometry. The perylene-3,4,9,10-tetracarboxylic-dianhydride (PTCDA) molecule is part of this class. It consists of a perylene core with dual anhydride groups attached to either end of the molecule. The structure of the molecule is rendered in fig. 5.3.

Together with its associated class of perylene-3,4,9,10-tetracarboxylic-diimide (PTCDI) derivatives, it forms a family of economically relevant organic pigments. In this function, PTCDA is also known as C.I. Pigment Red 224, or by its constitution number, 71127 [44]. PTCDA readily forms molecule crystals, macroscopically appearing as a bluish-red, crystalline solid. Due to their long-term stability and high dissociation temperature, perylene-based pigments have seen widespread use, *e.g.*, in coloring plastic products, as well as in automotive paints [228].

For bulk PTCDA under ambient conditions, two crystal structures, designated the α and β modifications, are known [175]. Both are monoclinic crystals, in the $P2_1/c$ space group, but differing in their lattice parameters. In both polymorphs, the alignment of the molecules is such that their plane closely matches the (102) lattice plane. Thus, the structure can be understood in terms of a layered crystal, the individual molecular layers

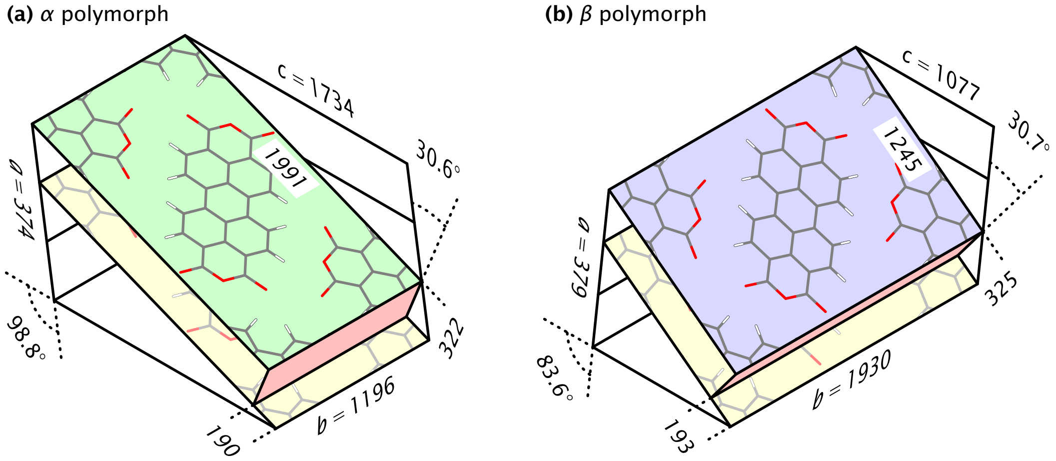
(a) α polymorph

(b) β polymorph

Figure 5.3 – Structure of the two PTCDA bulk modifications. Isometric view of **(a)** α and **(b)** β polymorphs, showing $3 \times 1 \times 1$ bulk unit cells. All dimensions are given in pm. The b and c lattice directions are aligned with the coordinate axes, while the a direction is inclined by 8.8° (−6.4°) toward c. Two adjoining layers of PTCDA, and their interlayer separation of 0.322 nm (0.325 nm) are shown. The orientation of the molecular planes is given by the [010] and [$\bar{2}$01] vectors. Layers are displaced laterally toward the [$\bar{2}$01] direction, by 0.190 nm (0.193 nm). As the role of long and short planar lattice vectors are interchanged between polymorphs, the effective displacement direction differs.

being arranged in a square lattice. A planar unit cell contains two molecules, their long axes nearly perpendicular to each other.

The planar unit cell vectors are oriented along the [010] and [$\bar{2}$01] bulk directions, respectively. The polymorphs differ in which one of these vectors is the longer one. In β-PTCDA, the vector coinciding with the b bulk crystallographic direction is the longer one, while in the α modification, the long axis of the unit cell is aligned with the [$\bar{2}$01] vector. In both cases, the dimensions of the unit cell are roughly similar, with long vectors of 1.991 nm and 1.930 nm, and short vectors of 1.196 nm and 1.244 nm, respectively, for α- and β-PTCDA.

Subsequent layers are stacked with their unit cell displaced along the [$\bar{2}$01] planar unit cell vector, by a similar amount. This displacement is 0.190 nm in α-PTCDA, and 0.193 nm in β-PTCDA. Since the roles of long and short planar unit cell vectors are interchanged between the polymorphs, the effective displacement directions are different. A summary of both bulk and planar lattice parameters for the two modifications is given in table 5.4, and represented graphically in fig. 5.3.

PTCDA as an organic semiconductor. In conventional, inorganic semiconductors, the band gap marks the separation between the occupied valence band and the unoccupied conduction band, at absolute zero temperature. Within the context of organic semi-

α-PTCDA	β-PTCDA	Dimension
0.374	0.378	[100] unit cell vector a (nm)
1.196	1.930	[010] unit cell vector b (nm)
1.174	1.077	[001] unit cell vector c (nm)
98.8°	83.6°	$\angle(a,c)$
1.991	1.244	[$\bar{2}$01] planar unit cell vector (nm)
1.991	1.930	long planar unit cell vector (nm)
1.196	1.244	short planar unit cell vector (nm)
0.322	0.325	interlayer distance d_p (nm)
0.190	0.193	lateral interlayer displacement d_l (nm)
30.6°	30.7°	$\angle(a,d_p)$

Table 5.4 – Lattice parameters of bulk PTCDA. Data for both bulk crystal polymorphs are given. Data for α polymorph taken from ref. [148], β polymorph from ref. [167].

conductors, the highest occupied molecular orbital (HOMO) and the lowest unoccupied molecular orbital (LUMO) are analogous to the top of the valence band and the bottom of the conduction band, respectively. The width of the band gap is given by the difference between HOMO and LUMO energies.

The electronic transport properties of PTCDA films have previously been studied within the context of semiconductor device structures. Particularly, an extensive study was published by Forrest *et al.* in 1984 [66, 67]. It has been found that the electronic transport properties of PTCDA thin films are highly anisotropic. Measurements in contact barrier diode [66] and OLED setups [33] have demonstrated that normal to the molecular layer planes, PTCDA may transport holes, while electron transport is not favored [177].

Adsorption characteristics. The adsorption characteristics of PTCDA on monocrystalline substrates has been the focus of considerable attention. Depending on the substrate, it has been found to exhibit both epitaxic and QE growth. A study on the alkali halides NaCl(001) and KCl(001) [167] has demonstrated epitaxic growth in a bulk-like planar structure. PTCDA adsorbed on the Ag(110) surface has also been shown to grow epitaxically [207]. On this substrate, the molecules arrange in a brick-wall-like structure, with their molecular axis aligned with the substrate [100] direction. The superstructure is commensurate; Its lattice vectors match the substrate plane [32] and [3$\bar{2}$] directions, respectively.

Regarding quasi-epitaxically grown PTCDA films, the substrate studied in most detail is highly-ordered pyrolytic graphite (HOPG). PTCDA films on HOPG assume a structure that qualitatively matches the bulk [102] planar herringbone structure [149]. Compared to the molecular crystal, the superlattice unit cell dimensions are slightly expanded. The orientation of the adsorbate lattice relative to the substrate can be inferred from the Moiré patterns exhibited by the layer [99], or by lithographic removal of the adsorbate layer [33]. Consistently, two incommensurate superstructures have been found, with domain orientations of 3° and 10° to the substrate, respectively. A compilation of results can be found in ref. [65].

5.3 The Au(111) surface

Bulk gold forms a metal crystal with a face-centered cubic (fcc) structure, with a lattice constant of $a = 0.4079$ nm [51, 152]. Its {111} bulk planes have a hexagonal structure with a nearest neighbor distance of $d_\mathrm{N} = \sqrt{1/2}\,a = 0.2884$ nm. The distance of two adjacent atomic rows is $d_\mathrm{R} = \sqrt{3/8}\,a = 0.2498$ nm, and the perpendicular interlayer distances is $d_\mathrm{L} = \sqrt{1/3}\,a = 0.2366$ nm. In projection onto the plane, atoms of every third layer share positions, thereby forming an *ABCABC* stacking pattern.

Similar to the Cu(111) and Ag(111) faces, the electronic structure of the Au(111) surface is characterized by Shockley surface states located within the bulk band gap at the L point. Surface state electrons exhibit an approximately two-dimensional free electron behavior. Their dispersion follows a parabolic law given by

$$E(k_\parallel) = E_0 + \frac{\hbar^2 k_\parallel^2}{2m^*}, \tag{5.1}$$

with an onset energy of $E_0 - E_F = (-487 \pm 1)$ meV and an effective mass of $m^* = 0.255 m_\mathrm{e}$ [191].

While the Cu(111) and Ag(111) surfaces prefer the bulk termination, in Au(111), a unique and very distinctive surface reconstruction was found to exist [100, 182]. Due to its peculiar appearance, the reconstruction is called the *herringbone* or *chevron* reconstruction. To avoid ambiguity, the latter designation will be used here.

Atom positions on the surface have been modeled by competition of a longer-range many-body interaction, and a pairwise interatomic interaction [60, 92]. In the case of Au(111), an increase in atom density on the surface, and thus a reduction in interatomic distance, yields a net energy gain that outweighs the cost of interrupting the bulk crystal periodicity. As a result, the surface lattice is uniaxially compressed along one of the $[01\bar{1}]$ directions, accommodating 46 ± 2 surface atoms onto 44 ± 2 bulk lattice sites inside a $(22 \pm 1) \times \sqrt{3}$ surface cell. This amounts to a surface compression of $\approx 4.5\%$. The compression is established by alternating stacking of top layer atoms twice per surface cell, switching between bulk-like fcc (*ABCABC*) stacking and hexagonally close-packed (hcp) stacking. The latter means that atoms in the topmost layer share lattice sites with atoms two layers underneath, resulting in an *ABCABA* termination. The packing density, and thus the distance between surface and subsurface layers, is similar in the fcc and hcp regions. The fcc type is energetically slightly more favorable, being the bulk stacking type, thus the fcc regions are wider than the hcp regions.

The regions are separated by relatively broad boundaries where the atomic positions within the lattice gradually transition between fcc and hcp sites. These bridging positions are slightly elevated from the subsurface layer, by up to 15 pm [89]. Thus, in STM

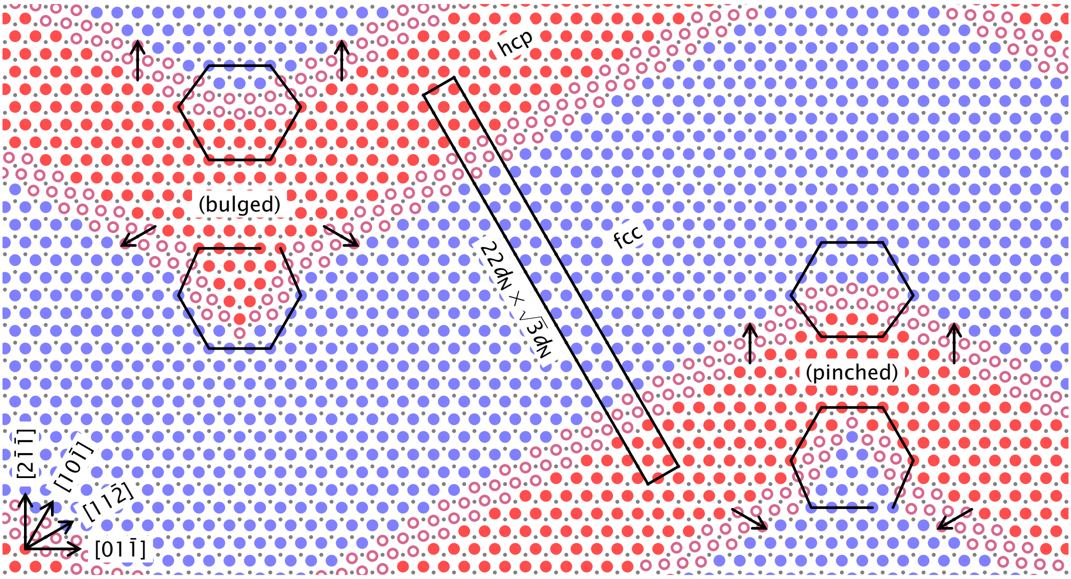

Figure 5.5 – Model of the reconstructed Au(111) surface, after ref. [34]. Large circles denote surface atoms, small gray dots represent the first subsurface layer. Locally, the surface contains fcc (blue filled circles) and hcp (red filled circles) regions, joined by transition regions forming elevated ridges (purple hollow circles) of two types. Arrows indicate the directions of atom displacement while moving from fcc to hcp region. Locally, the ridges are straight, giving a $(22 \pm 1) \times \sqrt{3}$ surface unit cell. On a larger scale, the reconstruction undulates, with each ridge type curving in a specific manner, forming elbows with bulged (left) and pinched (right) geometry. Hexagonal Burgers circuits are plotted around the elbow sites. For type X ridges, open circuits are obtained, indicating a dislocation site.

topographic mapping, the reconstruction locally appears as pairs of discommensuration lines, in the form of elongated protrusions, or ridges, along the $\langle\bar{2}11\rangle$ direction.

This surface contraction is uniaxial, and thus anisotropic. To further relieve surface stress, the contraction direction varies across the surface. This is accomplished by the formation of large domains in which two of the three possible orientations for the surface contraction alternate. The result is a zig-zag pattern, with the pairs of discommensuration lines changing their alignment in a characteristic elbow-like pattern. At these elbows, the azimuthal direction of the dislocation lines changes by 60°, thus providing six possible orientations of elbows.

Two different types of elbows exist, which, due to their distinctive appearance, have previously been designated *pinched* and *bulged* elbows [35]. In fig. 5.6, these elbows have been marked by the letters P and B, respectively. This is due to each discommensuration line of a pair having a separate Burgers vector: In type X ridges, the Burgers vector varies by 120° on the two segments flanking the elbow, while in type Y ridges, it stays the same [34]. As a consequence of this, type X ridges contain a dislocation site at each elbow,

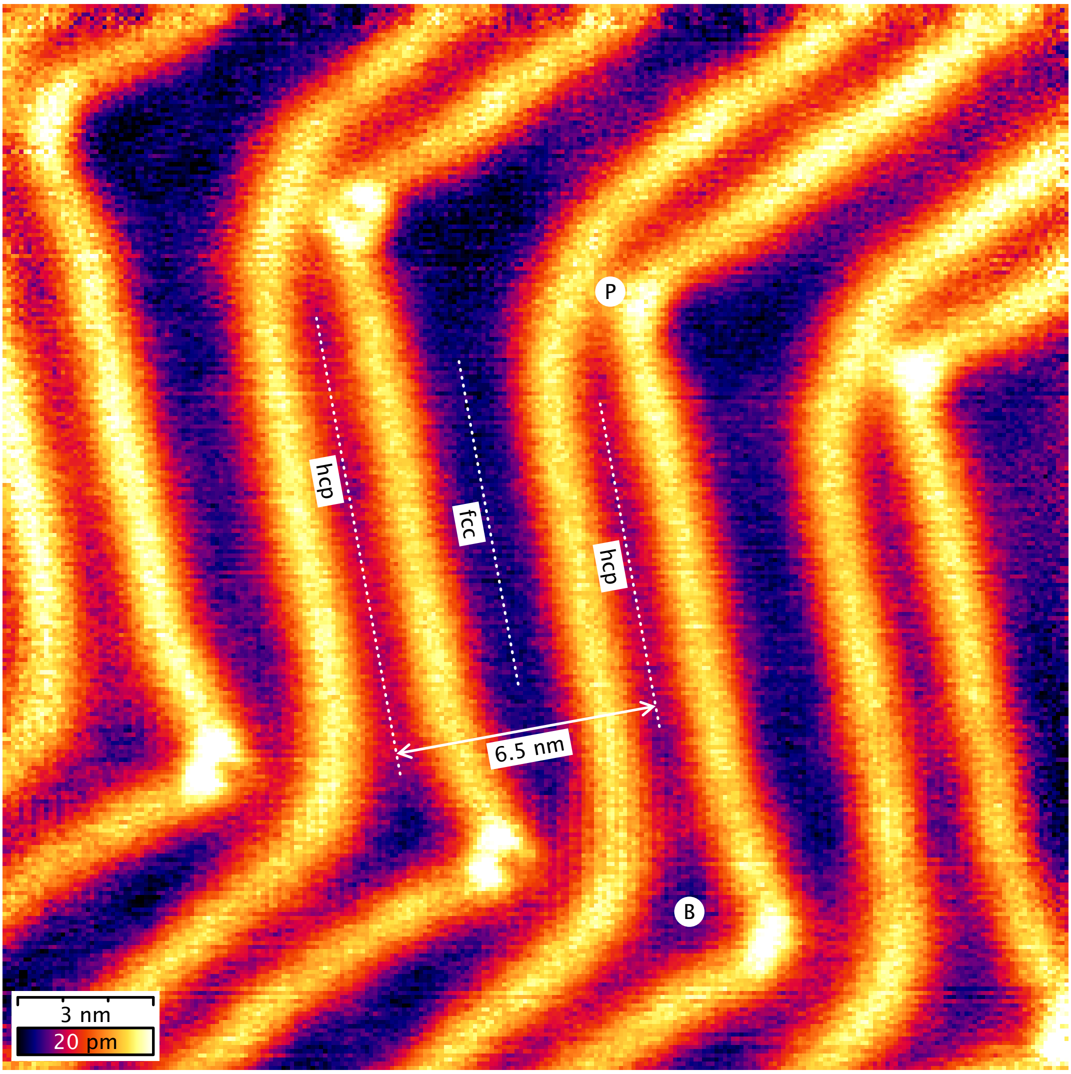

Figure 5.6 – Closeup of the Au(111) reconstruction, $(23.5\text{ nm})^2$ topograph, $V = +800$ mV, $I = 260$ pA, showing the chevron surface reconstruction. The pairs of discommensuration lines separate regions of fcc and hcp top layer stacking. The elbows alternate between pinched and bulged morphology, as indicated by the letters P and B, respectively. The left-hand ridges of each pair are of type Y, which is curving more smoothly. The right-hand ridges are of type X and provide dislocations at each elbow that facilitate adsorption. Here, impurities of unknown type have adsorbed on several of the type X elbow sites.

that may serve as preferred nucleation site of certain adsorbates. This is visible in fig. 5.6, where at several of the type X elbows, adsorbed material is present. The chevron reconstruction was found to be stable up to a temperature of 865 K, beyond which the surface transforms to an disordered, isotropically compressed state, in a first order phase transition [101]. It can be modeled within the Frenkel–Kontorova framework, which describes a chain of atoms reduced to harmonic nearest-neighbor interactions, embedded within an external periodic potential [13, 69].

5.4 The stepped Au(111) surface

The non-reconstructed Au(111) surface has a structure similar to the Ag(111) surface, described in section 2.1. The hexagonal structure offers three principal axes along which the six in-plane nearest neighbors of each atom are aligned. These directions are given by the $[0\bar{1}1]$, $[10\bar{1}]$ and $[\bar{1}10]$ vectors. Straight surface steps can proceed along any of these three directions. At a step, the outermost atoms of the topmost plane and their nearest neighbors on the atomic plane below form a microfacet. Depending on the orientation of the step, up or down, these microfacets are either of {111} or of {100} type. The normal vectors of the three possible {111} hexagonal microfacets are given by $(\bar{1}11)$, $(1\bar{1}1)$, and $(11\bar{1})$. The normal vectors of the {100} microfacets, in which the atoms form a rectangular arrangement, are the (100), (010), and (001) vectors. On reconstructed Au(111), the presence of dislocations and steps influences the distribution of compression directions. Depending on the geometry of the disturbed surface, a plethora of morphological phenomena has been observed [11]. Generally, the discommensuration lines prefer to cross steps with {111} microfacets perpendicularly without disturbance [194].

Fig. 5.7 shows a stepped Au(111) region additionally treated with sputtering to produce vacancy defects, as described in section 2.3. It gives an example of the many morphological peculiarities seen with the chevron reconstruction. On the right-hand side, the interaction between the reconstruction and steps is seen, with the discommensuration ridges preferably crossing {111} type steps. Extraneous ridge pairs that cannot further connect frequently self-terminate in a U shape. Otherwise, small vacancies often serve as hub sites where three ridge pairs intersect. Larger vacancies are seen with both flat and reconstructed insides. The latter frequently exhibit ridge pairs in a three-pointed star pattern, perpendicular to the {111} steps. The shape of many of the vacancy islands visibly deviates from the regular hexagon, with the three {111} type edges longer than the {100} edges.

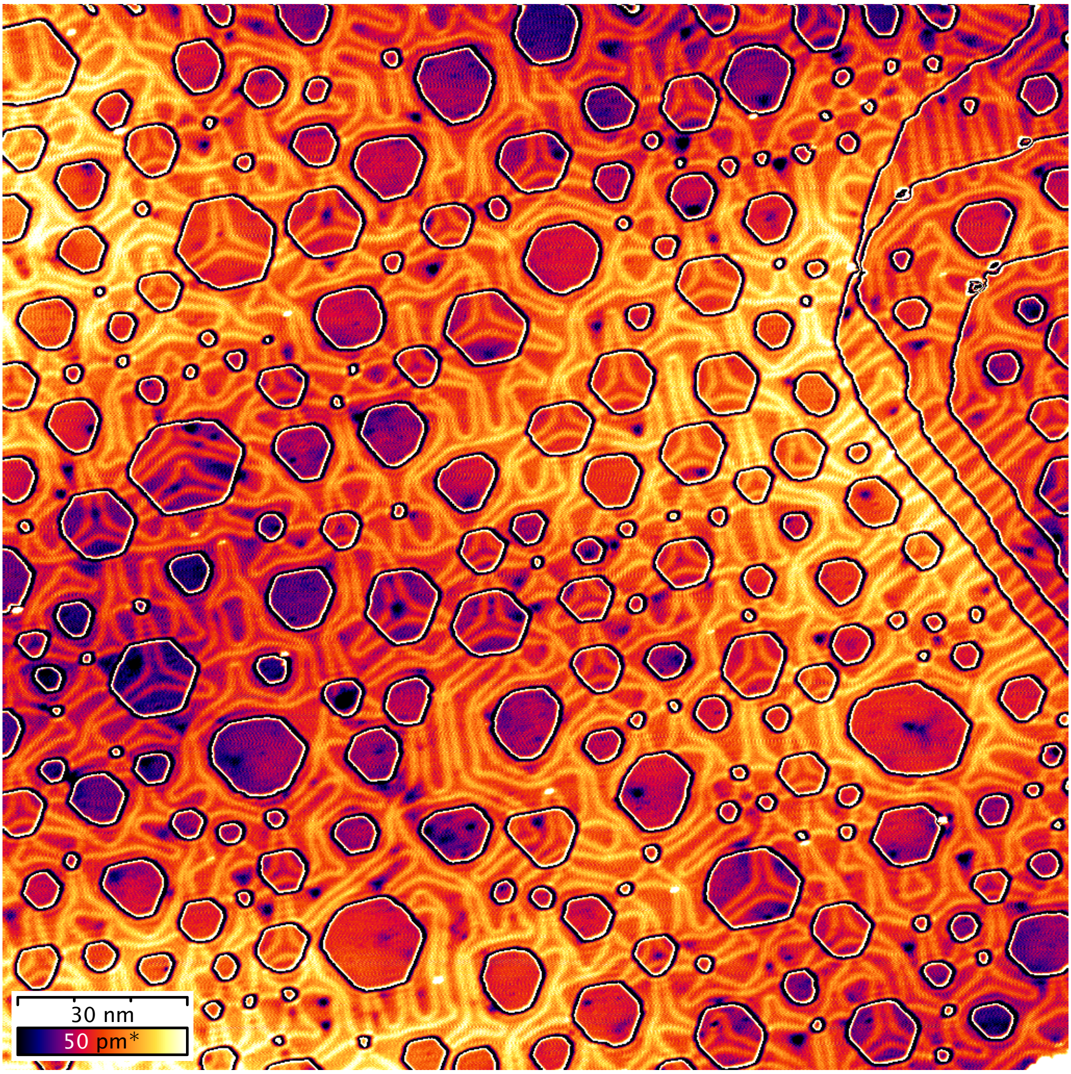

Figure 5.7 – Vacancy islands on Au(111). (189 nm)^2 topograph, $V = 240$ mV, $I = 200$ pA. The path of the discommensuration lines prefers to perpendicularly intersect {111} steps (top, bottom left and bottom right edges of each vacancy island). Inside, both a three-pointed star pattern and the absence of any reconstruction are frequently seen. Several hexagons are visibly irregular, with the {111} type edges being longer than the {100} edges, presumably due to the former being energetically more favorable.

Chapter 6

PTCDA on Au(111)

The adsorption of PTCDA films on the Au(111) surface itself has been the objective of various previous studies. A GIXD and RHEED experiment on a ≈ 17 ML PTCDA film has demonstrated a quasi-epitaxic layer-by-layer growth [63]. The adsorbate lattice was found to be rectangular, similar to the adsorbate (102) bulk planes. While the lattice exhibits a slight rectangular distortion, the unit cell area remains largely unchanged. The substrate chevron reconstruction is retained below the film.

In additional, the structural properties of sub- or near-monolayer coverages have also been studied in detail. An STM and RHEED study imaged a superstructure similar to the (102) planes of the bulk PTCDA polymorphs both in lattice dimensions and molecular orientation [205]. PTCDA was found to form islands with a thickness of a single atomic layer, a regular herringbone-like structure and a rectangular ($90^\circ \pm 2^\circ$) unit cell with dimensions $a = (1.97 \pm 0.04)$ nm and $b = (1.22 \pm 0.02)$ nm, amounting to a density of one molecule per (1.20 ± 0.05) nm^2. The Au(111) surface reconstruction is preserved below the molecular layer. Several possible orientations of the adsorbate lattice coexist, their lattice constants being identical within the accuracy of STM.

In a later STM study of the same system [39], a second adsorption phase with a square unit cell of $a = b = (1.7 \pm 0.1)$ nm was observed. This square phase does not correspond to any known PTCDA bulk structure. With one molecule per (1.44 ± 0.18) nm^2, its density is lower than that of the herringbone phase. Under the square phase, the Au(111) chevron reconstruction is preserved as well. Growth of any monolayers beyond the first one invariably takes place in herringbone geometry.

6.1 Preparation

In preparation of the present experiment, the substrate surface was cleaned by repeated cycles of Ar^+ ion bombardment and annealing, using the usual technique as described in section 1.7. In total, 3 cycles were performed, with a reduced intensity for the final cycle. After preparation the surface was allowed to directly cool down to room temperature. The PTCDA molecules, kindly provided by M. Sokolowski, University of Bonn, Germany,

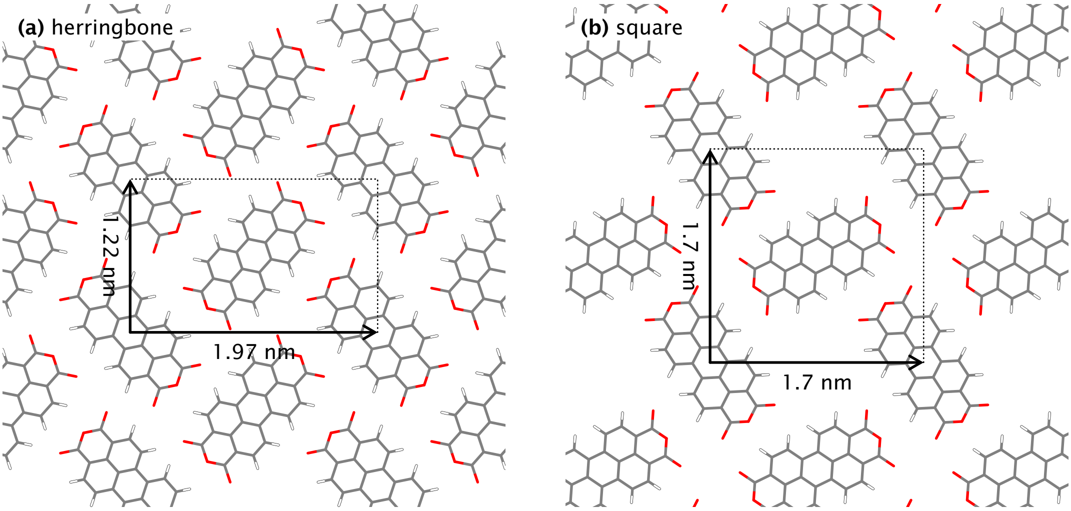

Figure 6.1 – Lattice structures in PTCDA/Au(111), showing unit cell and dimensions for **(a)** herringbone phase [205] and **(b)** square phase [39].

were evaporated from a button heater cell with a directed nozzle. The cell was heated until the quartz balance detected an evaporation rate, then the substrate was exposed to the molecular beam for 10 s. The sample was then transferred to the precooled 7 K low-temperature STM.

The evaporator could not be initially calibrated, as the PTCDA sticking coefficient was not known beforehand. Thus, the first large-scale topographs of the PTCDA-covered Ag(111) surface serve to ascertain whether the preselected parameters result in a coverage of desired magnitude. Fig. 6.2 shows a sample topograph of the prepared system, indicating that after evaporation, the molecules remained mobile on the surface at room temperature, eventually forming large two-dimensional regularly ordered islands. It is determined that the preparation conditions result in a coverage of ≈ 0.2 ML, a monolayer being defined as a the number of molecules per area needed to provide complete coverage of the surface with a monatomic layer. Note that this definition is not accurate, as the various possible adsorbate lattice configurations have differing unit cell sizes, and consequently differing packing densities.

6.2 Experimental findings: topography

In accordance with previous work, two different types of PTCDA superstructure are seen: The first one is a phase whose structure resembles the herringbone arrangement within the (102) crystalline planes of bulk PTCDA. The measured lattice dimensions for this phase are $a = 1.80 \pm 0.09$ nm for the long unit cell vector and $b = 1.22 \pm 0.07$ nm for the short unit cell vector. The second superstructure is the previously reported

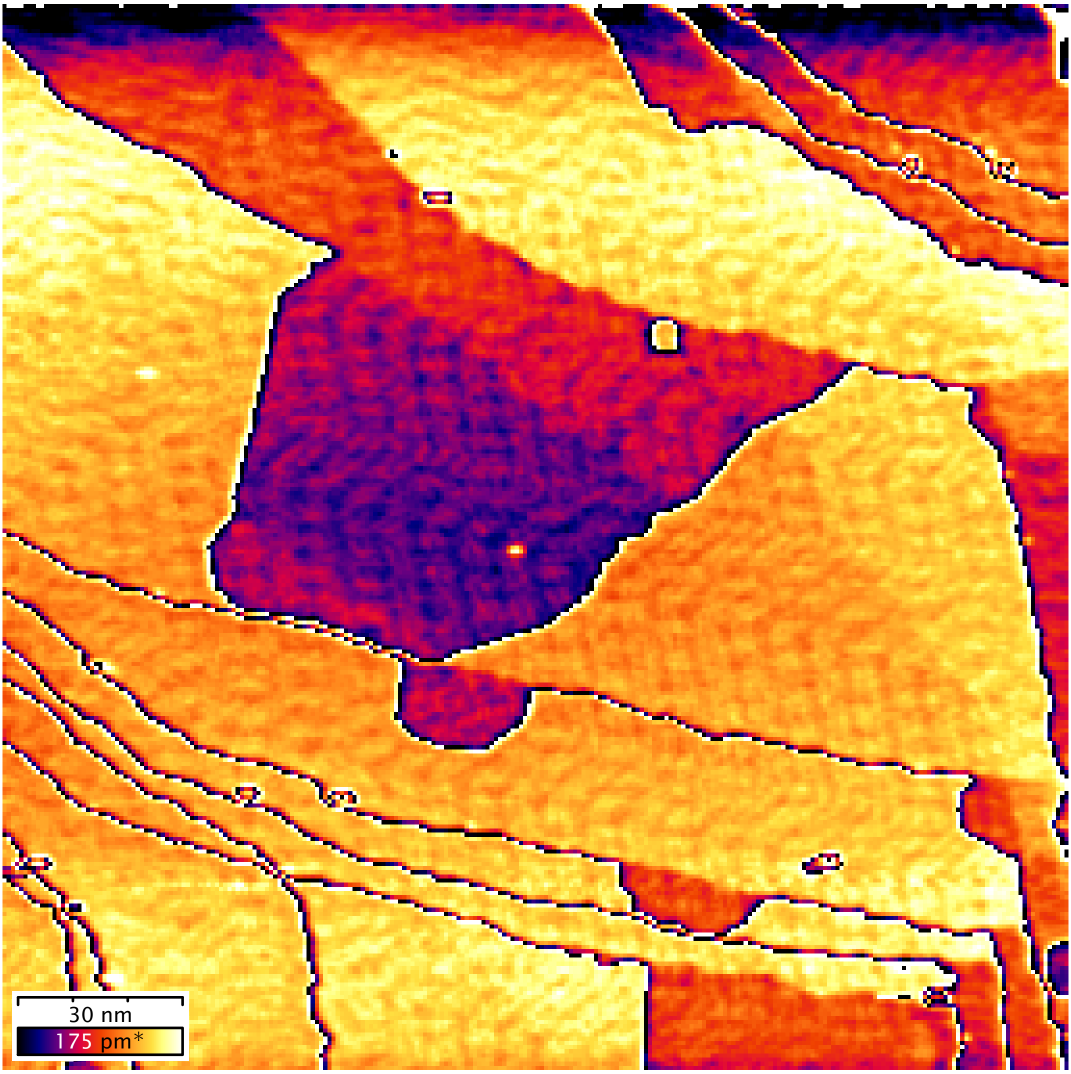

Figure 6.2 – PTCDA islands on Au(111), $(194\ \text{nm})^2$ topograph, $V = -1000$ mV, $I = 200$ pA. The z values displayed are modulo nominal Au(111) interlayer period d_L, hence each substrate terrace appears in the same hue. As PTCDA islands have a slightly smaller apparent height of $h \approx 0.7 d_\text{L}$, they appear as dark regions. Also, covered and clean surface portions can be discriminated by the path of the discommensuration lines, which cross $\{111\}$ type surface steps only perpendicularly, but can pass island boundaries undisturbed at oblique angles.

square phase [39]. In this phase, on each of the lattice points, the anhydride ends of four molecules converge in a slightly staggered fashion, thereby forming a propeller- or windmill-like coordination. The phase bears a fourfold rotational symmetry. For square phase PTCDA, the unit cell vectors are $a = b = 1.56 \pm 0.08$ nm. A notable property of the square phase is that in the positions where the anhydride ends of four molecules converge, occasionally small, circular objects are entrapped, appearing as 'windmill hubs' in the topograph. The nature of these objects could not be conclusively determined; It is suspected that these are single Au atoms that were entrapped while diffusing across the surface. Their presence does not noticeably perturb the molecular lattice.

As expected, all of the above lattice parameters are in reasonable agreement with previous results. It has been previously reported that the Au(111) chevron surface reconstruction is conserved below a PTCDA monolayer. This is the case for both observed lattice types. Fig. 6.3 shows the substrate reconstruction as a faint imprint in the height variation of PTCDA islands. The availability of the substrate reconstruction facilitates measuring the orientation of the adsorbate lattice relative to the substrate crystallographic directions.

On a large scale, the average apparent topographic height of PTCDA islands in square lattice configuration is about $h = 0.18$ nm. This number is comparable to the height of Au(111) monatomic steps, $d_{\mathrm{L}} = 0.2366$ nm. As fig. 6.2 suggests, these two heights are fairly similar. Nevertheless, island boundaries and surface steps may be discriminated from the direction of the substrate reconstruction, even at scales where resolution of individual PTCDA molecules is not available. As established in section 5.3, the discommensuration lines tend to perpendicularly intersect {111} steps, whereas they may cross adsorbate island boundaries at oblique angles.

The hexagonal substrate lattice itself provides a threefold rotational symmetry. The herringbone phase has a glide reflection symmetry, resulting in a total of six equivalent angles, whereas the square phase may exist in two, mirror inverted, phases. Here, the same configuration can also be realized with six different angles. To determine the number of possible orientations of the adsorbate, these equivalences need to be taken into account.

6.3 Experimental findings: electronic structure

The most striking observation in this experiment relates to the electronic structure of the adsorbed PTCDA. Previously, an absence of bias and polarity dependence on the topographic appearance of both PTCDA phases was reported [39]. However, in this study it was found that, for topographs taken at positive sample voltages beyond a specific threshold, a notable transition in intramolecular contrast takes place:

Molecules in both square and herringbone phase appear as elongated shapes at negative sample voltages, and at positive sample voltages below ≈ 700 mV, as shown in fig. 6.4a. No intramolecular substructure is discernible. However, at voltages in the range of $700 \ldots 900$ mV, the apparent shape of molecules in the square phase undergoes

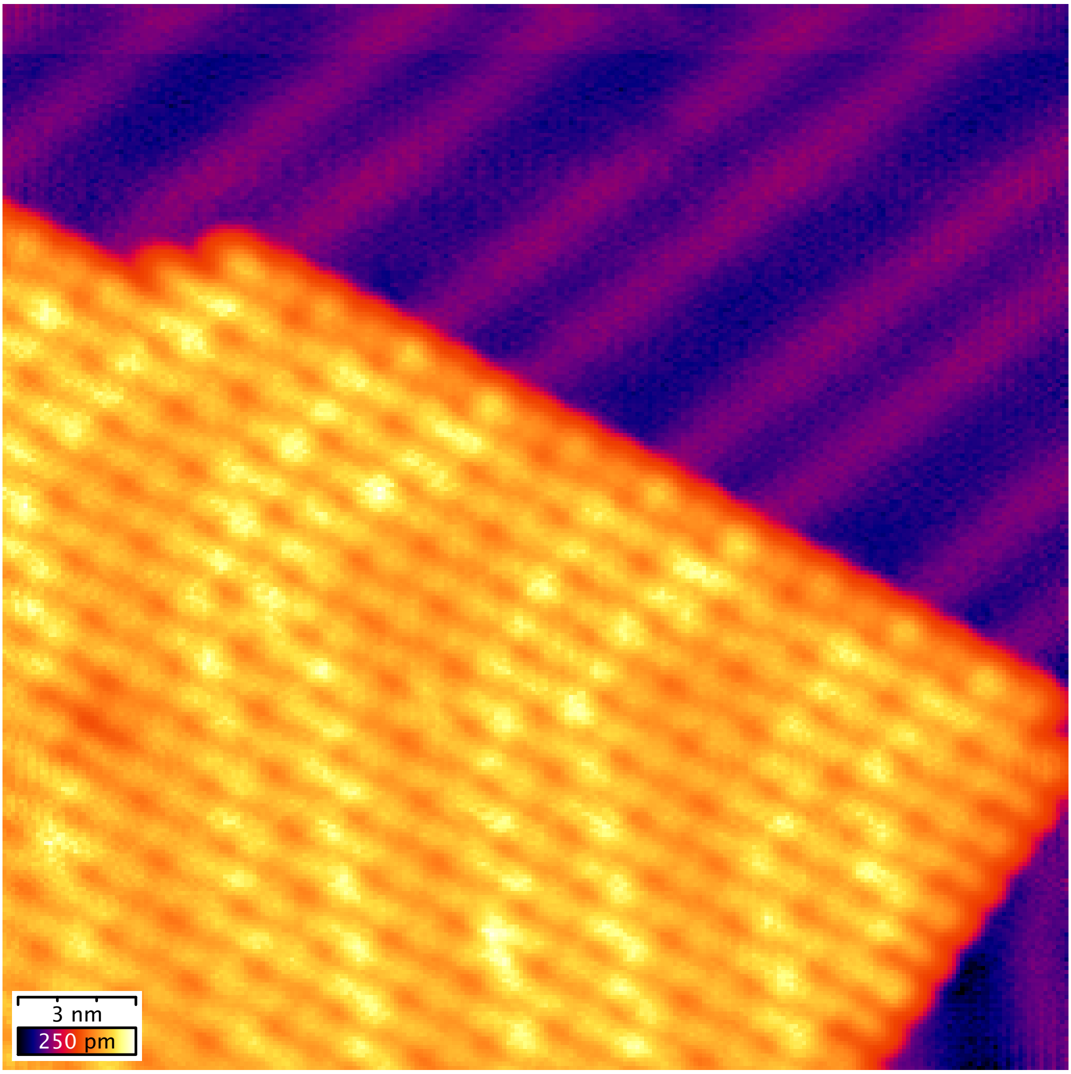

Figure 6.3 – Single PTCDA island on Au(111), square phase. $(27.1\ \mathrm{nm})^2$ topograph, $V = +800\ \mathrm{mV}$, $I = 220\ \mathrm{pA}$. The chevron reconstruction is preserved underneath the molecular layer and is visible as a faint modulation in apparent height.

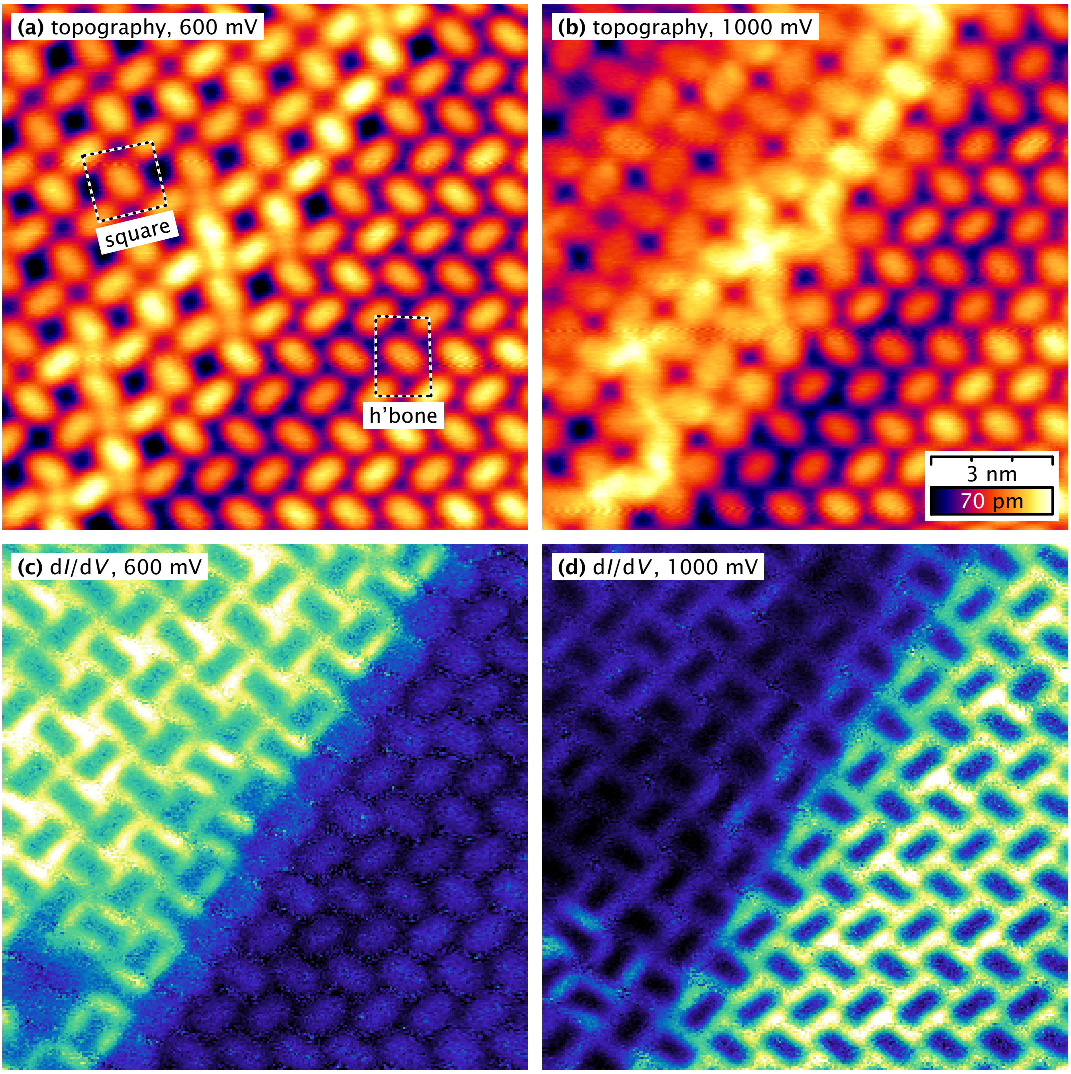

Figure 6.4 – Intramolecular contrast transition in PTCDA/Au(111), (13 nm)^2 maps, $I = 180$ pA. The same sample region is scanned twice, at sample bias voltages of 0.6 V and 1 V, respectively. The region comprises both square (top left parts of each image) and herringbone (bottom right parts) domains. **(a)** Topograph at 0.6 V. Molecules in both domains are imaged as slender, elongated features without visible internal structure. In the square phase, circular features are visible in a small portion of the hub locations. The overall modulation in picture brightness is due to the chevron reconstruction. **(b)** Topograph at 1 V. Here, molecules in the square phase are imaged as wider, flatter, more rectangular shapes. Molecules in the herringbone phase still appear as in image (a). **(c)** constant current dI/dV map at 0.6 V. Molecules in the square phase are shown as outlines in high contrast. Molecules in the herringbone phase are imaged in low contrast. **(d)** constant current dI/dV map at 1.0 V. At this voltage, molecules in both phases are shown as outlines, with high contrast in the herringbone phase. Square phase molecules are imaged with low contrast.

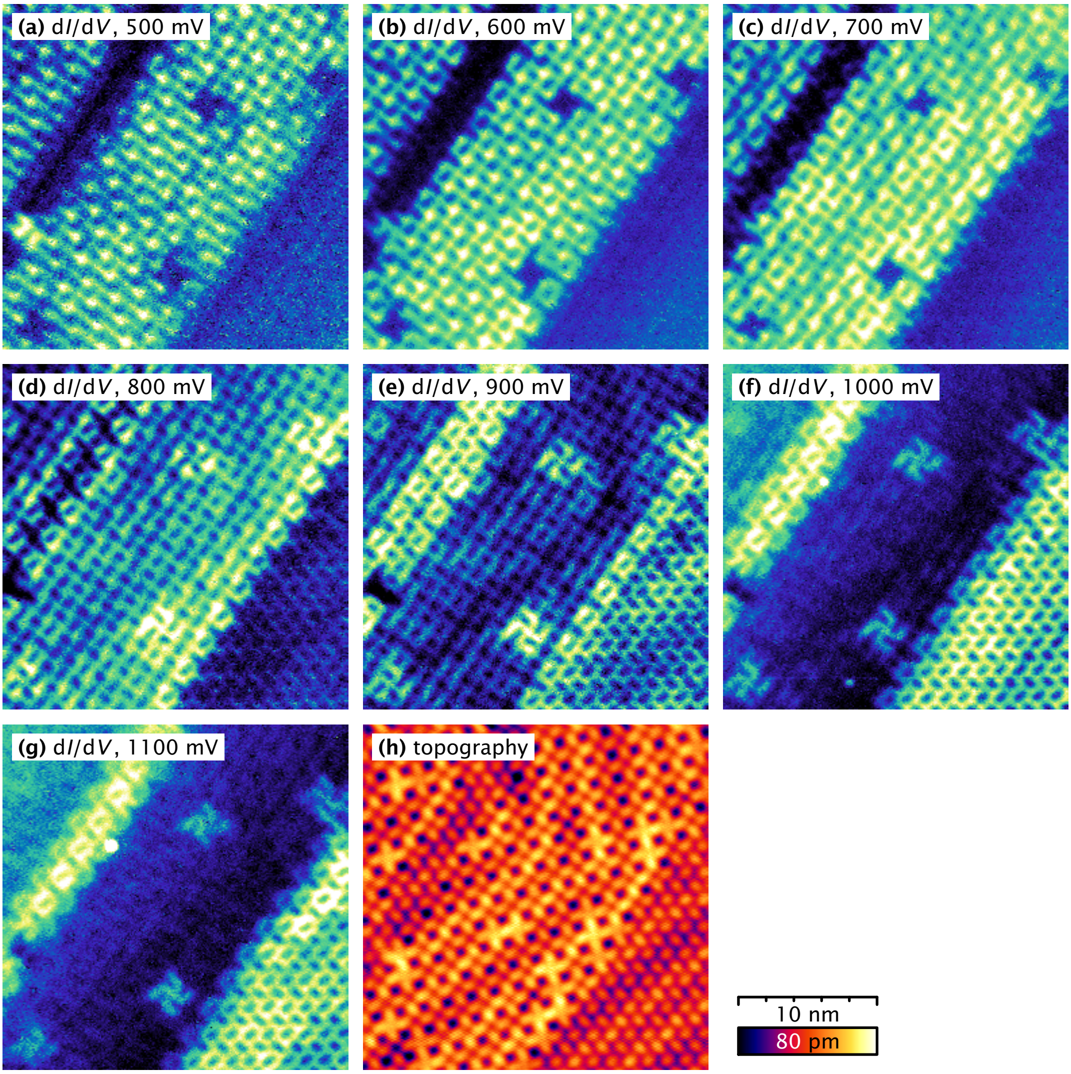

Figure 6.5 – Differential conductance maps of PTCDA/Au(111), (25 nm)^2, $I = 180$ pA. Two square domains (center and top left) and both an extended domain (bottom right) and a single molecular line in herringbone arrangement are imaged at a series of bias voltages. **(a–g)** dI/dV maps, modulation 1 mV$_{\mathrm{rms}}$ at 2.4 kHz. In the low voltage range, up to 0.7 V, high contrast is confined to the square regions. In the intermediate range of 0.8...0.9 V, the rows of molecules at the square-herringbone domain boundaries are imaged in high contrast. At 1 V and above, the row and domain with herringbone arrangement appear in high contrast. **(h)** Reference topograph at 500 mV, showing molecular arrangement and substrate reconstruction.

a transition. Beyond 900 mV, the molecules appear as shapes with a roughly hexagonal outline (fig. 6.4b). At these voltages, the apparent width of the molecules exceeds their apparent length, falsely suggesting a rotation of the molecules. Additionally, the molecules undergo a contrast change which exhibits an intramolecular substructure. A detailed discussion of this will be given in section 7.4. Meanwhile, molecules in the herringbone phase still appear elongated and structureless in the aforementioned sample voltage range. However, the apparent shape of these molecules undergoes a similar transition, albeit in a higher sample voltage range of 1000…2000 mV.

Differential conductance maps. This transition is also reflected in $\mathrm{d}I/\mathrm{d}V$ maps acquired at sample voltages in the aforementioned range. Fig. 6.4c shows a constant current $\mathrm{d}I/\mathrm{d}V$ map at a sample voltage of 600 mV, which is within the transition interval for square phase PTCDA. The image shows a substantially higher brightness in the square region than in the herringbone region. This corresponds to an increased LDOS in the square region. The PTCDA molecules themselves are imaged as dark rectangles. This is likely a consequence of the constant current technique. As established in section 1.4, the tip follows a trajectory of constant integral LDOS. On the molecules, the total sample elevation is increased locally. To maintain a constant current, the tip z position is increased by the feedback loop. Meanwhile, the spatial variation in LDOS at the energy corresponding to the sample voltage is less localized. Thus, the molecules are imaged in inverted contrast.

Fig. 6.4d shows a constant current $\mathrm{d}I/\mathrm{d}V$ map at a higher sample voltage of 1000 mV. At this energy, the intramolecular transition within the square phase is complete, and the molecules in the square regions appear dark. However, the sample voltage lies within the transition interval for the herringbone phase molecules, which are in turn imaged as a bright region with the individual molecules appearing as inverted shapes, for similar reasons as stated above.

The image series reproduced in fig. 6.5 demonstrates in detail the voltage dependence of $\mathrm{d}I/\mathrm{d}V$ maps of PTCDA on Au(111). The imaged region contains a herringbone domain (in the bottom right of the image) and two square domains (in the center and in the top left). The transition between the latter two domains is made by a narrow stripe of molecules in herringbone arrangement. In the accompanying topograph, the substrate chevron reconstruction is clearly visible. The image series comprises bias voltages in the range of 500…1100 mV.

The $\mathrm{d}I/\mathrm{d}V$ maps exhibit the contrast transition described in the previous paragraphs. At voltages below 900 mV, the square regions appear brighter, while at higher voltages the herringbone regions are emphasized. Notably, molecules at a square–herringbone transition boundary are brightest as intermediate voltages (*i.e.*, in the 800 and 900 mV images). Several types of structural defects are visible in the images: three imperfections within the central square domain that are visible as dark spots in the low voltage region, and as bright structures in the higher voltage images, additionally a single imperfection within the transition stripe, near the left edge of the image, that appears brightest in

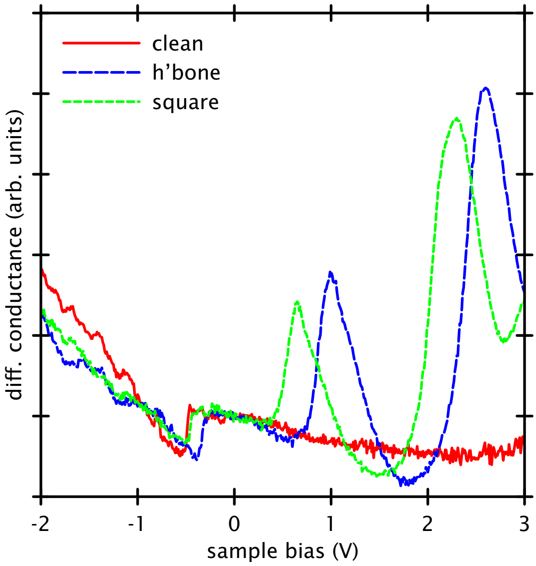

Figure 6.6 – Differential conductance spectra of PTCDA/Au(111), modulation 1 mV_{rms} at 2.4 kHz, feedback loop opened at $V = +850$ mV, $I = 200$ pA. Blue (green) trace shows normalized dI/dV(CH) spectra, averaged over 12 (14) molecules in herringbone (square) coordination. Spectra were acquired with the tip placed on the center of a molecule in the respective phase. The red curve shows a reference spectrum on a clean substrate area. Visible features include the surface state onset and peaks attributed to the LUMO and LUMO+1.

the 500 mV image, and a bright object that appears only above 1000 mV. None of these five imperfections are readily visible in the topography plot. The nature of these impurities is unknown, but the faultlessness of the molecular layer that is evident from the topography indicates that they are substrate defects.

Differential conductance spectra. Fig. 6.6 reproduces a set of constant height dI/dV spectra acquired with the tip positioned at the center of molecules within each of the two phases. The spectra shown are the averages of multiple measurements. A spectrum acquired on a clean substrate area has been included for comparison, which appears featureless except for the expected upward step at the onset of the Shockley surface state, at −0.50 V. On the adsorbate-covered regions this feature is maintained, in agreement with ref. [172], although shifted to a higher energy of −0.45 V in the square phase, and −0.33 V in the herringbone phase. This shift is likely due to charge transfer from the substrate, similar to those seen in rare gases [4] and Pd [221] on Au(111).

In the voltage region where contrast transition in the dI/dV maps was observed, a broad peak is detected at a sample bias of 0.73 V in the square phase, and 1.08 V in the herringbone phase. The peak, reproduced in fig. 6.6, is asymmetric and remarkably congruent across the two phases. It is found to be associated with the lowest unoccupied molecular orbital (LUMO) of the adsorbate molecules, the rationale being given in section 7.5, below. Around a higher sample bias of 2.39 V and 2.71 V, respectively, for the two phases, another broad peak is seen, attributed to the next highest molecular orbital (LUMO+1). At negative bias, a sloped background exists which appears similar in spectra on covered and clean surfaces. The highest occupied molecular orbital (HOMO), which is expected around −2 V [172], is not detected in the experiment.

Feature	Clean Au(111)	Square phase	H’bone phase	Energy shift
Surface state	−0.50 V	−0.45 V	−0.33 V	0.12 V
LUMO	-	0.73 V	1.08 V	0.35 V
LUMO + 1	-	2.39 V	2.71 V	0.32 V

Table 6.7 – Energy positions of spectral features in PTCDA/Au(111) and their relative energy shift between square and herringbone regions.

Chapter 7

PTCDA on Au(788)

As seen in the preceding chapter, the weak periodic corrugation of the reconstructed Au(111) surface and the adsorbate lattice have not demonstrated an interaction. To increase the strength of the substrate patterning, substituting the substrate with a vicinal surface appears like a natural choice. The structural diversity of Au vicinals provides a wide choice of substrate preordering, comprising bulk-stacked and reconstructed terraces, with a one- or two-dimensionally periodic corrugation.

7.1 Au(111) vicinal surfaces

Surfaces with a small miscut angle to a highly symmetric base plane, *i.e.*, one with low integer Miller indices, are called vicinal surfaces. In these surfaces, the direction of the normal vector is closely adjacent to that of the base plane. Miscuts of this type generally lead to a surface with the local geometry of the base plane, interspersed with a periodic distribution of surface features. In the case where the azimuth of the miscut vector corresponds to a direction of close packing of the base surface, cutting a model bulk crystal yields a surface consisting of terraces of the base surface interspersed with equidistant, monatomic steps. These terraces get narrower with increasing miscut angle.

Whether such a structure is a stable equilibrium surface or whether it is unstable toward refaceting depends on the energy balance of the surface. The equilibrium structure of a surface is generally the one with minimized surface tension. Within the terrace–ledge–kink model [124], the total surface tension of a stepped surface is determined by three contributions: the surface tension per area of the base terrace, the free energy requirement per step, and the nature and strength of the pairwise interactions between steps [85]. The latter is governed by the interplay of multiple phenomena: Since atoms at a step edge have a different local coordination compared to those embedded within a terrace, their equilibrium position deviates from the surface lattice. The resulting lattice distortions around a step can be described in terms of a local strain field. The overlap of strain fields originating from two steps in close proximity leads to a repulsive interaction. Additionally, a local charge redistribution at each step due to Smoluchowski smoothing [213] leads to a dipole–dipole interaction between steps. Both effects result in a contribution following an inverse square law. Consequently, on surfaces where these effects yield a repulsive net contribution, the formation of an evenly spaced step array and terraces with a narrow Gaussian width distribution is encouraged [238].

An additional effect stems from the observation that the wandering of steps due to thermal excitation is restricted in regions of high step density, as steps can not freely cross each other. In this case, the reduction of configurational entropy has an unfavorable effect on the surface tension. Modeling steps within an otherwise non-interacting Fermion model leads to an essentially repulsive step–step interaction [115].

Refaceting. If the base terrace type forms a surface reconstruction, the interaction between steps may get more complicated. Specifically, terrace widths that match the preferred unit cell of the reconstruction may prove energetically favorable [12]. In this case, the surface structure refacets to exhibit these preferred, 'magic' terrace widths. The ratio of the terrace widths, in a large scale average, is determined by the miscut angle. Additionally, the surface may exhibit phase separation, forming large domains, each comprising terraces of a single width. Whether this phase separation occurs or the terrace widths alternate locally depends on the interplay between the surface tension within the domains and the energy of domain edges. This has been described within the Marchenko model [155].

Faceting of vicinals has been observed for a variety of reconstructed base surfaces. For example, vicinals of the Si(111) surface, that exhibits the famous 7×7 reconstruction, are known to undergo refaceting [185] and phase separation [184].

Geometry of Au(111) vicinals. On the (111) faces of fcc materials, such as Au(111), the possible monatomic step types contain either {100} or {111} microfacets. Vicinals containing these basic step types can be created by a miscut vector deviating from the surface normal in the $[2\bar{1}\bar{1}]$ and $[\bar{2}11]$ directions, respectively. If the Miller indices of the miscut plane are given as (MNN), the miscut angle θ can be calculated as

$$\theta = \arctan \frac{\sqrt{2}(M-N)}{M+2N}. \tag{7.1}$$

With the fcc lattice constant a and the atomic row distance $d_\mathrm{R} = \sqrt{3/8}a$, the nominal terrace width (in the absence of refaceting) is

$$\Delta x = \left| \frac{M+2N}{\sqrt{6}(M-N)} \right| a = \left| \frac{2N}{M-N} + \frac{2}{3} \right| d_\mathrm{R}. \tag{7.2}$$

The structural properties of selected Au(111) vicinals have previously been reviewed in detail [202]. The terraces may accommodate discommensuration lines that, in {111}-stepped vicinals, run perpendicular to the steps and, in {100}-stepped vicinals, parallel to them. As the steps partially relieve surface stress, the reconstruction unit cell may differ from the $(22 \pm 1) \times \sqrt{3}$ unit cell observed on the Au(111) base surface. Additionally, the reconstruction-induced variation in top layer stacking may result in a local change of step type [193]. For clarity, in the following, surfaces will be called {111}- and {100}-facing vicinals on account of their nominal, nonreconstructed geometry, disregarding any refaceting which may locally have changed the step microfacet.

Among the {111}-facing vicinals, several orientations exhibit equidistant arrays of monatomic steps: The Au(233) surface, with a miscut angle of 10.02°, has unreconstructed terraces. In contrast, surfaces such as Au(788) and Au(11·12·12), with lower miscut angles of 3.52° and 2.31°, respectively, exhibit pairs of discommensuration lines on the terraces, arranged in a V shape pointing toward the ascending step direction. Consequently, the relative width of the hcp domain is bigger on the outward part of the terrace, close to a descending step.

For surfaces whose miscut angles lie between that of the stable reconstructed and unreconstructed vicinals, such as Au(455) and Au(577), the regular monatomic step array was determined to not be the energetically favored structure. After annealing, such surfaces refacet into alternating domains of reconstructed and unreconstructed regular step arrays. The latter correspond to the Au(233) structure, while the former resemble the Au(788) surface, with an average terrace width of 3.83 nm. The spatial extent of the domains is rather large, with a refaceting period in the order of 200 nm.

For {100}-facing vicinals, high miscut angles as in, *e.g.*, the Au(322) and Au(755) surfaces, result in a stable array of equidistant steps. The terraces, with their respective widths of 1.17 nm and 1.42 nm, are too narrow to accommodate a discommensuration line. Hence, these surfaces are unreconstructed and exhibit steps with unaltered {100} microfacets. For lower miscut angles, the FK model predicts a dependence of the surface energy on the step width, encouraging the presence of ‘magic’ terrace widths [193]. Among these, the stable configuration with the narrowest steps is the Au(988) surface, which consists of equidistant terraces with a width of 4.16 nm. On each of the terraces, a single discommensuration line runs parallel to the step, with the inward portion of the terrace retaining fcc stacking, and the outward portion having its topmost atomic layer reconstructed into hcp stacking. As a consequence, the steps themselves exhibit {111} microfacets throughout. Au(17·16·16) is expected to be the next stable configuration, with a more complex ‘super-kink’ reconstruction, and a nearly complete transformation of the steps into {111} microfacets [202].

In contrast to the high angle {100} type vicinals whose equilibrium shape stems from an interplay of various factors, the structure of the lower angle vicinals is strongly influenced by the reconstruction energy. On them, small changes in terrace width have a much more pronounced effect on the energetic favorability. As a result, the terrace width distribution of these samples is narrower than in the nonreconstructed high angle vicinals, or, *e.g.*, in vicinals of nonreconstructing surfaces like Cu(111). On miscut angles that do not correspond to a ‘magic’ terrace width, the surface refacets into sequences of different ‘magic’ terraces rather than deviating in terrace width. The Au(877) and Au(433) surfaces, introduced below, are examples of this.

Vicinal surfaces as pre-patterned substrates. The weak periodic corrugation of the reconstructed Au(111) surface and the adsorbate lattice have not demonstrated an interaction. To increase the strength of the substrate patterning, substituting the substrate with a vicinal surfaces appears like a natural choice. The structural diversity of Au vicinals provides a wide choice of substrate preordering:

- narrow unreconstructed or wide reconstructed terraces,
- one- or two-dimensional periodic superstructures,
- steps with pure {111}, {100} or periodically alternating microfacets,
- equidistant or refaceted step arrays.

These aspects may influence the arrangement of certain adsorbates. The {111} microfacet steps have been found to be preferred adsorption sites for single rows of Fe atoms, allowing the self-assembly of a regular nanowire array [209]. For certain types of adsorbates that are sensitive to the variation of the substrate top layer stacking, the terrace reconstruction in low miscut angle vicinals may result in modulation of the adsorption characteristics parallel to the steps. In this context, Co atoms were found to adsorb on the cold Au(788) surface in a well-ordered two-dimensional dot array [192]. The same has been observed for the CoPc [129] and C_{60} [131] molecules, with especially the latter showing a strongly selective adsorption to fcc sites and consequently, a very regular two-dimensional lattice of molecular islands.

7.2 Substrate properties

The Au(788) or $16(111) \times (111)$ surface is a vicinal surface to Au(111). It is misoriented by an angle of 3.5° toward the $[\bar{2}11]$ azimuth. Its structure consists of a regular array of terraces with a single preferred width, separated by monatomic steps with (111) microfacets. The nominal terrace width of the surface is $15\frac{1}{3}$ atomic row distances, or 3.83 nm. A real Au(788) crystal displays a statistical distribution of terrace widths, roughly centered around this nominal width [176]. This distribution is remarkably sharper than, *e.g.*, that of vicinals to the non-reconstructing Cu(111) surface [78].

The surface undergoes a stacking fault reconstruction, similar to the chevron reconstruction on the Au(111) base surface. On each terrace, pairs of discommensuration lines run perpendicular to the steps. Between the two ridges, the stacking of the top atomic layer is of hcp type, while on the outside, the fcc bulk stacking is continued. On the ridges, the atomic positions gradually transition between normal and faulted stacking. As in Au(111), transition atoms are slightly displaced into direction of the surface normal. The discommensuration ridges are not exactly parallel, but follow a V shape, pointing toward the ascending step, the hcp region being wider on the outward part of the terrace, close to the descending step. The reconstruction period in the $[01\bar{1}]$ direction, parallel to the steps, is approximately 7.2 nm. This is larger than the corresponding distance of

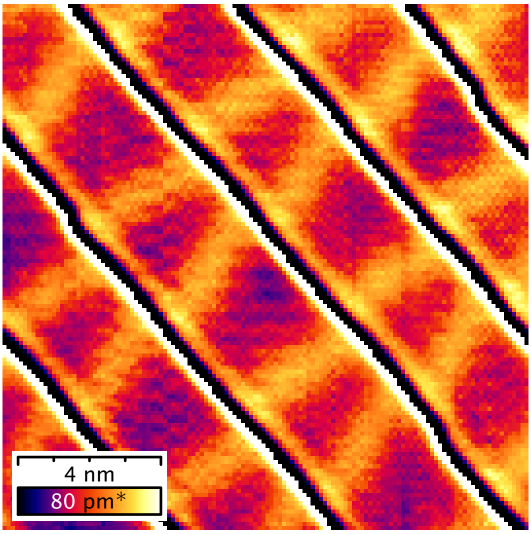

Figure 7.1 – Reconstruction of the Au(788) surface, $(14.7\ \mathrm{nm})^2$ topograph, $V = +1$ V, $I =$ 84 pA, with pairs of discommensuration lines running nearly perpendicularly to the steps, separating fcc- and hcp-stacked surface regions. The surface has a nominal terrace width of 3.83 nm, and a reconstruction period of ≈ 7.2 nm along the $[01\bar{1}]$ direction.

(6.5 ± 0.2) nm on the unstepped Au(111) surface. The reduced reconstruction density is due to the partial surface stress relief provided by the steps.

7.3 Experimental findings: topography

The experiment was performed on a Au(788) sample kindly provided by J. E. Ortega, UPV San Sebastián, Spain. After introduction into the preparation vacuum, the sample was cleaned by alternating cycles of ion bombardment and annealing. After the final annealing cycle, the heating power was gradually reduced to zero. The sample was then allowed to cool to room temperature. For details of the substrate preparation technique refer to section 1.7. PTCDA was evaporated from a tantalum button heater cell, as described in section 6.1. Evaporation was monitored by the quartz microbalance. Upon detection of a stable evaporation rate at $I = 1.3$ A, the sample surface was exposed to the beam for $t = 10$ s. Subsequently, the sample was transferred into the analysis chamber and cooled down to $T = 7$ K.

Overview scans of the prepared surface show a submonolayer PTCDA coverage. Within the accuracy of the rate determination, the sticking coefficient of PTCDA on Au(788) appears to be of the same order as that on the unstepped Au(111) surface. The images display PTCDA coalesced into compact islands. A sample image is reproduced in fig. 7.2. The shape of the PTCDA islands is largely irregular, as is their size distribution. However, the molecular layer frequently covers terraces across their whole width, the island boundaries coinciding with step edges, especially ascending ones. Due to this, islands with near-rectangular shapes or straight boundaries along the step edge direction are frequent.

Within the islands, the molecules arrange in three different phases, two of which are similar to the two phases observed on Au(111) and discussed in chapter 6. The

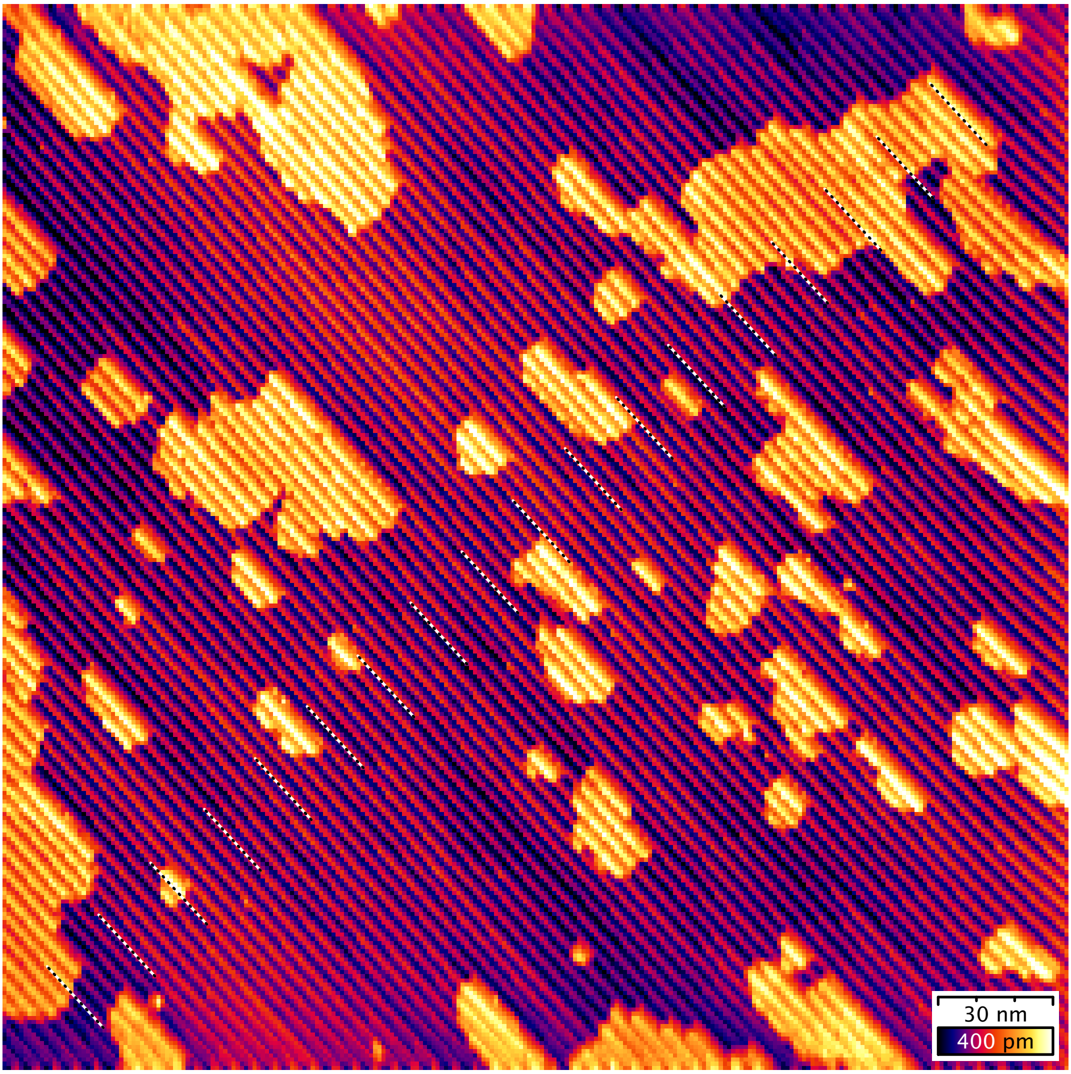

Figure 7.2 – Overview of PTCDA islands on Au(788). (278 nm)^2 topograph, $V = +1$ V, $I =$ 100 pA. The molecules form compact islands of various sizes that may span several terraces. Often, the island shape is guided by ascending steps. Large scale topographs are used to verify the lateral calibration, by comparing the average terrace widths with their nominal values (Here, helper lines mark every fifth terrace).

individual phases appear to freely cross the substrate steps. However, the possible orientations of the adsorbate lattice are influenced by the steps.

The first phase is a herringbone-like pattern similar to the arrangement of PTCDA within the (201) planes of the molecule crystal, and the herringbone phase on Au(111). The observed lattice constants are $a = (1.79 \pm 0.09)$ nm and $b = (1.12 \pm 0.07)$ nm. The second phase resembles the square phase also seen on Au(111). On Au(788), the measured lattice constants are $a = b = (1.44 \pm 0.12)$ nm.

A third observed phase, with a square unit cell and a general appearance resembling that of woven fabric, is designated the *mesh* phase. The two long ends of each molecule point toward the center of the adjacent molecules. The unit cell differs from the aforementioned square phase in its axial symmetry, while the square phase can appear in two equivalent, mirrored orientations, only bearing a fourfold rotational symmetry.

The boundary between mesh and square phases is marked by a gradual transition in molecule position. Mesh regions may provide the interface between enantiomorphic square phase regions. An example for this can be seen in fig. 7.3.

As with PTCDA on Au(111), the stacking fault reconstruction is conserved below the molecular layer. Due to the presence of the step array and the reconstruction lines, the orientations of the adsorbate unit cell can be directly determined from the topographs.

7.4 Experimental findings: electronic structure

Similar to the observations on an Au(111) substrate, a voltage dependence of the intramolecular contrast of the adsorbed PTCDA molecules is revealed in topography scans. This is reproduced for a sample region in fig. 7.4.

At sample voltages below a specific transition range, the molecules are imaged as prolonged shapes, lacking submolecular structure. At voltages above that range, the molecules appear as rather compact shapes, with the addition of an intramolecular substructure. This substructure consists of an elongated area of higher local electronic density along the long axis of the molecule. Additionally, on either side of the molecule, on a line parallel to its long axis, an pair of lobes is detected. In combination, these features result in a roughly hexagonal outline of the molecules. Averaged close-ups of the different molecular appearances are given in fig. 7.5

In both observed phases, the contrast transition encompasses a voltage range of approximately 200 mV. However, its energetic position varies with the PTCDA adsorption phase or, more specifically, with the local coordination of the individual examined molecule. Also, the transition is readily apparent in $\mathrm{d}I/\mathrm{d}V$ maps, reproduced in fig. 7.4, where at their respective transition voltages, the molecules appear in inverted contrast, as elongated outlines. This is seen at 600 mV for square domain molecules, at 1000...1200 mV for herringbone domain molecules, and at an intermediate voltage of 800...1000 mV for molecules at the domain boundary line. Also, single molecules right on top of a substrate step may appear bright at a lower voltage than those of the surrounding domain, such as some of the square phase molecules in the 400 mV image.

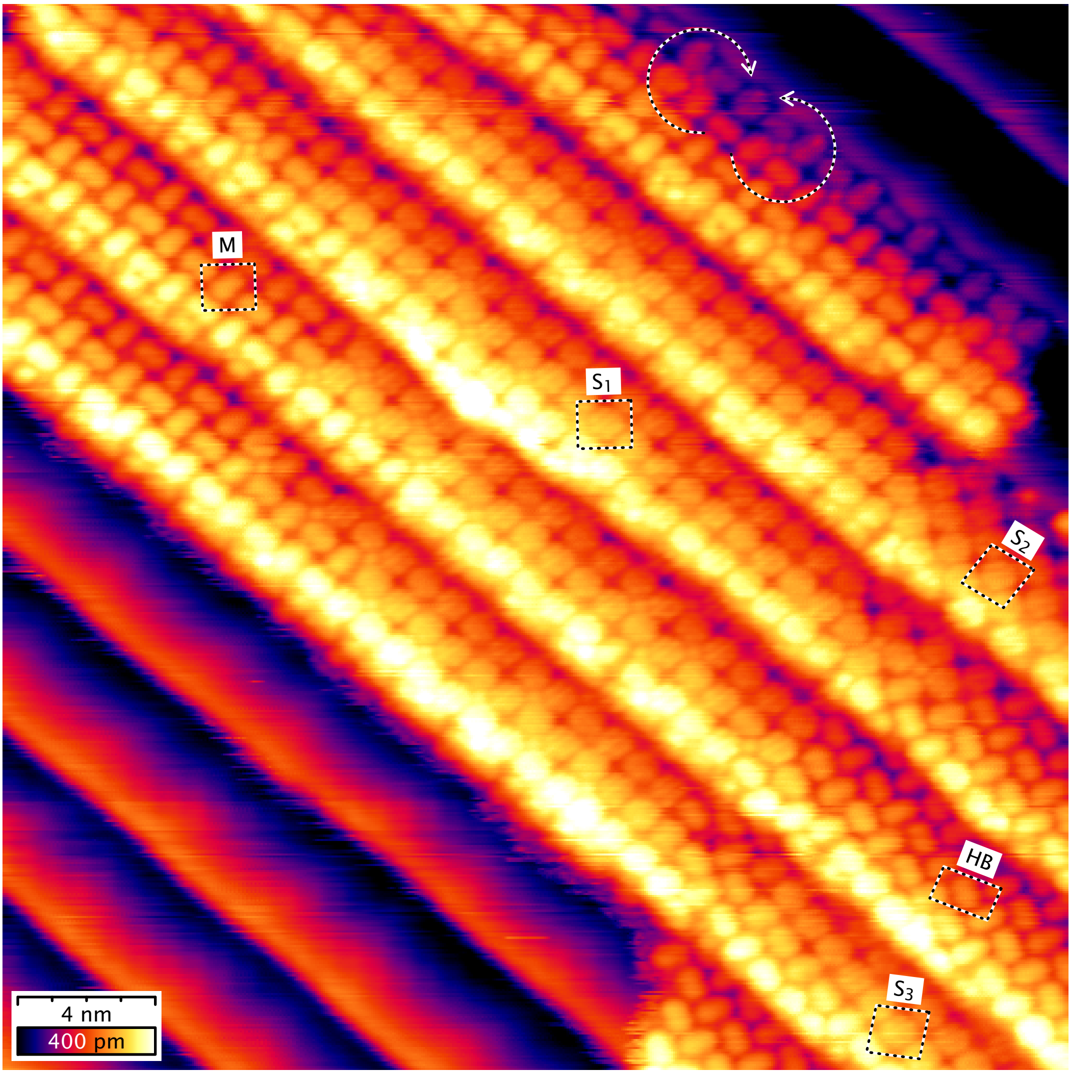

Figure 7.3 – Multiple phases within a PTCDA island on Au(788). (31 nm)^2 topograph, V = 750 mV, I = 12 pA. The island contains a herringbone (HB) domain, square phase regions with three different orientations ($S_1 \ldots S_3$), and a mesh region (M). The area also shows a transition between two enantiomorphic square regions, with a narrow mesh region providing the interface. The arrows mark the distinctive windmill arrangement of four square phase molecules, in both clockwise and counterclockwise orientation.

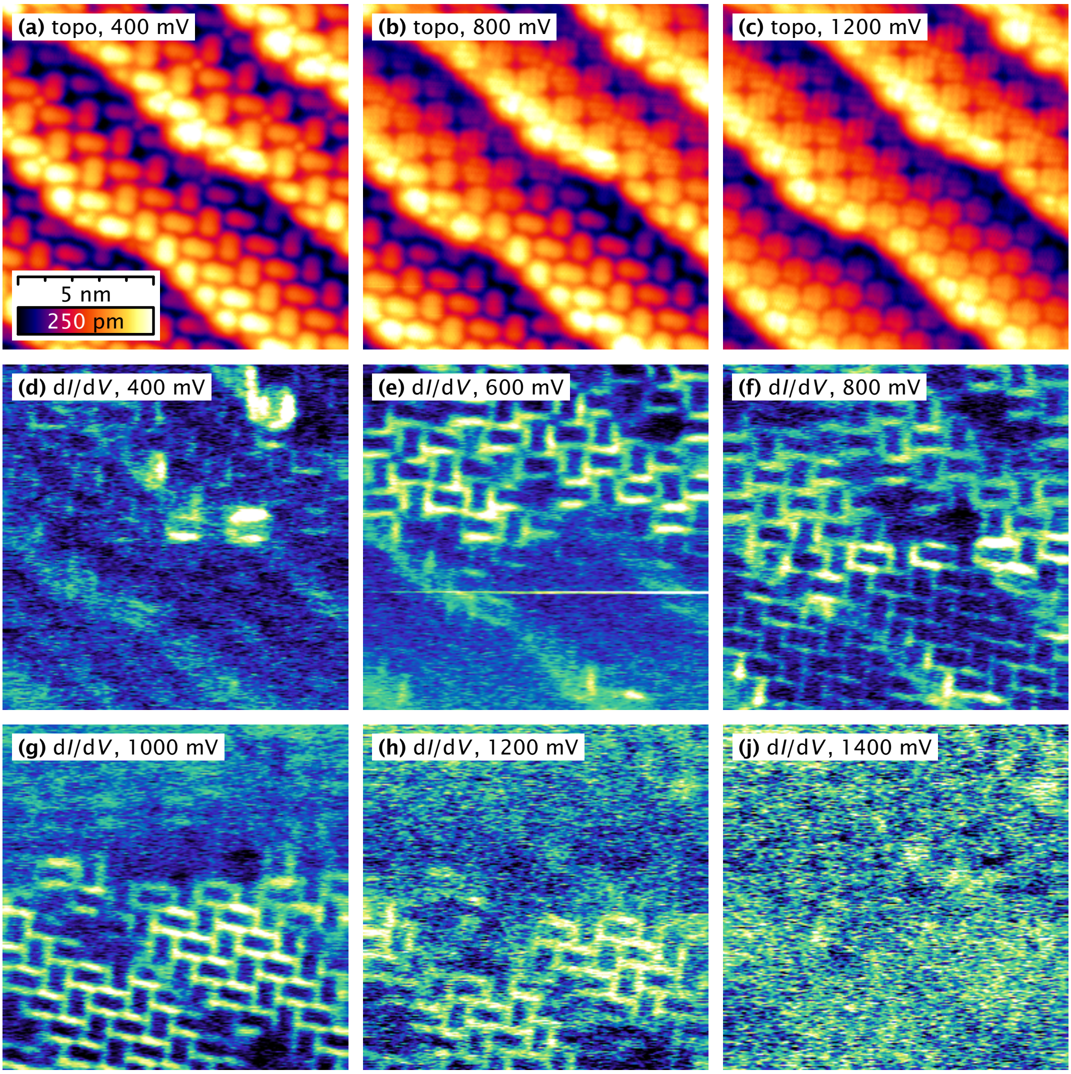

Figure 7.4 – Voltage dependence in PTCDA/Au(788). (12.7 nm)^2 maps, $I = 200$ pA. The imaged area shows a fully covered surface region, comprising both a square (top half) and a herringbone (bottom half) adsorption domain. **(a–c)** A series of z maps shows the evolution of the apparent molecular shape with increasing bias voltage. At ≤ 600 mV, the molecules in both domains appear as elongated shapes. In the range of 800…1000 mV, the square phase molecules have assumed a wider, compact shape with a visible internal lobe structure. At ≥ 1200 mV, the molecules in the herringbone phase follow suit. **(d–j)** The evolution of simultaneously acquired dI/dV maps shows an emphasis on the outlines of those molecules that undergo this contrast transition. At 600 mV, the outlines of the square phase molecules are seen in inverted contrast. At 800 mV, the molecules in the domain boundary line appear brightest. At 1000 mV, and in lesser intensity at 1200 mV, the molecules in the herringbone domain are visible as outlines.

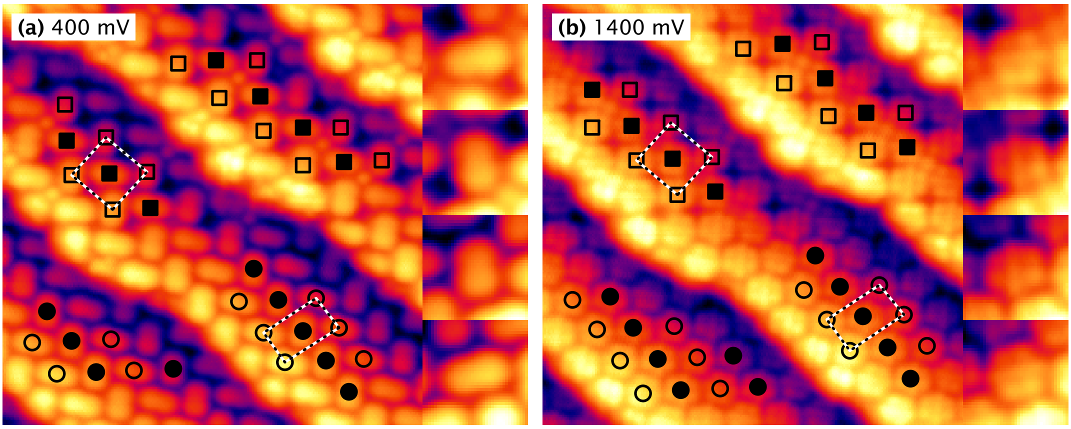

Figure 7.5 – Intramolecular contrast transition in PTCDA/Au(788). The lattice unit cells are shown for the two phases. Vicinities of marked molecules in herringbone (circles) and square (squares) phases have been averaged. At lower sample bias, the average shape of the molecules is elongated and featureless, while at high sample bias, a solid central crossbar and four outer lobes are observed. Notably, the latter show axial symmetry in the herringbone phase, and a shear distortion toward the hub positions in the square phase.

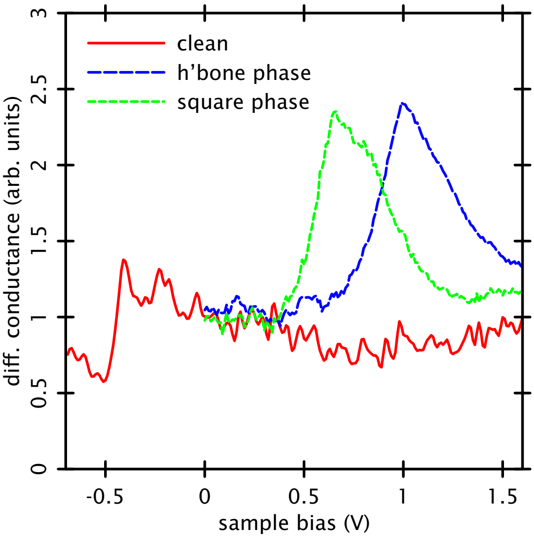

Figure 7.6 – Differential conductance spectra of PTCDA/Au(788), acquired on different sample locations. Constant height mode, feedback loop cut at $V = +850$ mV, $I = 20$ pA. Red line: average of 20 spectra acquired on an adsorbate-free Au(788) terrace, averaged over both fcc and hcp regions. Blue line: average of spectra acquired on 10 sites on herringbone phase PTCDA. Green line: average of spectra acquired at 9 sites on square phase PTCDA.

The transition is reflected in dI/dV spectroscopy. Fig. 7.6 shows averaged constant height dI/dV spectra acquired on different locations of the PTCDA/Au(788) sample. The spectra contain a characteristic structure corresponding to the aforementioned contrast transition. For spectra taken within the square phase (red solid line), the feature has a main peak at 0.66 ± 0.01 V. The main peak for the herringbone phase PTCDA (green dashed line) has an energy of 1.02 ± 0.01 V.

7.5 Theoretical model

In the preceding sections it has been demonstrated that in PTCDA on both Au(111) and Au(788), a molecular contrast transition is detected that coincides with an increased local density of states. The bias voltage at which this transition takes place varies with the adsorption phase. In both systems, at low bias voltages molecules appear devoid of internal structure, while at higher bias voltages they are imaged as roughly hexagonally-shaped objects, with a central crossbar and two lobes on each side. At intermediate voltages, some of the molecules reveal an internal structure whilst others do not, depending on the adsorption phase.

To complement the experimental data and to identify the electronic origin of this intramolecular structure, DFT calculations were kindly provided by Riccardo Rurali and Nicolás Lorente, with the *SIESTA* package, using a double-ζ basis set plus polarization functions for the valence electrons [5]. The Generalized Gradient Approximation was used for the exchange-correlation functional [183]. The calculations have been done for a system comprising a molecular layer above a Au(111) substrate slab. For the square phase a commensurate layer of 1.4814×1.5395 nm^2 was chosen. For the herringbone layer an incommensurate geometry of 1.900×1.185 nm^2 was used. It was established that the results are robust against compressions of the substrate geometry by $< 5\%$ [147]. The height of the molecular layer above the slab reflects the amount of hybridization with the substrate. The final choice for the substrate–layer distance was 350 pm. At shorter distances, the molecular hybridization is believed to be overestimated [147].

The raw calculations reveal a density of states with a nodal plane along the long axis of the molecule. This has also been reported in a previous room temperature STM study of the PTCDA/Au(111) system [172]. This nodal plane is not seen in the present experiment. This absence, and the ability to spatially resolve internal molecular contrast in general, may be influenced by tip status. Tips with a molecule adsorbed at the apex may exhibit a greatly enhanced resolution, in comparison to a clean metal tip [196]. Since for the experiments, the tips were prepared by controlled indentations into uncovered substrate regions, with the sharpness of the Shockley surface state onset in dI/dV spectroscopy used as a quality indicator, it can be assumed that the tip apex is gold-covered, and thus, insensitive to the presence of the aforementioned nodal plane.

The molecular orbital shift, however, is reproduced by the DFT calculation. Fig. 7.7 shows the calculated densities of states for molecular layers in both phases, at the selected substrate–layer distance. In each phase, above the Fermi level a single peak appears that is attributed to the LUMO. While DFT typically does not reproduce the absolute peak positions [147], the observation of a relative shift in the two systems remains relevant. In this particular case, the square phase shows a peak centered at 0.25 V, while the herringbone phase exhibits one at a higher energy of 0.6 V. Hence, both direction and magnitude of the shift are reproduced well from the experiment.

The hydrogen bonds between adjacent molecules were identified as a main channel of intermolecular interaction. In both structures, the anhydride groups of the long ends

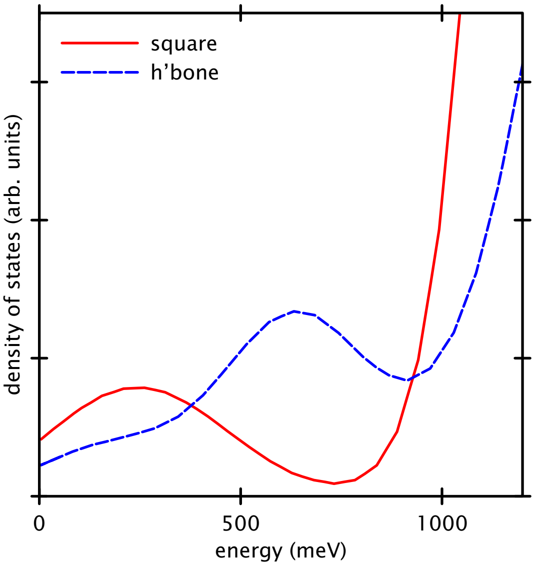

Figure 7.7 – Calculated spectra for PTCDA/Au(111), for herringbone and square phases. Calculations were done as described in the text, with molecules arranged in a grid of 1.185×1.900 nm^2 and 1.4815×1.5395 nm^2, respectively, 350 pm above the surface slab.

of a molecule, comprising 3 oxygen atoms each, lie opposite to the hydrogen atoms (4 each) along the sides of neighboring molecules. This leads to a total of 24 interacting H–O pairs. The calculations provide an average H–O distance of 205 pm for the square phase, and 237 pm for the herringbone phase. The stronger bonding in the square phase results in lower-lying orbitals.

7.6 Summary and conclusions

On the vicinal Au(788), a submonolayer PTCDA coverage arranges in the form of two-dimensional islands. These consist of domains with regularly arranged molecules. The two main adsorbate lattice types seen are a herringbone pattern with a rectangular unit cell, similar to layers in the bulk PTCDA crystal, and a less dense chiral, windmill-like arrangement with a square unit cell. Low-order integer adsorbate lattice vectors tend to align with the substrate steps. Single islands can contain multiple domains with differing structures and alignments. All of this has previously been observed in Au(111), indicating a weak influence of the vicinal surface.

In STM topographs, the molecules undergo a contrast transition from an elongated to a compact shape, at the energy where the LUMO+1 starts to contribute to the tunneling current. This energy is lower for molecules in the square phase. The transition is accompanied by an emphasized contrast of molecular outlines in $\mathrm{d}I/\mathrm{d}V$ maps. The main spectral features in $\mathrm{d}I/\mathrm{d}V$ point spectroscopy, corresponding to LUMO and LUMO+1, are found to shift by ≈ 350 mV between the two phases. Molecules at phase boundaries show an intermediate shift. A theoretical calculation indicates that the hydrogen bonds, providing the main interaction between molecules, are stronger in square phase molecules, leading to the observed orbital shift.

Chapter 8

PTCDA on Au(433) and Au(877)

Two further experiments with PTCDA on surfaces vicinal to Au(111) have been performed. The substrates used were Au(433) and Au(877). In these, the normal vector of the miscut plane deviates toward $[2\bar{1}\bar{1}]$, the opposite direction to that in Au(788). The nominal (unreconstructed) steps on the surface provide {100} microfacets. Both surfaces are not among the stable vicinals reported in ref. [202], so a faceted morphology is expected.

In Au(433), the surface normal deviates by an angle of 8.05° toward $[2\bar{1}\bar{1}]$, leading to a nominal terrace width of 1.665 nm. Literature data on the morphology of the surface describe a faceting with a period of 11.5 nm, comprising a phase of ≈ 6 unreconstructed terraces, with an average width of 1.5 nm, plus one reconstructed terrace of 3.8 nm width [201]. In Au(877) the miscut angle of 3.68° toward $[2\bar{1}\bar{1}]$ yields a nominal terrace width of 3.664 nm. For comparison, the predicted 'magic' vicinal surface Au(988) has a slightly smaller miscut angle of 3.24° [202].

8.1 Faceting model

The atomic structure of the surfaces can be modeled from the nominal geometry. The approximate terrace widths, taken from the STM images, are matched to the known values of 'magic' vicinals. The ratio of terrace types is selected to maintain the overall miscut angles.

In Au(433), the wide terraces are matched best to a nominally unreconstructed terrace of $\frac{47}{3}d_\mathrm{R} = 3.91$ nm, corresponding to Au(17·15·15), which the reconstruction contracts to $\frac{45}{3}d_\mathrm{R} = 3.75$ nm. From the gamut of 'magic' vicinals given in ref. [202], the narrow terraces are identified with Au(755), with a nominal width of $\frac{17}{3}d_\mathrm{R} = 1.42$ nm. For the narrow terrace directly adjacent to the contracted wider terrace, the closest possible match is $\frac{16}{3}d_\mathrm{R} = 1.33$ nm. Using these nominal widths, to attain the overall miscut angle of 8.05°, the ratio of narrow to wide terraces is expected to be $8:1$. This leads to a superperiod of

$$\frac{45 + 16 + 7 \times 17}{3} \cdot \frac{d_\mathrm{R}}{\cos(8.05^\circ)} = 15.14 \text{ nm.} \tag{8.1}$$

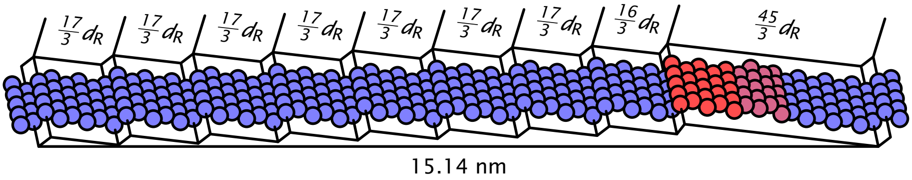

Figure 8.1 – Faceting model for the Au(433) surface in axonometric projection, showing the sequence of a single wider reconstructed terrace and a region of 8 narrower unreconstructed terraces, modeled after those of the unfaceted Au(755) surface. For illustrative purposes, the corrugation amplitude of the discommensuration line has been amplified. Descending steps of the large terraces are of $\{111\}$ type, all other steps are of $\{100\}$ type.

Both of these slightly exceed observed values of $\approx 6:1$ and 11.5 nm, respectively, possibly due to deviations in miscut angle. The faceting model is represented in fig. 8.1.

The Au(877) surface structure is found to comprise a wider terrace type resembling the stable configuration of Au(988), containing a single discommensuration line along the $[01\bar{1}]$ direction, parallel to the steps, and a narrower unreconstructed terrace type similar to those seen in the Au(755) and Au(322) surfaces. The miscut direction corresponds to a base $\{100\}$ step type, and this is maintained in the descending steps of narrower terraces. In contrast, the outward portions of the wider terraces are reconstructed, causing their descending steps to bear $\{111\}$ microfacets. To obtain the global miscut angle of the Au(877) surface from combining facets corresponding to the step types of Au(988) (3.24°, 4.16 nm) and Au(755) (9.45°, 1.42 nm), they need to be present in an overall ratio of $9:2$, *i.e.*, one narrow terrace for every $4\ldots5$ wide reconstructed terraces.

8.2 Results on Au(433)

Initially, topographs of the clean substrate are acquired. A typical image comprising several periods of the refaceting is shown in fig. 8.2a, indicating a satisfactory surface condition. The large terraces exhibit a ridge along their length, with a corrugation of ≈ 12 pm. This is not immediately visible in topographic maps, due to the large overall z range involved, but can be made visible in averaged z linescans perpendicular to the steps, such as in fig. 8.2b.

In the next step, PTCDA is evaporated onto the clean surface at room temperature, from a crucible that is gradually heated until the quartz balance registers a deposition rate, at a heating current of 1.3 A. The cleaned sample is then exposed to the nozzle for a given period of time, transferred to the analysis chamber, and cooled down to 9 K. Subsequently, constant current overview topographs are acquired to assess the coverage. A typical surface area is reproduced in fig. 8.3a. The image shows two general adsorption processes:

Firstly, molecules are adsorbed in rows along both sides of the wide terraces. Their apparent shape suggests an orientation perpendicular to the step edge direction. On

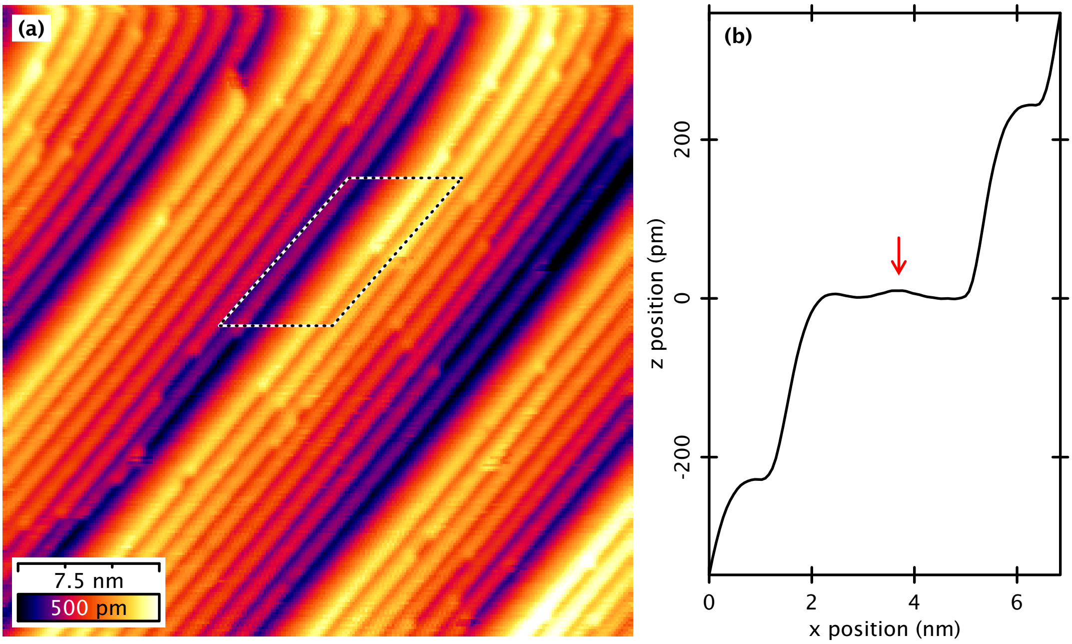

Figure 8.2 – Refaceted Au(433) surface. **(a)** (33 nm)^2 topograph, $V = +500$ mV, $I = 150$ pA. The surface refacets into sequences of one wide and several narrow terraces. **(b)** Averaged line cross-section across marked region, x axis corrected for shear. One wide terrace plus the two adjacent narrow terraces are shown. The wide terrace contains a bump with a corrugation of ≈ 12 pm (marked with an arrow), which is attributed to an fcc–hcp discommensuration line.

both sides the molecules appear to adsorb across the substrate step, with one end of the molecule on the wide terrace, while the other end is situated on the adjacent narrow terrace.

Additionally, small two-dimensional arrangements of molecules are found both on the narrow-stepped facets and across the wide terraces. The molecules covering the stepped facets form areas of random coordination as well as visually compressed herringbone and square regions. Across the terraces, the molecules are arranged in a largely disordered manner, with occasional areas of square-phase-like coordination. The placement of the individual molecules appears subordinate to the regular arrangement of the surrounding molecular rows, indicating a stronger adsorption of the latter.

Another sample is prepared identically, but after PTCDA deposition and prior to transfer and cooldown, the sample is annealed at a temperature of 480 K, for a short period of 13 s. This preparation leads to a surface structure as reproduced in fig. 8.3b. In this system, molecules remain neither on the large terrace nor across the bundles of small terraces. However, there are still chains of molecules along the two steps flanking the large terrace.

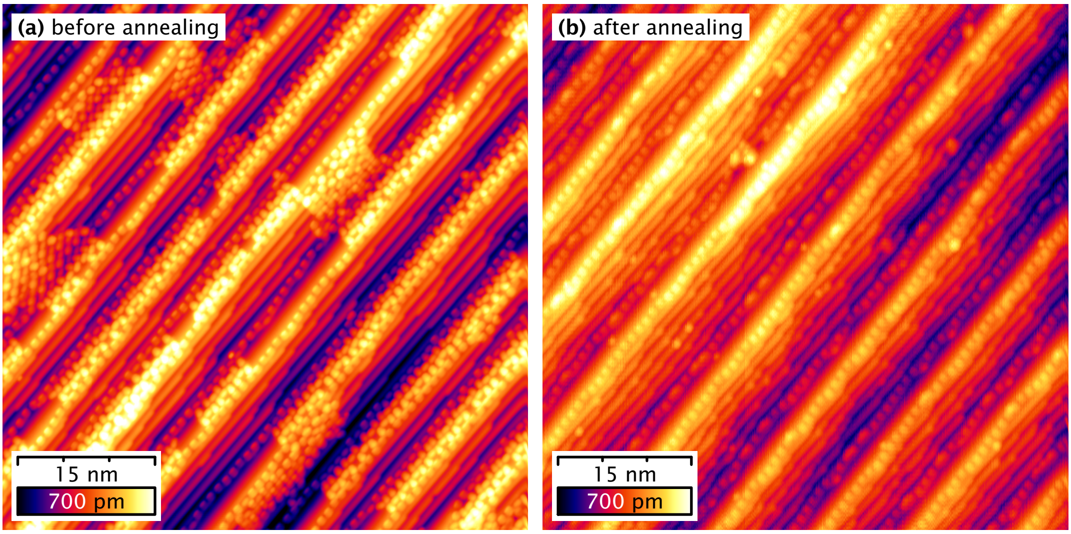

Figure 8.3 – PTCDA/Au(433) before and after annealing. **(a)** After evaporation. $(57.4\ \text{nm})^2$ topograph, $V = -100$ mV, $I = 260$ pA. The steps adjacent to the large terraces are found to be fully decorated by regular chains of PTCDA molecules. The terraces themselves are partly covered by PTCDA in an irregular two-dimensional fashion. The coverage on the narrow terrace bundles is lower, with occasional compact regions of molecules, in both rectangular and amorphous arrangements. **(b)** After annealing the prepared surface, at 480 K for 13 s. $(59.1\ \text{nm})^2$ topograph, $V = +300$ mV, $I = 200$ pA. No PTCDA islands on the terraces are observed, with only occasional molecules remaining on the terrace bundles. The molecular chains adjacent to the terraces appear unaffected by the annealing process, indicating a stronger binding to the substrate.

8.3 Results on Au(877)

On this substrate, three different preparations were made. In all of them, the Au(877) sample was cleaned by cycles of sputtering and annealing at room temperature in the standard fashion, with gradual cooldown after the last cycle, then exposed to the PTCDA evaporation cell at a heating current of 1.3 A. For the low coverage preparation, the exposure time was 3 s. The high submonolayer coverage was obtained by a 10 s evaporation. Finally, to ascertain the effect of annealing, after 15 s of exposure, the sample was heated for 15 minutes, to ≈ 480 K (filament current 2.4 A). For the high exposure preparation, a coexistence of PTCDA islands in both herringbone and square arrangement is observed, as seen in fig. 8.4. These match the structures previously described for PTCDA/Au(111) and PTCDA/Au(788). After annealing, there were still islands present, however, only the square arrangement could be readily found. This is illustrated in fig. 8.5.

For the low coverage preparation, however, the surface outlook was found to be markedly different, as seen in fig. 8.6. Here, the few adsorbed molecules adsorbed as chains at the descending steps of the wide (*i.e.*, reconstructed) terraces, with the

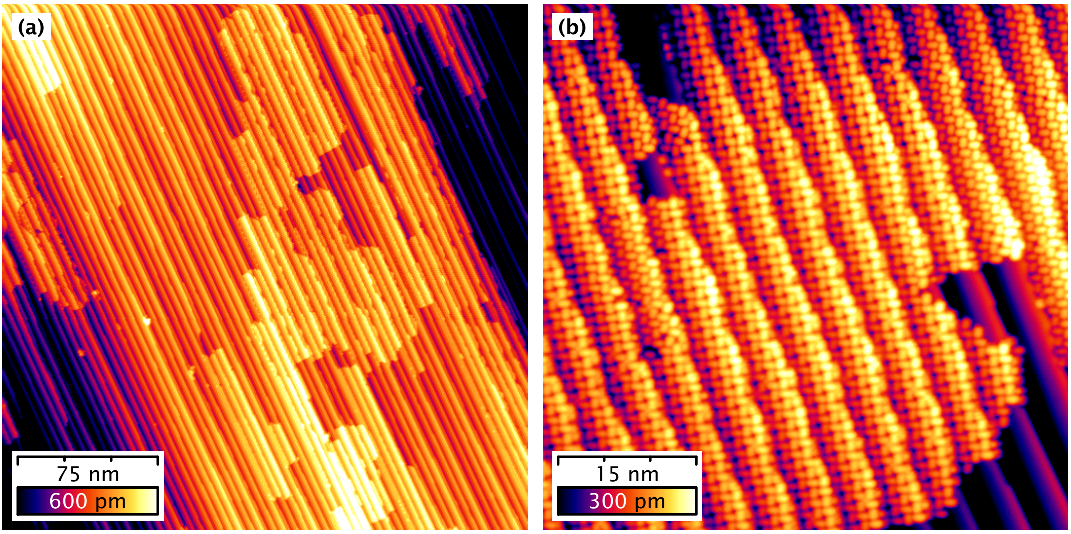

Figure 8.4 – Island formation in PTCDA/Au(877), high submonolayer coverage. **(a)** (281 nm)^2 overview topograph, $V = +500$ mV, $I = 200$ pA, showing a submonolayer coverage of ≈ 0.2 ML. **(b)** (57 nm)^2 topograph, $V = +500$ mV, $I = 400$ pA. In this region, the substrate is refaceted to only one terrace type. The adsorbate shows the coexistence of large-scale ordered square and herringbone domains.

molecular long axis oriented perpendicular to the step. One end of the molecule was located on the wide terrace, and the other on the lower adjacent terrace. The type of the latter seemed not to influence the adsorption; It could be either of the wide or narrow variety. These chains are similar to those observed in the PTCDA/Au(433) system. Specifically, again the microfacet of the descending step, which is {111} for the wide reconstructed Au(988)-like terraces and {100} for the narrower, unreconstructed Au(755)-like terraces, is found to have a decisive influence on adsorption desirability, with only the former showing PTCDA decoration.

8.4 Summary and conclusions

In summary, two different Au(111) vicinals with {100} nominal step type have been used as substrates for the adsorption of PTCDA. Both surfaces do not correspond to 'magic' miscut angles, resulting in refaceted morphologies, alternating between narrower and wider terraces. The latter are reconstructed by a uniaxial compression similar to the Au(111) chevron reconstruction, thereby changing the outward steps of the wide terraces to a {111} microfacet.

These changed microfacets were found to be preferred sites for the initial adsorption of PTCDA, with the molecules forming chains by docking, side-by-side, onto the step from the lower-hand terrace. At higher coverages, on Au(877), PTCDA forms the known

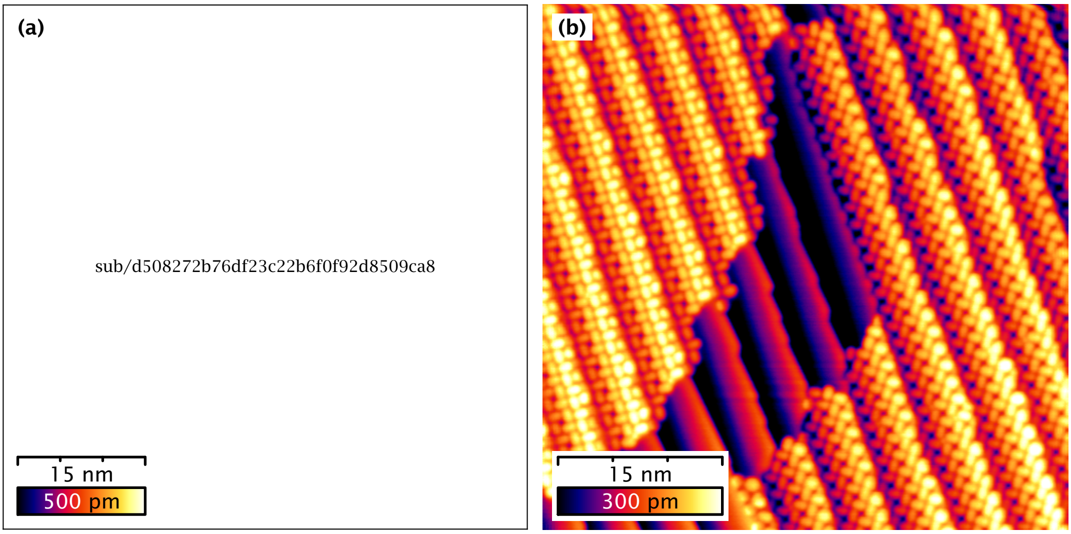

Figure 8.5 – PTCDA/Au(877) after annealing for 15 minutes. 15 s evaporation (see text). **(a)** (62 nm)^2 topograph, $V = +460$ mV, $I = 180$ pA. The adsorbate is found to have formed compact islands, Square arrangement of the molecules is strongly preferred. Both outer boundaries and lattice alignment largely coincide with the substrate steps. These islands may span both wide and narrow steps. **(b)** (48 nm)^2 topograph, $V = +460$ mV, $I = 180$ pA. Two islands in square arrangement are shown, with different lattice orientation relative to the substrate step direction. In both regions, the adsorbate geometry strongly locks to the substrate, yielding a very regular lattice.

square and herringbone phases. Annealing appears to increase the alignment of the adsorbate lattice to the substrate steps. Meanwhile, on the narrower terraces of Au(433), islands with a disordered arrangement are seen spanning the denser {100}-type step arrays. Annealing causes them to desorb, leaving only the more strongly bound chains at the {111} steps.

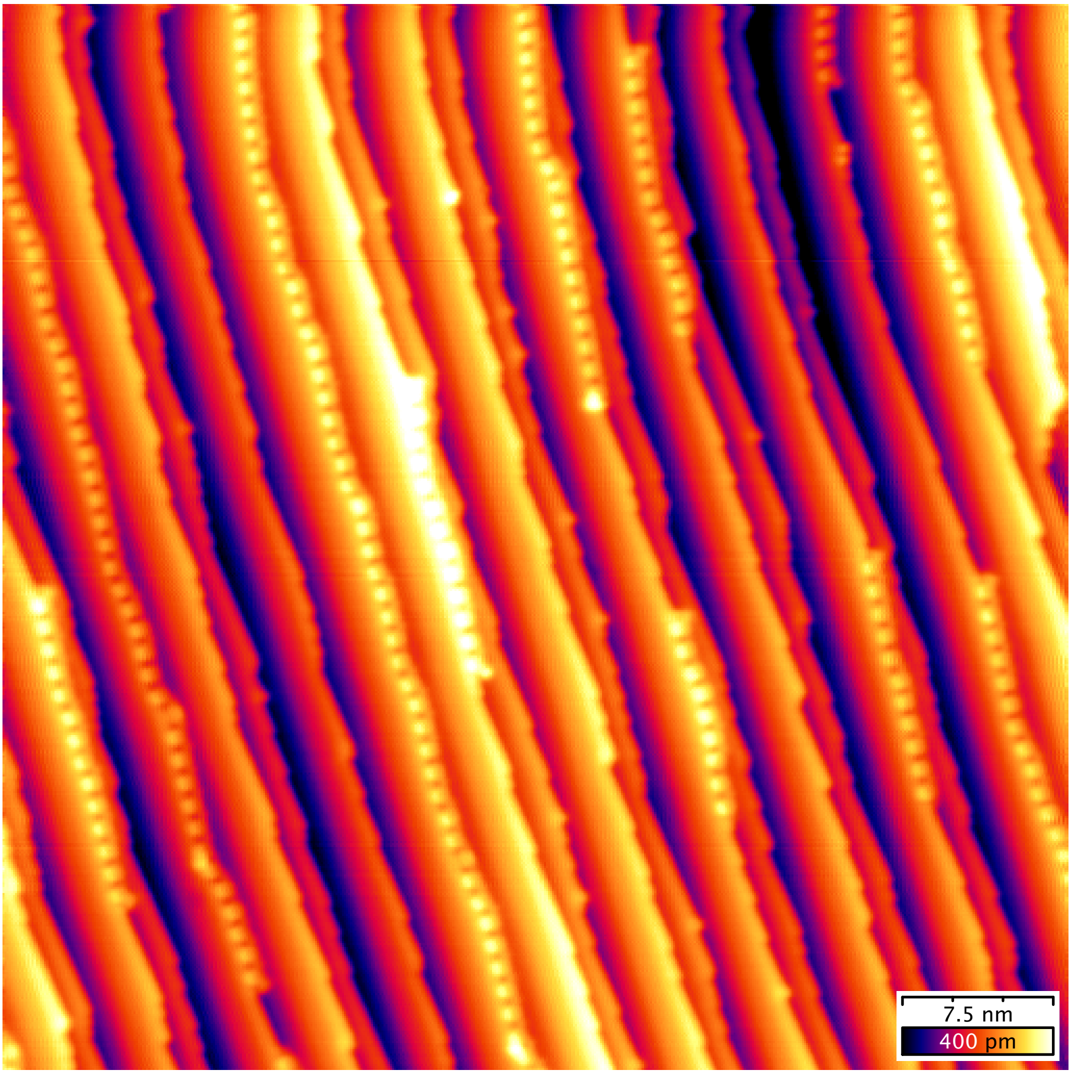

Figure 8.6 – Chain formation of low-coverage PTCDA/Au(877), 3 s evaporation (see text). (69 nm)^2 topograph, $V = +500$ mV, $I = 250$ pA. The imaged region comprises terraces of both wide and narrow types. PTCDA has been found to adsorb exclusively onto the descending steps of the wide terrace types, with the larger part of the molecule located on the lower neighboring terrace, independent on the type of the latter.

Chapter 9

PTCDA on niobium diselenide

A final PTCDA deposition experiment is done on a transition metal dichalcogenide substrate. The selected substrate is the 2H-$NbSe_2$ layered crystal, that bears a prominent electronic superstructure in the form of a charge density wave. As the spatial dimensions of this charge density wave are similar to the lattice constants of the known adsorbate configurations of PTCDA, the experiment aims at determining whether the substrate-adsorbate interaction influences the preferred adsorption geometry. In comparison with noble metals, STM experiments with these substrates face some technical obstacles, an account of which will be given below. This particular experiment was previously published as

> J. Kröger, H. Jensen, T. Jürgens, T. von Hofe, J. Kuntze, and R. Berndt, *Adsorption geometry of PTCDA on 2H-NbSe$_2$*, Appl. Phys. A **81** (6), 1285–1289 (2005), DOI: `10.1007/s00339-004-3039-6`.

9.1 Transition metal dichalcogenides

Compounds of chalcogens (specifically sulfur, selenium and tellurium) with transition metals have been found to demonstrate a rather complex behavior [107]. Depending on the specific choice of materials, stable homogeneous compounds with a variety of stoichiometric compositions exist. These include compounds with simple integral ratios, such as sesqui-, di-, and trichalcogenides. Beyond that, compounds with more complex non-integral ratios exist, such as derivatives of mono- and dichalcogenides with a specific surplus or deficit of metal atoms. Some of these exhibit superstructures in which the vacancies or additional atoms are more or less regularly distributed [87, 106].

The transition metal dichalcogenides (TMDC), despite their stoichiometric similarity, exhibit diverse structural and electrical characteristics [239]. These materials commonly form layered crystal structures, consisting of a stacking of planar sandwich-like slabs that each contain three atomic sheets. Of these, the top and bottom sheets consist of chalcogen atoms, while the metal atoms are situated in the center sheet. The atoms within a single slab are bound covalently. The interaction between neighboring slabs is of van der Waals type, and as such, rather weak. As a consequence, the equilibrium slab–slab separation is considerably larger than the distance between the atomic sheets.

Atoms within the layers are arranged in a planar hexagonal configuration. Each metal atom is equidistantly surrounded by six chalcogen atoms, either in trigonal prismatic or in octahedral coordination. Various different polytypes with different stacking sequences exist, determined by the relative lateral displacement of the individual layers. Depending on this, the polytypes may exhibit periods along the slab normal axis varying between 1 and 6 slabs [117]. As a notation for these structures, a set of prefixes introduced by Ramsdell [189] is generally used, consisting of a number designating the number of layers in the unit cell, a letter describing its symmetry, and an optional subscript to further disambiguate structure.

TMDC compounds, particularly the naturally occurring ore MoS_2, have seen large scientific and technical interest, including use as a dry lubricant [42], as a host for reversible intercalation in lithium-based batteries [28], and as a desulfurization catalyst in petrochemistry. The structural variety of transition metal chalcogenide compounds is accompanied by a plethora of electronic phenomena [83], *e.g.*, the evolution of semiconducting properties with decreasing film thickness, and transitions to superconducting and charge density wave (CDW) phases [178]. Quasi-one- or two-dimensional conductors, including some TMDC compounds, may undergo a Peierls transition [168]. Below a specific threshold temperature, materials with a partially filled conduction band may see a net energy gain by a small periodic modulation of the ion lattice that opens a band gap around the Fermi level [181]. A related fluctuation then appears in the conduction electron density, called a charge density wave (CDW). The CDW superlattice is frequently incommensurate to the ion lattice, pinning to impurities.

9.2 The niobium diselenide crystal

The 2H-$NbSe_2$ crystal consists of Se–Nb–Se slabs in trigonal prismatic coordination, with a stacking sequence of $AbA\ CbC$, where capital and small letters denote chalcogen and metal layers, respectively. The lattice periods are $a_1 = a_2 = 0.344$ nm in the layer plane, and $c = 1.254$ nm perpendicular to the layers, with one unit cell accommodating two slabs [156, 200]. Within a slab, the distance between the Nb layer and each adjoining Se layer is $d = 0.167$ nm [158].

In 2H-$NbSe_2$, a hexagonal CDW phase appears below a transition temperature of $T_0 = 33.5$ K. The lattice constants of the superlattice bear a slight temperature dependence, but remain incommensurate throughout. Below a temperature of $T_c = 7.2$ K, a superconducting phase appears that coexists with the CDW phase [88]. For comparison, in 2H-$TaSe_2$, a hexagonal CDW superlattice forms at a temperature below $T_0 = 122.3$ K, that is also initially incommensurate with the layered crystal lattice. However, below $T \approx 90$ K, the superlattice locks into commensurate registry with the substrate in a first-order transition [10, 169].

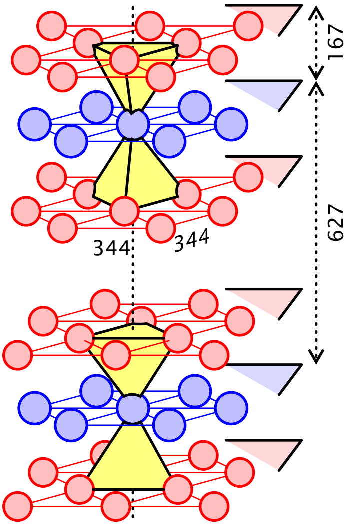

Figure 9.1 – Structure model of 2H–NbSe$_2$, showing the two slabs (six layers) comprising the unit cell. The stacking sequence is *AbA CbC*. Nb layers shown in blue, Se layers in red. Each Nb atom is surrounded by six nearest Se atoms in trigonal prismatic coordination (marked in yellow). Interslab, interlayer and interatomic distances are all given in pm.

9.3 Sample preparation

The 2H–NbSe$_2$ crystals, kindly provided by L. Kipp and W. Krüger, Christian-Albrechts-Universität Kiel, were grown by chemical vapor transport [204], using iodine as a transport agent. The substrate surface is prepared by cleaving a single crystal in the preparation chamber, at room temperature under ultra-high vacuum conditions ($p \leq 10^{-7}$ Pa). For this, a suitable single crystal piece is glued on a sample holder using conducting epoxy resin. Care must be taken that, while the electrical contact needs to be sufficient, any mounds of resin next to the crystal be lower than the crystal itself. The glued sample is then cured in an oven at 120°C for several hours. After this, a rectangular metal lever is glued perpendicularly on top of the crystal with epoxy resin, taking care that no direct contact is made between the resin and the sample holder or the first layer of glue. The finished setup is then cured again, as above.

After curing and cooling down, the sample holder is inserted into the vacuum vessel. In the preparation chamber, the lever is pried off the sample holder using the wobble-stick. As the epoxy glue is stronger than the interlayer cohesion of the crystal, the crystal is cleaved, and some top layers of it stay attached to the lever. The rest of the crystal remains on the sample holder, where its surface is visually inspected for smoothness.

Evaporation of PTCDA onto the crystal surface was done from a button heater cell. The details of the evaporation procedure are described in section 6.1. Since initially, specifics of the adhesion of PTCDA on the 2H–NbSe$_2$ surface were unknown, the quartz balance could not be calibrated, and evaporation was done with a time of exposition to the molecular beam similar to those used in the Au(111) vicinal experiments. After this, the sample was transferred into the STM, where a sample temperature of ≈ 9 K was maintained during the experiment. Calibration of the deposition rate was done after the fact, by measuring the statistical ratio of covered to uncovered substrate surfaces with the STM. From this, an estimate of 0.5 ML per minute was deduced, where 1 ML (monolayer) designates a surface fully covered with a closed molecular layer.

9.4 Experimental findings: substrate

When compared to, *e.g.*, metal surfaces, working with 2H–$NbSe_2$ and related TMDC substrates presents several difficulties. For one, the noise level of the tunneling current in TMDC experiments exceed that found in experiments with metal substrates, by a factor of 2 to 5. Similar effects have been observed on HfS_2, TaS_2, WSe_2 and $(PbS)_{1.14}(NbS_2)_2$). The high value and anisotropy of the sample resistivity may be an issue. For reference, in an STM study of WSe_2 a relationship between the resistivity of the material and the image quality was demonstrated. Two different batches of tungsten powder of the same nominal purity were used, and a variation of resistivity was caused by the respective types of contaminants present. For the low-resistivity material, atomic resolution was easily achieved, while the high-resistivity material showed an increased noise level (see [119] and references therein).

Another issue lies in the unavailability of most *in situ* tip preparation techniques. The substrate is brittle and easily cleaved, and tip–substrate contact can cause widespread sample destruction, and an accumulation of sample fragments on the tip. This can lead to a high frequency of unwanted tip changes. Classical tip preparation methods that apply successfully for metal surfaces, such as indentation or field emission techniques, are not expected to improve imaging conditions, even if performed remote from regions of interest. Thus, a tip needs to be prepared and verified in a preceding experiment, and it has to retain optimum tunneling conditions during the course of sample preparation, transfer and course approach.

On clean 2H–$NbSe_2$ regions, atomic resolution was possible and attained, although the tip–sample junction remained unstable throughout the experiment. Fig. 9.2 shows a typically observed constant current topograph on a clean substrate region, at a sample voltage of 263 mV and a target current of 100 pA. Several different contrast regions are visible along the vertical image axis, corresponding to the slow scan direction. The contrast changes are attributed to spontaneous tip restructuring, reflecting the general observation that the tunneling junction in TMDC experiments is significantly less stable, compared to metal substrates. Also, there is an elevated current noise level, as stated above.

Both the hexagonal arrangement of the outermost Se atoms and the CDW are visible. Their corrugation amplitudes are roughly equal, with (25 ± 5) pm for the atomic lattice, and (20 ± 5) pm for the charge density wave, in agreement with a previously published value of 50 pm for the total z deflection [43]. The Se atoms are imaged as protrusions and depressions, strongly depending on the local tip state. In the former, their appearance matches previous results [38, 43]. In most tip states, the surface atoms are clearly visible, the and the lattice constant of the hexagonal Se layer can be easily read out from the topograph, giving $a = (0.33 \pm 0.03)$ pm.

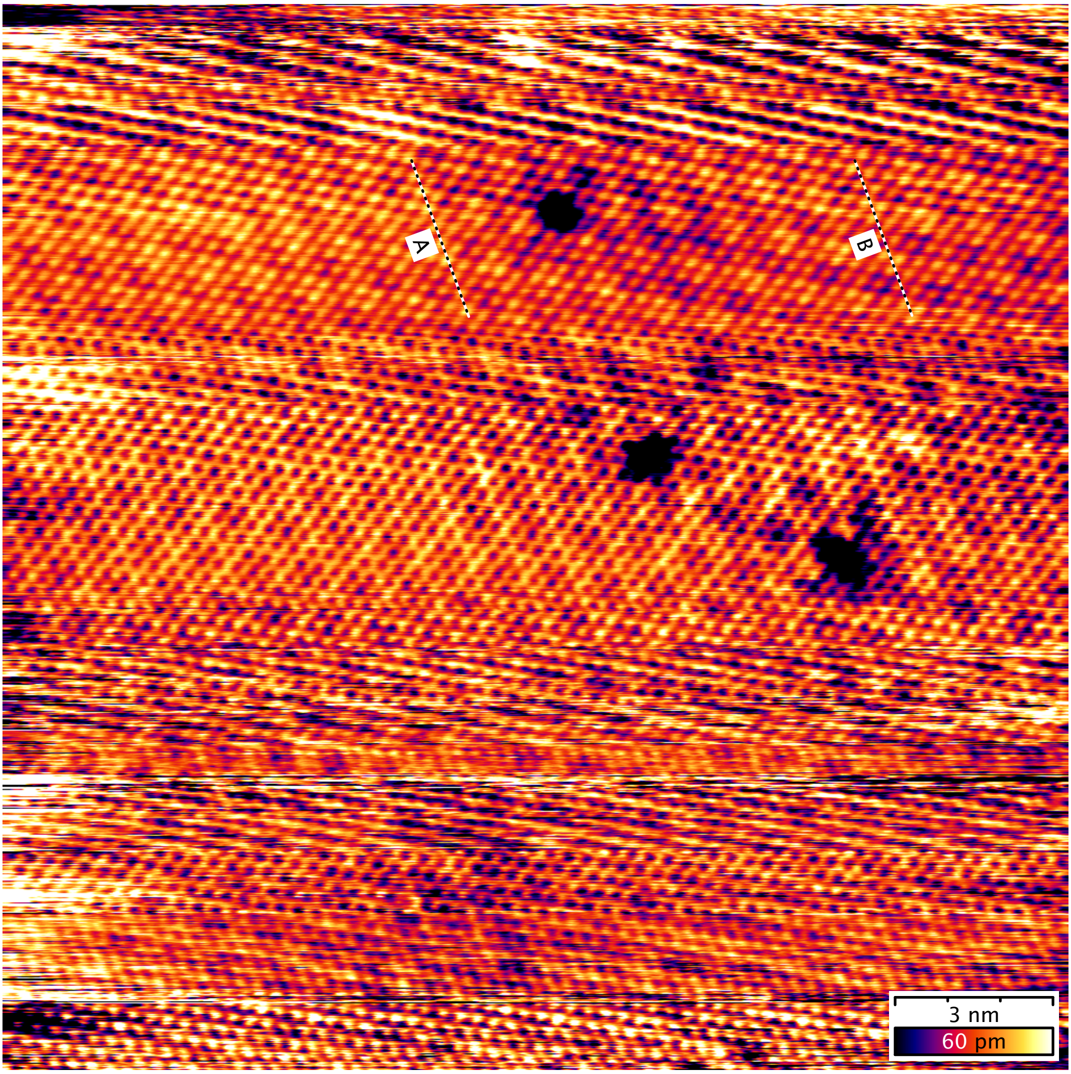

Figure 9.2 – Atomic lattice and charge density wave of 2H-NbSe$_2$, (19.5 nm)^2 topograph, $V = 260$ mV, $I = 100$ pA, showing multiple tip changes. For the atomically-resolved substrate, a lattice constant of $a = (0.33 \pm 0.03)$ nm is obtained. The auxiliary lines A and B, situated on maxima of the CDW, show the incommensurability of the CDW period: While line A is on top of an atomic row, line B falls between two adjacent rows. This gives a CDW period of $(3.06 \pm 0.01)a$. Abrupt changes in image contrast are due to frequently occurring tip changes.

Also, the charge modulation associated with the CDW can be readily seen. In relation to the atomic period, a progressive phase shift of the modulation can be detected, indicating incommensurability. For example, in the region around the atomic row marked A in fig. 9.2, the maximum of the modulation coincides with the position of the atoms, resulting in a single brightest row. At marker B, the maximum of the modulation falls in the gap between two atomic rows, giving two adjacent rows of similar, locally maximal brightness. In the space between the marker lines, which are 27.5 atomic rows apart, 9 full periods of the CDW are accommodated, leading to an estimate of $a_{CDW} = (3 + \delta)a$ with $\delta = 0.06 \pm 0.01$ for the CDW periodicity. This is in good agreement with previously published data [169]. In addition, the area exhibits three dark spots, indicating local topographic depressions, supposedly attributable to surface defects. The exact nature of the defects was not conclusively determined.

9.5 Experimental findings: adsorbate

A typical topograph of a region with a partial PTCDA coverage is shown in fig. 9.3. The picture shows several instances of surface contaminants whose corrugation surpasses that of the surface structure by an order of magnitude. The faint shadows seen especially on the right-hand side indicate the presence of additional satellite tips. In this particular picture, two distinct domains are visible. The periodic pattern on the left-hand side of the picture is attributed to adsorbed PTCDA, arranged in a bulk-like herringbone pattern similar to that described in the previous sections. A detailed analysis of this adsorption pattern is given below.

Compared to the corrugation of the covered area, the right-hand side appears flat and nearly featureless. In addition, its apparent elevation is similar to that of the adjacent, adsorbate-covered region. Similar effects have been reported for PTCDA/Ag(110) at room temperature [25], Dependent on the tunneling current, a contrast transition between uncovered and covered substrate regions was observed. Specifically, at elevated currents, the molecular island exhibited the same topographic height as the surrounding substrate areas.

A possible interpretation of these observations is the presence of a gas of mobile PTCDA molecules on the terrace, from which the tip may pick up a molecule upon traversing the boundary between covered and uncovered regions. In this case, the tip would not need to descend toward the substrate terrace to maintain a constant current. Consequently, the apparent height difference between covered and clean substrate would be reduced by the apparent height of the PTCDA molecule caught by the tip.

In these cases, dragging the molecule across the surface allows to probe the spatial distribution of the molecule–substrate bond. Variations in bond strength may manifest in a height modulation of the dragged molecule. Also, a periodic locking of the dragged object into its most favorable substrate lattice site may be observed. These effects can be detected as modulations or periodic discontinuities in the tunneling current, respectively. In the present case, the absence of the aforementioned phenomena and

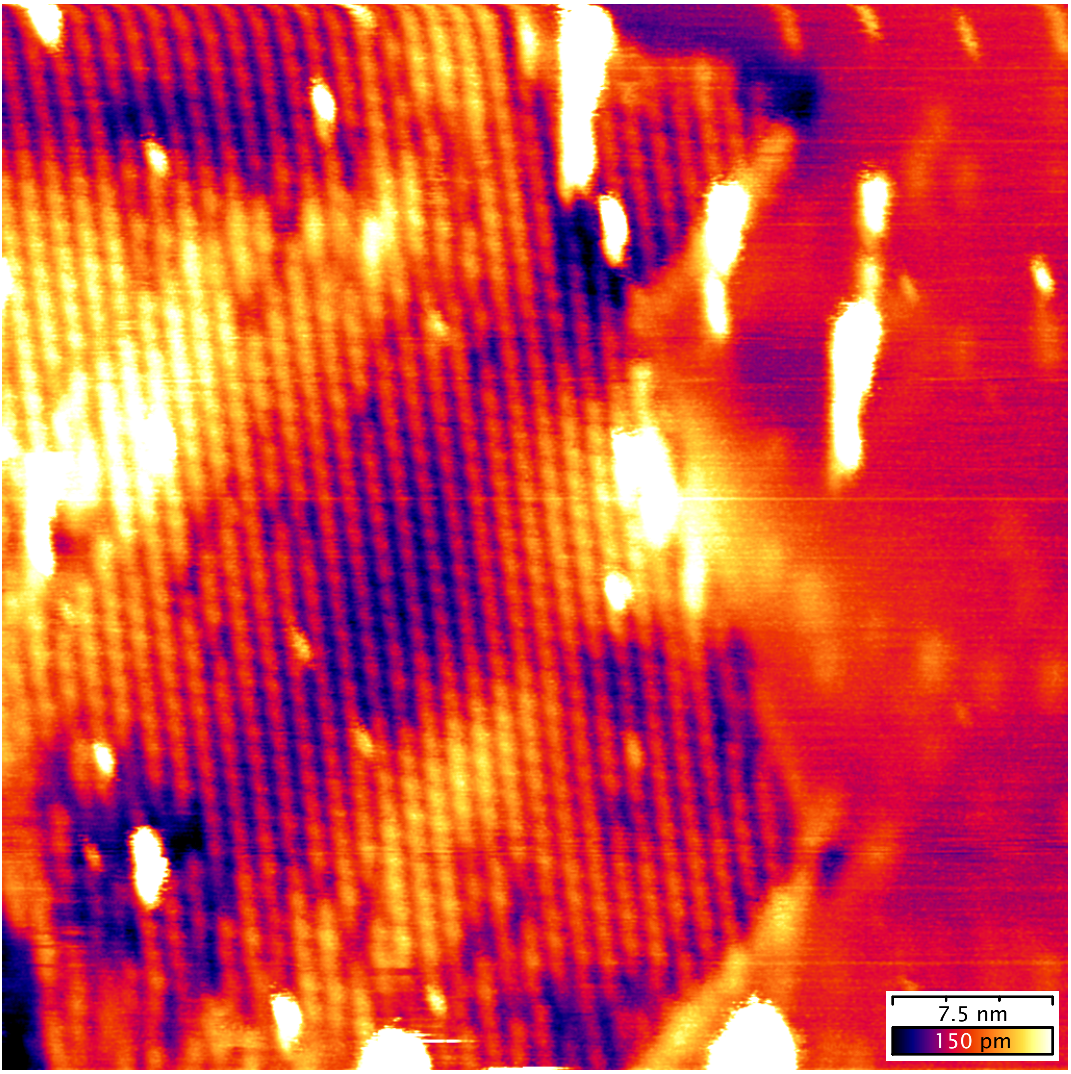

Figure 9.3 – Boundary of a PTCDA-covered NbSe$_2$ region. (50 nm)^2 topograph, $V = +1$ V, $I = 30$ pA, showing a periodic array of PTCDA molecules on the left-hand side, and the uncovered NbSe$_2$ substrate on the right-hand side. Several high-corrugation contaminants are visible in the image.

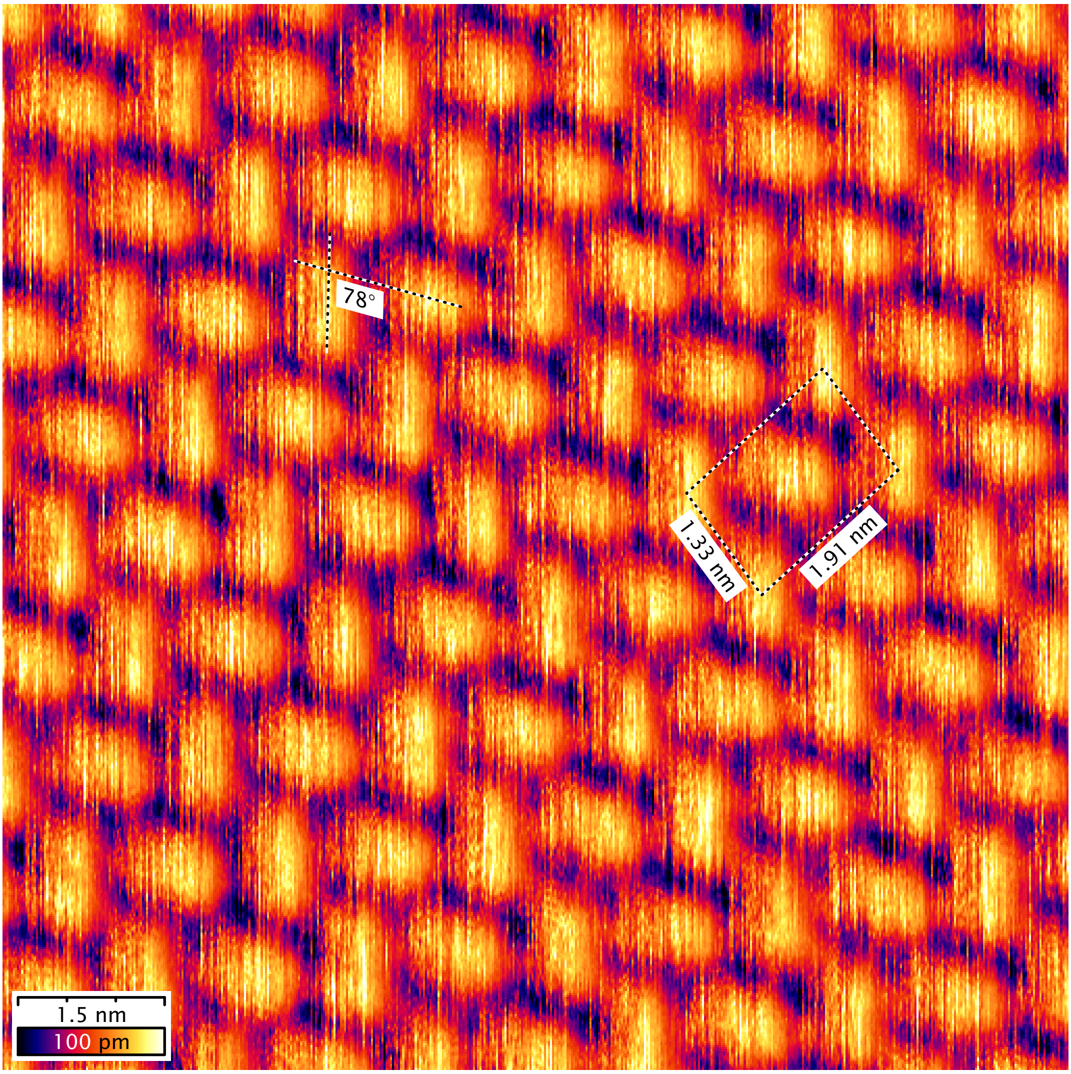

Figure 9.4 – Closed monolayer coverage of PTCDA/NbSe$_2$. (10.9 nm)^2 topograph, $V = 537$ mV, $I = 80$ pA, showing the molecular arrangement in a bulk-like herringbone pattern. Helper lines denote the rectangular unit cell and the apparent angle between the two molecular long axes.

the featureless appearance of the surface hint at a relatively low spatial variation of the bond strength and, consequently, at a weak substrate–adsorbate interaction.

Fig. 9.4 shows a close-up topograph of the interior of a close-packed PTCDA island. The molecules are arranged in a rectangular lattice, similar to the bulk-like herringbone structure introduced in the previous sections. This allows to determine the superlattice parameters, The adsorbate unit cell is obtained by measuring an average of the inter-

Substrate	a(nm)	b(nm)	A(nm^2)	γ	τ	Ref.
MoS_2	1.97	1.24	2.44	88.8°	-	[150]
HOPG	1.922	1.269	2.44	89.5°	-	[99]
GeS(010)	1.96	1.3	2.57	90.0°	-	[244]
Ag(111)	1.895	1.260	2.39	89.0°	-	[81]
2H-$NbSe_2$	1.91 ±0.08	1.33 ±0.07	2.54 ±0.23	88° ± 4°	78° ± 4°	this work
(bulk, α)	1.991	1.196	2.38	90.0°	80°	[148]
(bulk, β)	1.930	1.245	2.40	90.0°	78°	[167]

Table 9.5 – Lattice constants of herringbone PTCDA. Previously published data are collected for bulk polymorphs and monolayers adsorbed on various substrates.

molecular distances across several topographs. The obtained values are (1.91 ± 0.08) nm and (1.33 ± 0.07) nm, with an included angle of $\gamma = 88° \pm 4°$. The error bars, stemming from the limited lateral precision inherent to STM, make it difficult to decide whether this lattice corresponds to the bulk α or β phase. The orientation relative to the substrate lattice is not known, as no topograph with both partial PTCDA coverage and atomic resolution on the uncovered substrate could be obtained. The angle between the long axes of molecules in each orientation is $\tau \approx 78° \pm 4°$, with some uncertainty as tip shape effects cannot be ruled out. However, the axes are likely not exactly perpendicular. A visual estimate of the apparent dimensions of a single PTCDA molecule embedded in an island leads to a length of (1.43 ± 0.05) nm, and a width of (0.91 ± 0.05) nm.

Table 9.5 reproduces the adsorbate superlattice dimensions, in comparison with previous experiments on other substrates that exhibit a herringbone-type superlattice in a PTCDA monolayer, such as MoS_2 [150], HOPG [99, 149], and Ag(111) [81].

9.6 Summary and conclusions

In summary, the submonolayer adsorption of PTCDA on 2H-$NbSe_2$ leads to weakly bound molecules. Single molecules are not seen in STM, indicating a large mobility, and possibility of tip capture and tip-induced movement. Larger compact PTCDA regions are seen, with a rectangular molecular lattice strongly resembling the bulk (102) planes, albeit with minor geometrical distortions. The adsorbate is found to be incommensurate to both the substrate lattice and the charge density wave. Thus, it can be concluded that the 2H-$NbSe_2$ substrate provides no adsorption template properties for the PTCDA molecule, and the structure of the film is primarily governed by intermolecular interactions.

Appendix A

Lock-in amplification

The use of a lock-in amplifier is a cornerstone of STS techniques. However, correct setup of the demodulation filter requires knowledge about its properties. This appendix describes the basics of detection and the broadening of spectral features, models two basic demodulation filters, compares the results with actual performance characteristics of two commercial lock-in amplifiers, and provides some recommendations for the choice of measurement parameters.

A.1 Historical notes

Given an arbitrary input channel, many technical setups require detection of the amplitude (and occasionally, phase) of the spectral component at a specific frequency. A prominent historical example for this is the reception of amplitude modulated radio signals. Difficulties arise if the desired component is dominated by other, unwanted signals, either periodic or noise-like. For this, a naïve signal path would consist of a narrow and steep bandpass filter in the form of a complex RLC circuit pre-tuned to the desired frequency, followed by some kind of rectifier circuit.

As a drawback of this approach, in order to change the detection frequency the filter needs to be retuned, which involves the modification of many interdependent parameters. For flexibility in a sufficiently large frequency range, this is prohibitively difficult to realize in practice.

To avoid this problem, the principle of heterodyning can be employed. This approach involves a mixing stage where the input is multiplied with the output of a local oscillator, resulting in new signals which are frequency shifted counterparts of the original input. The oscillator frequency determines the amount of frequency shift and can be conveniently tuned so that the desired signal is downconverted to a predetermined, fixed intermediate frequency (IF). A carefully designed bandpass filter with a fixed passband can then be employed for detection.

If the frequencies of oscillator and desired signal match, the resulting intermediate frequency is zero. This special case is called homodyning, and demodulation is accomplished with a single lowpass filter, instead of a bandpass and rectifier. Homodyne detectors avert the problem of long-term detuning of the bandpass filter. However, long-term frequency instability of the local oscillator may result in a phase drift and low-frequency beating, which can be averted by continually retuning the local oscillator with a phase-locked loop. It has been suggested that such a setup be labeled a synchrodyne detector [226].

The design of a frequency-selective, phase-sensitive general purpose detector circuit based on the homodyne principle was reported as early as 1934 [46]. By 1941, the term *lock-in amplifier* was in general use for such a device [162], which in its most basic form consists of a reference source (oscillator or input), a mixer (multiplicator) and a rectifier (lowpass demodulator) stage.

The design of the mixer stage provides the principal difficulty in lock-in amplifier design. Early analog designs provided multiplication by feeding the sum of input and reference signals through a vacuum tube with a square-law characteristic. Alternatively, the multiplication can be eschewed in favor of periodic signal polarity flips at the reference frequency, effectively resulting in a multiplication with a square wave.

Depending on the characteristics of the lowpass filter, it is sensitive only to signals in a tunable narrow frequency band around the reference frequency. In the case of phase coherence of desired signal and reference oscillation, the output signal is directly proportional to the signal amplitude. To allow exact recovery of signals whose phase relation to the reference is unknown, many lock-in amplifiers, including some of the earliest designs, contain two separate signal paths whose respective reference sources are out of phase of each other, ideally by 90°.

Typically, modern high-performance lock-in amplifiers are implemented as digital systems. Early in the signal path, the input channel is converted to a digital signal, and further processing is done in DSP-hosted software, avoiding the difficulties of analog multiplication and allowing a flexible design of the demodulator according to digital filter theory.

A.2 Basic principle

The following considerations assume an arbitrary input signal $S(t)$, given as

$$S(t) = \int_0^\infty Z(\omega)\cos[\omega t - \varphi(\omega)]\,\mathrm{d}\omega, \tag{A.1}$$

where $Z(\omega)$ and $\varphi(\omega)$ designate magnitude and phase of the individual frequency components, respectively. The demodulation stage involves multiplication of this signal by a reference oscillation $R_\mathrm{X}(t)$ of angular frequency $\omega_\mathrm{R} > 0$,

$$R_\mathrm{X}(t) := \cos(\omega_\mathrm{R} t). \tag{A.2}$$

Introducing shorthands for sum and difference frequencies $\Sigma := \omega + \omega_\mathrm{R}$, $\Delta := \omega - \omega_\mathrm{R}$, the product can be written as

$$\begin{aligned} R_\mathrm{X}(t)S(t) &= \int_0^\infty Z(\omega)\cos[\omega t - \varphi(\omega)]\cos(\omega_\mathrm{R} t)\,\mathrm{d}\omega \\ &= \int_0^\infty \frac{Z(\omega)}{2}\Big(\cos[\Delta t - \varphi(\omega)] + \cos[\Sigma t - \varphi(\omega)]\Big)\mathrm{d}\omega \\ &= \int_0^\infty \frac{Z(\omega)\cos[\varphi(\omega)]}{2}[\cos(\Delta t) + \cos(\Sigma t)]\mathrm{d}\omega \\ &\quad - \int_0^\infty \frac{Z(\omega)\sin[\varphi(\omega)]}{2}[\sin(\Delta t) + \sin(\Sigma t)]\mathrm{d}\omega. \end{aligned} \tag{A.3}$$

Thus, the obtained signal is the sum of two frequency shifted signals where any spectral component ω is shifted to $\omega + \omega_\mathrm{R}$ and $\omega - \omega_\mathrm{R}$, respectively. Ideal lowpass filtering of the resulting signal is accomplished by averaging the signal over an infinite time window. This eliminates all nonzero frequency components:

$$\begin{aligned} &\lim_{t\to\infty} \int_{-t}^{t} \frac{R_\mathrm{X}(\tau)S(\tau)}{2t}\mathrm{d}\tau \\ &= \int_0^\infty \frac{Z(\omega)\cos[\varphi(\omega)]}{2} \lim_{t\to\infty}\int_{-t}^{t}\left[\frac{\cos(\Delta\tau)}{2t} + \frac{\cos(\Sigma\tau)}{2t}\right]\mathrm{d}\tau\,\mathrm{d}\omega \\ &\quad - \int_0^\infty \frac{Z(\omega)\sin[\varphi(\omega)]}{2} \lim_{t\to\infty}\int_{-t}^{t}\left[\frac{\sin(\Delta\tau)}{2t} + \frac{\sin(\Sigma\tau)}{2t}\right]\mathrm{d}\tau\,\mathrm{d}\omega \\ &= \int_0^\infty \frac{Z(\omega)\cos[\varphi(\omega)]}{2}[\delta(\Delta) + \delta(\Sigma)]\mathrm{d}\omega \\ &= \frac{Z(\omega_\mathrm{R})\cos[\varphi(\omega_\mathrm{R})]}{2} =: \frac{X(\omega_\mathrm{R})}{2}. \end{aligned} \tag{A.4}$$

If the ω_R component of the input signal has no phase shift with regard to the reference, then the result after filtering, $X(\omega_\mathrm{R})$, is equal to the total magnitude of the ω_R spectral component, $Z(\omega_\mathrm{R})$. If the phases are not equal, a smaller portion of the signal is recovered. Hence, $X(\omega_\mathrm{R})$ is called the *in-phase* output signal.

If the signal processing is done simultaneously with both R_X and a second reference signal R_Y that has a phase offset of 90° relative to R_X,

$$R_\mathrm{Y}(t) := \cos\Big(\omega_\mathrm{R} t - \tfrac{\pi}{2}\Big) = \sin(\omega_\mathrm{R} t), \tag{A.5}$$

a similar calculation of

$$\lim_{t\to\infty}\int_{-t}^{t}\frac{R_{\mathrm{Y}}(\tau)S(\tau)}{2t}\mathrm{d}\tau=\frac{Z(\omega_{\mathrm{R}})\sin[\varphi(\omega_{\mathrm{R}})]}{2}=:\frac{Y(\omega_{\mathrm{R}})}{2} \tag{A.6}$$

leads to the so-called *quadrature* output signal $Y(\omega_{\mathrm{R}})$. The total magnitude of the ω_{R} component can then be recovered by

$$Z(\omega_{\mathrm{R}})=\sqrt{X(\omega_{\mathrm{R}})^2+Y(\omega_{\mathrm{R}})^2}, \tag{A.7}$$

and the phase by

$$\varphi(\omega_{\mathrm{R}})=\arctan\left[\frac{Y(\omega_{\mathrm{R}})}{X(\omega_{\mathrm{R}})}\right]. \tag{A.8}$$

The lowpass filter idealization assumed in equation (A.4) has an infinitely narrow bandwidth, but also an infinite time delay. Any practical demodulator implementation contains a lowpass filter with a finite bandwidth. This causes imperfect rejection of spectral components within a frequency band around ω_{R}, and thus typically the presence of noise in $X(\omega_{\mathrm{R}})$, $Y(\omega_{\mathrm{R}})$ and derived quantities.

A.3 Detection of derivatives

A lock-in amplifier can be employed to measure specific derivatives of a given electronic system's transfer function. In STM applications, this transfer function is the current vs. bias voltage characteristic of the tunneling junction, and the desired derivative is typically the first one (the differential conductance), but occasionally, *e.g.*, in vibrational spectroscopy [217], the second or higher derivatives.

For this type of measurement, a sinusoidal modulation with a small finite amplitude A and a frequency of ω_{M} is added onto the bias voltage V_0, giving an output voltage of

$$V(t)=V_0+A\cos(\omega_{\mathrm{M}}t). \tag{A.9}$$

The current-voltage characteristic $I(V)$ of the tunneling junction is represented by its Taylor expansion around V_0,

$$I[V_0+A\cos(\omega_{\mathrm{M}}t)]=\sum_{n=0}^{\infty}I^{(n)}(V_0)\frac{A^n}{n!}\cos^n(\omega_{\mathrm{M}}t), \tag{A.10}$$

where $I^{(n)}$ designates the nth derivative of the function I, and $I^{(0)}$ the function itself. The higher powers of the cosine function can now be replaced by series in cosines of integer multiples of the original argument, according to

$$\cos^n(\omega_{\mathrm{M}}t)=\sum_{k=0}^{n}C_{n,k}\cos(k\omega_{\mathrm{M}}t), \tag{A.11}$$

with coefficients of

$$C_{n,k} = \begin{cases} \frac{1}{2^n}\binom{n}{\frac{n}{2}} & k = 0,\ n \text{ even} \\ \frac{2}{2^n}\binom{n}{\frac{n-k}{2}} & 0 < k \leq n,\ n-k \text{ even} \\ 0 & \text{otherwise.} \end{cases} \tag{A.12}$$

This leads to

$$\begin{aligned} I[V_0 + A\cos(\omega_\mathrm{M} t)] &= \sum_{n=0}^{\infty} I^{(n)}(V_0)\frac{A^n}{n!}\sum_{k=0}^{n} C_{n,k}\cos(k\omega_\mathrm{M} t) \\ &= \sum_{k=0}^{\infty}\left[\sum_{n=k}^{\infty} C_{n,k}\frac{A^n}{n!}I^{(n)}(V_0)\right]\cos(k\omega_\mathrm{M} t) \\ &=: \sum_{k=0}^{\infty} B_k\cos(k\omega_\mathrm{M} t). \end{aligned} \tag{A.13}$$

Thus, the tunneling current in response to the modulated bias voltage consists of a series of higher harmonics of the modulation, where B_k denotes the spectral intensity of the kth harmonic. The B_k themselves are weighted sums of higher derivatives $I^{(n)}$, $n \geq k$. As an example, the lowest-order B_k are given by

$$B_0 = I(V_0) + \frac{A^2}{4}I''(V_0) + \frac{A^4}{64}I^{(4)}(V_0) + \mathcal{O}\left(A^6\right), \tag{A.14}$$

$$B_1 = AI'(V_0) + \frac{A^3}{8}I'''(V_0) + \frac{A^5}{192}I^{(5)}(V_0) + \mathcal{O}\left(A^7\right), \tag{A.15}$$

$$B_2 = \frac{A^2}{4}I''(V_0) + \frac{A^4}{48}I^{(4)}(V_0) + \frac{A^6}{1536}I^{(6)}(V_0) + \mathcal{O}\left(A^8\right), \tag{A.16}$$

$$B_3 = \frac{A^3}{24}I'''(V_0) + \frac{A^5}{384}I^{(5)}(V_0) + \frac{A^7}{15360}I^{(7)}(V_0) + \mathcal{O}\left(A^9\right). \tag{A.17}$$

The B_k in turn can be recovered as the in-phase signal $X(k\omega_\mathrm{M})$ of a lock-in demodulator operating at a reference frequency that is the kth multiple of the modulation frequency, $\omega_\mathrm{R} = k\omega_\mathrm{M}$.

In the case of sufficiently small modulation amplitude A, the B_k can be approximated by their lowest-order term in A, allowing recovery of the kth derivative by calculating

$$I^{(k)}(V_0) \approx I^{(k)}_\mathrm{meas.}(V_0) := \frac{k!}{A^k C_{k,k}}B_k = \frac{2^{k-1}k!}{A^k}X(k\omega_\mathrm{M}) \tag{A.18}$$

making B_k roughly proportional to the kth derivative $I^{(k)}$. As mentioned above, due to the finite bandwidth of a practical demodulator, $X(k\omega_\mathrm{M})$ will typically not be noise-free. Since A^k appears in the denominator of the recovery formula (A.18), reducing the modulation amplitude amplifies such unwanted noise. Hence, the choice of amplitude involves a trade-off between noise and a systematic error.

In principle, it is possible to retrieve several spectral components in parallel from a single modulated signal. A suitable linear combination of these can then eliminate the higher-order derivatives, up to any desired order [203]. For example, to recover the first derivative, by calculating $B_1 - 3B_3$, the A^3 term can be eliminated, as evident from equations (A.15) and (A.17). However, if the summed components contain mutually uncorrelated noise, this technique also results in additional noise in the recovered signal.

Modulation amplitude and broadening. In (A.13), the systematic error induced by finite modulation amplitudes has been described in terms of higher-order derivatives of $I(V)$. As an alternative approach, the same phenomenon can be described directly in the voltage domain [120], as a characteristic broadening of the acquisition of a specific derivative $I^{(k)}(V)$.

As stated above, recovery of the kth derivative is done by demodulating with a reference frequency of $\omega_\mathrm{R} := k\omega_\mathrm{M}$, the kth multiple of the modulation frequency. Inserting the modulation (A.9) into the idealized in-phase demodulation formula (A.4) yields

$$X(k\omega_\mathrm{M}) = 2\lim_{t\to\infty}\int_{-t}^{t}\frac{I[V_0 + A\cos(\omega_\mathrm{M}\tau)]\cos(k\omega_\mathrm{M}\tau)}{2t}\mathrm{d}\tau \tag{A.19}$$

$$= \frac{2\omega_\mathrm{M}}{\pi}\int_{0}^{\pi/\omega_\mathrm{M}} I[V_0 + A\cos(\omega_\mathrm{M}\tau)]\cos(k\omega_\mathrm{M}\tau)\mathrm{d}\tau. \tag{A.20}$$

Substituting $\beta := \cos(\omega_\mathrm{M}\tau)$, the integral is transformed into

$$X(k\omega_\mathrm{M}) = \frac{2}{\pi}\int_{-1}^{1} I(V_0 + A\beta)\mathrm{T}_k(\beta)\frac{1}{\sqrt{1-\beta^2}}d\beta, \tag{A.21}$$

where the

$$\mathrm{T}_k(\beta) := \cos(k\arccos\beta) \tag{A.22}$$

denote the Chebyshev polynomials of the first kind. As the T_k satisfy the generalized Rodrigues' formula [154],

$$\mathrm{T}_k(\beta) = \frac{(-1)^n}{(2k-1)!!}\sqrt{1-\beta^2}\left[\frac{\mathrm{d}}{\mathrm{d}\beta}\right]^k\left(1-\beta^2\right)^{k-\frac{1}{2}}, \tag{A.23}$$

the integral can be further transformed, giving

$$X(k\omega_\mathrm{M}) = \frac{2(-1)^n}{\pi(2k-1)!!}\int_{-1}^{1} I(V_0 + A\beta)\left[\frac{\mathrm{d}}{\mathrm{d}\beta}\right]^k\left(1-\beta^2\right)^{k-\frac{1}{2}}\mathrm{d}\beta. \tag{A.24}$$

Performing k-fold integration by parts yields

$$X(k\omega_\mathrm{M}) = \frac{2A^k}{\pi(2k-1)!!}\int_{-1}^{1} I^{(k)}(V_0 + A\beta)\left(1-\beta^2\right)^{k-\frac{1}{2}}\mathrm{d}\beta, \tag{A.25}$$

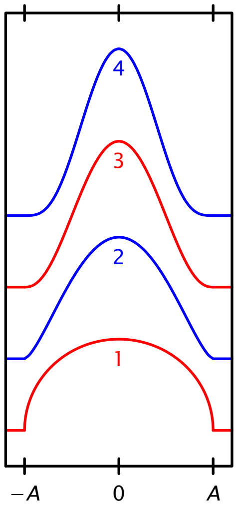

Figure A.1 – Lock-in amplifier broadening functions $\Xi_{k,A}(\gamma)$, while detecting the first four derivatives, $k = 1\dots4$, using a modulation amplitude of A. These graphs show the characteristic functions with which the spectral features are convoluted during detection. The area below each curve is, by definition, 1.

with $I^{(k)}$ denoting the kth derivative of I. Introducing $\gamma := A\beta$, this can be written as

$$X(k\omega_\mathrm{M}) = \frac{2}{\pi A^k(2k-1)!!} \int_{-A}^{A} I^{(k)}(V_0+\gamma)\left(A^2-\gamma^2\right)^{k-\frac{1}{2}} \mathrm{d}\gamma. \tag{A.26}$$

Recovery of the kth derivative can now be done according to formula (A.18), giving

$$I^{(k)}_{\mathrm{meas.}}(V_0) = \frac{2^{k-1}k!}{A^k} X(k\omega_\mathrm{M}) \tag{A.27}$$

$$= \frac{2^k k!}{\pi A^{2k}(2k-1)!!} \int_{-A}^{A} I^{(k)}(V_0+\gamma)\left(A^2-\gamma^2\right)^{k-\frac{1}{2}} \mathrm{d}\gamma \tag{A.28}$$

$$=: \int_{-\infty}^{\infty} I^{(k)}(V_0+\gamma)\Xi_{k,A}(-\gamma)\mathrm{d}\gamma \tag{A.29}$$

$$= \left[I^{(k)} * \Xi_{k,A}\right](V_0), \tag{A.30}$$

where $*$ denotes the convolution operation,

$$[f*g](x) := \int_{-\infty}^{\infty} f(x-y)g(y)\mathrm{d}y, \tag{A.31}$$

and

$$\Xi_{k,A}(\gamma) := \begin{cases} \frac{2^k k!}{\pi A^{2k}(2k-1)!!}\left(A^2-\gamma^2\right)^{k-\frac{1}{2}} & \text{for} \quad |\gamma| \le A \\ 0 & \text{for} \quad |\gamma| > A. \end{cases} \tag{A.32}$$

Thus, the measured signal is the convolution of the real kth derivative with a characteristic broadening function $\Xi_{k,A}$. In particular, for the first and second derivatives, the expressions read

$$I'_{\text{meas.}}(V_0) = \int_{-A}^{A} I'(V_0 + \gamma)\frac{2\sqrt{A^2 - \gamma^2}}{\pi A^2}\mathrm{d}\gamma \tag{A.33}$$

and

$$I''_{\text{meas.}}(V_0) = \int_{-A}^{A} I''(V_0 + \gamma)\frac{8\left(A^2 - \gamma^2\right)^{\frac{3}{2}}}{3\pi A^4}\mathrm{d}\gamma. \tag{A.34}$$

Notably, eq. (A.33) simply describes the convolution of $I'(V)$ with a half-ellipse function of area 1. A graphical representation of the first four broadening functions is given in fig. A.1.

A.4 Demodulation filter design

A digital filter operates on a series of input values x_i, sampled at a uniform rate of one value per sample period T_S, with the highest index designating the most recent value. From these values the filter generates its output values y_i according to the prescription

$$y_i = \sum_{k=0}^{\infty} b_k x_{i-k} - \sum_{k=1}^{\infty} a_k y_{i-k}. \tag{A.35}$$

The series of filter coefficients a_k and b_k describe the properties of the filter. For a practical implementation, the calculation needs to be finished in a finite time, thus there exists a number n such that for all $k \geq n$, $a_k = b_k = 0$. In this case, the summation must only be performed from 0 to $n - 1$. The number n is called the number of taps of the filter. If any of the a_k are nonzero, it is called a recursive, or IIR (infinite impulse response), filter. Otherwise, it is referred to as an FIR (finite impulse response) filter.

This nomenclature reflects that if a pulse, *i.e.*, a series of numbers where $x_j \neq 0$ for a single sample j and $x_i = 0$ for all other $i \neq j$, is fed into an IIR filter, the output sequence y_i will never reach zero again for any finite $i > j$. Thus, its output will have a causal relation to said pulse for an infinite time in the future. In contrast, the response of an n-tap FIR filter to the same pulse will return to $y_i = 0$ for all $i \geq n + j$, thus having ‘forgotten’ the pulse after the nth subsequent sample.

The properties of a digital filter are reflected in its transfer function, which is given by the Z-transform of the filter function,

$$H(z) = \frac{Y(z)}{X(z)} = \frac{\sum_{k=0}^{n} b_k z^{-k}}{1 + \sum_{k=1}^{n} a_k z^{-k}}. \tag{A.36}$$

The EMA filter. The most computationally simple design for a recursive digital filter is a first order, 2-tap design where $b_1 = 0$, *i.e.*, a filter with the recursion

$$y_i = b_0 x_i - a_1 y_{i-1}, \tag{A.37}$$

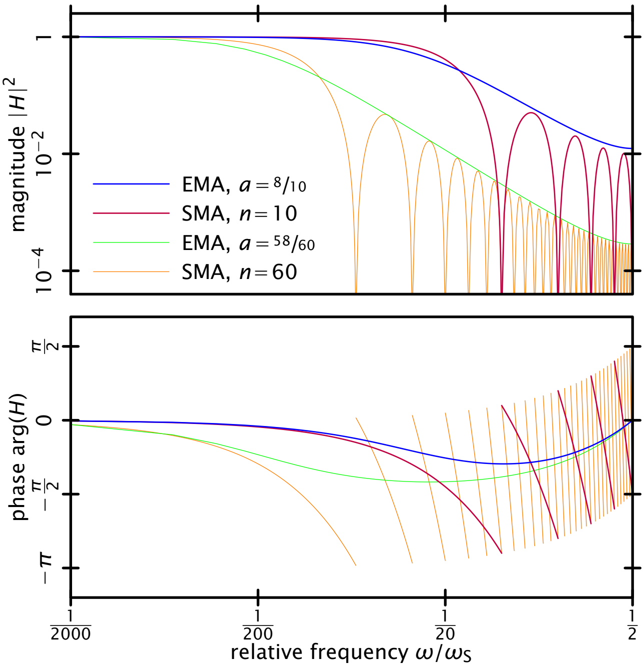

Figure A.2 – Bode plot of filter transfer functions. Comparison of **(a)** power spectrum and **(b)** phase shift of EMA and SMA filters, for filter parameters a, n corresponding to different time constants τ, according to (a.51) and (a.53). $\omega_S := 2\pi/T_S$ designates the sample frequency. The SMA filter has $\frac{n}{2}$ zeroes, where the phase jumps by π.

whose transfer function is

$$H(z) = \frac{b_0}{1 - a_1 z^{-1}}. \tag{A.38}$$

To establish a DC gain of unity, the condition $H(0) = 1$ must be fulfilled. Under this condition, a_1 and b_0 are no longer independent, and a single new parameter $a := -a_1 = 1 - b_0$ can be introduced, giving a filter equation of

$$y_i = (1 - a)x_i + a y_{i-1}. \tag{A.39}$$

This system is called *exponentially-weighted moving average* (EMA) filter, or *leaky integrator*. It functions as an integrator by accumulating the stream of incoming x_i. However, its total value is not completely retained, but for any $a < 1$, it 'leaks', as with each new sample, it is diminished by a portion of $1 - a$ of its total.

The transfer function of this filter can be written as

$$H_a(z) = (1 - a)\frac{z}{z - a}, \tag{A.40}$$

and its power spectrum is

$$\left|H_a\left(e^{j\omega}\right)\right|^2 = \frac{(1 - a)^2}{1 + a^2 - 2a\cos\omega}. \tag{A.41}$$

Bode plots of this power spectrum, and the phase shift of the filter, for different coefficients a are reproduced in fig. A.2. The roll-off, *i.e.*, the decrease of transmitted signal amplitude within the stopband, of this particular filter is 6 dB/octave, or proportional to f^{-1}. This is the maximum attainable with a 2-tap recursive filter, but is usually not sufficient for lock-in applications. To obtain a sharper roll-off, a number m of these filters can be cascaded, by feeding the output of each filter stage into the input of a subsequent stage. The transfer function of such a cascade of order m is given by $[H(z)]^m$, where $H(z)$ denotes the transfer function of a single constituent filter stage.

The SMA filter. As stated above, an n-tap digital filter is called an incursive or FIR filter if all feedback coefficients a_k are zero, resulting in a filter equation of

$$y_i = \sum_{k=0}^{n-1} b_k x_{i-k}, \tag{A.42}$$

and a transfer function of

$$H(z) = \sum_{k=0}^{n-1} b_k z^{-k}. \tag{A.43}$$

FIR filters have a set of advantageous characteristics, such as numerical stability (bounded input leading to bounded output) and the possibility of linear phase. However, as computational intensity and memory requirements of FIR filter algorithms increase with the number of taps, they are generally unsuitable for real-time lowpass filter applications with large time constants.

This shortcoming can be worked around by designing a filter where all coefficients b_k for $0 \le k < n$ are equal. Then, the condition of unity DC gain requires that $H(0) = 1$, and thus all $b_k = \frac{1}{n}$ for $0 \le k < n$, giving a filter equation of

$$y_i = \frac{1}{n} \sum_{k=0}^{n-1} x_{i-k} \tag{A.44}$$

The output of this system is simply the moving, uniformly weighted average of the n most recent input samples. Thus, it is called a *simple moving average* (SMA) filter, or, due to the shape of its weighting function as it moves across the stream of input values, a *boxcar* filter. This filter can be implemented with much less computational complexity. Its transfer function can be rewritten using the geometric series, giving

$$H_n(z) = \frac{1}{n} \frac{1 - z^{-n}}{1 - z^{-1}}. \tag{A.45}$$

Calculation of the power spectrum results in

$$\left| H_n\left(e^{j\omega}\right) \right|^2 = \frac{1}{n^2} \frac{1 - \cos n\omega}{1 - \cos \omega}, \tag{A.46}$$

which, along with the phase response, is reproduced graphically in fig. A.2. As the filter coefficients are symmetric, the filter offers a phase linear response, with

$$\arg\left[H_n\left(e^{j\omega}\right) \right] = -\frac{n-1}{2} \omega, \tag{A.47}$$

in the passband and, apart from phase jumps of π (*i.e.*, sign inversions) that occur at every zero of the transfer function, also beyond.

Equivalent noise bandwidth. The equivalent noise bandwidth (ENBW) of a filter is defined as the cut-off frequency f_E of an hypothetical low-pass filter with perfectly steep roll-off whose total transmitted power, integrated over the whole frequency range, equals that of the described filter.

As a baseline reference, for an analog RC lowpass circuit with a time constant of $\tau := RC$ and a transfer function of $H_{RC}(j\omega) = (1 + j\omega\tau)^{-1}$, the ENBW is equal to

$$f[H_{RC}] = \frac{1}{2\pi}\int\limits_0^\infty |H_{RC}(j\omega)|^2 \mathrm{d}\omega = \frac{1}{2\pi}\int\limits_0^\infty \left|\frac{1}{1+j\omega\tau}\right|^2 \mathrm{d}\omega = \frac{1}{4}\tau^{-1}. \tag{A.48}$$

In the case of digital filters, the integration only takes place up to the Nyquist frequency $\frac{\omega_S}{2} = \frac{1}{4\pi T_S}$. Any higher spectral components would be projected back into this frequency range, unless eliminated beforehand by an anti-aliasing filter on the analog side. Then, the ENBW of a digital filter can be calculated by

$$f_E[H] = \frac{1}{2\pi T_S}\int\limits_0^\pi \left|H\left(e^{j\omega}\right)\right|^2 \mathrm{d}\omega. \tag{A.49}$$

Use of a filter's ENBW to estimate transmitted noise power requires that white noise, *i.e.*, noise with a frequency independent power spectrum, is a reasonably good approximation to the real input noise. In such a case, the ENBW can be used as a metric to compare different filter designs, such as the aforementioned EMA and SMA filters. For the EMA filter, the integrand is given in (A.41), and the ENBW is

$$\tilde{f}_E[H_a] = \frac{1}{2\pi T_S}\int\limits_0^\pi \left|H_a\left(e^{j\omega}\right)\right|^2 \mathrm{d}\omega = \frac{1-a}{2T_S(a+1)} \tag{A.50}$$

If a time constant τ is introduced by defining

$$\tau := \frac{T_S}{1-a} \quad \Rightarrow \quad a(\tau) = 1 - \frac{T_S}{\tau}, \tag{A.51}$$

when decreasing sample granularity, the ENBW asymptotically approaches the RC reference value,

$$\lim_{T_S\to 0} \tilde{f}_E[H_{a(\tau)}] = \lim_{T_S\to 0} \frac{1}{4\tau - 2T_S} = \frac{1}{4}\tau^{-1}. \tag{A.52}$$

For the SMA filter, a similar calculation can be made. When the time constant τ is defined as

$$\tau := \frac{n}{2}T_S \quad \Rightarrow \quad n(\tau) = \frac{2\tau}{T_S}, \tag{A.53}$$

integrating over (A.46) gives an ENBW of

$$\tilde{f}_E[H_n] = \frac{1}{2\pi T_S n^2}\int\limits_0^\pi \frac{1-\cos(n\omega)}{1-\cos(\omega)} \mathrm{d}\omega = \frac{1}{2nT_S} = \frac{1}{4}\tau^{-1}, \tag{A.54}$$

which is also equal to the RC reference. Thus, with the parameters introduced in equations (A.51) and (A.53), respectively, the EMA and SMA filters have a matching ENBW. If several filters with these parameters are cascaded, the resulting ENBW can be calculated accordingly. The results are compiled in tables A.3 for the EMA filter, and A.4 for the SMA filter.

Note that different filter designs with a similar ENBW are comparable in performance only if the unwanted noise is sufficiently white. In STS, the power density spectrum of the current signal contains shot noise (due to statistical current fluctuations resulting from charge quantization) and Johnson-Nyquist noise (due to thermal fluctuations), which are both generally white. Additionally, the current may contain quasiperiodic components from mechanical resonances of the system. The total signal is bandwidth-limited by the cut-off frequency of the transimpedance amplifier.

The lock-in demodulation stage multiplies the input signal by the reference oscillation, thereby shifting the frequency by ω_R, prior to low-pass filtering. Thus, the output noise results from the input noise frequency components in a narrow band around ω_R. For the ENBW to provide a useful metric of actual measurement noise, the power spectrum must be sufficiently uniform in this frequency band. This is generally the case, provided that there is no significant deviation from the white noise characteristic close to ω_R. The operator must ensure that no mechanical resonances or other sources of spectral power are present in the frequency band. Note that for a narrow enough bandwidth, this whiteness criterion is also sufficiently fulfilled beyond the cut-off frequency, due to the way the upper and lower sidebands are mixed during demodulation.

Order m	$\tilde{f}_\mathrm{E}[H_a]$	$f_\mathrm{E}(\tau) := \lim\limits_{T_\mathrm{S}\to 0} \tilde{f}_\mathrm{E}[H_{a(\tau)}]$
1	$\frac{1-a}{2(a+1)} T_\mathrm{S}^{-1}$	$\frac{1}{4}\tau^{-1}$
2	$\frac{1-a}{2(a+1)^3}\left(a^2+1\right) T_\mathrm{S}^{-1}$	$\frac{1}{8}\tau^{-1}$
3	$\frac{1-a}{2(a+1)^5}\left(a^4+4a^2+1\right) T_\mathrm{S}^{-1}$	$\frac{3}{32}\tau^{-1}$
4	$\frac{1-a}{2(a+1)^7}\left(a^6+9a^4+9a^2+1\right) T_\mathrm{S}^{-1}$	$\frac{5}{64}\tau^{-1}$

Table A.3 – EMA filter equivalent noise bandwidth for cascades of order $m = 1\ldots4$, as a function of parameter a for finite sample rates T_S, and in the limit for infinitely fine sample rate, as a function of target time constant τ.

Order m	$\tilde{f}_\mathrm{E}[H_n]$	$f_\mathrm{E}(\tau) := \lim\limits_{T_\mathrm{S}\to 0} \tilde{f}_\mathrm{E}[H_{n(\tau)}]$
1	$\frac{1}{2n} T_\mathrm{S}^{-1}$	$\frac{1}{4}\tau^{-1}$
2	$\frac{2n^2+1}{6n^3} T_\mathrm{S}^{-1}$	$\frac{1}{6}\tau^{-1}$
3	$\frac{11n^4+5n^2+4}{40n^5} T_\mathrm{S}^{-1}$	$\frac{11}{80}\tau^{-1}$
4	$\frac{151n^6+70n^4+49n^2+45}{630n^7} T_\mathrm{S}^{-1}$	$\frac{151}{1260}\tau^{-1}$

Table A.4 – SMA filter equivalent noise bandwidth for cascades of order $m = 1\ldots 4$, as a function of number n of taps for finite sample rates T_S, and in the limit for infinitely fine sample rate, as a function of time constant τ.

A.5 Filter step response

A valuable quantity in assessing the properties of a linear system is its step response. This is defined as the response of the system to a step-like input series of

$$x_k = \begin{cases} 0 & \text{for} \quad k < 0 \\ 1 & \text{for} \quad k \geq 0. \end{cases} \tag{A.55}$$

The response of the system to an arbitrary input series can be determined by treating each change of input value as a step, and summing up the respective step responses. The step response of the EMA filter can be expressed as a continuous function

$$\tilde{\zeta}_1(a,k) := \begin{cases} 0 & \text{for} \quad k < 0 \\ 1 - a^{k+1} & \text{for} \quad k \geq 0. \end{cases} \tag{A.56}$$

For integer k, the sequence of values $\tilde{\zeta}_1(a,k)$ is equal to the response y_k of the discrete filter to the step-like input series x_k from equation (A.55). If the time constant $\tau := \frac{T_\mathrm{S}}{1-a}$ from equation (A.51) is used, the transition to an arbitrarily fine sample rate can be made, giving

$$\zeta_1(\tau,t) := \lim_{T_\mathrm{S}\to 0} \tilde{\zeta}_1\left(1 - \frac{T_\mathrm{S}}{\tau}, \frac{t}{T_\mathrm{S}}\right) = \begin{cases} 0 & \text{for} \quad t < 0 \\ 1 - e^{-t/\tau} & \text{for} \quad t \geq 0, \end{cases} \tag{A.57}$$

a step response identical to that of a simple analog RC low-pass filter with time constant τ. The step response functions for higher order cascades of EMA filters can be calculated similarly. They are compiled in table A.5, and represented graphically in fig. A.7a,b.

The step response of an n-tap SMA filter can be described by the function

$$\tilde{\eta}_1(n,k) := \begin{cases} 0 & \text{for} \quad k < -1 \\ \frac{k+1}{n} & \text{for} \quad -1 \leq k < n-1 \\ 1 & \text{for} \quad n-1 \leq k, \end{cases} \tag{A.58}$$

m	$\tilde{\zeta}_m(a,k)$	$\zeta_m(\tau,t) := \lim_{T_S\to 0} \tilde{\zeta}_m\left(1-\frac{T_S}{\tau}, \frac{t}{T_S}\right)$
1	$1-a^{k+1}$	$1-e^{-\frac{t}{\tau}}$
2	$1-a^{k+1}(p_0-p_1a)$ $p_0 := k+2$ $p_1 := k+1$	$1-e^{-\frac{t}{\tau}}\left(1+\frac{t}{\tau}\right)$
3	$1-a^{k+1}\left(p_0-p_1a+p_2a^2\right)$ $p_0 := \frac{1}{2}\left(k^2+5k+6\right)$ $p_1 := \frac{1}{2}\left(2k^2+8k+6\right)$ $p_2 := \frac{1}{2}\left(k^2+3k+2\right)$	$1-e^{-\frac{t}{\tau}}\left(1+\frac{t}{\tau}+\frac{t^2}{2\tau^2}\right)$
4	$1-a^{k+1}\left(p_0-p_1a+p_2a^2-p_3a^3\right)$ $p_0 := \frac{1}{6}\left(k^3+9k^2+26k+24\right)$ $p_1 := \frac{1}{6}\left(3k^3+24k^2+57k+36\right)$ $p_2 := \frac{1}{6}\left(3k^3+21k^2+42k+24\right)$ $p_3 := \frac{1}{6}\left(k^3+6k^2+11k+6\right)$	$1-e^{-\frac{t}{\tau}}\left(1+\frac{t}{\tau}+\frac{t^2}{2\tau^2}+\frac{t^3}{6\tau^3}\right)$

Table A.5 – EMA filter step response functions $\tilde{y}_a(t)$ for cascades of orders $m = 1\ldots4$. In the limit of infinitely fine sample rate T_S, if the parameter a is adjusted to maintain a constant $\tau = \frac{T_S}{1-a}$, the step functions converge to the expressions on the right hand side. In practical STS lock-in applications, where $\frac{1}{T_S} \geq 200$ kHz and $\tau \geq 1$ ms, they provide a good approximation to the filter behavior.

such that the values of the function $\tilde{\eta}_1(n,k)$ for integer k match the filter output sequence y_k. With the time constant $\tau = \frac{n}{2}T_S$ from equation (A.53), this gives a fine sample rate limit of

$$\eta_1(\tau,t) := \lim_{T_S\to 0} \tilde{\eta}_1\left(\frac{2\tau}{T_S}, \frac{t}{T_S}\right) = \begin{cases} 0 & \text{for} \quad t<0 \\ \frac{t}{2\tau} & \text{for} \quad 0 \leq t < 2\tau \\ 1 & \text{for} \quad 2\tau \leq t. \end{cases} \tag{A.59}$$

The step response functions for cascades of up to four SMA filters are compiled in table A.6 and plotted in fig. A.7c,d.

Order m	$\eta_m(\tau,t) := \lim\limits_{T_S\to 0} \tilde{\eta}_m\left(\frac{2\tau}{T_S},\frac{t}{T_S}\right)$	Time segment
any	0	$t < 0$
	1	$t \geq 2m\tau$
1	$b := t/2\tau$	$0 \leq t < 2\tau$
2	$\frac{1}{2}b^2$	$0 \leq t < 2\tau$
	$\frac{1}{2}\left(-b^2+4b-2\right)$	$2\tau \leq t < 4\tau$
3	$\frac{1}{6}b^3$	$0 \leq t < 2\tau$
	$\frac{1}{6}\left(-2b^3+9b^2-9b+3\right)$	$2\tau \leq t < 4\tau$
	$\frac{1}{6}\left(b^3-9b^2+27b-21\right)$	$4\tau \leq t < 6\tau$
4	$\frac{1}{24}b^4$	$0 \leq t < 2\tau$
	$\frac{1}{24}\left(-3b^4+16b^3-24b^2+16b-4\right)$	$2\tau \leq t < 4\tau$
	$\frac{1}{24}\left(3b^4-32b^3+120b^2-176b+92\right)$	$4\tau \leq t < 6\tau$
	$\frac{1}{24}\left(-b^4+16b^3-96b^2+256b-232\right)$	$6\tau \leq t < 8\tau$

Table A.6 – SMA filter step response functions for filter cascades of orders $m = 1\ldots4$, in their piecewise representations. Only the functions in the limit of infinitely fine sample rate are reproduced here, where the number of taps n is adjusted such that $\tau = \frac{n}{2}T_S$ remains constant. For finite sample rates, the functions can also be expressed as piecewise polynomials, where the coefficients of the b^k are themselves replaced each by a polynomial of mth order in $\frac{1}{n}$.

A.6 Considerations in practice

When choosing a lock-in amplifier for STS, care must be taken to meet the specific demands that the measurement setup places on the device. In particular, it should allow fine-grained phase adjustment, a suitable range of time constants in the millisecond range, and possibly demodulation on higher harmonics, *e.g.*, for vibrational spectroscopy. Also, as the bandwidth of the tunneling circuit is limited, so is the modulation frequency, and a filter steeper than 6 dB is necessary to reject the $2f$ component.

In most STM control systems (including the SPM 1000 used in this work) all the measurements for a point in a spectrum or scanline must be finished before the system advances to the next point; Asynchronously scheduling an acquisition at a later time is not possible. This means that in STS, the minimum dwell time t_D per data point is determined by the demodulation filter settle time t_S plus any applicable processing and refresh delays t_P of the amplifier. The latter should be as small as possible. Long pipeline delays and filters with large phase shifts are highly disadvantageous, since for

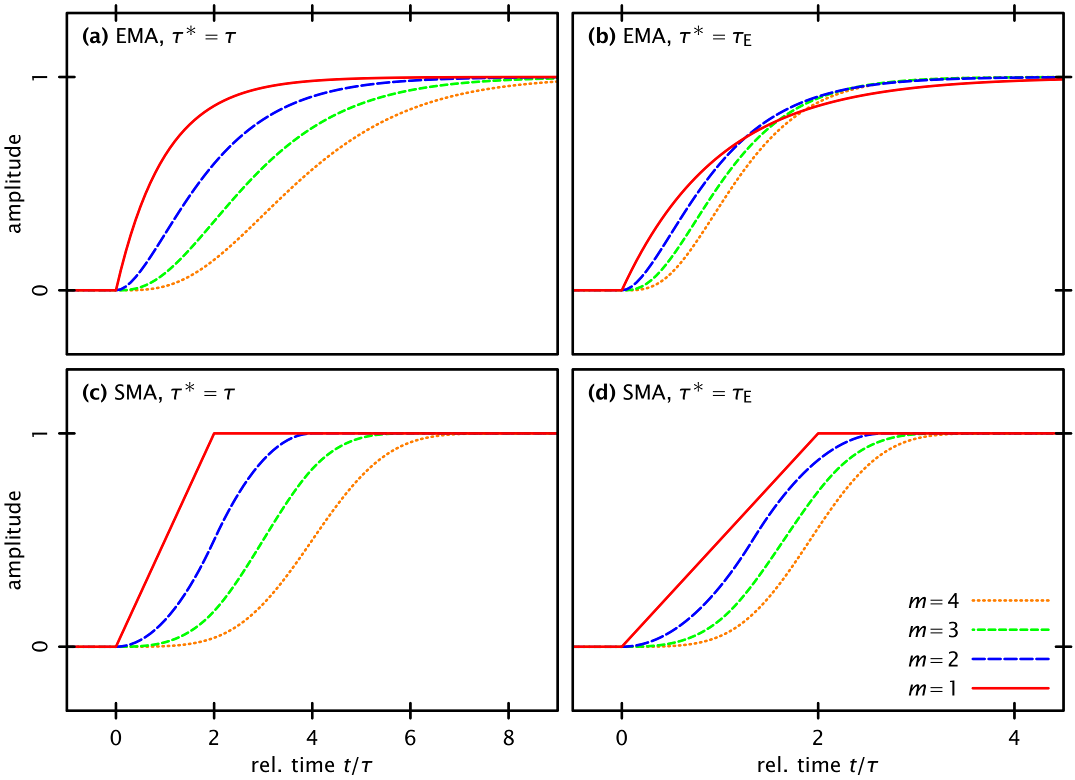

Figure A.7 – Filter step response plots for **(a,b)** EMA and **(c,d)** SMA filter cascades of order $m = 1 \ldots 4$, with time constant τ^* (fine sample rate limit). The SMA responses are piecewise polynomials of order m and reach the target value after $t = 2m\tau^*$. The EMA responses approach the target value exponentially. The left-hand side shows constant $\tau^* = \tau$, the right-hand side shows constant ENBW, with $\tau^* = \tau_E$ chosen such that $f_E(\tau_E) = (4\tau)^{-1}$.

any chosen t_D selected by the experimenter, they impose limits on time constant, and thus, noise rejection.

Choice of roll-off and time constant. For a given filter type and cascading order m, the filter settle time t_S depends on the target ratio R, *i.e.*, the percentage of the target value that the step response is supposed to reach before acquisition, and, linearly, on the time constant τ. For the latter, commercial lock-in amplifiers typically offer a selection of fixed values. This, however, is mainly a choice of implementation and UI design on the manufacturer's part. For a given time constant, the settle times can be calculated from the step responses given in tables A.5 and A.6. Example settle times for common target ratios are given in tables A.8 and A.9. These allow several observations:

- While the step response curves in fig. A.7 solicit the assumption that the SMA

Percentage of target value	EMA settle time t/τ						
	Constant τ				Constant ENBW		
$1 - e^{-1} \approx 63.2\%$	1.000	2.146	3.258	4.352	1.073	1.221	1.360
$1 - e^{-2} \approx 86.5\%$	2.000	3.505	4.878	6.186	1.753	1.829	1.933
$1 - e^{-3} \approx 95.0\%$	3.000	4.749	6.302	7.760	2.375	2.363	2.425
50.0%	0.693	1.678	2.674	3.672	0.839	1.002	1.148
90.0%	2.302	3.890	5.322	6.681	1.945	1.995	2.088
99.0%	4.605	6.638	8.406	10.05	3.319	3.152	3.139
99.9%	6.908	9.233	11.23	13.06	4.616	4.211	4.082
100.0%				∞			
Order m	1	2	3	4	2	3	4
τ^*	τ	τ	τ	τ	$\frac{1}{2}\tau$	$\frac{3}{8}\tau$	$\frac{5}{16}\tau$

Table A.8 – EMA filter settle times, relative to the original time constant τ, for filter cascades with modified time constant τ^*. Values shown for both constant ENBW (varying τ^* with filter order) and constant $\tau^* = \tau$. For the former, shaded cells denote cases where the configuration outperforms the corresponding SMA filter (table A.9). The stated times must elapse in order for the filter step response to reach the percentage of the target output value given in the left-hand column. The EMA filter output does not reach 100% of the target value after any finite time.

filter settle times are superior throughout, this is not generally the case when the differing ENBW for filter cascades are taken into account. Then, the EMA filters are more favorable for all but the largest target ratios.

- Higher order filters with steeper roll-off are better suited to reject the $2f$ modulation component. One would expect this to be counterbalanced by a slower settle time. This is indeed the case for the SMA filter. With the EMA filter, however, settle times of different order cascades are competitive, with higher orders m strictly superior for larger target ratios.

- As a consequence, the EMA filter should be preferred for most practical target ratios $R < 99\%$. Then, the highest order filter, $m = 4$, is a safe choice for $R \gtrsim 80\%$ that offers best $2f$ rejection, with comparable performance (within 10% of noise reduction) to lower-order filters. If only an SMA filter is available, or an extreme $R \approx 100\%$ is desired, the lowest possible order with sufficient $2f$ rejection[1] should be chosen.

- Many lock-in amplifiers have a front panel bar graph for the output channel levels. This may lead to a mistaken preference for high filter orders, as the flutter of

---

[1] By selecting a modulation frequency such that the filter averaging interval is an integer multiple of the $2f$ period, perfect rejection is possible in principle, independent of filter order. Some commercial lock-in amplifiers support such synchronous operation, including the models 7265 and SR830, but only at frequencies (< 10 Hz and < 200 Hz, respectively) that are generally too low for use as an STS modulation source.

Percentage of target value	SMA settle time t/τ						
	Constant τ				Constant ENBW		
$1 - e^{-1} \approx 63.2\%$	1.264	2.284	3.357	4.404	1.523	1.846	2.111
$1 - e^{-2} \approx 86.5\%$	1.729	2.959	4.134	5.303	1.973	2.274	2.542
$1 - e^{-3} \approx 95.0\%$	1.900	3.369	4.663	5.909	2.246	2.565	2.832
50.0%	1.000	2.000	3.000	4.000	1.333	1.650	1.917
90.0%	1.800	3.106	4.313	5.506	2.070	2.372	2.640
99.0%	1.980	3.717	5.217	6.600	2.478	2.869	3.163
99.9%	1.998	3.911	5.637	7.213	2.607	3.100	3.458
100.0%	2.000	4.000	6.000	8.000	2.667	3.300	3.835
Order m	1	2	3	4	2	3	4
τ^*	τ	τ	τ	τ	$\frac{2}{3}\tau$	$\frac{11}{20}\tau$	$\frac{151}{315}\tau$

Table A.9 – SMA filter settle times, relative to the original time constant τ, for filter cascades of order m, with modified time constant τ^*. Values shown for both constant ENBW (varying τ^* with filter order) and constant $\tau^* = \tau$. For the former, shaded cells denote cases where the configuration outperforms the corresponding EMA filter (table A.8). The stated times must elapse in order for the filter step response to reach the percentage of the target output value given in the left-hand column.

high-frequency noise components appears subjectively more striking than the same power in low-frequency noise.

For the same dwell time, a lower R involves a higher time constant, which reduces statistical noise, but lowers the rejection of transient pulses when advancing to the next data point, and the influence of previous filter input values associated with previous data points. The effect of latter on the spectrum can be modeled by sampling the pulse response of the filter with a sample period of t_D, and convolving an ideal spectrum or linescan with this pulse response. The result is a smoothed curve with features shifted toward the ramp direction. This may falsify the energy positions of spectral features in STS. As a method to ascertain the extent of this effect, spectra or linescans can be obtained pairwise, with ramps in either direction, comparing shapes and positions of features.

Lock-in amplifier comparison. In the final section, two instruments are assessed for their suitability in STS applications. These are the Model 7265[2] and the SR830[3]. Both are dual-phase lock-in amplifiers that can generate and output a reference signal, have selectable time constants and filter roll-offs between 6 and 24 dB, and can demodulate to higher harmonics. For the test, the modulation signal is gated with an external low-frequency square wave, and then fed into the respective input channels. The magnitude

---

[2] AMETEK Inc. (Signal Recovery), Oak Ridge, TN, USA

[3] Stanford Research Systems, Inc., Sunnyvale, CA, USA

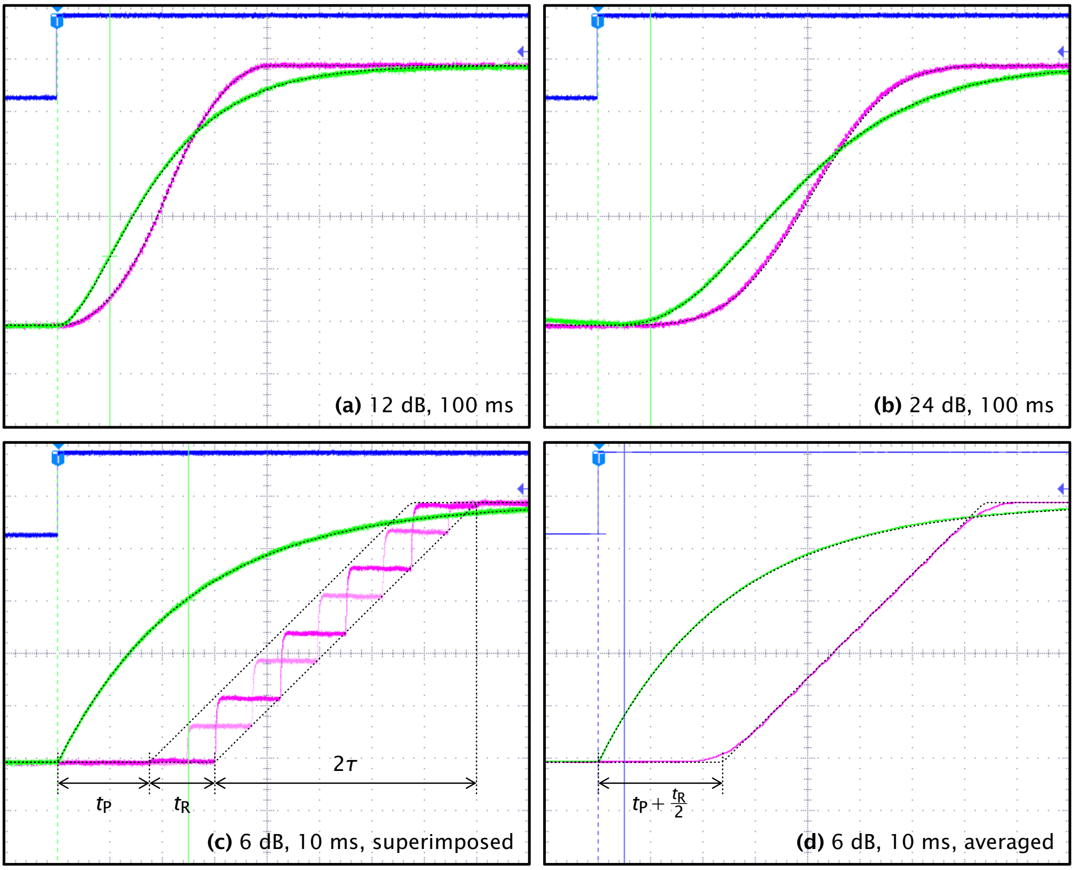

(a) 12 dB, 100 ms

(b) 24 dB, 100 ms

(c) 6 dB, 10 ms, superimposed

(d) 6 dB, 10 ms, averaged

Figure A.10 – Comparison of commercial lock-in amplifiers (annotated oscilloscope traces). Response of models 7265 (purple) and SR830 (green) to a gated 10 kHz oscillator. Scope is edge-triggered on gate signal (blue). Dashed lines show theoretical filter step responses given in tables A.6 and A.5. **(a,b)** The higher-order demodulation filters in the devices ($\tau = 100$ ms, $m = 2, 4$) match the step response curves of the model filters. **(c)** Two superimposed bursts, $\tau = 10$ ms, $m = 1$. Model 7265 demonstrates pipeline delay $t_P \approx 7$ ms and quantization noise when output refresh (t_R) and gate periods are incommensurate. **(d)** Averaging over a number of bursts reduces this quantization noise.

output channels are displayed on an oscilloscope, triggered on the rising edge of the gate signal. The obtained oscilloscope traces are reproduced in fig. A.10.

The top row of fig. A.10 shows measurements of the output signal with a time constant of $\tau = 100$ ms, at an overview timescale, for different filter roll-offs. The dashed lines show the expected step response functions for SMA and EMA filter cascades of the same order. The good agreement indicates that the demodulators are characterized well by the respective descriptions of the filters.

The bottom row shows close-up traces for the 6 dB filter, for a lower time constant of

$\tau = 10$ ms, more relevant to everyday STS applications. This establishes that the 7265's FIR filter indeed has equally-weighted coefficients. Fig. A.10c shows two superimposed traces. The output of the SR830 shows an immediate reaction to the stimulus, at an update rate of 256 kHz. In contrast, the 7265 exhibits a pipeline delay of $t_{\mathrm{P}} \approx 7$ ms. Also, it has an upper limit of $1/t_{\mathrm{R}} = 20$ Hz for the update rate, which, when incommensurate with the gate signal (or the dwell period in an actual STS experiment), leads to quantization noise on the rising slope of the step response. Elimination of this noise source requires a target ratio of $R = 100\%$, and thus, a dwell time of $t_{\mathrm{D}} \geq t_{\mathrm{P}} + 2m\tau$. This results in a significant experimental slowdown for little gain; The pipeline delay alone amounts to a 15 minute increase in acquisition time for a standard, 256×256 pixel bidirectional $\mathrm{d}I/\mathrm{d}V$ map. An alternative, fast signal path is available, with an update rate of 166 kHz, but its filter is restricted to $\tau \leq 640$ µs and 6 dB roll-off, which is insufficient to reject the $2f$ response.

This illustrates that in STS applications, fast reaction times are a necessity for a lock-in amplifier, whether commercial or home-built. While the 7265 is undoubtedly an excellent device for many applications, even a few milliseconds of pipeline delay, not readily apparent from the specification sheet, prove very inconvenient in STS.

Appendix B

The Imaginary Time Propagation method

The calculation of eigenfunctions and eigenenergies for a particular Hamiltonian is a cornerstone of numerical quantum mechanics, and has been approached by a variety of methods. For this work, the imaginary time propagation (ITP) technique [153] to first order on a finite grid was used. This method is easy to implement, sufficiently fast for the size of the systems considered, and largely devoid of implementational pitfalls.

B.1 Basic principle

In the waveguide problem, the stationary Schrödinger equation is Laplace's equation with Dirichlet boundary conditions defining the allowed region for the wavefunctions. The ITP method has previously been used to calculate the eigenspectrum of a hexagonal waveguide to high precision [114], and those results, and the closed-form solutions, can serve to verify the implementation.

Solving the eigenvalue problem for a time-independent Hamiltonian involves a separable Schrödinger equation

$$\hat{H}\psi(\vec{r},t) = \mathrm{i}\hbar\frac{\partial}{\partial t}\psi(\vec{r},t) \quad \text{with} \quad \hat{H} = -\frac{\hbar^2}{2m}\Delta \tag{B.1}$$

that leads to stationary solutions $\psi_j(\vec{r},0)$ defined by

$$\hat{H}\psi_j(\vec{r},0) = E_j\psi(\vec{r},0), \tag{B.2}$$

with eigenenergies E_j and a temporal evolution given by

$$\psi_j(\vec{r},t) = \exp\left(\frac{-\mathrm{i}\hat{H}t}{\hbar}\right)\psi_j(\vec{r},0). \tag{B.3}$$

$\hat{H}$ is a Hermitean operator, hence its eigenvalues are real numbers, and the eigenfunctions can also be expressed as real-valued functions that form a basis of the underlying Hilbert space. Assuming an initial state of the system at $t = 0$, expressed in terms of these basis functions,

$$\psi(\vec{r},0) = \sum_j a_j \psi_j(\vec{r},0) \quad \text{with} \quad \hat{H}\psi_j(\vec{r},0) = E_j \psi_j(\vec{r},0), \tag{B.4}$$

(B.3) gives a time dependence of

$$\psi(\vec{r},t) = \exp\left(\frac{-\mathrm{i}\hat{H}t}{\hbar}\right)\psi(\vec{r},0) = \sum_j a_j \exp\left(\frac{-\mathrm{i}E_j t}{\hbar}\right)\psi_j(\vec{r},0). \tag{B.5}$$

Inserting an imaginary time value $t = -\mathrm{i}\tau$ into (B.5) gives

$$\psi(\vec{r},-\mathrm{i}\tau) = \exp\left(\frac{-\hat{H}\tau}{\hbar}\right)\psi(\vec{r},0) = \sum_j a_j \exp\left(\frac{-E_j\tau}{\hbar}\right)\psi_j(\vec{r},0). \tag{B.6}$$

Hence, applying this *imaginary time propagation* (ITP) operator $\exp\left(-\hat{H}\tau\big/\hbar\right)$ to a linear combination of eigenstates reduces each component by a factor that depends exponentially on its eigenenergy, attenuating high-energy states more than low-energy states. Since the operator is not unitary, the resulting wavefunction needs to be renormalized, defining

$$\nu_\tau(\vec{r}) := \frac{\psi(\vec{r},-\mathrm{i}\tau)}{|\psi(\vec{r},-\mathrm{i}\tau)|}. \tag{B.7}$$

In the limit $\tau \to \infty$, if the lowest-eigenenergy state ψ_ℓ, for which $a_\ell \neq 0$, is non-degenerate, the normalized wavefunction $\nu_\tau(\vec{r})$ converges toward that state,

$$\lim_{\tau\to\infty} \nu_\tau(\vec{r}) = \frac{a_\ell}{|a_\ell|}\psi_\ell(\vec{r},0) \quad \text{with } \ell \text{ such that} \quad E_\ell = \min_j\left\{E_j \,\middle|\, a_j \neq 0\right\}. \tag{B.8}$$

Otherwise, it converges to a lowest-eigenenergy mixed state,

$$\lim_{\tau\to\infty} \nu_\tau(\vec{r}) = \frac{\sum_{\ell\in L} a_\ell \psi_\ell(\vec{r},0)}{\sqrt{\sum_{\ell\in L} |a_\ell|^2}} \quad \text{with} \quad L = \left\{\ell \,\middle|\, E_\ell = \min_j\left\{E_j \,\middle|\, a_j \neq 0\right\}\right\}. \tag{B.9}$$

Hence, if the initial state is setup properly ($a_0 \neq 0$), taking this limit yields the ground state ψ_0 of the system. The next state (and higher states) can iteratively be obtained by using an initial state that has the ground state (and all other lower eigenstates) removed, *e.g.*, by Gram–Schmidt orthogonalization. The eigenenergies can be obtained by

$$E_j = \left\langle \psi_j(\vec{r},0) \,\middle|\, \hat{H}\psi_j(\vec{r},0)\right\rangle. \tag{B.10}$$

Finite differences and finite grid. For a practical implementation of this method, the region of interest is overlaid by a regular grid on which the wavefunction is sampled. The calculation takes place on the finite number of grid points within the region, while points outside the region are treated implicitly, according to the boundary conditions. As an exponentiated Hamiltonian, the ITP operator contains higher derivatives to arbitrary order. For a practical implementation, it may be Taylor expanded to, for instance, first order,

$$\exp\left(-\tau\hat{H}\big/\hbar\right) \approx 1 - \frac{\tau}{\hbar}\hat{H}, \tag{B.11}$$

and applied iteratively. For a mixed state, such as the one in (B.4), m successive steps give

$$\left[1 - \frac{\tau}{\hbar}\hat{H}\right]^m \psi(\vec{r},0) = \left[1 - \frac{\tau}{\hbar}\hat{H}\right]^m \sum_j a_j \psi_j(\vec{r},0) = \sum_j a_j \left[1 - \frac{\tau}{\hbar}E_j\right]^m \psi_j(\vec{r},0). \tag{B.12}$$

Evidently, with increasing m, the square-bracketed prefactors in (B.12) diverge for all terms where $\tau E_j > 2\hbar$, *i.e.*, never for any $\tau > 0$ when the spectrum is unbounded.

On a finite grid, however, the spectrum is bounded and likewise, an upper bound E_{max} exists for the eigenenergies. The prefactors converge for $\tau < 2\hbar/E_{\mathrm{max}}$, if (B.12) is taken alone. The renormalization (B.7) further reduces this convergence range. Formally, $\tau = 2\hbar/(E_{\mathrm{max}} + E_{\ell+1})$ provides fastest convergence for the ℓth eigenfunction, but this value depends on the eigenspectrum and is not known *a priori*. $\tau \lesssim \hbar/E_{\mathrm{max}}$ is a conservative choice[1] that is valid for all eigenfunctions [114]. Choosing a lower τ impacts convergence speed, but not the validity of the method.

B.2 Implementation

The procedure is implemented as a computer program, written in C99 and OpenCL C, that sets up the initial state, performs the time propagation, normalization, and orthogonalization procedures, and monitors the eigenvalues for convergence. The implementation natively supports a square grid, on which the wavefunctions are sampled. A hexagonal grid is emulated by the square grid, using a linear transformation of coordinates as shown in fig. B.1.

Eigenfunctions are iteratively calculated in order of increasing energy (unless slow convergence is detected, see below), starting from the ground state. The wavefunction array is initially seeded with pseudorandom noise within the region. Along the pixels forming the region boundary, Dirichlet boundary conditions are enforced by pinning the respective wavefunction values to zero.

Numerical differentiation for the Hamiltonian is performed by the discrete Laplacian stencils (B.18) and (B.21). The inner product integral is implemented by the composite Newton-Cotes formulae in table B.2. When a double buffer is used for the candidate waveform, the procedure is inherently vectorizable, and maps well to GPGPU stream processing. It is only required to implement two kernels on the stream processing device, which are given in pseudocode below. The kernel

```
    K_ITS := function ( W0, &W1, &e, &n, dt )
```

---

[1] E_{max} can be determined by running a couple of iterations at a grossly overestimated τ where $\nu_\tau(\vec{r})$ quickly diverges toward the maximum state.

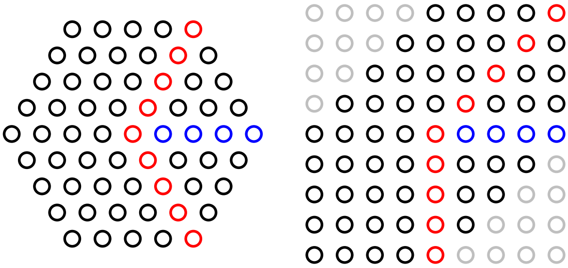

Figure B.1 – Representation of a hexagonal region of edge length 4 (left) as a region-of-interest within a 9×9 square grid (right), occupying $\gtrsim 75\%$ of grid points. Light gray grid points fall outside of the region.

```
    W1 := n*W0 - dt * H(n*W0) ;
    e := < H(n*W0) | n*W0 > ;
    n := < W1 | W1 > ;
  end
```

normalizes a given waveform using a precalculated factor, performs the imaginary time step, and calculates the eigenvalue and a factor for subsequent normalization. The kernel

```
  K_GS0 := function ( &W0, W1, W2, &m )
    W0 := W0 - m*W1 ;
    m := < W2 | W0 > ;
  end
```

serves as the building block for Gram-Schmidt orthogonalization. Other required housekeeping operations, such as copying, scaling and adding candidate waveforms, can also be performed by these two kernels, with suitable arguments specified.

Performance of the method is increased by several considerations. Formally, the orthogonalization needs to be done only once, for the initial state. In practice, eliminated wavefunctions tend to re-emerge from the quantization noise and then continue to be amplified every step, relative to the target wavefunction. Hence, the wavefunction needs to be re-orthogonalized after a certain number of steps. Similarly, normalization only needs to be done every couple of steps, before a loss of precision due to floating point underflow takes place.

The speed at which the process converges to a given eigenfunction is determined by the initial candidate function and the energetic distance of the next highest eigenfunctions. In the case of near-degenerate eigenfunctions[2], while a rough upper bound for the eigenenergy is obtained quickly, optimal unmixing of the near-degenerate states

---

[2] Due to the slight numerical inaccuracies that are intrinsic to calculations on a finite grid, this may also apply to actual incidental degeneracies. Rotational degeneracies sharing the grid symmetry are unaffected.

may take a prohibitively large number of iterations. This problem can be addressed by inserting an interlude of backtracking and mixing partially converged states, as follows:

An upper limit is placed on the maximum number of iterations permitted for each eigenstate. If for a state ψ_k, this limit is reached prior to convergence, it is marked as partially converged, and calculation proceeds regardless for the next few eigenstates (using the partially converged state in the Gram-Schmidt procedure). After that, the partially converged state ψ_k is linearly combined with these next higher states, with coefficients chosen by nonlinear optimization to minimize its eigenenergy. After this, the ITP procedure continues to refine the new ψ_k.

B.3 The discrete Laplacian

Square grid. The Laplacian of a 2-dimensional function f whose values are known on an evenly-spaced square grid can be approximated by discrete sums, the most basic and well-known of these is given by

$$\Delta_5 f(x,y) := \frac{1}{h^2}[f(x+h,y)+f(x-h,y)+f(x,y+h)+f(x,y-h)-4f(x,y)]. \tag{B.13}$$

This prescription, and others, are obtained by proposing a suitable ansatz, replacing f by its Taylor expansion on both sides, and then, starting from the lowest order, comparing coefficients. An alternative visual representation is in the form of a two-dimensional stencil. For the approximation (B.13), this appears as

$$\Delta_5 := \begin{pmatrix} & 1 & \\ 1 & -4 & 1 \\ & 1 & \end{pmatrix}. \tag{B.14}$$

To obtain the approximate Laplacian, the two-dimensional convolution with this stencil is calculated. The order to which such an approximation is exact can also be obtained from the Taylor series. For (B.14), also known as the 5-point quincunx stencil, this is

$$\begin{aligned} \Delta_5 f &= \frac{\partial^2 f}{\partial x^2} + \frac{\partial^2 f}{\partial y^2} + \frac{h^2}{12}\left(\frac{\partial^4 f}{\partial x^4} + \frac{\partial^4 f}{\partial y^4}\right) + \frac{h^4}{360}\left(\frac{\partial^6 f}{\partial x^6} + \frac{\partial^6 f}{\partial y^6}\right) + \mathcal{O}\left(h^6\right) \\ &= \Delta f + \mathcal{O}\left(h^2\right). \end{aligned} \tag{B.15}$$

Another option, the 5-point cross stencil, uses the diagonal neighbors of each point,

$$\Delta_\times := \begin{pmatrix} \frac{1}{2} & & \frac{1}{2} \\ & -2 & \\ \frac{1}{2} & & \frac{1}{2} \end{pmatrix}, \tag{B.16}$$

with

$$\begin{aligned}\Delta_\times f = {}& \frac{\partial^2 f}{\partial x^2} + \frac{\partial^2 f}{\partial y^2} + \frac{h^2}{12}\left(\frac{\partial^4 f}{\partial x^4} + 6\frac{\partial^4 f}{\partial x^2 \partial y^2} + \frac{\partial^4 f}{\partial y^4}\right) \\ & + \frac{h^4}{360}\left(\frac{\partial^6 f}{\partial x^6} + 15\frac{\partial^6 f}{\partial x^4 \partial y^2} + 15\frac{\partial^6 f}{\partial x^2 \partial y^4} + \frac{\partial^6 f}{\partial y^6}\right) + \mathcal{O}\left(h^6\right).\end{aligned} \tag{B.17}$$

For any γ, the convex combination $(1-\gamma)\Delta_5 + \gamma\Delta_\times$ of these is also usable. Choosing $\gamma = \frac{1}{3}$ yields the 9-point compact stencil

$$\Delta_9 := \begin{pmatrix} \frac{1}{6} & \frac{2}{3} & \frac{1}{6} \\ \frac{2}{3} & -\frac{10}{3} & \frac{2}{3} \\ \frac{1}{6} & \frac{2}{3} & \frac{1}{6} \end{pmatrix}, \tag{B.18}$$

which is remarkable in having a lowest-order error term expressible as an iterated Laplacian,

$$\begin{aligned}\Delta_9 f = {}& \frac{\partial^2 f}{\partial x^2} + \frac{\partial^2 f}{\partial y^2} + \frac{h^2}{12}\left(\frac{\partial^4 f}{\partial x^4} + 2\frac{\partial^4 f}{\partial x^2 \partial y^2} + \frac{\partial^4 f}{\partial y^4}\right) \\ & + \frac{h^4}{360}\left(\frac{\partial^6 f}{\partial x^6} + 5\frac{\partial^6 f}{\partial x^4 \partial y^2} + 5\frac{\partial^6 f}{\partial x^2 \partial y^4} + \frac{\partial^6 f}{\partial y^6}\right) + \mathcal{O}\left(h^6\right) \\ = {}& \Delta f + \frac{h^2}{12}\Delta^2 f + \mathcal{O}\left(h^4\right).\end{aligned} \tag{B.19}$$

This property is convenient for solving Poisson's equation, where these terms vanish by definition, but also for the imaginary time step technique. For pure eigenstates f_j, where $\Delta f_j = E_j f_j$, the Δ_9 stencil misestimates the Laplacian by a factor

$$\Delta_9 f_j = \left[1 + \frac{h^2 E_j}{12} + \mathcal{O}\left(h^4\right)\right]\Delta f_j. \tag{B.20}$$

During the iteration, this results in a deviation of the effective time step size, without disturbing the result once convergence is ensured. In the end, the determined eigenenergies are off by the same known factor. This can easily be corrected, increasing the accuracy by two orders.

Hexagonal grid. Calculations can also be done on a evenly spaced hexagonal grid, with a nearest-neighbor distance of h. The canonical 7-point stencil Δ_7 for the Laplacian then reads

$$\Delta_7 := \begin{pmatrix} & \frac{2}{3} & \frac{2}{3} \\ \frac{2}{3} & -4 & \frac{2}{3} \\ \frac{2}{3} & \frac{2}{3} & \end{pmatrix}. \tag{B.21}$$

Similar to the Δ_9 stencil shown above, the term in h^2 can be expressed by a higher Laplacian,

$$\begin{aligned}\Delta_7 f &= \frac{\partial^2 f}{\partial x^2} + \frac{\partial^2 f}{\partial y^2} + \frac{h^2}{16}\left(\frac{\partial^4 f}{\partial x^4} + 2\frac{\partial^4 f}{\partial x^2 \partial y^2} + \frac{\partial^4 f}{\partial y^4}\right) \\ &\quad + \frac{h^4}{640}\left(\frac{11}{9}\frac{\partial^6 f}{\partial x^6} + \frac{5}{3}\frac{\partial^6 f}{\partial x^4 \partial y^2} + 5\frac{\partial^6 f}{\partial x^2 \partial y^4} + \frac{\partial^6 f}{\partial y^6}\right) + \mathcal{O}\left(h^6\right) \\ &= \Delta f + \frac{h^2}{16}\Delta^2 f + \mathcal{O}\left(h^4\right).\end{aligned} \tag{B.22}$$

Higher orders. In principle, larger stencils can be designed for any desired order, but with the higher number of grid points involved, handling points near the boundaries becomes increasingly awkward. Some additional stencils of same or higher accuracy are given below. Operating on the square grid, these are $\Delta_{9\mathrm{W}}$ (the wide 9-point variant constructed from a higher order approximation [1] of the 1-dimensional second derivative),

$$\Delta_{9\mathrm{W}} := \begin{pmatrix} & & -\frac{1}{12} & & \\ & & \frac{4}{3} & & \\ -\frac{1}{12} & \frac{4}{3} & -5 & \frac{4}{3} & -\frac{1}{12} \\ & & \frac{4}{3} & & \\ & & -\frac{1}{12} & & \end{pmatrix} \tag{B.23}$$

with

$$\Delta_{9\mathrm{W}} f = \Delta f - \frac{h^4}{90}\left(\frac{\partial^6 f}{\partial x^6} + \frac{\partial^6 f}{\partial y^6}\right) + \mathcal{O}\left(h^6\right), \tag{B.24}$$

stencil Δ_{13} (diamond-shaped area),

$$\Delta_{13} := \begin{pmatrix} & & \frac{1}{60} & & \\ & \frac{1}{5} & \frac{8}{15} & \frac{1}{5} & \\ \frac{1}{60} & \frac{8}{15} & -3 & \frac{8}{15} & \frac{1}{60} \\ & \frac{1}{5} & \frac{8}{15} & \frac{1}{5} & \\ & & \frac{1}{60} & & \end{pmatrix} \tag{B.25}$$

with

$$\Delta_{13} f = \Delta f + \frac{h^2}{10}\Delta^2 f + \frac{h^4}{180}\Delta^3 f + \mathcal{O}\left(h^6\right), \tag{B.26}$$

and Δ_{25} (5×5 square area),

$$\Delta_{25} := \begin{pmatrix} \frac{1}{2520} & \frac{4}{315} & \frac{1}{30} & \frac{4}{315} & \frac{1}{2520} \\ \frac{4}{315} & \frac{8}{45} & \frac{8}{21} & \frac{8}{45} & \frac{4}{315} \\ \frac{1}{30} & \frac{8}{21} & -\frac{173}{70} & \frac{8}{21} & \frac{1}{30} \\ \frac{4}{315} & \frac{8}{45} & \frac{8}{21} & \frac{8}{45} & \frac{4}{315} \\ \frac{1}{2520} & \frac{4}{315} & \frac{1}{30} & \frac{4}{315} & \frac{1}{2520} \end{pmatrix} \tag{B.27}$$

with

$$\Delta_{25} f = \Delta f + \frac{h^2}{7}\Delta^2 f + \frac{4h^4}{315}\Delta^3 f + \frac{h^6}{1260}\Delta^4 f + \mathcal{O}\left(h^8\right). \tag{B.28}$$

On the hexagonal grid, Δ_{H19} is given by

$$\Delta_{\mathrm{H19}} := \begin{pmatrix} & & \frac{1}{70} & \frac{16}{315} & \frac{1}{70} \\ & \frac{16}{315} & \frac{16}{35} & \frac{16}{35} & \frac{16}{315} \\ \frac{1}{70} & \frac{16}{35} & -\frac{47}{15} & \frac{16}{35} & \frac{1}{70} \\ \frac{16}{315} & \frac{16}{35} & \frac{16}{35} & \frac{16}{315} & \\ \frac{1}{70} & \frac{16}{315} & \frac{1}{70} & & \end{pmatrix} \tag{B.29}$$

with

$$\Delta_{H19} f = \Delta f + \frac{3h^2}{28}\Delta^2 f + \frac{3h^4}{140}\Delta^3 f + \frac{3h^6}{8960}\Delta^4 f + \mathcal{O}\left(h^8\right). \tag{B.30}$$

B.4 Numerical quadrature

To calculate the inner product of two waveforms, an integration across the bounded region must be performed. Naïvely, this can be done by simply summing up the function values across all enclosed grid points. Higher order integration methods may offer better results.

For one-dimensional integrands that are known on N evenly-spaced grid points $jh, j = 0 \ldots N-1$, Newton–Cotes quadrature formulae [188] involve a weighted sum of the function values,

$$\int_0^{(N-1)h} f(x)dx \approx h \sum_{j=0}^{N-1} q_{N,j} f(jh). \tag{B.31}$$

The weights can be obtained by symbolic Taylor expansion of the integrand. Sets of coefficients can be constructed that accurately deal with polynomials up to order $N-1$. For non-polynomial integrands, however, higher order does not necessarily mean higher accuracy.

N	Order	$q_{N,i}, i = 0\ldots N-1$	Common name
2	1	$\frac{1}{2}$ $\frac{1}{2}$	Trapezoid
3	3	$\frac{1}{3}$ $\frac{4}{3}$ $\frac{1}{3}$	Simpson's
4		$\frac{3}{8}$ $\frac{9}{8}$ $\frac{9}{8}$ $\frac{3}{8}$	Simpson's $\frac{3}{8}$
5	3	$\frac{3}{8}$ $\frac{7}{6}$ $\frac{11}{12}$ $\frac{7}{6}$ $\frac{3}{8}$	
≥ 6		$\frac{3}{8}$ $\frac{7}{6}$ $\frac{23}{24}$ $*$ $\frac{23}{24}$ $\frac{7}{6}$ $\frac{3}{8}$	
5	5	$\frac{14}{45}$ $\frac{64}{45}$ $\frac{8}{15}$ $\frac{64}{45}$ $\frac{14}{45}$	Boole's
6		$\frac{95}{288}$ $\frac{125}{96}$ $\frac{125}{144}$ $\frac{125}{144}$ $\frac{125}{96}$ $\frac{95}{288}$	
7		$\frac{95}{288}$ $\frac{317}{240}$ $\frac{359}{480}$ $\frac{433}{360}$ $\frac{359}{480}$ $\frac{317}{240}$ $\frac{95}{288}$	
8		$\frac{95}{288}$ $\frac{317}{240}$ $\frac{23}{30}$ $\frac{1559}{1440}$ $\frac{1559}{1440}$ $\frac{23}{30}$ $\frac{317}{240}$ $\frac{95}{288}$	
9		$\frac{95}{288}$ $\frac{317}{240}$ $\frac{23}{30}$ $\frac{793}{720}$ $\frac{77}{80}$ $\frac{793}{720}$ $\frac{23}{30}$ $\frac{317}{240}$ $\frac{95}{288}$	
≥ 10		$\frac{95}{288}$ $\frac{317}{240}$ $\frac{23}{30}$ $\frac{793}{720}$ $\frac{157}{160}$ $*$ $\frac{157}{160}$ $\frac{793}{720}$ $\frac{23}{30}$ $\frac{317}{240}$ $\frac{95}{288}$	

Table B.2 – Newton–Cotes coefficients for 3rd and 5th order target accuracy for integrating a function known at N evenly-spaced points. Common names for the rules from established literature are given, where applicable. The asterisk ($*$) denotes a run of consecutive weights of 1.

For a given maximum order, the integrand can be approximated by a piecewise polynomial. For any number of grid points, the weights employed are given in table B.2. Where applicable, the rules' common names are noted. The coefficients are designed to be accurate to the desired order (given sufficient grid points), while deviating from 1 only close to the boundaries. This is in contrast to, *e.g.*, the extended Simpson's rule, whose weights oscillate throughout. Two-dimensional quadrature can in principle be done by tiling the region with bivariate polynomial approximants, and then deriving proper weights from those. However, the treatment of tiles containing boundary points becomes a big issue, with each local geometry requiring a custom set of coefficients. If both the integrand and the shape of the region are reasonably well-behaved, a workaround involves iterative integration. Each grid row is integrated first, where contiguous runs of interior points are treated with the Newton–Cotes coefficients given above. Then, these row integrals are similarly accumulated.

Acknowledgments

This work could not have been possible without the support and contributions of various individuals. Firstly, I wish to express my gratitude to my supervisor, Prof. Richard Berndt, for the opportunity to perform this work in his group, for his patient encouragement and spot-on suggestions, and for fostering a pleasant work environment.

I am also indebted to my co-supervisor, Prof. Jörg Kröger, who designed and oversaw the instrument that made this work possible, and under whose guidance the experiments were performed.

I'd like to thank all my colleagues for providing a marvelous environment over the years, and for their experience, assistance, and enlightening break room conversations. Particular thanks go out to my coworkers in the lab, Dr. Thomas von Hofe, Dr. Nicolas Néel, Dr. Martin Ziegler, and Dr. Alexander Sperl, and my long-time office mates Peter-Jan Peters and Dr. Sujoy Karan, for fruitful discussions and tolerating my occasional monologue.

For further discussions and valuable input I'd like to thank Dr. Thomas Jürgens, Dr. Alexander Weismann, Dr. Michael Becker, Dr. Laurent Limot (U Strasbourg) and Prof. Aitor Mugarza (ICN2 Barcelona). For support on administrative matters, my gratitude goes to Monika Seeger and Ursula Goetzke, and on technical matters, to Jörg Neubauer, Dr. Jürgen Rathlev, and the excellent staff of our local workshop.

Additionally, I am indebted to Dr. Simon Crampin (U Bath), Dr. Nicolás Lorente (CFM San Sebastián), Dr. Riccardo Rurali (ICMAB Barcelona), and Prof. Bernd Hartke, for all the invaluable theoretical insights. I thank Prof. Lutz Kipp, Wilfried Krüger, Prof. Moritz Sokolowski (U Bonn), and Prof. Enrique Ortega (UPV San Sebastián), for kindly supplying some of the specimens used in this work. I gratefully acknowledge financial support for this work by the Deutsche Forschungsgemeinschaft and the European Science Foundation.

Finally, and emphatically, I would like to thank my parents, Renate and Dr. Ingo Jensen, for their patient and unwavering support.

Bibliography

[1] M. Abramowitz and I. A. Stegun, *Handbook of mathematical functions with formulas, graphs and mathematical tables*, United States Department of Commerce, National Bureau of Standards, Washington, DC, USA, 1972.

[2] I. Adawi, *Electron-density oscillations in a general potential*, Phys. Rev. **146** (2), 379–386 (1966), DOI: `10.1103/PhysRev.146.379`.

[3] T. Ando, A. B. Fowler, and F. Stern, *Electronic properties of two-dimensional systems*, Rev. Mod. Phys. **54** (2), 437–672 (1982), DOI: `10.1103/RevModPhys.54.437`.

[4] T. Andreev, I. Barke, and H. Hövel, *Adsorbed rare-gas layers on Au(111): Shift of the Shockley surface state studied with ultraviolet photoelectron spectroscopy and scanning tunneling spectroscopy*, Phys. Rev. B **70** (20), 205426(13) (2004), DOI: `10.1103/PhysRevB.70.205426`.

[5] E. Anglada, J. M. Soler, J. Junquera, and E. Artacho, *Systematic generation of finite-range atomic basis sets for linear-scaling calculations*, Phys. Rev. B **66** (20), 205101(4) (2002), DOI: `10.1103/PhysRevB.66.205101`.

[6] R. J. Asaro and W. A. Tiller, *Interface morphology development during stress corrosion cracking: Part I. Via surface diffusion*, Metall. Trans. **3** (7), 1789–1796 (1972), DOI: `10.1007/BF02642562`.

[7] Ph. Avouris, I.-W. Lyo, R. E. Walkup, and Y. Hasegawa, *Real space imaging of electron scattering phenomena at metal surfaces*, J. Vac. Sci. Technol. B **12** (3), 1447–1455 (1994), DOI: `10.1116/1.587314`.

[8] S. W. Bailey, V. A. Frank-Kamenetskii, S. Goldsztaub, A. Kato, H. Schulz, H. F. W. Taylor, M. Fleischer, and A. J. C. Wilson, *Report of the International Mineralogical Association (IMA)–International Union of Crystallography (IUCr) Joint Committee on Nomenclature*, Acta Cryst. A **33**, 681–684 (1977), DOI: `10.1107/S056773947701703`.

[9] J. Bardeen, *Tunnelling from a many-particle point of view*, Phys. Rev. Lett. **6** (2), 57–59 (1961), DOI: `10.1103/PhysRevLett.6.57`.

[10] M. Barmatz, *Elastic measurements in one and two-dimensional compounds*, Proc. 1974 Ultrason. Symp. 461–467 (1974), DOI: `10.1109/ULTSYM.1974.196379`.

[11] J. V. Barth, H. Brune, G. Ertl, and R. J. Behm, *Scanning tunneling microscopy observations on the reconstructed Au(111) surface: Atomic structure, long-range superstructure, rotational domains, and surface defects*, Phys. Rev. B **42** (15), 9307–9318 (1990), DOI: `10.1103/PhysRevB.42.9307`.

[12] A. Bartolini, F. Ercolessi, and E. Tosatti, *'Magic' vicinal surfaces stabilized by reconstruction*, Phys. Rev. Lett. **63** (8), 872–875 (1989), DOI: `10.1103/PhysRevLett.63.872`.

[13] M. El-Batanouny, S. Burdick, K. M. Martini, and P. Stancioff, *Double-Sine-Gordon solitons: A model for misfit dislocations on the Au(111) reconstructed surface*, Phys. Rev. Lett. **58** (26), 2762–2765 (1987), DOI: `10.1103/PhysRevLett.58.2762`.

[14] E. Bauer, *Phänomenologische Theorie der Kristallabscheidung an Oberflächen. I*, Z. Kristallogr. **110** (1–6), 372–394 (1958), DOI: `10.1524/zkri.1958.110.1-6.372`.

[15] L. Bauer and E. L. Reiss, *Cutoff wavenumbers and modes of hexagonal waveguides*, SIAM J. Appl. Math. **35** (6), 508–514 (1978), DOI: `10.1137/0135042`.

[16] R. S. Becker, J. A. Golovchenko, and B. S. Swartzentruber, *Electron interferometry at crystal surfaces*, Phys. Rev. Lett. **55** (9), 987–990 (1985), DOI: `10.1103/PhysRevLett.55.987`.

[17] G. Binnig, K. H. Frank, H. Fuchs, N. Garcia, B. Reihl, H. Rohrer, F. Salvan, and A. R. Williams, *Tunneling spectroscopy and inverse photoemission: Image and field states*, Phys. Rev. Lett. **55** (9), 991–994 (1985), DOI: `10.1103/PhysRevLett.55.991`.

[18] G. Binnig, C. F. Quate, and C. Gerber, *Atomic force microscope*, Phys. Rev. Lett. **56** (9), 930–933 (1986), DOI: `10.1103/PhysRevLett.56.930`.

[19] G. Binnig and H. Rohrer, *Scanning tunneling microscopy*, Helv. Phys. Acta **55** (6), 726–735 (1982), DOI: `10.5169/seals-115309`.

[20] G. Binnig, H. Rohrer, C. Gerber, and E. Weibel, *Tunneling through a controllable vacuum gap*, Appl. Phys. Lett. **40** (2), 178–180 (1982), DOI: `10.1063/1.92999`.

[21] G. Binnig, H. Rohrer, C. Gerber, and E. Weibel, *7×7 reconstruction on Si(111) resolved in real space*, Phys. Rev. Lett. **50** (2), 120–123 (1983), DOI: `10.1103/PhysRevLett.50.120`.

[22] K. B. Blodgett, *Monomolecular films of fatty acids on glass*, J. Am. Chem. Soc. **56** (2), 495 (1934), DOI: `10.1021/ja01317a513`.

[23] K. B. Blodgett, *Films built by depositing successive monomolecular layers on a solid surface*, J. Am. Chem. Soc. **57** (6), 1007–1022 (1935), DOI: `10.1021/ja01309a011`.

[24] M. Bode, *Spin-polarized scanning tunnelling microscopy*, Rep. Prog. Phys. **66** (4), 523–582 (2003), DOI: `10.1088/0034-4885/66/4/203`.

[25] M. Böhringer, W.-D. Schneider, R. Berndt, K. Glöckler, M. Sokolowski, and E. Umbach, *Corrugation reversal in scanning tunneling microscope images of organic molecules*, Phys. Rev. B **57** (7), 4081–4087 (1998), DOI: `10.1103/PhysRevB.57.4081`.

[26] A. Bondi, *Van der Waals volumes and radii*, J. Phys. Chem. **68** (3), 441–451 (1964), DOI: `10.1021/j100785a001`.

[27] V. Bostanov, R. Roussinova, and E. Budevski, *Multinuclear growth of dislocation-free planes in electrocrystallization*, J. Electrochem. Soc. **119** (10), 1346–1347 (1972), DOI: `10.1149/1.2403992`.

[28] K. Brandt and F. C. Laman, *Reproducibility and reliability of rechargeable lithium/molybdenum disulfide batteries*, J. Power Sources **25** (4), 265–276 (1989), DOI: `10.1016/0378-7753(89)85014-1`.

[29] K.-F. Braun and K.-H. Rieder, *Engineering electronic lifetimes in artificial atomic structures*, Phys. Rev. Lett. **88** (9), 096801(4) (2002), DOI: `10.1103/PhysRevLett.88.096801`.

[30] L. Brillouin, *La mécanique ondulatoire de Schrödinger; une méthode générale de résolution par approximations successives*, C. R. Hebd. Séanc. Acad. Sci. **183**, 24–26 (1926).

[31] L. Bürgi, O. Jeandupeux, H. Brune, and K. Kern, *Probing hot-electron dynamics at surfaces with a cold scanning tunneling microscope*, Phys. Rev. Lett. **82** (22), 4516–4519 (1999), DOI: `10.1103/PhysRevLett.82.4516`.

[32] L. Bürgi, O. Jeandupeux, A. Hirstein, H. Brune, and K. Kern, *Confinement of surface state electrons in Fabry–Pérot resonators*, Phys. Rev. Lett. **81** (24), 5370–5373 (1998), DOI: `10.1103/PhysRevLett.81.5370`.

[33] P. E. Burrows and S. R. Forrest, *Electroluminescence from trap-limited current transport in vacuum deposited organic light emitting devices*, Appl. Phys. Lett. **64** (17), 2285–2287 (1994), DOI: `10.1063/1.111645`.

[34] D. D. Chambliss and R. J. Wilson, *Ordered nucleation of Ni and Au islands on Au(111) studied by scanning tunneling microscopy*, J. Vac. Sci. Technol. B **9** (2), 933–937 (1991), DOI: `10.1116/1.585498`.

[35] D. D. Chambliss, R. J. Wilson, and S. Chiang, *Nucleation of ordered Ni island arrays on Au(111) by surface-lattice dislocations*, Phys. Rev. Lett. **66** (13), 1721–1724 (1991), DOI: `10.1103/PhysRevLett.66.1721`.

[36] M. Chelvayohan and C. H. B. Mee, *Work function measurements on (110), (100) and (111) surfaces of silver*, J. Phys. C **15** (10), 2305–2312 (1982), DOI: `10.1088/0022-3719/15/10/029`.

[37] C. J. Chen, *Theory of scanning tunneling spectroscopy*, J. Vac. Sci. Technol. A **6** (2), 319–322 (1988), DOI: `10.1116/1.575444`.

[38] T. Chen, S. Tessmer, J. R. Tucker, J. W. Lyding, and D. J. Van Harlingen, *Scanning tunneling microscopy and spectroscopy of thin film superconductor Pb*, J. Vac. Sci. Technol. B **9** (2), 1000–1005 (1991), DOI: `10.1116/1.585797`.

[39] I. Chizhov, A. Kahn, and G. Scoles, *Initial growth of 3,4,9,10-perylene-tetracarboxylic-dianhydride (PTCDA) on Au(111): A scanning tunneling microscopy study*, J. Cryst. Growth **208** (1–4), 449–458 (2000), DOI: `10.1016/S0022-0248(99)00382-6`.

[40] N. E. Christensen, *The band structure of silver and optical interband transitions*, Phys. Status Solidi B **54** (2), 551–563 (1972), DOI: `10.1002/pssb.2220540219`.

[41] E. V. Chulkov, V. M. Silkin, and P. M. Echenique, *Image potential states on metal surfaces: Binding energies and wave functions*, Surf. Sci. **437** (3), 330–352 (1999), DOI: `10.1016/S0039-6028(99)00668-8`.

[42] F. L. Claus, *Solid lubricants and self-lubricating solids*, Academic Press, New York, NY, USA, 1972.

[43] R. V. Coleman, B. Giambattista, P. K. Hansma, A. Johnson, W. W. McNairy, and C. G. Slough, *Scanning tunneling microscopy of charge-density waves in transition metal chalcogenides*, Adv. Phys. **37** (6), 559–644 (1988), DOI: `10.1080/00018738800101439`.

[44] *The Colour Index*, 3rd ed., Society of Dyers and Colourists, Bradford, UK and American Association of Textile Chemists and Colorists, Lowell, MA, USA, 1971–1992, ISBN: 0-901956-06-6.

[45] J. H. Coombs, J. K. Gimzewski, B. Reihl, J. K. Sass, and R. R. Schlittler, *Photon emission experiments with the scanning tunnelling microscope*, J. Microsc. **156** (2), 325–336 (1988), DOI: `10.1111/j.1365-2818.1988.tb01393.x`.

[46] C. R. Cosens, *A balance-detector for alternating-current bridges*, Proc. Phys. Soc. **46** (6), 818–823 (1934), DOI: `10.1088/0959-5309/46/6/310`.

[47] S. Crampin, H. Jensen, J. Kröger, L. Limot, and R. Berndt, *Resonator design for use in scanning tunneling spectroscopy studies of surface electron lifetimes*, Phys. Rev. B **72** (3), 035443(6) (2005), DOI: `10.1103/PhysRevB.72.035443`.

[48] S. Crampin, J. Kröger, H. Jensen, and R. Berndt, *Phase coherence length and quantum interference patterns at step edges*, Phys. Rev. Lett. **95** (2), 029701(1) (2005), DOI: `10.1103/PhysRevLett.95.029701`.

[49] S. Crampin, M. Nekovee, and J. E. Inglesfield, *Embedding method for confined quantum systems*, Phys. Rev. B **51** (11), 7318–7320 (1995), DOI: `10.1103/PhysRevB.51.7318`.

[50] M. F. Crommie, C. P. Lutz, and D. M. Eigler, *Confinement of electrons to quantum corrals on a metal surface*, Science **262** (5131), 218–220 (1993), DOI: `10.1126/science.262.5131.218`.

[51] W. P. Davey, *Precision measurements of the lattice constants of twelve common metals*, Phys. Rev. **25** (6), 753–761 (1925), DOI: `10.1103/PhysRev.25.753`.

[52] G. Decher, J. D. Hong, and J. Schmitt, *Buildup of ultrathin multilayer files by a self-assembly process: III. Consecutively alternating adsorption of anionic and cationic polyelectrolytes on charged surfaces*, Thin Solid Films **210–211**, 831–315 (1992), DOI: `10.1016/0040-6090(92)90417-A`.

[53] D. E. Eastman, *Geometrical and electronic structure of Si(001) and Si(111) surfaces: A status report*, J. Vac. Sci. Technol. **17** (1), 492–500 (1980), DOI: `10.1116/1.570492`.

[54] P. M. Echenique and J. B. Pendry, *The existence and detection of Rydberg states at surfaces*, J. Phys. C **11** (10), 2065–2075 (1978), DOI: `10.1088/0022-3719/11/10/017`.

[55] G. Ehrlich and F. G. Hudda, *Atomic view of surface self-diffusion: Tungsten on tungsten*, J. Chem. Phys. **44** (3), 1039–1049 (1966), DOI: `10.1063/1.1726787`.

[56] D. M. Eigler and E. K. Schweizer, *Positioning single atoms with a scanning tunnelling microscope*, Nature **344** (6266), 524–526 (1990), DOI: `10.1038/344524a0`.

[57] A. Eiguren, B. Hellsing, E. V. Chulkov, and P. M. Echenique, *Phonon-mediated decay of metal surface states*, Phys. Rev. B **67** (23), 235423(16) (2003), DOI: `10.1103/PhysRevB.67.235423`.

[58] A. Eiguren, B. Hellsing, F. Reinert, G. Nicolay, E. V. Chulkov, V. M. Silkin, S. Hüfner, and P. M. Echenique, *Role of bulk and surface phonons in the decay of metal surface states*, Phys. Rev. Lett. **88** (6), 066805(4) (2002), DOI: `10.1103/PhysRevLett.88.066805`.

[59] R. Eisenschitz and F. London, *Über das Verhältnis der van der Waalsschen Kräfte zu den homöopolaren Bindungskräften*, Z. Phys. **60** (7–8), 491–527 (1930), DOI: `10.1007/BF01341258`.

[60] F. Ercolessi, A. Bartolini, M. Garofalo, M. Parrinello, and E. Tosatti, *Molecular dynamics studies of gold surfaces*, Phys. Scr. **T19** (B), 399–404 (1987), DOI: `10.1088/0031-8949/1987/T19B/013`.

[61] M. P. Everson, L. C. Davis, R. C. Jaklevic, and W. Shen, *Effects of surface features upon the Au(111) surface state local density of states studied with scanning tunneling spectroscopy*, J. Vac. Sci. Technol. B **9** (2), 891–896 (1991), DOI: `10.1116/1.585490`.

[62] R. M. Feenstra, J. A. Stroscio, and A. P. Fein, *Tunneling spectroscopy of the Si(111)2×1 surface*, Surf. Sci. **181** (1–2), 295–306 (1987), DOI: `10.1016/0039-6028(87)90170-1`.

[63] P. Fenter, P. E. Burrows, P. Eisenberger, and S. R. Forrest, *Layer-by-layer quasi-epitaxial growth of a crystalline organic thin film*, J. Cryst. Growth **152** (1–2), 65–72 (1995), DOI: `10.1016/0022-0248(95)00064-X`.

[64] S. Fölsch, P. Hyldgaard, R. Koch, and K. H. Ploog, *Quantum confinement in monatomic Cu chains on Cu(111)*, Phys. Rev. Lett. **92** (5), 056803(4) (2004), DOI: `10.1103/PhysRevLett.92.056803`.

[65] S. R. Forrest, *Ultrathin organic films grown by organic molecular beam deposition and related techniques*, Chem. Rev. **97** (6), 1793–1896 (1997), DOI: `10.1021/cr941014o`.

[66] S. R. Forrest, M. L. Kaplan, and P. H. Schmidt, *Organic-on-inorganic semiconductor contact barrier diodes. I. Theory with applications to organic thin films and prototype devices*, J. Appl. Phys. **55** (6), 1492–1507 (1984), DOI: `10.1063/1.333407`.

[67] S. R. Forrest, M. L. Kaplan, and P. H. Schmidt, *Organic-on-inorganic semiconductor contact barrier diodes. II. Dependence on organic film and metal contact properties*, J. Appl. Phys. **56** (2), 543–551 (1984), DOI: `10.1063/1.333944`.

[68] R. H. Fowler and L. Nordheim, *Electron emission in intense electric fields*, Proc. R. Soc. London A **119** (781), 173–181 (1928), DOI: `10.1098/rspa.1928.0091`.

[69] Ya. I. Frenkel and T. A. Kontorova, *On the theory of plastic deformation and twinning*, Phys. Z. Sowjetunion **13**, 1–10 (1938).

[70] J. Friedel, *Metallic alloys*, Nuovo Cimento **7** (Suppl. 2), 287–311 (1958), DOI: `10.1007/BF02751483`.

[71] A. Fukui, H. Hasai, and A. Okiji, *Many-body effects on the lifetime of Shockley states on metal surfaces*, Surf. Sci. **493** (1–3), 671–679 (2001), DOI: `10.1016/S0039-6028(01)01281-X`.

[72] R. Gaisch, J. K. Gimzewski, B. Reihl, R. R. Schlittler, and M. Tschudy, *Low-temperature ultra-high-vacuum scanning tunneling microscope*, Ultramicroscopy **42–44**, 1621–1626 (1992), DOI: `10.1016/0304-3991(92)90495-6`.

[73] G. Gamov, *Zur Quantentheorie des Atomkernes*, Z. Phys. **51** (3–4), 204–212 (1928), DOI: `10.1007/BF01343196`.

[74] P. O. Gartland and B. J. Slagsvold, *Transitions conserving parallel momentum in photoemission from the (111) face of copper*, Phys. Rev. B **12** (10), 4047–4058 (1975), DOI: `10.1103/PhysRevB.12.4047`.

[75] T. K. Ghanty, V. N. Staroverov, P. R. Koren, and E. R. Davidson, *Is the hydrogen bond in water dimer and ice covalent?* J. Am. Chem. Soc. **122** (6), 1210–1214 (2000), DOI: `10.1021/ja9937019`.

[76] I. Giaever, *Energy gap in superconductors measured by electron tunneling*, Phys. Rev. Lett. **5** (4), 147–148 (1960), DOI: `10.1103/PhysRevLett.5.147`.

[77] K. Giesen, F. Hage, F. J. Himpsel, H. J. Riess, and W. Steinmann, *Binding energy of image-potential states: Dependence on crystal structure and material*, Phys. Rev. B **35** (3), 971–974 (1987), DOI: `10.1103/PhysRevB.35.971`.

[78] M. Giesen and T. L. Einstein, *Analysis of terrace width distributions on vicinal copper surfaces using the 'Wigner surmise': Comparison with Gaussian approach*, Surf. Sci. **449** (1-3), 191–206 (2000), DOI: `10.1016/S0039-6028(99)01254-6`.

[79] J. K. Gimzewski and R. Möller, *Transition from the tunneling regime to point contact studied using scanning tunneling microscopy*, Phys. Rev. B **36** (2), 1284–1287 (1987), DOI: `10.1103/PhysRevB.36.1284`.

[80] J. K. Gimzewski, B. Reihl, R. R. Schlittler, and M. A. R. Tschudy, *Problem-specific sample carriers*, IBM Tech. Disclosure Bull. **32** (8B), 247–249 (1990).

[81] K. Glöckler, C. Seidel, A. Soukopp, M. Sokolowski, E. Umbach, M. Böhringer, R. Berndt, and W.-D. Schneider, *Highly ordered structures and submolecular scanning tunnelling microscopy contrast of PTCDA and DM-PBDCI monolayers on Ag(111) and Ag(110)*, Surf. Sci. **405** (1), 1–20 (1998), DOI: `10.1016/S0039-6028(97)00888-1`.

[82] H.-J. Gossmann, F. W. Sinden, and L. C. Feldman, *Evolution of terrace size distributions during thin-film growth by step-mediated epitaxy*, J. Appl. Phys. **67** (2), 745–752 (1990), DOI: `10.1063/1.345754`.

[83] V. Grasso, ed., *Electronic structure and electronic transitions in layered materials*, Reidel, Dordrecht, The Netherlands, 1986.

[84] M. A. Grinfel'd, *Instability of the separation boundary between a non-hydrostatically stressed elastic body and a melt*, Sov. Phys. Dokl. **31** (10), 831–834 (1986).

[85] E. E. Gruber and W. W. Mullins, *On the theory of anisotropy of crystalline surface tension*, J. Phys. Chem. Solids **28** (5), 875–887 (1967), DOI: `10.1016/0022-3697(67)90017-0`.

[86] K. H. Gundlach, *Zur Berechnung des Tunnelstroms durch eine trapezförmige Potentialstufe*, Solid State Electron. **9** (10), 949–957 (1966), DOI: `10.1016/0038-1101(66)90071-2`.

[87] H. Haraldsen, *Contributions to the chemistry of the binary compounds of the transition elements*, Angew. Chem. Int. Ed. Engl. **5** (1), 58–66 (1966), DOI: `10.1002/anie.196605581`.

[88] J. M. E. Harper, T. H. Geballe, and F. J. DiSalvo, *Heat capacity of 2H–NbSe$_2$ at the charge density wave transition*, Phys. Lett. **54A** (1), 27–28 (1975), DOI: `10.1016/0375-9601(75)90592-7`.

[89] U. Harten, A. M. Lahee, J. P. Toennies, and C. Wöll, *Observation of a soliton reconstruction of Au(111) by high-resolution helium-atom diffraction*, Phys. Rev. Lett. **54** (24), 2619–2622 (1985), DOI: `10.1103/PhysRevLett.54.2619`.

[90] Y. Hasegawa and Ph. Avouris, *Direct observation of standing wave formation at surface steps using scanning tunneling spectroscopy*, Phys. Rev. Lett. **71** (7), 1071–1074 (1993), DOI: `10.1103/PhysRevLett.71.1071`.

[91] P. Heimann, H. Neddermeyer, and H. F. Roloff, *Ultraviolet photoemission for intrinsic surface states of the noble metals*, J. Phys. C **10** (1), L17–L22 (1977), DOI: `10.1088/0022-3719/10/1/004`.

[92] V. Heine and L. D. Marks, *Competition between pairwise and multi-atom forces at noble metal surfaces*, Surf. Sci. **165** (1), 65–82 (1986), DOI: `10.1016/0039-6028(86)90664-3`.

[93] E. J. Heller, M. F. Crommie, C. P. Lutz, and D. M. Eigler, *Scattering and absorption of surface electron waves in quantum corrals*, Nature **369** (3480), 464–466 (1994), DOI: `10.1038/369464a0`.

[94] I. Heyvaert, J. Krim, C. Van Haesendonck, and Y. Bruynseraede, *Surface morphology and kinetic roughening of Ag on Ag(111) studied with scanning tunneling microscopy*, Phys. Rev. E **54** (1), 349–353 (1996), DOI: `10.1103/PhysRevE.54.349`.

[95] T. von Hofe, *Electron dynamics of Cs covered Cu(111): A scanning tunneling spectroscopy investigation at low temperatures*, Dissertation, Christian-Albrechts-Universität Kiel, Germany, 2005.

[96] H. Hong, D. Davidov, Y. Avny, H. Chayet, E. Z. Faraggi, and R. Neumann, *Electroluminescence, photoluminescence and X-ray reflectivity studies of self-assembled ultra-thin films*, Adv. Mater. **7** (10), 846–849 (1995), DOI: `10.1002/adma.19950071006`.

[97] G. Hörmandinger, *Imaging of the Cu(111) surface state in scanning tunneling microscopy*, Phys. Rev. B **49** (19), 13897–13905 (1994), DOI: `10.1103/PhysRevB.49.13897`.

[98] G. Hörmandinger and J. B. Pendry, *Interaction of surface states with rows of adsorbed atoms and other one-dimensional scatterers*, Phys. Rev. B **50** (24), 18607–18620 (1994), DOI: `10.1103/PhysRevB.50.18607`.

[99] A. Hoshino, S. Isoda, H. Kurata, and T. Kobayashi, *Scanning tunneling microscope contrast of perylene-3,4,9,10-tetracarboxylic-dianhydride on graphite and its application to the study of epitaxy*, J. Appl. Phys. **76** (7), 4113–4120 (1994), DOI: `10.1063/1.357361`.

[100] M. A. van Hove, R. J. Koestner, P. C. Stair, J. P. Bibérian, L. L. Kesmodel, I. Bartoš, and G. A. Somorjai, *The surface reconstructions of the (100) crystal faces of iridium, platinum and gold*, Surf. Sci. **103** (1), 189–217 (1981), DOI: `10.1016/0039-6028(81)90107-2`.

[101] K. H. Huang, D. Gibbs, D. M. Zehner, A. R. Sandy, and S. G. J. Mochrie, *Phase behavior of the Au(111) surface: Discommensurations and kinks*, Phys. Rev. Lett. **65** (26), 3313–3316 (1990), DOI: `10.1103/PhysRevLett.65.3313`.

[102] F. Hund, *Zur Deutung der Molekelspektren. III*, Z. Phys. **43** (11–12), 805–826 (1927), DOI: `10.1007/BF01397249`.

[103] J. P. Ibe, P. P. Bey Jr., S. L. Brandow, R. A. Brizzolara, N. A. Burnham, D. P. DiLella, K. P. Lee, C. R. K. Marrian, and R. J. Colton, *On the electrochemical etching of tips for scanning tunneling microscopy*, J. Vac. Sci. Technol. A **8** (4), 3570–3575 (1990), DOI: `10.1116/1.576509`.

[104] J. E. Inglesfield, *A method of embedding*, J. Phys. C **14** (26), 3795–3806 (1981), DOI: `10.1088/0022-3719/14/26/015`.

[105] H. Jeffreys, *On certain approximate solutions of linear differential equations of the second order*, Proc. London Math. Soc. (Ser. 2) **23** (1), 428–436 (1925), DOI: `10.1112/plms/s2-23.1.428`.

[106] F. Jellinek, *Sulfides of the transition metals of groups IV, V and VI*, Ark. Kemi **20**, 447–480 (1963).

[107] F. Jellinek, G. Brauer, and H. Müller, *Molybdenum and niobium sulphides*, Nature **185** (4710), 376–377 (1960), DOI: `10.1038/185376a0`.

[108] H. Jensen, *Zusammenbau eines Rastertunnelmikroskops und erste Messungen an einkristallinen Metalloberflächen*, Diploma thesis, Christian-Albrechts-Universität Kiel, Germany, 2003.

[109] H. Jensen, J. Kröger, R. Berndt, and S. Crampin, *Electron dynamics in vacancy islands: Scanning tunneling spectroscopy on Ag(111)*, Phys. Rev. B **71** (15), 155417(5) (2005), DOI: `10.1103/PhysRevB.71.155417`.

[110] H. Jensen, J. Kröger, N. Néel, and R. Berndt, *Silver oligomer and single fullerene electronic properties revealed by a scanning tunnelling microscope*, Eur. Phys. J. D **45** (3), 465–469 (2007), DOI: `10.1140/epjd/e2007-00157-x`.

[111] I. Jensen, *Immunosuppression und Immunotoleranz nach Injektion allogener Zellen: Untersuchungen in einem Rattenmodell*, Dissertation, Christian-Albrechts-Universität Kiel, Germany, 1973.

[112] J. F. Jia, K. Inoue, Y. Hasegawa, W. S. Yang, and T. Sakurai, *Local work function for Cu(111)-Au surface studied by scanning tunneling microscopy*, J. Vac. Sci. Technol. B **15** (6), 1861–1864 (1997), DOI: `10.1116/1.589568`.

[113] P. Johansson, R. Monreal, and P. Apell, *Theory for light emission from a scanning tunneling microscope*, Phys. Rev. B **42** (14), 9210–9213 (1990), DOI: `10.1103/PhysRevB.42.9210`.

[114] R. S. Jones, *Solutions of the two-dimensional Helmholtz equation*, Dissertation, Ohio State University, Columbus, OH, USA, 1993.

[115] B. Joós, T. L. Einstein, and N. C. Bartelt, *Distribution of terrace widths on a vicinal surface within the one-dimensional free-fermion model*, Phys. Rev. B **43** (10), 8153–8162 (1991), DOI: `10.1103/PhysRevB.43.8153`.

[116] M. Kalff, G. Comsa, and T. Michely, *Temperature dependent morphological evolution of Pt(111) by ion erosion: Destabilization, phase coexistence and coarsening*, Surf. Sci. **486** (1–2), 103–135 (2001), DOI: `10.1016/S0039-6028(01)01015-9`.

[117] H. Katzke, P. Tolédano, and W. Depmeier, *Phase transition between polytypes and intralayer superstructures in transition metal dichalcogenides*, Phys. Rev. B **69** (13), 134111(8) (2004), DOI: `10.1103/PhysRevB.69.134111`.

[118] S. D. Kevan and R. H. Gaylord, *High-resolution photoemission study of the electronic structure of the noble-metal (111) surfaces*, Phys. Rev. B **36** (11), 5809–5818 (1987), DOI: `10.1103/PhysRevB.36.5809`.

[119] A. Klein, P. Dolatzoglou, M. Lux-Steiner, and E. Bucher, *Influence of material synthesis and doping on the transport properties of* WSe_2 *single crystals grown by selenium transport*, Sol. Energy Mater. Sol. Cells **46** (3), 175–186 (1997), DOI: `10.1016/S0927-0248(96)00093-1`.

[120] J. Klein, A. Léger, M. Belin, D. Défourneau, and M. J. L. Sangster, *Inelastic-electron-tunneling spectroscopy of metal–insulator–metal junctions*, Phys. Rev. B **7** (6), 2336–2348 (1973), DOI: `10.1103/PhysRevB.7.2336`.

[121] J. Kliewer, R. Berndt, E. V. Chulkov, V. M. Silkin, P. M. Echenique, and S. Crampin, *Dimensionality effects in the lifetime of surface states*, Science **288** (5470), 1399–1402 (2000), DOI: `10.1126/science.288.5470.1399`.

[122] J. Kliewer, R. Berndt, and S. Crampin, *Scanning tunnelling spectroscopy of electron resonators*, New J. Phys **3** (1), 22(11) (2001), DOI: `10.1088/1367-2630/3/1/322`.

[123] B. Koslowski, C. Dietrich, A. Tschetschetkin, and P. Ziemann, *Evaluation of scanning tunneling spectroscopy data: Approaching a quantitative determination of the electronic density of states*, Phys. Rev. B **75** (3), 035421(8) (2007), DOI: `10.1103/PhysRevB.75.035421`.

[124] W. Kossel, *Zur Theorie des Kristallwachstums*, Nachr. Ges. Wiss. Göttingen Math. Phys. Kl. **1927**, 135–143 (1927).

[125] H. A. Kramers, *Wellenmechanik und halbzahlige Quantisierung*, Z. Phys. **39** (10-11), 828–840 (1926), DOI: `10.1007/BF01451741`.

[126] J. Kröger, M. Becker, H. Jensen, T. von Hofe, N. Néel, L. Limot, R. Berndt, S. Crampin, E. Pehlke, C. Corriol, V. M. Silkin, D. Sánchez-Portal, A. Arnau, E. V. Chulkov, and P. M. Echenique, *Dynamics of surface-localized electronic excitations studied with the scanning tunnelling microscope*, Prog. Surf. Sci. **82** (4–6), 293–312 (2007), DOI: `10.1016/j.progsurf.2007.03.003`.

[127] J. Kröger, H. Jensen, R. Berndt, R. Rurali, and N. Lorente, *Molecular orbital shift of perylenetetracarboxylic-dianhydride on gold*, Chem. Phys. Lett. **438** (4–6), 249–253 (2007), DOI: `10.1016/j.cplett.2007.03.001`.

[128] J. Kröger, H. Jensen, T. Jürgens, T. von Hofe, J. Kuntze, and R. Berndt, *Adsorption geometry of PTCDA on 2H-*$NbSe_2$, Appl. Phys. A **81** (6), 1285–1289 (2005), DOI: `10.1007/s00339-004-3039-6`.

[129] J. Kröger, H. Jensen, N. Néel, and R. Berndt, *Self-organization of cobalt-phthalocyanine on a vicinal gold surface revealed by scanning tunnelling microscopy*, Surf. Sci. **601** (18), 4180–4184 (2007), DOI: `10.1016/j.susc.2007.04.091`.

[130] J. Kröger, L. Limot, H. Jensen, R. Berndt, S. Crampin, and E. Pehlke, *Surface state electron dynamics of clean and adsorbate-covered metal surfaces studied with the scanning tunnelling microscope*, Prog. Surf. Sci. **80** (1–2), 26–48 (2005), DOI: `10.1016/j.progsurf.2005.10.002`.

[131] J. Kröger, N. Néel, H. Jensen, R. Berndt, R. Rurali, and N. Lorente, *Molecules on vicinal Au surfaces studied by scanning tunnelling microscopy*, J. Phys. Condens. Matter **18** (13), S51–S66 (2006), DOI: `10.1088/0953-8984/18/13/S04`.

[132] J. A. Kubby, Y. R. Wang, and W. J. Greene, *Electron interferometry at a heterojunction interface*, Phys. Rev. Lett. **65** (17), 2165–2168 (1990), DOI: `10.1103/PhysRevLett.65.2165`.

[133] J. Lagoute, X. Liu, and S. Fölsch, *Link between adatom resonances and the Cu(111) Shockley surface state*, Phys. Rev. Lett. **95** (13), 136801(4) (2005), DOI: `10.1103/PhysRevLett.95.136801`.

[134] N. D. Lang, *Spectroscopy of single atoms in the scanning tunneling microscope*, Phys. Rev. B **34** (8), 5947–5950 (1986), DOI: `10.1103/PhysRevB.34.5947`.

[135] N. D. Lang, *Apparent barrier height in scanning tunneling microscopy*, Phys. Rev. B **37** (17), 10395–10398 (1988), DOI: `10.1103/PhysRevB.37.10395`.

[136] I. Langmuir, *The constitution and fundamental properties of solids and liquids. II. Liquids*, J. Am. Chem. Soc. **39** (9), 1848–1906 (1917), DOI: `10.1021/ja02254a006`.

[137] J. E. Lennard-Jones, *Cohesion*, Proc. Phys. Soc. **43** (5), 461–482 (1931), DOI: `10.1088/0959-5309/43/5/301`.

[138] K. Levenberg, *A method for the solution of certain nonlinear problems in least squares*, Quart. Appl. Math. **2**, 164–168 (1944), DOI: `10.1090/qam/10666`.

[139] J. Li, *Manipulation and spectroscopy at the atomic level*, Dissertation, Université de Lausanne, Switzerland, 1997.

[140] J. Li, W.-D. Schneider, and R. Berndt, *Local density of states from spectroscopic scanning-tunneling-microscope images: Ag(111)*, Phys. Rev. B **56** (12), 7656–7659 (1997), DOI: `10.1103/PhysRevB.56.7656`.

[141] J. Li, W.-D. Schneider, R. Berndt, O. R. Bryant, and S. Crampin, *Surface-state lifetime measured by scanning tunneling spectroscopy*, Phys. Rev. Lett. **81** (20), 4464–4467 (1998), DOI: `10.1103/PhysRevLett.81.4464`.

[142] J. Li, W.-D. Schneider, R. Berndt, and S. Crampin, *Electron confinement to nanoscale Ag islands of Ag(111): A quantitative study*, Phys. Rev. Lett. **80** (15), 3332–3335 (1998), DOI: `10.1103/PhysRevLett.80.3332`.

[143] J. Li, W.-D. Schneider, S. Crampin, and R. Berndt, *Tunnelling spectroscopy of surface state scattering and confinement*, Surf. Sci. **422** (1–3), 95–106 (1999), DOI: `10.1016/S0039-6028(98)00890-5`.

[144] W.-K. Li and S. M. Blinder, *Solution of the Schrödinger equation for a particle in an equilateral triangle*, J. Math. Phys. **26** (11), 2784–2786 (1985), DOI: `10.1063/1526701`.

[145] L. Limot, J. Kröger, R. Berndt, A. Garcia-Lekue, and W. A. Hofer, *Atom transfer and single-adatom contacts*, Phys. Rev. Lett. **94** (12), 126102(4) (2005), DOI: `10.1103/PhysRevLett.94.126102`.

[146] L. Liu and W. A. Bassett, *Compression of Ag and phase transformation of NaCl*, J. Appl. Phys. **44** (4), 1475–1479 (1973), DOI: `10.1063/1.1662396`.

[147] N. Lorente, private communication.

[148] A. J. Lovinger, S. R. Forrest, M. L. Kaplan, P. H. Schmidt, and T. Venkatesan, *Structural and morphological investigation of the development of electrical conductivity in ion-irradiated thin films of an organic material*, J. Appl. Phys. **55** (2), 476–482 (1984), DOI: `10.1063/1.333049`.

[149] C. Ludwig, B. Gompf, W. Glatz, J. Petersen, W. Eisenmenger, M. Möbus, U. Zimmermann, and N. Karl, *Video-STM, LEED and X-ray diffraction investigations of PTCDA on graphite*, Z. Phys. B **86** (3), 397–404 (1992), DOI: `10.1007/BF01323733`.

[150] C. Ludwig, B. Gompf, J. Petersen, R. Strohmaier, and W. Eisenmenger, *STM investigations of PTCDA and PTCDI on graphite and MoS_2. A systematic study of epitaxy and STM image contrast*, Z. Phys. B **93** (3), 365–373 (1994), DOI: `10.1007/BF01312708`.

[151] J. Maclennan, G. Decher, and U. Sohling, *Freely suspended liquid crystal film transfer: A new method of creating thin smectic films on solid substrates*, Appl. Phys. Lett. **59** (8), 917–919 (1991), DOI: `10.1063/1.106300`.

[152] A. Maeland and T. B. Flanagan, *Lattice spacings of gold–palladium alloys*, Can. J. Phys. **42** (11), 2364–2366 (1964), DOI: `10.1139/p64-213`.

[153] W. Magnus, *On the exponential solution of differential equations for a linear operator*, Comm. Pure Appl. Math. **7** (4), 649–673 (1954), DOI: `10.1002/cpa.3160070404`.

[154] W. Magnus and F. Oberhettinger, *Formeln und Sätze für die speziellen Funktionen der mathematischen Physik*, Springer, Berlin, Germany, 1943.

[155] V. I. Marchenko, *Theory of the equilibrium shape of crystals*, Sov. Phys. JETP **54** (3), 605–607 (1981).

[156] M. Marezio, P. D. Dernier, A. Menth, and G. W. Hull Jr., *The crystal structure of $NbSe_2$ at 15řK*, J. Solid State Chem. **4** (3), 425–429 (1972), DOI: `10.1016/0022-4596(72)90158-2`.

[157] D. W. Marquardt, *An algorithm for least-squares estimation of nonlinear parameters*, J. Soc. Indust. Appl. Math. **11** (2), 431–441 (1963), DOI: `10.1137/0111030`.

[158] A. Meerschaut and C. Deudon, *Crystal structure studies of the 3R-$Nb_{1.09}S_2$ and the 2H-$NbSe_2$ compounds: Correlation between nonstochiometry and stacking type (= polytypism)*, Mater. Res. Bull. **36** (9), 1721–1727 (2001), DOI: `10.1016/S0025-5408(01)00646-8`.

[159] K. Meinel, M. Klaua, and H. Bethge, *On twin and stacking fault formation during the epitaxial film growth of f.c.c. materials on (111) substrates*, Phys. Status Solidi A **110** (1), 189–196 (1988), DOI: `10.1002/pssa.2211100118`.

[160] K. Meinel, M. Klaua, and H. Bethge, *The influence of the substrate microtopography on the growth of thin films studied for the Au–Ag system by TEM and EAS*, J. Cryst. Growth **89** (4), 447–458 (1988), DOI: `10.1016/0022-0248(88)90205-9`.

[161] J. A. Meyer and R. J. Behm, *Comment on: Layer-by-layer growth of Ag on Ag(111) induced by enhanced nucleation: A model study for surfactant-mediated growth*, Phys. Rev. Lett. **73** (2), 364 (1994), DOI: `10.1103/PhysRevLett.73.364`.

[162] W. C. Michels and N. L. Curtis, *A pentode lock-in amplifier of high frequency selectivity*, Rev. Sci. Instrum. **12** (9), 444–447 (1941), DOI: `10.1063/1.1769919`.

[163] T. Michely, K. H. Besocke, and G. Comsa, *Observation of sputtering damage on Au(111)*, Surf. Sci. Lett. **230** (1–3), L135–L139 (1990), DOI: `10.1016/0039-6028(90)90002-P`.

[164] T. Michely and G. Comsa, *Temperature dependence of the sputtering morphology of Pt(111)*, Surf. Sci. **256** (3), 217–226 (1991), DOI: `10.1016/0039-6028(91)90865-P`.

[165] T. Michely and G. Comsa, *Generation and nucleation of adatoms during ion bombardment of Pt(111)*, Phys. Rev. B **44** (15), 8411–8414 (1992), DOI: `10.1103/PhysRevB.44.8411`.

[166] W. H. Miller, *A treatise on crystallography*, Deighton, Cambridge, UK, 1839.

[167] M. Möbus, N. Karl, and T. Kobayashi, *Structure of perylene-tetracarboxylic-dianhydride thin films on alkali halide crystal substrates*, J. Cryst. Growth **116** (3–4), 495–504 (1992), DOI: `10.1016/0022-0248(92)90658-6`.

[168] P. Monçeau, N. P. Ong, A. M. Portis, A. Meerschaut, and J. Rouxel, *Electric field breakdown of charge-density-wave–induced anomalies in $NbSe_3$*, Phys. Rev. Lett. **37** (10), 602–605 (1976), DOI: `10.1103/PhysRevLett.37.602`.

[169] D. E. Moncton, J. D. Axe, and F. J. DiSalvo, *Study of superlattice formation in 2H-$NbSe_2$ and 2H-$TaSe_2$ by neutron scattering*, Phys. Rev. Lett. **34** (12), 734–737 (1975), DOI: `10.1103/PhysRevLett.34.734`.

[170] J. C. Nash, *Compact numerical methods for computers: Linear algebra and function minimization*, 2nd ed., Adam Hilger, Bristol, UK, 1990.

[171] J. A. Nelder and R. Mead, *A simplex method for function minimization*, Comput. J. **7** (4), 308–311 (1965), DOI: `10.1093/comjnl/7.4.308`.

[172] N. Nicoara, E. Román, J. M. Gómez-Rodríguez, J. A. Martí-Gago, and J. Méndez, *Scanning tunneling and photoemission spectroscopies at the PTCDA/Au(111) interface*, Org. Electron. **7** (11), 287–294 (2006), DOI: `10.1016/j.orgel.2006.03.010`.

[173] N. Nilius, T. M. Wallis, and W. Ho, *Development of one-dimensional band structure in artificial gold chains*, Science **297** (5588), 1853–1856 (2002), DOI: `10.1126/science.1075242`.

[174] S. Nogaki and M. Ohta, *An overlapped block motion compensation for high quality motion picture coding*, Proc. 1992 IEEE Int. Symp. Circuits Syst. **1**, 184–187 (1992), DOI: `10.1109/ISCAS.1992.229983`.

[175] T. Ogawa, K. Kuwamoto, S. Isoda, T. Kobayashi, and N. Karl, *3,4:9,10-perylenetetracarboxylic dianhydride (PTCDA) by electron crystallography*, Acta Cryst. B **55**, 123–130 (1999), DOI: `10.1107/S0108768198009872`.

[176] J. E. Ortega, A. Mugarza, V. Repain, S. Rousset, V. Pérez-Dieste, and A. Mascaraque, *One-dimensional versus two-dimensional surface states on stepped Au(111)*, Phys. Rev. B **65** (16), 165413(7) (2002), DOI: `10.1103/PhysRevB.65.165413`.

[177] J. R. Ostrick, A. Dodabalapur, L. Torsi, A. J. Lovinger, E. W. Kwock, T. M. Miller, M. Galvin, M. Berggren, and H. E. Katz, *Conductivity-type anisotropy in molecular solids*, J. Appl. Phys. **81** (10), 6804–6808 (1997), DOI: `10.1063/1.365238`.

[178] A. W. Overhauser, *Exchange and correlation instabilities of simple metals*, Phys. Rev. **167** (1), 691–698 (1968), DOI: `10.1103/PhysRev.167.691`.

[179] R. Paniago, R. Matzdorf, G. Meister, and A. Goldmann, *Temperature dependence of Shockley-type surface energy bands on Cu(111), Ag(111) and Au(111)*, Surf. Sci. **336** (1–2), 113–122 (1995), DOI: `10.1016/0039-6028(95)00509-9`.

[180] F. Patthey and W.-D. Schneider, *Layer-by-layer-resolved quantum-well states in ultrathin silver islands on graphite: A photoemission study*, Phys. Rev. B **50** (23), 17560–17563 (1994), DOI: `10.1103/PhysRevB.50.17560`.

[181] R. Peierls, *Zur Theorie der elektrischen und thermischen Leitfähigkeit von Metallen*, Ann. Phys. **396** (2), 121–148 (1930), DOI: `10.1002/andp.19303960202`.

[182] J. Perdereau, J. P. Bibérian, and G. E. Rhead, *Adsorption and surface alloying of lead monolayers on (111) and (110) faces of gold*, J. Phys. F **4** (5), 798–806 (1974), DOI: `10.1088/0305-4608/4/5/022`.

[183] J. P. Perdew, K. Burke, and M. Ernzerhof, *Generalized gradient approximation made simple*, Phys. Rev. Lett. **77** (18), 3865–3868 (1996), DOI: `10.1103/PhysRevLett.77.3865`.

[184] R. J. Phaneuf, N. C. Bartelt, E. D. Williams, W. Święch, and E. Bauer, *Low-energy electron-microscopy investigations of orientational phase separation on vicinal Si(111) surfaces*, Phys. Rev. Lett. **67** (21), 2986–2989 (1991), DOI: `10.1103/PhysRevLett.67.2986`.

[185] R. J. Phaneuf, E. D. Williams, and N. C. Bartelt, *Temperature dependence of vicinal Si(111) surfaces*, Phys. Rev. B **38** (3), 1984–1993 (1988), DOI: `10.1103/PhysRevB.38.1984`.

[186] A. Pockels, *On the relative contamination of the water-surface by equal quantities of different substances*, Nature **46** (1192), 418–419 (1892), DOI: `10.1038/046418e0`.

[187] B. Poelsema, K. Lenz, L. S. Brown, L. K. Verheij, and G. Comsa, *Lateral distribution of ion bombardment induced effects on Pt(111) at 80 K*, Surf. Sci. **162** (1–3), 1011–1016 (1985), DOI: `10.1016/0039-6028(85)91015-5`.

[188] W. H. Press, S. A. Teukolsky, W. T. Vetterling, and B. P. Flannery, *Numerical recipes in C. The art of scientific computing*, 2nd ed., Cambridge University Press, Cambridge, UK, 1992.

[189] L. S. Ramsdell, *Studies on silicon carbide*, Am. Mineral. **32** (1–2), 64–82 (1947).

[190] J. W. Strutt, 3rd Baron Rayleigh, *On the superficial viscosity of water*, Proc. R. Soc. London **48** (293), 127–140 (1890), DOI: `10.1098/rspl.1890.0018`.

[191] F. Reinert, G. Nicolay, S. Schmidt, D. Ehm, and S. Hüfner, *Direct measurements of the L-gap surface states on the (111) face of noble metals by photoelectron spectroscopy*, Phys. Rev. B **63** (11), 115415(7) (2001), DOI: `10.1103/PhysRevB.63.115415`.

[192] V. Repain, G. Baudot, H. Ellmer, and S. Rousset, *Ordered growth of cobalt nanostructures on a Au(111) vicinal surface: Nucleation mechanisms and temperature behavior*, Mater. Sci. Eng. B **96** (2), 178–187 (2002), DOI: `10.1016/S0921-5107(02)00315-X`.

[193] V. Repain, J. M. Berroir, B. Croset, S. Rousset, Y. Garreau, V. H. Etgens, and J. Lecœur, *Interplay between atomic and mesoscopic order on gold vicinal surfaces*, Phys. Rev. Lett. **84** (23), 5367–5370 (2000), DOI: `10.1103/PhysRevLett.84.5367`.

[194] V. Repain, J. M. Berroir, S. Rousset, and J. Lecœur, *Interaction between steps and reconstruction on Au(111)*, Europhys. Lett. **47** (4), 435–441 (1999), DOI: `10.1209/epl/i1999-00406-6`.

[195] J. Repp, G. Meyer, K.-H. Rieder, and P. Hyldgaard, *Site determination and thermally assisted tunneling in homogenous nucleation*, Phys. Rev. Lett. **91** (20), 206102(4) (2003), DOI: `10.1103/PhysRevLett.91.206102`.

[196] J. Repp, G. Meyer, S. M. Stojković, A. Gourdon, and C. Joachim, *Molecules on insulating films: Scanning-tunneling microscopy imaging of individual molecular orbitals*, Phys. Rev. Lett. **94** (2), 026803(4) (2005), DOI: `10.1103/PhysRevLett.94.026803`.

[197] G. Rosenfeld, K. Morgenstern, M. Esser, and G. Comsa, *Dynamics and stability of nanostructures on metal surfaces*, Appl. Phys. A **69** (5), 489–496 (1999), DOI: `10.1007/s003390051448`.

[198] G. Rosenfeld, N. N. Lipkin, W. Wulfhekel, J. Kliewer, K. Morgenstern, B. Poelsema, and G. Comsa, *New concepts for controlled homoepitaxy*, Appl. Phys. A **61** (5), 455–466 (1995), DOI: `10.1007/BF10540247`.

[199] G. Rosenfeld, R. Servaty, C. Teichert, B. Poelsema, and G. Comsa, *Layer-by-layer growth of Ag on Ag(111) induced by enhanced nucleation: A model study for surfactant-mediated growth*, Phys. Rev. Lett. **71** (6), 895–898 (1993), DOI: `10.1103/PhysRevLett.71.895`.

[200] K. Rossnagel, O. Seifarth, L. Kipp, M. Skibowski, D. Voß, P. Krüger, A. Mazur, and J. Pollmann, *Fermi surface of 2H-NbSe$_2$ and its implications on the charge-density-wave mechanism*, Phys. Rev. B **64** (23), 235119(6) (2001), DOI: `10.1103/PhysRevB.64.235119`.

[201] S. Rousset, F. Pourmir, J. M. Berroir, J. Klein, J. Lecœur, P. Hecquet, and B. Salanon, *Self-organization on Au(111) vicinal surfaces and the role of surface stress*, Surf. Sci. **422** (1–3), 33–41 (1999), DOI: `10.1016/S0039-6028(99)00866-8`.

[202] S. Rousset, V. Repain, G. Baudot, Y. Garreau, and J. Lecœur, *Self-ordering of Au(111) vicinal surfaces and application to nanostructure organized growth*, J. Phys. Condens. Matter **15** (47), S3363–S3392 (2003), DOI: `10.1088/0953-8984/15/47/009`.

[203] A. M. Russell and D. A. Torchia, *Harmonic analysis in systems using phase sensitive detectors*, Rev. Sci. Instrum. **33** (4), 442–444 (1962), DOI: `10.1063/1.1717875`.

[204] H. Schäfer, *Chemische Transportreaktionen: Der Transport anorganischer Stoffe über die Gasphase und seine Anwendungen*, Verlag Chemie, Weinheim, FR Germany, 1962.

[205] T. Schmitz-Hübsch, T. Fritz, F. Sellam, R. Staub, and K. Leo, *Epitaxial growth of 3,4,9,10-perylene-tetracarboxylic-dianhydride on Au(111): A STM and RHEED study*, Phys. Rev. B **55** (12), 7972–7976 (1997), DOI: `10.1103/PhysRevB.55.7972`.

[206] R. L. Schwoebel and E. J. Shipsey, *Step motion on crystal surfaces*, J. Appl. Phys. **37** (10), 3682–3686 (1966), DOI: `10.1063/1.1707904`.

[207] C. Seidel, C. Awater, X. D. Liu, R. Ellerbrake, and H. Fuchs, *A combined STM, LEED and molecular modelling study of PTCDA grown on Ag(110)*, Surf. Sci. **371** (1), 123–130 (1997), DOI: `10.1016/S0039-6028(96)00981-8`.

[208] A. Selloni, P. Carnevali, E. Tosatti, and C. D. Chen, *Voltage-dependent scanning-tunneling microscopy of a crystal surface: Graphite*, Phys. Rev. B **31** (4), 2602–2605 (1985), DOI: `10.1103/PhysRevB.31.2602`.

[209] S. Shiraki, H. Fujisawa, M. Nantoh, and M. Kawai, *Confining barriers for surface state electrons tailored by monatomic Fe rows on vicinal Au(111) surfaces*, Phys. Rev. Lett. **92** (9), 096102(4) (2004), DOI: `10.1103/PhysRevLett.92.096102`.

[210] W. Shockley, *On the surface states associated with a periodic potential*, Phys. Rev. **56** (4), 317–323 (1939), DOI: `10.1103/PhysRev.56.317`.

[211] J. G. Simmons, *Generalized formula for the electric tunnel effect between similar electrodes separated by a thin insulating film*, J. Appl. Phys. **34** (6), 1793–1803 (1963), DOI: `10.1063/1.1702682`.

[212] N. V. Smith and D. P. Woodruff, *Inverse photoemission from metal surfaces*, Prog. Surf. Sci. **21** (4), 295–370 (1986), DOI: `10.1016/0079-6816(86)90004-3`.

[213] R. Smoluchowski, *Anisotropy of the electronic work function of metals*, Phys. Rev. **60** (9), 661–674 (1941), DOI: `10.1103/PhysRev.60.661`.

[214] A. Sommerfeld and H. Bethe, *Elektronentheorie der Metalle*, Springer, Berlin, FR Germany, 1967.

[215] A. Sperl, *Spektroskopie atomarer Silber-Cluster auf Ag(111)*, Diploma thesis, Christian-Albrechts-Universität Kiel, Germany, 2008.

[216] V. S. Stepanyuk, A. N. Klavsyuk, L. Niebergall, and P. Bruno, *End electronic states in Cu chains on Cu(111): Ab initio calculations*, Phys. Rev. B **72** (15), 153407(4) (2005), DOI: `10.1103/PhysRevB.72.153407`.

[217] B. C. Stipe, M. A. Rezaei, and W. Ho, *Single-molecule vibrational spectroscopy and microscopy*, Science **280** (5370), 1732–1735 (1998), DOI: `10.1126/science.280.5370.1732`.

[218] I. N. Stranski and L. Krastanov, *Zur Theorie der orientierten Ausscheidung von Ionenkristallen aufeinander*, Sitzungsber. Akad. Wiss. Wien Math. Naturwiss. Kl. IIb **146**, 797–810 (1938).

[219] J. A. Stroscio, R. M. Feenstra, and A. P. Fein, *Electronic structure of the Si(111)* 2×1 *surface by scanning-tunneling microscopy*, Phys. Rev. Lett. **57** (20), 2579–2582 (1986), DOI: `10.1103/PhysRevLett.57.2579`.

[220] W. B. Su, S. M. Lu, H. T. Shih, C. L. Jiang, C. S. Chang, and T. T. Tsong, *Manifestation of the quantum size effect in transmission resonance*, J. Phys. Condens. Matter **18** (27), 6299–6305 (2006), DOI: `10.1088/0953-8984/18/27/013`.

[221] T. Suzuki, Y. Hasegawa, Z.-Q. Li, K. Ohno, Y. Kawazoe, and T. Sakurai, *Electron standing-wave observation in the Pd overlayer on Au(111) and Cu(111) surfaces by scanning tunneling microscopy*, Phys. Rev. B **64** (8), 081403(4) (2001), DOI: `10.1103/PhysRevB.64.081403`.

[222] I. Tamm, *Über eine mögliche Art der Elektronenbindung an Kristalloberflächen*, Z. Phys. **76** (11–12), 849–850 (1932), DOI: `10.1007/BF01341581`.

[223] E. C. Teague, *Room temperature gold–vacuum–gold tunneling experiment*, J. Res. Nat. Bur. Stand. **91** (4), 171–233 (1986), DOI: `10.6028/jres.091.027`.

[224] J. Tersoff and D. R. Hamann, *Theory and application for the scanning tunneling microscope*, Phys. Rev. Lett. **50** (25), 1998–2001 (1983), DOI: `10.1103/PhysRevLett.50.1998`.

[225] F. Theilmann, R. Matzdorf, G. Meister, and A. Goldmann, *Influence of surface structural disorder on linewidths in angle-resolved photoemission spectra*, Phys. Rev. B **56** (7), 3632–3635 (1997), DOI: `10.1103/PhysRevB.56.3632`.

[226] D. G. Tucker, *The history of the homodyne and synchrodyne*, J. Brit. Inst. Radio Eng. **14** (4), 143–154 (1954), DOI: `10.1049/jbire.1954.0021`.

[227] V. A. Ukraintsev, *Data evaluation technique for electron-tunneling spectroscopy*, Phys. Rev. B **53** (16), 11176–11185 (1996), DOI: `10.1103/PhysRevB.53.11176`.

[228] *Ullmann's encyclopedia of industrial chemistry*, 6th ed., **vol. 27**, Wiley-VCH, Weinheim, Germany, 2003.

[229] J. A. Venables, G. D. T. Spiller, and M. Hanbücken, *Nucleation and growth of thin films*, Rep. Prog. Phys. **47** (4), 399–459 (1984), DOI: `10.1088/0034-4885/47/4/002`.

[230] J. Villain, *Continuum models of crystal growth from atomic beams with and without desorption*, J. Phys. I **1** (1), 19–42 (1991), DOI: `10.1051/jp1:1991114`.

[231] L. Vitali, P. Wahl, M. A. Schneider, K. Kern, V. M. Silkin, E. V. Chulkov, and P. M. Echenique, *Inter- and intraband inelastic scattering of hot surface state electrons at the Ag(111) surface*, Surf. Sci. Lett. **523** (1–2), L47–L52 (2003), DOI: `10.1016/S0039-6028(02)02406-8`.

[232] P. Wahl, M. A. Schneider, L. Diekhöner, R. Vogelgesang, and K. Kern, *Quantum coherence of image-potential states*, Phys. Rev. Lett. **91** (10), 106802(4) (2003), DOI: `10.1103/PhysRevLett.91.106802`.

[233] S. C. Wang, *Die gegenseitige Einwirkung zweier Wasserstoffatome*, Phys. Z. **28**, 663–666 (1927).

[234] H. Watanabe and S. Singhal, *Windowed motion compensation*, Proc. SPIE **1605**, 582–589 (1991), DOI: `10.1117/12.50301`.

[235] G. N. Watson, *A treatise on the theory of Bessel functions*, 2nd ed., Cambridge University Press, Cambridge, UK, 1944.

[236] G. Wentzel, *Eine Verallgemeinerung der Quantenbedingungen für die Zwecke der Wellenmechanik*, Z. Phys. **38** (6–7), 518–529 (1926), DOI: `10.1007/BF01397171`.

[237] R. Wiesendanger, *Spin mapping at the nanoscale and atomic scale*, Rev. Mod. Phys. **81** (4), 1495–1550 (2009), DOI: `10.1103/RevModPhys.81.1495`.

[238] E. D. Williams, *Surface steps and surface morphology: Understanding macroscopic phenomena from atomic observations*, Surf. Sci. **299–300**, 502–524 (1994), DOI: `10.1016/0039-6028(94)90678-5`.

[239] J. A. Wilson and A. D. Yoffe, *The transition metal dichalcogenides: Discussion and interpretation of the observed optical, electrical and structural properties*, Adv. Phys. **18** (73), 193–335 (1969), DOI: `10.1080/00018736900101307`.

[240] C. Y. Young, R. Pindak, N. A. Clark, and R. B. Meyer, *Light-scattering study of two-dimensional molecular-orientation fluctuations in a freely suspended ferroelectric liquid-crystal film*, Phys. Rev. Lett. **40** (12), 773–776 (1978), DOI: `10.1103/PhysRevLett.40.773`.

[241] R. Young, J. Ward, and F. Scire, *The Topografiner: An instrument for measuring surface microtopography*, Rev. Sci. Instrum. **43** (7), 999–1011 (1972), DOI: `10.1063/1.1685846`.

[242] Y. Zhang and S. R. Forrest, *Mechanisms of quasiepitaxial ordering at organic molecular thin film interfaces*, Phys. Rev. Lett. **71** (17), 2765–2768 (1993), DOI: `10.1103/PhysRevLett.71.2765`.

[243] M. Ziegler, N. Néel, A. Sperl, J. Kröger, and R. Berndt, *Local density of states from constant-current tunneling spectra*, Phys. Rev. B **80** (12), 125402(6) (2009), DOI: `10.1103/PhysRevB.80.125402`; revised in: Phys. Rev. B **91** (3), 039902(1) (2015), DOI: `10.1103/PhysRevB.91.039902`.

[244] U. Zimmermann, G. Schnitzler, M. Schneider, M. Kaiser, R. Herde, V. Wüstenhagen, J. Taborski, N. Karl, R. Dudde, E.-E. Koch, and E. Umbach, *Monolayer adsorption and thin film growth of big aromatic molecules on Si(111)*, Vacuum **41** (7–9), 1795–1796 (1990), DOI: `10.1016/0042-207X(90)94095-8`.

Eidesstattliche Versicherung

Hiermit erkläre ich an Eides statt, dass ich die vorliegende Arbeit selbständig unter Beratung meiner wissenschaftlichen Lehrer und nur mit den angegebenen Quellen und Hilfsmitteln verfasst habe. Sie wurde unter Einhaltung der Regeln guter wissenschaftlicher Praxis der Deutschen Forschungsgemeinschaft erstellt und weder in Gänze noch in Teilen jemals an anderer Stelle im Rahmen eines Prüfungsverfahrens vorgelegt, veröffentlicht oder zur Veröffentlichung eingereicht. Frühere Promotionsversuche wurden von mir nicht vorgenommen.